Two-Dimensional Ferromagnetism and Topology at the Surface of $MnBi_2Te_4$ - Bi_2Te_3 Heterostructures – MBE Growth, Magnetism and Electronic Properties

Dissertation zur Erlangung des
naturwissenschaftlichen Doktorgrades
der Julius-Maximilians-Universität Würzburg

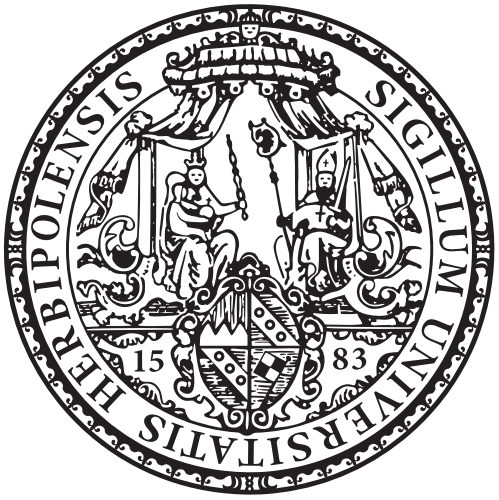

vorgelegt von

Philipp Thomas Kagerer

aus Neustadt a.d. Aisch

Würzburg, 2023

Eingereicht am:
bei der Fakultät für Physik und Astronomie

1. Gutachter: Prof. Dr. Hendrik Bentmann
2. Gutachter: Prof. Dr. Matthias Bode
3. Gutachter:
der Dissertation.

Vorsitzende(r):
1. Prüfer: Prof. Dr. Hendrik Bentmann
2. Prüfer: Prof. Dr. Matthias Bode
3. Prüfer: Prof. Dr. Giorgio Sangiovanni
im Promotionskolloquium.

Tag des Promotionskolloquiums: 03.05.2024

Doktorurkunde ausgehändigt am:

Abstract

As a result of the observation of peculiar properties such as quantised conductance, topological insulators (TI) have become a highly intriguing research topic in recent years, both from the perspective of fundamental physics and with a view to application. After first observations of the topological surface states (TSS) present in topological insulators, the search for the interplay between magnetism and topology as a consequence of the breaking of fundamental bulk symmetries such as time-reversal has emerged as a central question in the research on TI. This work aims to address the consequences of this interplay in a system, where two-dimensional magnetism is introduced locally to the surface of a 3D TI. To this end, a model system is utilized, namely a heterosystem consisting of a single ferromagnetic septuple-layer (SL) of $MnBi_2Te_4$ on the surface of the three-dimensional topological insulator Bi_2Te_3, which has been fabricated by means of molecular beam epitaxy (MBE).

The first step in this regard is to establish a suitable mechanism for the fabrication of such van der Waals (vdW) heterostructures. By using the method of MBE and developing a specialized experimental setup, the first part of this thesis deals with the growth of Bi_2Te_3 and thin films of $MnBi_2Te_4$ on BaF_2-substrates by the co-evaporation of its binary constituent materials. The structural analysis is conducted along several suitable probes such as X-ray diffraction (XRD, XRR), atomic force microscopy (AFM) and scanning tunnelling electron microscopy (STEM). These findings map out the phase diagram of the MBE growth and its in depth understanding allows to transfer the growth mechanism to more complex structures. In particular, it is found that the growth of a single septuple-layer of $MnBi_2Te_4$ on the surface of Bi_2Te_3 can be facilitated. The remainder of the first part concerns the structural properties of this heterostructure and the use of functional substrates, especially the layered ferromagnet Fe_3GeTe_2.

By predominantly using X-ray absorption and X-ray circular magnetic dichroism (XAS, XMCD) as a probe, the magnetic properties of $MnBi_2Te_4$ are explored down to the monolayer limit. It is shown, that the layered nature of the vdW crystal and a strong uniaxial magnetocrystalline anisotropy establish stable out-of plane magnetic order at the surface of $MnBi_2Te_4$ crystals, which is stable even down to the monolayer limit, where magnetic coupling is only present along the two-dimensional sheet of Mn ions. Pushing the material system to its 2D limit, i.e. a single SL $MnBi_2Te_4$ further allows to study the phase transition of this 2D ferromagnetic material in more detail and extract its critical behaviour over the phase transition with a critical temperature of $T_c = 14.89\,\mathrm{K}$ and a critical coefficient of $\beta = 0.484$.

An appropriate choice of substrate – in this case bulk crystals of the aforementioned ferromagnetic Fe_3GeTe_2 – allows to influence, enhance and bias the magnetism in the

single SL of $MnBi_2Te_4$. By growing heterostructures of the type $MnBi_2Te_4$ – n layer Bi_2Te_3 – Fe_3GeTe_2 for n between 0 and 2, it is shown, that a considerable magnetic coupling can be introduced between the $MnBi_2Te_4$ top-layer and the substrate. The coupling ranges from strongly antiferromagnetic for $n = 0$ up to effectively ferromagnetic for $n = 2$.

The last part of this thesis aims to study the interplay between topology and magnetism in the ferromagnetic extension directly by angle-resolved photoemission spectroscopy. The heterostructure is found to host a linearly dispersing TSS at the $\overline{\Gamma}$-point of the Brillouin zone, whose shape is significantly altered from the parent material Bi_2Te_3 with the Dirac point placed in the centre of the bulk band gap. Using low temperature and high-resolution ARPES a large magnetic gap opening of $\sim 35\,\text{meV}$ is found at the Dirac point of the TSS. By following its temperature evolution, it is apparent that the scaling behaviour coincides with the magnetic order parameter of the modified surface.

In conclusion, this thesis addresses the experimental realisation of the ferromagnetic extension concept. A heterostructure of a single SL of $MnBi_2Te_4$ on the surface of a thick film of Bi_2Te_3 is grown by MBE. Probing its magnetic and electronic properties confirms stable 2D ferromagnetism at the surface, which strongly interacts with the TSS. A large magnetic gap opening can be observed together with the onset of magnetism and the magnetic properties can further be engineered by the use of ferromagnetic substrates. The findings show the feasibility of the ferromagnetic extension approach and hence present a paradigm to efficiently incorporate magnetism in topological insulators without the fundamental limitation of strong disorder.

Zusammenfassung

Aufgrund der Beobachtung besonderer Eigenschaften wie der quantisierten Leitfähigkeit haben sich topologische Isolatoren (TI) in den letzten Jahren zu einem hochinteressanten Forschungsthema entwickelt, sowohl aus Sicht der Grundlagenphysik als auch mit Blick auf potentielle Anwendungsfälle. Nach den ersten Beobachtungen der topologischen Oberflächenzustände (engl. *topological surface state,* TSS) in topologischen Isolatoren hat sich die Suche nach dem Wechselspiel zwischen Magnetismus und Topologie als Folge der Brechung fundamentaler Symmetrien zu einem wichtigen Teil dieses Gebiets entwickelt. Diese Arbeit zielt darauf ab, die Konsequenzen dieses Zusammenspiels in einem System zu untersuchen, in dem zweidimensionaler Magnetismus lokal auf die Oberfläche eines 3D TI eingebracht wird. Zu diesem Zweck wird ein Heterosystem verwendet, das aus einer einzelnen ferromagnetischen Septupellage (SL) aus $MnBi_2Te_4$ auf der Oberfläche des dreidimensionalen topologischen Isolators Bi_2Te_3 besteht, das mittels Molekularstrahlepitaxie (engl. *molecular beam epitaxy,* MBE) hergestellt wurde. Der erste Schritt in dieser Hinsicht ist das Etablieren eines geeigneten Mechanismus für die Herstellung derartiger van der Waals-Heterostrukturen. Unter Verwendung der Methode der MBE und der Entwicklung eines geeigneten Versuchsaufbaus wird im ersten Teil dieser Arbeit das Wachstum von Bi_2Te_3 und dünnen Filmen von $MnBi_2Te_4$ auf BaF_2 Substraten durch das Ko-Verdampfen ihrer binären Bestandteile beschrieben. Die strukturelle Analyse erfolgt mit Hilfe mehrerer geeigneter Methoden zur Strukturanalyse wie Röntgenbeugung (*engl. X-ray diffraction and reflectivity* XRD, XRR), Rasterkraftmikroskopie (*engl. atomic force microscopy,* AFM) und Rastertransmissionselektronenmikroskopie (*engl. scanning tunneling electron microscopy,* STEM). Die Ergebnisse zeichnen das Phasendiagramm dieses MBE-Wachstums nach, was es wiederum ermöglicht, den Wachstumsmechanismus auf komplexere Strukturen zu übertragen. Es wird ein Mechanismus für das Wachstum von $MnBi_2Te_4$ auf der Oberfläche von Bi_2Te_3 erarbeitet, und der Rest des ersten Teils befasst sich mit den strukturellen Eigenschaften dieser Heterostruktur und der Verwendung von funktionalen Substraten, insbesondere dem geschichteten Ferromagneten Fe_3GeTe_2.
Unter Verwendung der element- und magnetismusempfindlichen Röntgenabsorption und des zirkularen magnetischen Röntgendichroismus (*engl. X-ray absorption and magnetic circular dichroism,* XAS, XMCD) als primäre Methode, unterstützt durch Magnetotransportexperimente, werden die magnetischen Eigenschaften von $MnBi_2Te_4$ bis zur Monolagengrenze erforscht. Es wird gezeigt, dass die geschichtete Natur des vdW-Kristalls und eine starke uniaxiale magnetokristalline Anisotropie eine stabile magnetische Ordnung entlang der Oberflächennormale an der Oberfläche von $MnBi_2Te_4$-

Kristallen etablieren. Diese ist bis hinunter zur Monolagengrenze stabil, wo die magnetische Kopplung nur entlang der zweidimensionalen Schicht von Mn Ionen stattfindet. Die Verwendung einer einzelnen Septupellage von $MnBi_2Te_4$ ermöglicht es, den Phasenübergang dieses 2D ferromagnetischen Materials genauer zu untersuchen und sein kritisches Verhalten über den Phasenübergang mit einer kritischen Temperatur von $T_c = 14.89\,\mathrm{K}$ herauszuarbeiten. Durch eine geeignete Wahl des Substrats, in diesem Fall Volumenkristalle des oben genannten ferromagnetischen Fe_3GeTe_2, kann der Magnetismus in der einzelnen SL $MnBi_2Te_4$ beeinflusst werden. Durch Aufwachsen von Heterostrukturen der Form $MnBi_2Te_4$ - n Lagen Bi_2Te_3 - Fe_3GeTe_2 für n zwischen 0 und 2 wird gezeigt, dass eine beträchtliche magnetische Kopplung zwischen der aufgewachsenen Schicht und dem Substrat erzeugt werden kann. Die Kopplung reicht von stark antiferromagnetisch für $n = 0$ bis zu effektiv ferromagnetisch für $n = 2$.
Der letzte Teil dieser Arbeit zielt darauf ab, das Zusammenspiel zwischen Topologie und Magnetismus in der modifizierten Oberfläche direkt durch winkelaufgelöste Photoemissionsspektroskopie (*engl. angle resolved photoemission spectroscopy,* ARPES) zu untersuchen. Es wird festgestellt, dass die Heterostruktur einen linear dispergierenden TSS am $\bar{\Gamma}$-Punkt der Brillouin Zone aufweist, dessen Form gegenüber dem Ausgangsmaterial Bi_2Te_3 deutlich verändert ist, wobei der Dirac-Punkt in der Mitte der Volumenbandlücke liegt. Unter Verwendung von hochauflösendem ARPES bei sehr niedrigen Temperaturen kann am Dirac-Punkt des TSS eine große magnetische Energielücke von $\sim 35\,\mathrm{meV}$ aufgelöst werden. Eine Analyse der Temperaturabhängigkeit zeigt des Weiteren, dass das Skalierungsverhalten mit dem des magnetischen Ordnungsparameters der modifizierten Oberfläche übereinstimmt.
Zusammengefasst befasst sich diese Arbeit mit der experimentellen Umsetzung des Konzepts der ferromagnetischen Oberflächenmodifizierung. Eine Heterostruktur aus einer einzelnen SL $MnBi_2Te_4$ auf der Oberfläche eines epitaktischen Films aus Bi_2Te_3 wird durch MBE hergestellt. Die Untersuchung ihrer magnetischen und elektronischen Eigenschaften bestätigt stabile 2D ferromagnetische Eigenschaften auf der Oberfläche, die stark mit dem an der Oberfläche vorhandenen TSS wechselwirken. Zusammen mit dem Einsetzen des Magnetismus unterhalb der kritischen Temperatur kann eine große Öffnung einer magnetischen Lücke in der Dispersion des TSS beobachtet werden. Des weiteren können die magnetischen Eigenschaften der Oberfläche durch die Verwendung von ferromagnetischen Substraten beeinflusst werden. Die Ergebnisse zeigen, dass der oben genannte Ansatz die theoretische Vorhersage einer starken Wechselwirkung zwischen Topologie und Magnetismus erfüllt und somit ein Paradigma für die effiziente Einbindung von Magnetismus in topologische Isolatoren darstellt – ohne die grundlegende Einschränkung einer starken kristallinen Unordnung.

Contents

1. Introduction

The field of topology in solid state physics has been pioneered by a set of groundbreaking discoveries and theoretical concepts starting with the discovery of the quantum Hall effect[1] and its explanation in terms of integer quantum numbers[2]. These findings have opened up a new paradigm involving the idea of a phase transition that does not fall into any of the known thermodynamic classifications, but rather describes the division of electronic structures into classes whose boundaries cannot be crossed by any smooth transformation. Especially in the last decades the field of topological matter has significantly evolved and widened, starting with the discovery of the quantum spin Hall effect[3] and the general notion of Z_2-invariant topological insulators driven by intrinsic spin-orbit coupling[4,5]. Research areas by now include a great number of material classes, such as time-reversal symmetric topological insulators (TI), topological crystalline insulators[6] and Weyl semimetals[7].

Considering topological insulators and, in particular, the peculiar spin-polarised helical edge states, the question naturally arises, which consequences the breaking of time-reversal symmetry (TRS) may have[8–10]. As detailed out later in this work, the most straightforward way to break TRS is the introduction of an out-of-plane magnetic field at the surface of the TI[9]. The consequences of this symmetry breaking open the field of quantum anomalous Hall and axion insulator physics carrying a variety of intriguing properties[11]. The quantum anomalous Hall (QAH) state is characterized by the presence of a single spin-polarised edge state, whose propagation direction depends on the sign of the magnetic polarisation. The QAH effect has created interest not only from a fundamental viewpoint of physics, but also due to its potential applicability as a switchable, spin polarising unit in spintronic devices[12]. Axion physics on the other hand relates to a specific coupling between magnetic and electric fields in the bulk of a TI coming to play once the metallicity of the surface is broken[13–15]. The named effects all depend on the opening of a magnetic gap in the TSS of the TI, which may be experimentally realized by coupling the TSS to a ferromagnetic material or layer[16].

In recent years, numerous experimental attempts have been made to efficiently incorporate magnetism into TI. In these attempts, the way in which magnetism is induced varies greatly, which is further reflected in the symmetries that are broken or preserved. Straightforwardly introducing magnetism by magnetic doping of thin films or the sur-

face near regions has been found to break TRS and indeed result in transport signatures corresponding to the QAH effect [12,17–20]. Frequently used systems here are $(Bi,Sb)_2Te_3$ films doped with the transition metals vanadium and chromium [12,21], whereas rare-earth doping has failed to achieve stable long range magnetic order despite the prospect of high local spin moments [22,23]. While the critical temperatures for the V-doped compounds range around 23 K and higher, the temperature up to which a full quantisation – a hallmark for transport solely through the edge states – can be achieved lies well below 1 K [17,21,24]. The reasons are inherent to the introduction of magnetism by doping, which naturally imposes structural disorder onto the sample. Disorder and related structural inhomogeneities lead to a spatial variation of the chemical environment and effectively lower the size of the magnetic gap. While the edge channels continue to exist away from mK temperatures, excitations over the small gap enable parasitic bulk conductance and destroy the quantized transport signature [25]. The absence of clear gap signatures in photoemission experiments on dilute doped TI is speculated to be due to the same reasons [26,27]. The doping introduces disorder and the effective magnetic gap is reduced to well below the resolution limit of any photoemission experiment.
In the recent years, intrinsic magnetic TI have gained extensive interest. This is because magnetism is part of the crystalline structure and, consequently, these materials have the potential to overcome the principle problem of disorder. The first discovered material of this class was $MnBi_2Te_4$, a septuple layer based material in which individual layers align ferromagnetically, while the interlayer coupling is of antiferromagnetic nature [28,29]. Such a material breaks time-reversal symmetry locally at the surface, while in the bulk of the compound TRS is conserved in connection with half a lattice translation. The new symmetry operator reads

$$S = T\tau_{1/2} \tag{1.1}$$

where $\tau_{1/2}$ denotes the translation by half of the magnetic unit cell and T is the time-reversal operator [30]. Indeed, for this symmetry a Z_2 invariant can be derived, which establishes the class of antiferromagnetic 3D TI [30]. One set of surfaces of the antiferromagnetic TI – in the case of $MnBi_2Te_4$ the [0001] surface to which the Néel vector is the surface normal – breaks this symmetry and enables the existence of edge currents and an axion response of the bulk. The topological phase depends on the number of layers with a pronounced even-odd effect, switching between QAH and zero plateau QAH states [31]. $MnBi_2Te_4$ and its derivatives have attracted great research interest in the recent years. However, it has turned out that observing a clear magnetic gap signature in photoemission on the antiferromagnetic $MnBi_2Te_4$ is far from straightforward [32–34] and often obstructed [35–38], for which a variety of reasons from disorder

up to the complicated (surface-)magnetism are discussed [39–42]. $MnBi_2Te_4$ derivatives with larger magnetic layer spacing tend to a more isolated layered magnetism with ferromagnetic tendencies [43–45] and first clear observations of a magnetic gap have been made in bulk compounds of $MnBi_8Te_{13}$ [46].
The approach chosen in this work is closely aligned with the aforementioned observation in attempting to create heterostructures which are terminated by a single ferromagnetic layer at the surface of a non-magnetic Z_2 TI. Here the choice of materials is a critical parameter and first predictions indicate that, if the TSS is allowed to live in the ferromagnetic surface layer, a large coupling between the ferromagnetic density of states (DOS) and the TSS can be established [47,48]. The concept makes use of the van der Waals nature of many 3D TI such as Bi_2Te_3, Bi_2Se_3 and $MnBi_2Te_4$ [28,49,50], which makes it possible to achieve almost perfect sharp interfaces in heterostructures.
The aforementioned heterosystems require an elaborate way of fabrication which is realized by the growth via molecular beam epitaxy (MBE). MBE allows for the creation of heterostructures away from the thermodynamic limit with a control over individual layer properties and can reach a very high interface quality. Going further, the approach also enables the creation of more complex structures. In order to manipulate the magnetic properties of the surface magnetic layer, it may be attempted to incorporate different ferromagnetic materials into the sample structure and study the respective coupling.
This thesis tries to answer two main questions: How can magnetism be incorporated into TI, allowing for a strong coupling between topology and magnetism and how well is the interplay captured by a simple, effective theoretical picture? How can stable two-dimensional ferromagnetic order be achieved and modified at the surface of a TI?
The thesis consists of 6 main chapters, whose content will be outlined in the following. In chapter 2, basic concepts concerning the most important magnetic interaction mechanisms, topology and the interplay between topology and magnetism are introduced. Material specific aspects are then further elaborated in chapter 3, individually addressing the properties of the compounds Bi_2Te_3, $MnBi_2Te_4$ and Fe_3GeTe_2 relevant to this thesis. Chapter 4 addresses the experimental methods applied in this work, as well as specific setups and facilities with a high significance for the results. The methods presented range from MBE and its most common characterization methods X-ray diffraction (XRD), atomic force microscopy (AFM), low-energy electron diffraction (LEED) and reflective high-energy electron diffraction (RHEED) up to spectroscopic probes for a more elaborate analysis of electronic and magnetic properties. The latter include (angle-resolved) photoemission spectroscopy (PES, ARPES) and X-ray absorption and magnetic circular dichroism (XAS, XMCD). This chapter and the appendix of

the thesis also include a detailed documentation of the MBE setups and software developed in the frame of this work.
The experimental results are subsequently presented in three main chapters. Chapter 5 describes the MBE growth and structural analysis of all thin film structures grown in the scope of this work: bulk-films of Bi_2Te_3 and $MnBi_2Te_4$, heterostructures of single septuple-layer (SL) $MnBi_2Te_4$ on Bi_2Te_3, as well as more complex structures incorporating the 2D magnet Fe_3GeTe_2. It aims to give a large overview of growth techniques, dynamics and the resulting structures.
Chapter 6 addresses the magnetic interactions present in $MnBi_2Te_4$ and related heterostructures. Starting from the magnetism in bulk $MnBi_2Te_4$, a close analysis is given to magnetic properties of the surface and later transferred to understanding the emergent two-dimensional magnetism in single SL $MnBi_2Te_4$. The chapter also presents a study on the magnetic coupling between different van der Waals (vdW) magnets across more complex $MnBi_2Te_4$–Bi_2Te_3–Fe_3GeTe_2 heterostructures, which is presented as an example on how to influence and bias the magnetism in the single SL of $MnBi_2Te_4$.
Chapter 7 addresses the electronic structure and the interplay between magnetism and topology in the ferromagnetic extension. Using ARPES and spin-polarised ARPES, the emergent topological surface state (TSS) is examined. Subsequent temperature dependent measurements across the magnetic phase transition study the fingerprint of the magnetic order on the TSS.

2. Topology and magnetism

The work in this thesis mainly concerns the interplay of two central phenomena in solid state physics, namely magnetism – more precisely magnetism in layered van der Waals (vdW) materials – and topology. Both of these topics will be introduced individually in the following in the extent necessary to explain the experimental findings presented in chapter 5-7. Starting from chapter 2.2.2 a closer light will be shed upon the interplay between magnetism and topology. To motivate the experiments and structures presented later in this thesis the chapters following from there will cover a short introduction into transport signatures arising from this interplay and present device concepts and realisations together with their respective strengths and weaknesses. It should however be noted that the experimental work aims to understand such structures at a fundamental level and will not contain any attempts to observe topological transport signatures. On the contrary, the aim of this thesis will be to gain a close understanding of the aforementioned phenomena by the use of surface spectroscopic methods.

If not noted otherwise the description of topology and related effects in this chapter is adapted from the description in the review articles [9,51], while the description of fundamental magnetic phenomena is written along the lines of [52,53]. All equations are given in the SI unit system.

2.1. Magnetism

Solid state systems with the potential for an internal magnetic polarisation can be categorised along their response to an external magnetic field, where a distinction is made between diamagnetic materials repulsing an external field and paramagnets which align with an external field. A special role is assigned to materials which keep an internal magnetic order parameter even in the absence of an external field. Two distinct classes include ferro- and antiferromagnets, which will both be relevant in the course of this work. Magnetic materials are typically thought of to carry a kind of spin or orbital degree of freedom, which may lead to a magnetic polarisation. For a paramagnetic

two-level system – e.g. a spin 1/2 system – the response to an external magnetic field can be described as

$$M(H,T) = N\mu_{\mathrm{B}} \frac{e^{x} - e^{-x}}{e^{x} + e^{-x}} = N\mu_{\mathrm{B}} \tanh(x) \tag{2.1}$$

with $x = -g\mu_{\mathrm{B}}B/k_{\mathrm{B}}T$, B as the external magnetic field, the Landé factor g, the temperature of the system T, the Bohr magneton μ_B and the number of available spins N. For larger spin quantum numbers of more available sub-levels, the equation complicates accordingly[52]. The relevant energy scales in this equation are the average thermal energy $k_{\mathrm{B}}T$ and the Zeeman energy

$$\hat{H}_{\mathrm{Z}} = \mu_{\mathrm{B}} g \hat{\vec{s}} \cdot \vec{B} \tag{2.2}$$

describing the energy of a spin $|s\rangle$ in an external magnetic field $\vec{B}$.
When looking at an ensemble of available spins, the response to an external magnetic field is described using the suszeptibility χ, defined as

$$\chi = \left.\frac{\partial M}{\partial H}\right|_{\mathrm{T}}. \tag{2.3}$$

Up to this point all quantities were defined for an ensemble of non-interacting spins in the absence of any long range order. To model the magnetic properties of materials beyond the notion of paramagnetism, interactions between individual spins – often spins on a lattice – have to be considered. Only in such interacting systems emergent phenomena as e.g. ferromagnetism or antiferromagnetism may emerge. One general model describing interacting spins on a lattice is the Heisenberg model. The corresponding Hamiltonian is expressed as

$$\hat{H}_{\mathrm{Heisenberg}} = -\sum_{i,j} J_{i,j} \hat{\vec{S}}_i \cdot \hat{\vec{S}}_j \text{ [53]} \tag{2.4}$$

where $J_{i,j}$ is the coupling constant and i, j denote the summation over all possible paris of spins $\hat{\vec{S}}_{\mathrm{i}} \cdot \hat{\vec{S}}_{\mathrm{j}}$. Often, the interaction between neighbouring spins – the nearest neighbour coupling – is significantly stronger than between lattice sites with larger spacing, allowing to set $J_{\mathrm{i,j}}$ to zero for any non-neighbouring pairs (i,j). Furthermore it should be noted that in the Heisenberg model the spin coupling is assumed to be fully isotropic, which allows for an alignment of the spins in any given direction. Contrary to this assumption, often the alignment of the orbital moment is energetically favoured along certain crystalline high-symmetry directions or planes as imposed by the crystal or ligand field structure. If spin-orbit coupling between the spin and orbital degrees of

freedom couples both, the breaking of full rotational symmetry for the orbital degree of freedom may be imposed on the spin component [52]. Contrary to the shape anisotropy which is a consequence of the macroscopic shape of a magnet, this type of anisotropy is referred to as magneto-crystalline or single ion anisotropy. For the case of a preferred alignment along a single crystalline axis, the anisotropy can be handled by adding an additional energy contribution to the Hamiltonian. Assuming an uniaxial anisotropy along the z-axis this may be written as

$$\hat{H}_{\mathrm{A}} = -\sum_i K_i (\hat{S}_i^z)^2 \text{ [53]} \tag{2.5}$$

where K_i is the anisotropy energy assigned to a single lattice site. Magnetocrystalline anisotropy can play a crucial role in stabilizing magnetic order in a material, especially in lower dimensional cases as shown in chapter 6. Its main role can be viewed as effectively reducing the dimensionality of the subspace available to the individual spins. In the case of strong uniaxial anisotropy, the Heisenberg model can be reduced by assuming a spin orientation only along the z-axis of the system, resulting in the so-called Ising model. Here the corresponding energy of the system is defined by the expression

$$\hat{H}_{\mathrm{Ising}} = -\sum_{i \neq j} J_{i,j} \hat{S}_i^z \cdot \hat{S}_j^z \tag{2.6}$$

where a coupling is only assumed between the projected spin components along the anisotropy axis.

2.1.1. Phase Transitions and Critical Behaviour

In the frame of statistical physics or thermodynamics, magnetism is often understood in the notion of phase transitions. In the classification of Ehrenfest, a phase transition is a change in the state of a material – typically caused by the temperature of the system – with which the n^{th} derivative of a chosen thermodynamic potential exhibit a discontinuity. The order of the derivative then corresponds to the order of the phase transition [54]. In the case of a magnetic transition, e.g. a ferromagnetic transition at the critical or Curie temperature T_c and antiferromagnetic with the Néel temperature T_N, the phase transition is accompanied by a sudden jump in the specific heat [55]. Below the transition temperature, the very short range interaction between the individual lattice sites leads to an order parameter over the extent of the whole system. In the fer-

romagnetic case at T_c, the order parameter is defined as the average magentisation in the limit of the external field going to zero

$$m = \frac{1}{N}\sum_i m_i \tag{2.7}$$

while for an antiferromagnet it may be defined as

$$n = m_1 - m_2 \tag{2.8}$$

where 1 and 2 denote the two different sublattices or spin species carrying opposite polarisation. It should be noted that these order parameters are defined globally, indicating that the order induced into the system is by far larger than the interaction distance. In other words, while the interaction is mainly determined by the nearest neighbour interaction, the correlation length within the system diverges at the critical temperature. This finding has let to the understanding that the behaviour of a system below T_c may be described by an universal theory, which is independent of the underlying microscopic interactions. This theory is often referred to as a critical behaviour of a system in the vicinity of phase transition. It attempts to describe the evolution of the global thermodynamic quantities as defined by a set of unified equations. In this regard a temperature scale τ is defined

$$\tau = \frac{T - T_c}{T_c} \tag{2.9}$$

as a normalisation of the sample temperature T with respect to the critical temperature T_c. The order parameter of the system – the magnetisation m for a ferromagnet – is then expected to show a temperature dependent behaviour defined as

$$m \propto (-\tau)^{\beta} \tag{2.10}$$

for $T < T_c$. This equation allows to describe the behaviour by using only two parameters, the reduced temperature τ which is a measure of the relevant temperature scale and by that the interaction strength in the system and the critical exponent β. This critical exponent is expected to only depend on the underlying model of the magnetic interaction and may be used to assign the system under question into a set of universality classes. Next to the order parameter also the scaling of the suszeptibility of the system χ can be defined as

$$\chi \propto |\tau|^{-\gamma} \tag{2.11}$$

Table 2.1.: Critical exponents for different magnetic models and dimensions [56].

Model	β	γ	Anisotropy
Mean field	0.5	1	–
Ising - 2D	0.125	1.75	easy axis
Ising - 3D	0.3265	1.237	easy axis
XY - 2D* [57]	0.227	2.2	easy plane
XY - 3D	0.348	1.318	easy plane
Heisenberg - 3D	0.369	1.396	isotropic

with the critical parameter γ. The critical exponents can be calculated for an underlying magnetic model defined by the nature of the coupling mechanism, e.g. isotropic vs. anisotropic, the range of interactions and the overall dimensionality of the system. An analytic calculation of critical coefficients is only possible for a very limited number of systems. The relevant quantities in this regard are listed in table 2.1. While these models are naturally strong simplifications, a knowledge of the critical behaviour of a system may nevertheless be used to gain a deeper understanding into the symmetries and constraints driving the magnetism. The models listed in tab. 2.1 may be divided into three main categories. As listed above the Heisenberg model and the mean field approach describe a fully isotropic spin coupling. The XY magnetic models are cases in which the dimensionality of the spin degrees of freedom is limited to an easy plane, in which the spins may align. In the case of the Ising models an uniaxial anisotropy is required leaving only an one-dimensional degree of freedom [56].

2.1.2. Magnetic Coupling Mechanisms

While the previous chapter has mainly discussed magnetism using a generic representation of the magnetic coupling as $J_{i,j}$, the origin and mechanisms of magnetic coupling will be discussed in the following. The most direct way by which two spins may couple is the direct dipolar interaction, which may be interpreted as the Zeeman energy of one spin in the field of its neighbour. The dipolar interaction may be expressed as

$$H_{\mathrm{D}} = \sum_{i \neq j} D_{i,j} \left(\hat{\vec{S}}_i \hat{\vec{S}}_{\mathrm{j}} - 3 \left(\hat{\vec{S}}_i \cdot \vec{e}_{i,j} \right) \left(\hat{\vec{S}}_j \cdot \vec{e}_{i,j} \right) \right) \text{ [53]} \tag{2.12}$$

$$D_{i,j} = \frac{\mu_0}{4\pi} \frac{g_{\mathrm{j}}^2 \hbar^2}{\left| \vec{R}_i - \vec{R}_j \right|^3} \tag{2.13}$$

where the $\vec{R}_i$ are the respective lattice sites the spins are located and g_j is the gyromagnetic ratio of the individual spins. In most magnetic materials the dipolar interaction between neighbouring lattice sites is negligibly small compared to the energy scale im-

posed by the critical temperature leading to the conclusion that other mechanisms are needed to explain the emergence of magnetic order. A variety of such mechanisms is known, ranging from carrier mediated magnetism such as the RKKY interaction up to more bond and orbital oriented mechanisms [52]. The materials, discussed in this thesis are mainly small bandgap semiconductors or insulators and their magnetism is mainly discussed in the context of the superexchange interaction [24,29,58], which will be introduced in the following. The direct exchange interaction is a consequence imposed

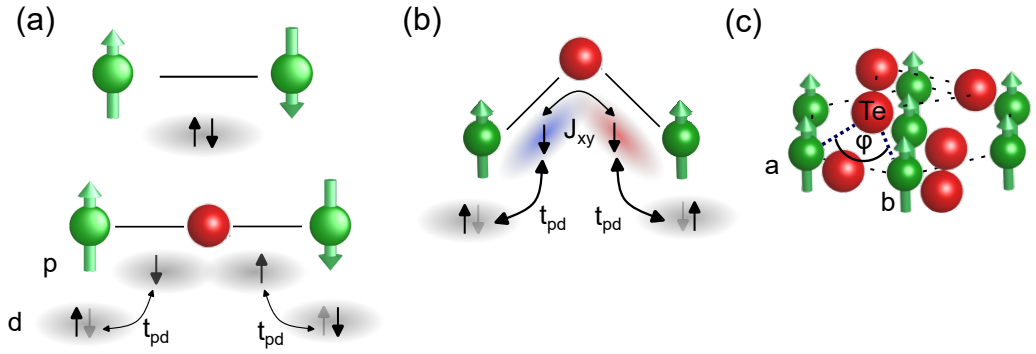

Figure 2.1.: Exchange mechanisms and their application to $MnBi_2Te_4$. a) Direct and 180° superexchange mechanisms. The combination of Pauli principle and p-d-hopping mediate an antiferromagnetic interaction in both cases. b) Superexchange in orthogonal geometry. The two magnetic atoms are bound to orthogonal orbitals. Contrary to the 180° case, a chain of p-d-hopping, the Pauli exclusion principle and Hund's rule mediates a ferromagnetic interaction. c) Bonding between Mn sites in a $MnBi_2Te_4$ vdW layer. The bonding angle of the Mn-Te-Mn bond of ~ 93.9° favours a ferromagnetic in-plane coupling. [52,59–62]

by the Pauli principle, when a bond between two atoms is considered as depicted in Fig. 2.1a). As the bonding orbital may only be occupied by two electrons of opposite spin a singlet state is enforced, which may be viewed as an antiferromagnetic coupling between the two electrons. Following from direct exchange, the concept of superexchange has been put forward, when explaining the coupling between magnetic atoms via an intermediate bonding partner, especially connected to the case of low conductance materials [63]. One possible underlying bonding scheme is sketched in the lower panel of Fig. 2.1a) on the example of d-orbital derived magnetism. Two transition metal atoms are connected via a shared ligand atom in a 180° geometry. Introducing a hopping term between the d-orbitals and the ligand p-orbital oriented along the bonding axis allows the system to lower its energy for certain configurations of spins in which this hopping is possible. As in the p-orbital the singlet state is enforced by the Pauli principle, the antiferromagnetically coupled singlet state of the two spins located on the d-orbitals also poses the lowest energy state for the hole system. The d-p-d path-

way therefore mediates an antiferromagnetic interaction [64].
If the bonding angle deviates from the straight geometry shown in a), the direct d-p-d pathway gradually decreases in efficiency. For angles close to 90°, the two transition metal atoms are bound to an orthogonal pair of ligand p-orbitals. Hopping between those is symmetry forbidden and a singlet configuration is not enforced. On the contrary in the case of two singly occupied p-orbitals, a parallel alignment of the single electron spins is energetically favoured, also known as Hunds rule or Coulomb exchange [64]. Taking into account p-d hopping between the transition metal d-states and the respective ligand p-orbital, the preferred parallel spin alignment on the ligand mediates an overall ferromagnetic interaction between the two transition metal atoms. The transition from antiferromagnetic to ferromagnetic interaction dependent on the bonding angle is known as Goodenough-Kanamori rule. Typically the energies associated with the antiferromagnetic coupling strongly exceed the ones in the ferromagnetic case as, $J_{\text{ferro}} << J_{\text{antiferro}}$. Nevertheless, ferromagnetic superexchange is known to be the driving mechanism in many magnetic materials and has been found to be of special importance in magnetic topological systems [24]. In the case of one of the materials relevant for this thesis – $MnBi_2Te_4$ – the magnetism between the individual Mn sites is mediated by a network of connecting ligand Te atoms as depicted in Fig. 2.1c). The bonding angle via the Te atoms yields ~ 93.9° and therefore strongly favours a ferromagnetic alignment between the individual Mn sites. The interaction between the individual layers in the material is mediated by so-called super-superexchange, which is an interaction channel along multiple atomic bonds even bridging the van der Waals (vdW) gap in the material by a small orbital overlap [65]. The strength of this interaction is again significantly smaller than the superexchange channel within the plane, but suffices in introducing an antiferromagnetic coupling between the layers.

2.1.3. Magnetism in van der Waals Materials

After the general discussion of magnetism and magnetic coupling, this chapter aims to highlight a few of the peculiarities connected with magnetism in layered materials. These so-called van der Waals (vdW) materials consist of individual layers, within which the bonding is commensurate. The planes have a height typically between three and up to more than ten atoms. The interaction between the layers is only mediated by vdW forces and no direct bonds bridge these vdW gaps. As a direct consequence for the magnetic coupling in such compounds, the coupling constants within the plane are significantly stronger then in between the individual planes as discussed above in the case of $MnBi_2Te_4$ [66]. Nevertheless, the interlayer coupling can be the defining quantity for the type of magnetic ground state in the materials distinguishing between ferro-

and antiferromagnetic order. This coupling is often mediated by an orbital overlap within the vdW gap and is therefore highly sensitive to the size of this gap [67].
Given the inherent two-dimensional character of the crystalline structure, vdW magnets are prototypical candidates for the realisation of two-dimensional magnetism. The notion of 2D magnetism describes magnetic order arising from a purely two-dimensional grid of magnetic atoms and was long thought to be impossible. The well known Mermin Wagner theorem, which states that there can be no stable magnetic order in less than three dimensions, because quantum fluctuations cause order instability, is now interpreted differently in the light of magnetocrystalline anisotropy. While still holding for the fully isotropic case, reducing the dimensionality of the spin degree of freedom by easy plane or easy axis anisotropy can lead to a ferromagnetic ground state above zero temperature. The two underlying models are the xy-model and the Ising model and for both an experimental realisation has been found e.g. in $CrCl_3$ and Fe_3GeTe_2 [57,68]. In the scope of this work, mainly materials with an out-of-plane spin orientation – and thus Ising-type behaviour – will be of interest, as shown later in chapter 2.2.2.

2.2. Topological Insulators

Topology is a discipline originating in mathematics and can be utilized for the classification of surfaces or objects under a continuous deformations. A prototypical example here is the connection between a doughnut and a mug, which are both classified as objects containing a single hole [69]. In the last decades, topology has been established as a concept in solid state physics to describe phase transitions in matter, which do not fall under the scheme of spontaneous symmetry breaking as established by Landau [70]. The interest in topology in condensed matter physics has been fostered by its ability to explain quantized phenomena as the quantum hall and later quantum spin hall effect in a widely unified theory [1,9,71]. This chapter will cover the matters of direct relevance for the effects under investigation, namely the concept of Z_2-classified topological insulators and their protecting symmetries.
A more recent definition of topological insulators is given by the statement that

> *An insulator (or, more generally a filled group of bands) is topologically non-trivial if it cannot be continued to any atomic limit without either closing a gap or breaking a symmetry.* [72]

The interpretation of this statement is manifold and defines topology as a highly non-local property of a crystal. A special weight is also put onto the matter of symmetries,

which are often found to be strong arguments in this context.
A main step in the understanding of topological materials was the introduction of integer quantum numbers, differentiating between different topological phases and especially allowing to explain the existence of surface, edge and interface states as arising from properties of the bulk of a crystal. There are two quantum numbers of relevance when investigating magnetic topological insulators.
The Chern number C is an integer number, first defined in the topological interpretation of the quantum Hall effect (QHE) [2]. The Chern number can be considered as a count for the number of edge states present at the boundary of a 2D sample. In the QHE, each change of the sample Hall conductance is accompanied by an in- or decrement of C. In the quantum spin hall effect (QSHE), two counterpropagating edge states are present carrying opposite Chern numbers of ± 1, resulting in a global Chern number of zero. The quantum anomalous Hall effect (QAHE) can be viewed as eliminating one of these edge states through the intrinsic sample magnetisation, resulting in C of either +1 or -1. Generally speaking, the Chern number is a property of the bulk of a sample, defined as the integral of the Berry flux over the full Brillouin zone and can only take integer values [51]. The fact that a global property of an insulator can enforce the existence of conducting channels at its edge is often referred to as bulk-boundary correspondence and can be viewed as the foundation for all of the aforementioned effects [51].
As already apparent from the example of the QSHE in the case of time-reversal symmetric systems, a different classification has to be applied, as later detailed in chapter 2.2.1. The Z_2invariant is a quantum number defined modulo 2, therefore only allowing for two distinct states, which are typically regarded as topologically trivial or nontrivial. In the three-dimensional case, the classification is extended to a set of 4 invariants $(s, \alpha_0, \beta_0, \gamma_0)$, with one strong topological invariant and three weak invariants describing the properties of the three respective surfaces of a crystal [30].

2.2.1. Z_2-invariant Topological Insulators

The main material classes studied in this work are so-called Z_2-invariant topological insulators, which find representatives e.g. in van der Waals materials Bi_2Te_3, Bi_2Se_3 and Sb_2Te_3 [50]. All these materials share the property that the Hamiltonian describing their electronic structure is invariant under the time-reversal operation. In a formal way, time-reversal can be described by an operator

$$T : t \rightarrow -t \tag{2.14}$$

In mathematical terms, the time-reversal invariance of a Bloch Hamiltonian can be written as

$$T H\left(\vec{k}\right) T^{-1} = H\left(-\vec{k}\right) \text{ [51]} \tag{2.15}$$

One consequence of a crystal fulfilling this condition is given by Kramer's theorem. Following from time-reversal symmetry (TRS), each Bloch state in a solid has a Kramer's partner and Eq. 2.15 enforces them to be degenerate at every time-reversal invariant momentum (TRIM) in the Brillouin zone (BZ) [9]. Furthermore a single propagating edge state as known for Chern insulators would violate TRS and therefore TRS invariant system will always have a Chern number equal to zero [73]. Topological systems fulfilling TRS require a different classification, which can be achieved by the Z_2invariant. The invariant is defined as a result of the bulk band topology and therefore viewed as a bulk property of the crystal [51].
While the QHE effect strongly relies on the presence of a magnetic field, the topological properties of many Z_2-invariant systems such as Bi_2Te_3 are mainly a result of the strong spin-orbit coupling (SOC) induced by the heavy Bi atoms. SOC is expressed as a relativistic correction to the Hamiltonian as

$$H_{\text{SOC}} = -\frac{e}{m_e^2 c^2} \vec{\sigma}\, \vec{p} \times \nabla \Phi \tag{2.16}$$

and describes the interaction energy between an electron spin and its respective orbit [53]. Here Φ is the electrostatic potential, σ the Pauli matrix vector and $\vec{p}$ the momentum operator. If inversion symmetry is broken, e.g. by a sample surface, SOC allows to break the degeneracy of bands with different spin and is often viewed as an effective magnetic field conserving TRS. Staying with the example of Bi_2Te_3, the bulk band gap is framed by Te and Bi p_z-derived states with different parity eigenvalues. SOC acts differently on both and therefore at a certain strength reverts the order of the two states. As the global band gap is smallest at the $\overline{\Gamma}$-point, the band inversion occurs locally in k-space in the BZ centre. The parity inversion at a single TRIM in the BZ hence changes the Z_2invariant and renders Bi_2Te_3 as topological non-trivial [50].
As a consequence of the bulk-boundary correspondence, at the surface of the three-dimensional TI a metallic surface state has to exist. The existence of this metallic state is enforced by the aforementioned symmetry arguments and often referred to as being protected by time-reversal symmetry. As long as the bulk band gap inversion is not reverted or the protecting symmetry is broken, the metallic surface state can not be gapped out by any perturbation.

In a low-energy approximation, a model Hamiltonian can be constructed. The full derivation can be found in [9] and results in the linearly dispersion model

$$\hat{H}_{surf} = C + v\hbar(\hat{\sigma}^x\hat{k}_y - \hat{\sigma}^y\hat{k}_x) \text{ [9]} \tag{2.17}$$

where v is the group velocity of the surface state and C is an arbitrary constant. The spectrum of this Hamiltonian is a linearly dispersing double cone as depicted in Fig. 2.2a. The Pauli matrices coupled to the momentum terms enforce a helical spin structure, effectively locking the electron spin to the momentum for the topological surface state (TSS). For all of the above mentioned TI the existence of this surface state has been shown by photoemission experiments [49,74]. The TSS resides at the $\overline{\Gamma}$-point of the surface Brillouin zone and the helical spin structure was visualized using spin-resolved photoemission experiments [75].

2.2.2. Interplay of Topology and Magnetism

Following from the simple argument of TRS protection, the question arises, how breaking this symmetry will influence the topological properties of a Z_2-invariant TI. In this regard, the general notion can be made that, while changing the symmetries of the system, TRS breaking does not necessarily transfer the TI to a topologically trivial phase. In the remainder of this chapter, first the influence of TRS breaking on the model Hamiltonian for the TSS will be discussed. Following from that, a focus will be put on novel phases and effects arising from this model. As a last part a description on specific concepts of creating magnetic TI's will be given, discussing the consequences of different kinds of magnetic orders, both from a theoretical as well as an experimental viewpoint.

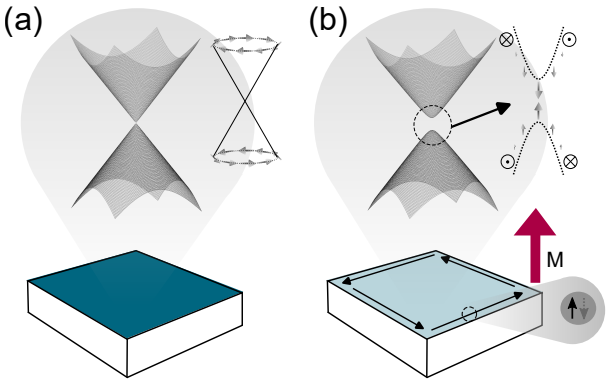

Figure 2.2.: Influence of magnetism on a 3D TI. The gapless linearly dispersing Dirac cone present in the non-magnetic phase is gapped out by the interaction with the magnetic order. In the magnetic exchange gap a 1D edge state disperses in the helical spin structure is altered to a meron configuration at the Dirac point.

While electric fields are generally even under time-reversal, magnetic fields enter the Hamiltonian as a vector potential $\vec{A}$. Similar to the transformation of the momentum

operator, the vector potential is odd under application of T. The transformation of electric and magnetic fields can thus be expressed as

$$T : \vec{B} \rightarrow -\vec{B}, \;\; \vec{E} \rightarrow \vec{E} \text{ [76]} \tag{2.18}$$

allowing for the statement that magnetic fields break time-reversal symmetry. Now a magnetic perturbation acting locally on the sample surface and directly entering the model Hamiltonian of the TSS (Eq. 2.17) can be considered. A general magnetic perturbation can be expressed as a set of mass terms connected with the Pauli matrices as

$$\hat{\mathrm{H}}_{\mathrm{perp}} = \sum_i m_i \hat{\sigma}^i \tag{2.19}$$

Together with the unity matrix, these matrices span a full basis set, allowing to look at the effect of a general magnetic perturbation in this fashion. Introducing this term into Eq. 2.17 and calculating the respective energy spectrum yields

$$E_{\vec{k}} = \pm\sqrt{(v\hbar k_{\mathrm{y}} + m_{\mathrm{x}})^2 + (v\hbar k_{\mathrm{x}} - m_{\mathrm{y}})^2 + m_{\mathrm{z}}^2} \text{ [9]}. \tag{2.20}$$

While m_{x} and m_{y} are absorbed as a shift in the in-plane momentum, the m_z term allows for an opening of a gap in the former linearly dispersing surface state. Unperturbed and perturbed spectra for arbitrarily chosen parameters are displayed in Fig. 2.2 to fully visualize the spectral changes imposed by the perturbation. The formerly gapless TSS a) acquires an open gap in close vicinity of the Dirac point b). Given a location of the Fermi energy at the Dirac point, this gap breaks the metallicity of the surface. The influence of the perturbation is strongest at the Dirac point and decays towards higher momenta. Looking at the spin structure of the perturbed model, the former strictly in-plane helical spin structure is broken up within the magnetic gap. The perturbation introduces an out-of-plane spin component with opposing polarisation for the upper and lower part of the TSS.

2.2.3. Quantum Anomalous Hall and Axion Insulator States

The out-of-plane spin component introduced at the Dirac point leads to a rotation of the former in-plane spin texture with a winding number of $\pm 1/2$, when crossing

over the magnetic gap. This spin structure – often referred to as meron configuration – introduces a Hall conductance of

$$\sigma_H = \frac{m_z}{|m_z|}\frac{e^2}{2h} \tag{2.21}$$

to the sample surface[9,42]. As this model handles magnetism as a property local to the surface, individual mass terms for the top and bottom surface can be imagined. Assigning the same sign to both terms, both surfaces carry the same Hall conductance. In a suitable geometry, with the perturbation placed on one sample surface, a transport experiment would see a Hall conductance of

$$\sigma_{QAH} = 2\sigma_H = \pm\frac{e^2}{h} \tag{2.22}$$

which coincides with the conductance of one edge channel in the QHE and allows to assign a Chern number of ±1. In analogy to the anomalous Hall effect – a Hall voltage caused by an intrinsic magnetisation in the absence of an external field – this case is referred to as the quantum anomalous Hall effect (QAHE). It can be seen as the most simple switchable topological device, where spin and direction of the edge states can be controlled by the sample magnetisation. The quantized transport behaviour can be observed experimentally and is switchable by reverting the internal magnetisation of the sample[12,77].

Imagining the opposite case, namely a situation in which the two opposing surfaces carry a magnetic mass term of opposite sign, and following Eq. 2.21, the two surfaces exhibit a Hall conductance of opposite sign and the overall Chern number of the system will be zero. Following from bulk-boundary correspondence, this state can nevertheless not be understood as being a trivial insulator and is referred to as the zero plateau QAH state[31,78]. The topological nature of this state cannot be assessed by a quantized transport signature. Instead it manifests in an additional term to the Maxwell-equations – the axion term – valid in the bulk of the material, coupling electric and magnetic fields as

$$L_\Theta = c\frac{\Theta}{2\pi}\vec{E}\vec{B}\ ^{[8,13]} \tag{2.23}$$

where Θ is defined as the axion angle. This term is present in all Z_2-invariant topological insulators but is typically only accessible, if the metallicity of the surface is broken[13]. The axion term has led to the concept of an axion insulator, which is often used in describing the zero plateau QAH case, in which no quantized edge states are present. It should nevertheless be noted that the coupling in Eq. 2.23 is a consequence

of the time-reversal symmetric bulk of the Z_2-invariant topological insulator, which can manifest, once time-reversal symmetry is broken locally at the surface [8,79,80].

2.2.4. The Ferromagnetic Extension Approach and Related Heterostructures

In many of the approaches described in the historical overview presented in the introduction, TRS is broken globally over the entire crystal. While this does allow for the observation of QAH edge channels in dilute doped TI, the bulk ferromagnetic nature obstructs any kind of individual control over the magnetism at the individual surfaces. Going back to the original idea of a magnetic mass term local to the sample surface, the approach of utilizing surface magnetism seems evident. The basic geometry of such a device is sketched in Fig. 2.3a). A 3D bulk TI (blue) is sandwiched between two thin ferromagnetic areas (green), which may be manipulated individually. Depending on the relative orientation of the surface magnetisation, the structure may achieve Chern numbers of +1, 0 and -1. First successful attempts use differently doped surface layers with V and Cr dopants and are able to show an individual switching behaviour for the two surfaces [20,81]. Trying to overcome the limitations inherent to doping an approach has been proposed closely similar to the concept of intrinsic magnetic TI, namely the ferromagnetic extension approach [47,48]. The approach requires a non-magnetic 3D TI and a structurally closely related magnetic counterpart as a surface modification. Fig. 2.3b) depicts the advantage of such material combinations on the example of the 3D TI Bi_2Te_3 and a single septuple layer of $MnBi_2Te_4$. The materials exhibit a similar in-plane crystalline structure and the first three atoms of a single building block are identical. Next to the structures, the spatially resolved density of states (DOS) of the TSS along the z-axis is displayed as adapted from [48]. At the Bi_2Te_3-vacuum interface, the TSS in mainly localized in the last QL of Bi_2Te_3 and quickly decays towards the interface. In the surface modified case, the $MnBi_2Te_4$ layer connects smoothly to the bulk and effectively pushes the boundary between non-trivial and trivial insulator further to the interface to vacuum. Enabled by the closely related potential landscape and hence low interface potential, the TSS can extend far into the surface extension and a strong interaction between the magnetic order carried by the 2D sheet of Mn and the TSS is achieved [47]. Calculated from DFT for the $MnBi_2Te_4$-Bi_2Te_3 system and following from symmetry arguments, a system as proposed in Fig. 2.3a) with two ferromagnetically extended surfaces may carry a Chern number of ± 1 depending on the orientation of the surface magnetisations [9,47,48]. Furthermore for a sufficient thickness of the Bi_2Te_3 epilayer, the surfaces will decouple magnetically and an individual control of both may

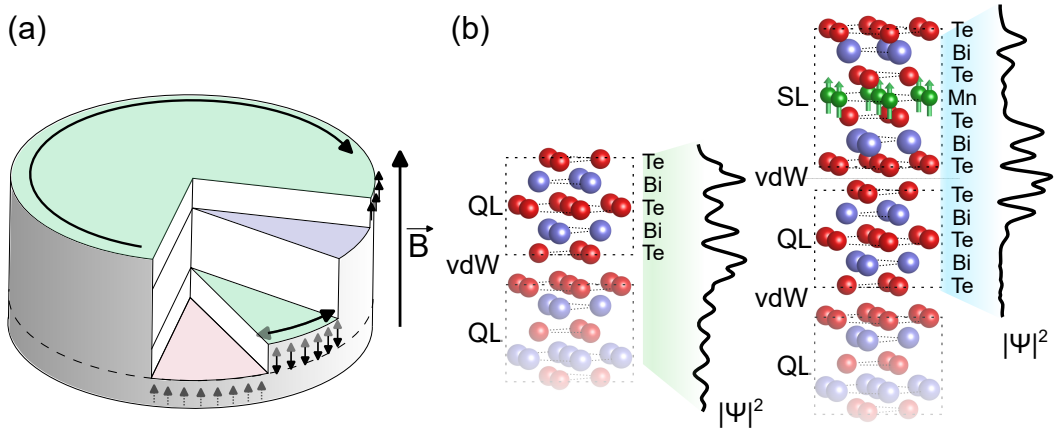

Figure 2.3.: The ferromagnetic extension approach a) Conceptual sketch for a switchable topological device. A 3D TI (blue) is enclosed by two ferromagnetic layers (green). An additional ferromagnet (red) can be utilized to bias the bottom surface and allow for individual switching of both. b) Crystalline structures of pristine Bi_2Te_3 and Bi_2Te_3 covered with a single SL of $MnBi_2Te_4$. The black lines show DFT calculation for the spatially resolved DOS of the TSS (adapted from [48]) in both cases and highlight the spatial relocation of the TSS into the surface extension. *Parts of figure b) used and adapted with permission of Springer Nature, from [47]; permission conveyed through Copyright Clearance Center, Inc.*

become feasible. While a few growth attempts have been made for the proposed ferromagnetically extended surface, some did not observe ferromagnetism in the surface layer [82,83] while others claim an observation backed by a highly inconclusive set of experimental results [84]. This motivates the two main aspects aimed to be studied in this thesis. First, a growth mechanism for the ferromagnetically extended surface will be developed and later accompanied by an analysis of the two-dimensional ferromagnetism at the surface and its influence on the TSS electronic structure. Second – going back to Fig. 2.3a) – in order to achieve an individual control over the layers in such a structure, the coupling to a ferromagnetic bias layer (red part of Fig. 2.3a) will be investigated. Many attempts exist in creating biased surfaces by stacking vdW layers of different magnets [85,86], but as will be shown, the situation is substantially different for MBE grown structures and requires a fundamental understanding of the interface structure and the tuneability of this effect.

3. Materials

The main goal of this thesis is the study of heterostructures combining magnetic and topological properties, resulting in emergent phenomena at the interface or surface of these structures. All materials used and presented below are chosen due to their layered van der Waals structure and hexagonal in-plane symmetries and include the prototypical TI Bi_2Te_3, the intrinsic magnetic TI $MnBi_2Te_4$ and Fe_3GeTe_2, a high-T_c van der Waals magnet. In this chapter, the physical and electronic properties of each of these materials will be introduced individually. The focus will be placed on parameters insightful for understanding the dynamics involved in the growth of heterostructures of these compounds as well as on the magnetic and topological properties.

3.1. Bi_2Te_3 and $MnBi_2Te_4$ Topological Insulators

Bi_2Te_3 is a material already discovered early in the 20th century and mainly known due to its semiconducting properties with applications in infrared sensing and thermoelectrics [87,88]. In the light of the discovery of topology in condensed matter physics Bi_2Te_3 has gained significant attention as one of the first 3D topological insulators [50,74]. Fig. 3.1a) displays the full unit cell of Bi_2Te_3. The structure consists of blocks of five atoms with a Te-Bi-Te-Bi-Te order, within which the bonding is commensurate. Consequently the bonding in between these blocks is only of van der Waals (vdW) type, which leads to a clear inequivalence between the in-plane and out-of-plane directions of the crystal. The stacking direction of the vdW layers also defines a clear axis of growth and a distinctly flat surface, namely the [0001] surface.

Bi_2Te_3 is a small bandgap semiconductor with a direct bandgap close to the Brillouin zone centre. Fig. 3.1b) depicts a density field theory (DFT) calculation along two high-symmetry directions of the Brillouin zone [74]. The band structure of Bi_2Te_3 hosts an inverted band gap at the $\overline{\Gamma}$-point, where the inversion is mainly driven by the strong spin-orbit coupling (SOC) [50]. As a consequence Bi_2Te_3 hosts a topological surface state (TSS) at its Brillouin zone centre, spanning over the entire bandgap and assigning a metallic character to the surface. The TSS in Bi_2Te_3 has its Dirac point located close to the bottom of the M-shaped bulk valence band (BVB) and therefore shows a characteristic shape with a very pronounced upper part of the TSS, while the lower part is already incorporated into the BVB [74]. The threefold rotational symmetry defined by

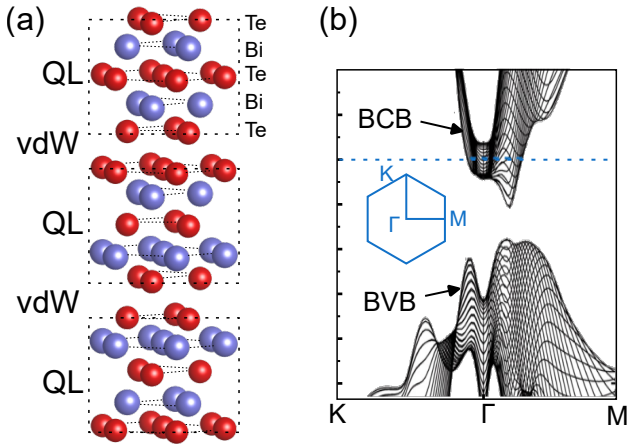

Spacegroup	$R\bar{3}m$
a	0.438 nm
b	0.438 nm
c	3.115 nm
Melting Point	580 °C
Bandgap	165 meV

Figure 3.1.: Electronic and crystalline structure of Bi_2Te_3. a) Full unit cell of Bi_2Te_3 consisting of three weakly bound quintuple layers[87]. b) Band structure of Bi_2Te_3 calculated by DFT together with the shape of the surface Brillouin zone.[74] c) Physical parameters of Bi_2Te_3 as taken from[74,89–91]. *Figure b) from*[74]. *Reprinted with permission from AAAS.*

the $R\bar{3}m$ symmetry group results in a hexagonal shape of the surface Brillouin zone with the distinct high-symmetry directions $\overline{\Gamma M}$ and $\overline{\Gamma K}$. All structural parameters relevant for the growth of Bi_2Te_3 are listed in Fig. 3.1c).

Introducing magnetism in Bi_2Te_3 particularly by doping with Mn was found to lead to an extended unit cell, incorporating an additional MnTe layer[92]. These extended vdW layers were identified to be the building blocks of the thermodynamically stable crystalline structure of $MnBi_2Te_4$. $MnBi_2Te_4$ was subsequently discovered as the first antiferromagnetic intrinsic topological insulator – a magnetic TI with magnetism as part of its crystalline structure[28,93]. $MnBi_2Te_4$ belongs to the same space group as Bi_2Te_3 and consists out of septuple layer blocks separated by van der Waals gaps. The unit cell of $MnBi_2Te_4$ in the non-magnetic phase is displayed in Fig. 3.2a) and consists of three SLs. Below a Neél temperature of 24.6 K the spins assigned to Mn couple ferromagnetically within each layer, while the interlayer coupling is of antiferromagnetic nature[28]. The coupling leads to A-type antiferromagnetism in $MnBi_2Te_4$ but nevertheless allows for an effective local magnetic polarisation at the [0001] surface of the crystal. The magnetic easy axis is aligned along the surface normal, potentially allowing for an interaction between the magnetic order and the TSS. Similarly to Bi_2Te_3 the electronic structure of $MnBi_2Te_4$ (see Fig. 3.2b) is characterized by a global direct bandgap in the infrared and a hexagonally shaped Brillouin zone. The band gap was found to be inverted around the $\overline{\Gamma}$-point and the material hosts a TSS. The structural parameters are listed in 3.2c). In particular it should be noted that the in-plane crystalline structure and lattice constant is closely similar to Bi_2Te_3. The melting point is

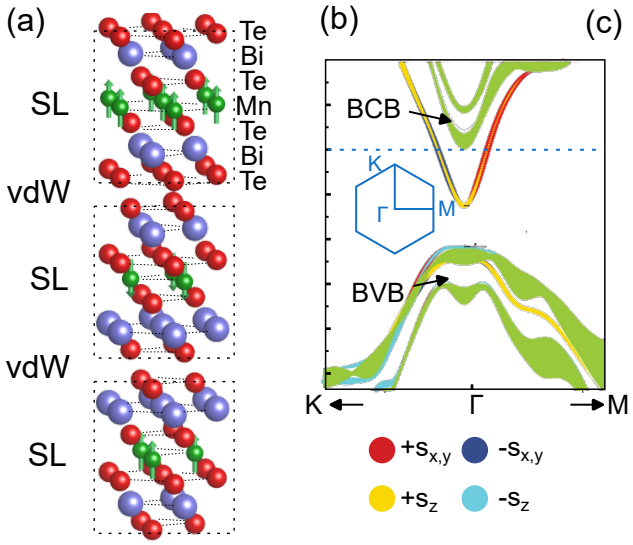

Spacegroup	$R\bar{3}m$
a	0.433 nm
b	0.433 nm
c	4.093 nm
Melting Point	600 °C
Bandgap	220 meV
T_{Neel}	24.6 K

Figure 3.2.: Crystalline and electronic structure of $MnBi_2Te_4$. a) Full non-magnetic unit cell of $MnBi_2Te_4$ consisting of three weakly bound septuple layers[95]. b) Bulk band structure of $MnBi_2Te_4$ by DFT. The electronic structure hosts a direct inverted band gap in the centre of the Brillouin zone. c) Relevant structural and electronic parameters of $MnBi_2Te_4$ [28,93]. *b) used and adapted with permission of Springer Nature, from[28]; permission conveyed through Copyright Clearance Center, Inc.*

slightly higher, which also results in a higher temperature needed during the growth of this compound[93,94].

3.2. The van der Waals Magnet Fe_3GeTe_2

Fe_3GeTe_2 is a representative of a class of novel van der Waals magnets – a set of materials with a layered crystalline structure hosting magnetic properties which are often stable down to the monolayer limit[56]. Magnetism in such truly two-dimensional systems has been experimentally discovered first in CrI_3 and $Cr_2Ge_2Te_6$ and has since gained a lot of interest, both from a perspective of fundamental physics as well as due to their prospective use in ultra miniaturized electronics[96,97].

The crystalline structure of Fe_3GeTe_2 is depicted in Fig. 3.3a) and its unit cell consists of two unit blocks. Each of the blocks is terminated by a hexagonal lattice of Te atoms, while the Fe and Ge atoms are placed in between. The structure hosts two inequivalent lattice sites for Fe, also differing in local screening properties[98]. The valence band structure as represented by DFT calculations in Fig. 3.3b) is mainly defined by Fe d-orbital derived bands and has a fully metallic character. In the ferromagnetic case a clear separation between spin majority and spin minority populated bands is

found and the magnetic properties are mainly defined by the Fe lattice sites. The lattice parameters of Fe_3GeTe_2 (Fig. 3.3c) give an lattice mismatch between $MnBi_2Te_4$ and Fe_3GeTe_2 of ~ 7.98 %, the comparably high melting temperature renders the compound a sufficiently stable substrate for the growth of heterostructures.

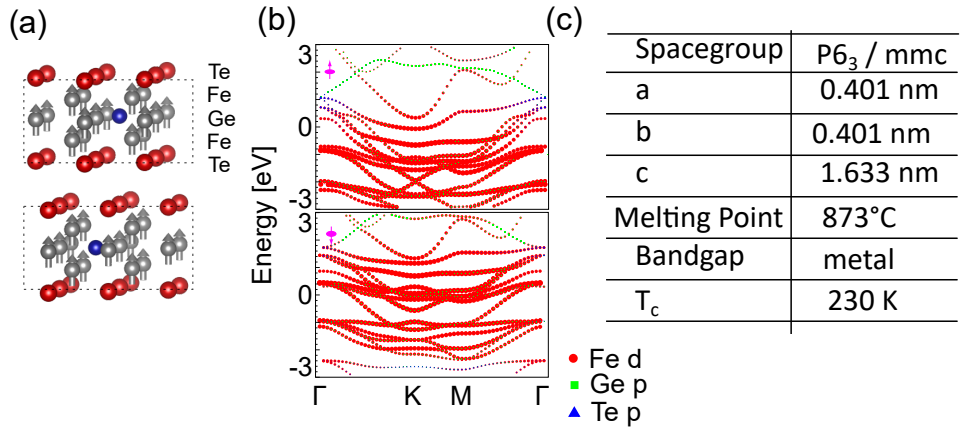

Figure 3.3.: Structural and electronic properties of the van der Waals magnet Fe_3GeTe_2. a) Unit cell of Fe_3GeTe_2 built out of Te (red), Fe(grey) and Ge (blue) atoms. The structure exhibits commensurate blocks with a complicate crystalline structure divided by weak van der Waals bonds [99]. b) Spin- and orbital-resolved DFT calculations of Fe_3GeTe_2 in the ferromagnetic state for spin majority and minority carriers [100]. c) Selected structural and magnetic parameters [99,101]. *Figure b) with permission from [100]. Copyright (2023) by the American Physical Society.*

Concerning its magnetic properties, Fe_3GeTe_2 is a strongly anisotropic ferromagnet with an out-of-plane easy axis and itinerant or metallic magnetic coupling properties [67,102]. The critical temperature of bulk crystals is estimated between 220 and 230 K, while decreasing below 200 K in the limit of microscopically thin flakes [99,102–104]. In bulk magnetometry, Fe_3GeTe_2 appears as a soft ferromagnet with a saturation field of ~ 400 mT and a very small coercive field, which is attributed to the easy emergence of domains with opposite magnetisation in bulk samples [105]. Experiments working with exfoliated or structured flakes of Fe_3GeTe_2 on the size of the typical length scale of the individual ferromagnetic domains however have shown that a hard ferromagnetic hysteresis behaviour can be achieved. For device scales of ≈ 10 µm, squared hysteresis loops with coercive fields up to aforementioned saturation field have been found [104,106]. These properties render Fe_3GeTe_2 as a material highly interesting for device applications and make it an intriguing field of study in the combination with topological materials.

4. Experimental Methods and Setups

As this thesis covers aspects from sample growth up to a spectroscopic analysis, a broad range of methods was applied and used to gain a picture as complete as possible. The following chapter aims to introduce the basic notions of the those experimental methods and introduce all relevant aspects necessary for the interpretation of the experimental results. The chapter starts with an introduction of molecular beam epitaxy (MBE), its relevant microscopic processes as well as the most commonly used probes on the structure of the samples.
Angle-resolved photoemission spectroscopy (ARPES) is the method of choice for the analysis of the electronic structure, especially allowing for a direct probe of the topological properties of the MBE samples in this thesis. Next to an introduction into the basic physics of the photoemission process, chapter 4.2, will present the details involved in angle-resolved measurements, resonant photoemission as well as spin-resolved photoemission.
Subsequently chapter 4.3 will introduce X-ray absorption spectroscopy and X-ray magnetic circular dichroism – two methods used for determining a broad spectrum of magnetic properties up to an element sensitive measurement of the local spin polarisation.
The last part of this chapter will then cover the experimental setups at which this work was conducted, as well as document the development of the combined MBE and photoemission systems that have been part of this thesis.

4.1. Molecular Beam Epitaxy and Related Characterisation Methods

Molecular Beam Epitaxy (MBE) is a broadly used method for the deposition of thin films with applications ranging from fundamental research up to large scale applications in the semiconductor industry. Given the plentiful amount of applications, MBE poses a very broad field of study. As a consequence, processes and systematics strongly depend on the material systems under investigation. This chapter mainly aims to introduce MBE processes relevant for the growth of Te based van der Waals compounds. For a more broad overview, the reader is refereed to e.g.[107,108] on which most of the discussion below will be based.

4.1.1. MBE Growth and Surface Dynamics

MBE allows for a high amount of control over growth properties and can be scaled from small laboratory applications up to industrial standards. The most general requirements of MBE are the use of (thermal) evaporation sources for the creation of molecular beams, ultra high vacuum conditions and the use of substrate materials as a fundament for the sample growth. The UHV conditions have to be sufficient to allow for a ballistic transport of the molecular beams to the substrate. The conditions present in most lab setups ranging down to 1×10^{-10} mbar typically overfulfil these requirements and are mainly maintained to avoid the incorporation of residual gas atoms into the film structure during the growth.

Contrary to other growth methods working with the spontaneous nucleation of crystallites, MBE uses substrate materials, which closely mimic the crystalline in-plane structure of the attempted film material. The choice of substrate material allows to influence film parameters as strain, growth direction and even attempted phase. A second important distinction is the ability of MBE to work out of the global thermodynamic equilibrium. The individually controlled cells allow to adjust the flux of the source materials individually and may even be used to prepare heterostructures of layers with sharp interfaces. The reaction on the surface is defined by the substrate temperature, which may be far away from the operating temperatures of the individual sources.

Generally, the MBE process is divided into three spatially separated zones in the chamber: Elements are evaporated mainly from Knudsen cells, where the cell content is heated to a certain evaporation temperature. Modern Knudsen cells contain partially open ceramic crucibles in which a mixture of the evaporant and its vapour coexist. The relevant quantity for MBE processes is the temperature dependent vapour pressure of the evaporant. Depending on the evaporant, the gas phase may consist of different type of molecules, e.g. elemental clusters, dimers or single atoms, which can strongly influence the dynamics occurring on the substrate surface. The molecular gas phase subsequently leaves the crucible and moves ballistically through the chamber, given the low background pressure. A shutter in front of the cell is used to control or block the beam reaching the sample. On the substrate surface, the individual beams mix and equilibrate to the substrate temperature, which is the defining quantity for all processes related to the film growth. The dynamics on the growing surface are visualized in Fig. 4.1a). The impinging atoms or molecules may adsorb at the substrate or film surface into a weakly bound and mobile state, also called physisorption. The relevant quantity is the so-called sticking coefficient defined as

$$c_s = \frac{n_{adh}}{n_{tot}} \tag{4.1}$$

and may greatly differ between different kinds of atoms or molecules. Here n_{adh} is the amount of adhesing atoms as compared to the number of impinging particles n_{tot}. The sticking coefficient is highly dependent on the substrate temperature and present chemical conditions. To give one example relevant for this work, Te will not stick on BaF_2 above ~ 210 °C. The presence of additional BiTe molecules however can chemically bind additional Te and lead to $c_s > 0$ [109]. For the growth of chalcogenides, often a large oversupply of the chalcogenide (Se, Te) is required to obtain stoichiometric films due to the large difference in sticking coefficients [110]. A measure for the beam flux, often used in MBE processes is the beam equivalent pressure (BEP), which is defined as the pressure difference at the sample position between opened and closed cell.
The elevated substrate temperatures allow for a certain mobility of the atoms on the surface. Atoms/molecules are still weakly bound in the physisorbed state and can hop on the surface. Diffusion is a thermally activated process and the typical length scales behave as $l_d \propto e^{\frac{E}{2k_B T}}$ with E as the hopping energy barrier. A certain mobility is required to achieve a reasonable crystalline quality, as atoms have to find a suitable lattice site, while a high mobility can also lead to pronounced island growth.
The mobile atoms will eventually bind to the substrate surface or to each other and start to nucleate. Depending on the growth conditions, nucleation – the formation of new islands – and incorporation – the chemisorption of a molecule to an existing island edge – are the defining processes for the surface morphology and will define the growth mode of the film. The desorption of molecules mainly concerns the physisorbed state, but can at certain substrate temperature also apply to chemisorbed atoms from the surface region. Atoms overcome the potential of the surface barrier and re-evaporate into vacuum. Similar to the sticking coefficient, desorption processes may subsequently shift the equilibrium conditions on the surface and lead to a change in crystalline phase. As one example, a Bi_2Te_3 surface exposed to high sample temperatures will gradually become Te deficient over time, especially in the absence of a stabilizing Te atmosphere.
For binary or ternary compounds intermixing of atoms can also emerge as a relevant process. It denotes the occurrence of antisite defect, which given the different number of bonding electrons may lead to isolated defect states. The process is more likely in structures with multiple sites carrying a similar oxidation state or atomic radii. One prototypical example are materials of the $MnBi_2Te_4$-family where Mn-Bi antisite de-

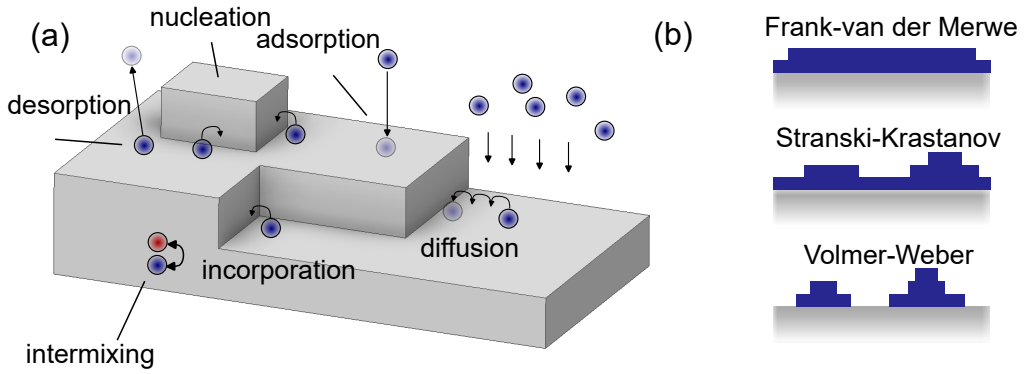

Figure 4.1.: MBE surface dynamics and growth modes. a) MBE growth dynamics on the surface of a growing film containing adsorption, hopping and desorption processes [107,108]. b) MBE growth modes on the surface of a substrate, ranging from flat layer growth up to island growth modes [107].

fects are discussed in great extent [43,44,111].

The MBE process applied in this thesis is mainly based on binary sources of Bi_2Te_3, MnTe and elemental Te. At the relevant temperatures Bi_2Te_3 evaporates as

$$2 \cdot Bi_2Te_3 \rightarrow 2 \cdot BiTe + Te_2 \text{ [112]} \tag{4.2}$$

and MnTe dissociates to its elemental constituents [113]. Te can be assumed to also evaporate in dimers of Te [114]. The reasons and properties of this approach will be detailed out in chapter 5.

Van der Waals Epitaxy

The materials in this thesis are grown on BaF_2, a substrate with a fully different atomic composition than the epitaxial layers. This type of process is referred to as heteroepitaxy [115]. The substrate is chosen such that its symmetries and lattice constants closely mimic the compound attempted to be grown. The [111] surface of BaF_2 exhibits a threefold rotational symmetry and an in-plane lattice constant very close to the one of Bi_2Te_3 and $MnBi_2Te_4$ with a lattice mismatch of 0.04 % [116,117]. The surface is terminated by fluorine ions with fully occupied orbitals and no dangling bonds are left on the surface, as desired for a van der Waals growth mode. Contrary to conventional substrates, the preparation of BaF_2 does not require very high annealing temperatures. The substrates are cleaved as flat slices off commercially available blocks and inserted into vacuum right after. Before growth they are once more degassed to desorb residual water molecules at 400 °C. Unless noted otherwise, this preparation approach is used

for all epitaxially grown samples in this work.
Growth modes occurring in MBE are depicted in Fig. 4.1b) and can be divided into three main categories, the layer by layer (Frank-van der Merwe), layer plus island (Stranski-Krastanov), pure island (Volmer-Weber) growth. Layer by layer growth occurs, when the bonding to the substrate is stronger than in between the epitaxial layers. The first layer is then adhered to the substrate. After the growth of the first layer, the influence of the substrate rapidly decays. If the bonding relaxes sufficiently smooth to the bulk conditions, layer by layer growth will occur. If the bonding properties change unfavourably or abruptly after the first layer is grown, the following layers may nucleate as isolated islands on the surface, leading to the Stranski-Krastanov growth mode. On the other hand, if the bonding between the atoms is always favoured to a substrate bond, island growth may be preferred[107].
In this regard, the growth of van der Waals compounds is a fringe case in many aspects. It concerns the growth of compounds with strongly bound building blocks, which mainly extend in the lateral direction. VdW materials tend to grow with the stacking direction along the surface normal and have a strong tendency to form closed layer units, e.g. quintuple layer block in the case of Bi_2Te_3. In this case islands once nucleated tend to grow sideways, while new islands may nucleate on top on the finished surface area. The interplay of nucleation and expansion leads to the emergence of pyramid-like growth modes[94,109]. As no direct bonding takes place between film and substrate, van der Waals materials are more tolerant towards lattice mismatch and the film may still grow in a relaxed structure. Nevertheless, this statement is to be taken with great care, as the surface morphology and growth mode still depend on the substrate of choice and a large phase diagram of growth modes from flat layers to wires can emerge[115]. Especially in vdW epitaxy, the symmetries of the substrate play an elevated role. In many cases more then one rotational orientation of the epitaxial layer on the substrate will lead to a local minimum in energy, such that multiple different rotational orientations of the film may occur[67]. In the case of Bi_2Te_3, this effect is called twinning and strongly depends on the thermodynamics of the growth[118].

Surface preservation and capping

In the context of single layer thin sample structures, an appropriate surface preservation technique is highly necessary, as even for the typically inert surface of $MnBi_2Te_4$, the first layer oxidizes within less than an hour at ambient conditions[119]. In this thesis three main methods of surface preservation have been used and will be introduced in the following. The most straightforward way of surface preservation are capping techniques. After the growth of the epitaxial film, a capping material is deposited to fully

cover the film surface and prevent oxygen from reaching to the film when the sample is exposed to ambient conditions. For van der Waals type samples it has been found that capping with elemental Te can protect the surface against oxidation on timescales up to several years. As apparent from STEM experiments shown later in this thesis, Te evaporation at room temperature starts to form a crystalline layer of Te on the sample surface. Typical capping thicknesses range up to 200 nm, where the growth of Te is found to be rather polycrystalline growing in large whiskers[116]. Given the sharp and weakly bound interface between the epilayer and the cap, a mechanical removal of the cap for further surface studies is possible. Samples are prepared ex-situ by fixing a metallic or ceramic pin onto the surface using epoxy adhesive. Subsequently a lateral force is applied in UHV conditions onto the pin, leading to a removal of the adhesive together with the protective Te layer. The success of decapping depends crucially on the fact that the bond between the capping layer and the film surface is the weakest link in the structure and therefore benefits greatly from flat sample surfaces.
Especially for transport experiments, metallic capping layers are no suitable method of surface preservation, as they open a large parallel conductive channel to the main film. In this regard BaF_2 has been found to be a suitable capping material, given the insulating character with a large band gap. When evaporated at the sample surface at elevated temperatures of ~ 240 °C, BaF_2 grows epitaxially on the surface of Bi_2Te_3 and $MnBi_2Te_4$. Typical layer thicknesses of 30 nm suffice in protecting the sample surface on timescales of several years. To contact the film through the insulating layer, parts of the cap can be removed by the controlled application of purified water. For very thin sample structures a more complicate technique has been used, as described e.g. in the supplement of[120]. Using a focused ion beam microscope small circular channels are cut into the sample. Subsequently elemental Pt is evaporated focused into the channels to produce small contact pads.

4.1.2. Growth Characterisation Methods

MBE – as most crystal growth methods – is highly reliant on a set of structural characterisation methods as a feedback for the growth optimisation. In this thesis, the sample growth recipes were optimized by first growing thin films with a set of parameters either estimated from first assumptions or calculated from a prior optimisation cycle. Subsequently the samples were analysed using multiple in- and ex-situ characterisation methods to gain information about crystal stoichiometry, phase and quality (X-ray diffraction, XRD), deposition rates (X-ray reflectivity, XRR) and surface structure, quality and morphology. In the following each method will be addressed in the detail neces-

sary for the interpretation of results shown later in this thesis. For an understanding of the underlying physics and a more detailed explanation, the reader is referred to a collection of specialized books on each topic [121–124].

X-ray diffraction

X-ray diffraction is the main characterisation method used to probe the crystalline structure of MBE layers prepared in this work. It utilizes hard X-ray radiation with wavelengths in the order of magnitude of interatomic distances in crystals and is able to probe a variety of structural parameters by scattering on the crystalline lattice. In the following, first a theory of scattering will be derived, which is valid beyond the scope of XRD. Afterwards the experimental details of typical XRD experiments and the data evaluation employed in this work will be addressed.

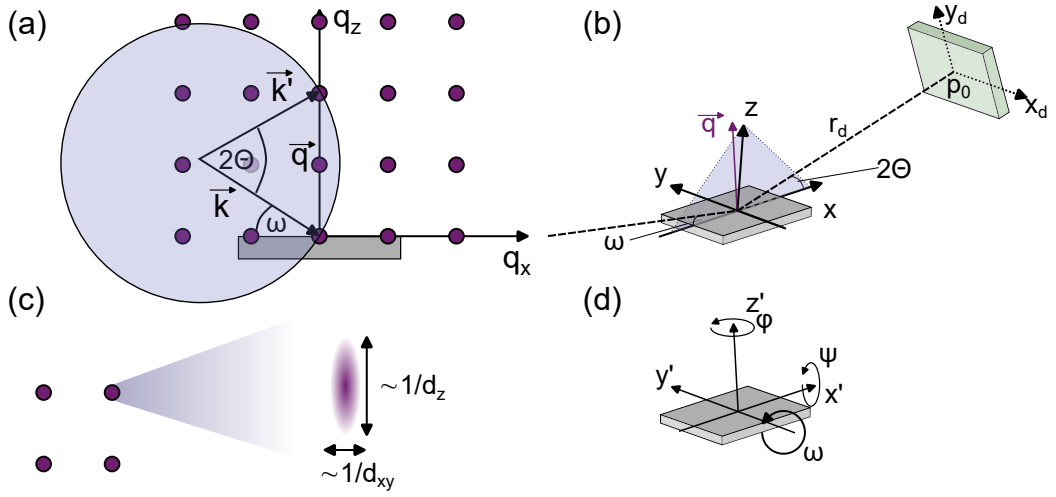

Figure 4.2.: Geometry and construction of the XRD experiment. a) Ewald-sphere construction. The in- and outgoing wave vectors may interfere constructively, when the scattering vectors connects reciprocal lattice points. b) Typical XRD experiment in $\omega - 2\theta$-geometry. The incoming beam is scattered off the sample and imaged by a detector unit. c) The shape of the individual diffraction peaks may be used to estimate the typical mean grain size of the epitaxial film. d) Definition of the relevant angles in the sample coordinate system.

A wave or beam impinging on a crystalline sample is subject to scattering from each individual lattice site, such that for an elastically scattered beam, each lattice site has to be viewed as an individual source of a wave. While this in general poses a profoundly complex situation, the periodic nature of a crystal may be used to greatly simplify the problem. All individually scattered parts of the incoming wave superimpose and interfere and in the case of an infinite, periodic lattice, only very few conditions lead

to constructive interference, while in all other cases the scattered intensity goes to zero due to destructive interference. The condition for constructive interference for a three-dimensional lattice is described by the Laue equation

$$\vec{q} = \vec{k}' - \vec{k} = \vec{Q}_{hkl} \text{ [125]} \tag{4.3}$$

stating that the scattering vector – e.g. the difference between the in-going and out-going wave vector $\vec{k}$ and $\vec{k}'$ – has to be a reciprocal lattice vector of the scattering lattice. The Laue condition is often visualized in the Ewald sphere representation as seen in Fig. 4.3a). The radius of the sphere is given by the length of the incident wave vector $\vec{k}$ defined by the energy of the incident photons and the elastic scattering condition implies the same length for the scattered wave vector $\vec{k}'$. Constructive interference occurs, when the scattering vector $\vec{q}$ connects two reciprocal lattice sites, represented here by the sphere with radius $|\vec{k}|$ intersecting two lattice points. The full reciprocal space available to the experiment is given by a sphere with the radius $2|\vec{k}|$ originating at the centre of the reciprocal lattice. The relation between a reciprocal lattice vector and the real space lattice is given by

$$\vec{Q}_i \cdot \vec{a}_k = 2\pi\delta_{ik} \text{ [126]} \tag{4.4}$$

with $\vec{a}_\mathrm{k}$ as the base vectors of the crystalline lattice. Up to now Eq. 4.3 only accounts for a periodic lattice carrying a single atom per unit cell. An unit cell containing multiple atoms significantly changes the scattering condition from the lattice and is accounted for by the structure factor

$$F_{hkl} = \sum_n f_n e^{2\pi i(hu_n + kv_n + lw_n)} \text{ [125]} \tag{4.5}$$

containing a sum over all atoms in the unit cell n with their respective atomic scattering factor f_n and the respective fractional coordinates u, v, w within the unit cell. The intensity of a diffraction maximum connected to the reciprocal lattice vector $\vec{Q}_{hkl}$ is then modified by a multiplication with $|F|^2$. Depending on the arrangement of atoms within the unit cell the structure factor may significantly alter or fully suppress the relative diffraction intensities.

The geometry of a typical XRD experiment is shown in Fig. 4.2b). An incident X-ray beam is guided onto the sample surface with the incident angle ω. The scattered beam leaves the sample and a detector is placed under the angle 2Θ away from the incident beam direction. Typically the sample is mounted on a six axis goniometer, which allows the adjustment in three spatial coordinates x,y,z and the three relevant sample angles

ϕ, ψ and ω. The scattering vector $\vec{q}$ corresponds to the deflection of the incident beam and is pointing along the surface normal z' of the sample in the case of the symmetric scattering geometry with $\omega = \Theta$. In laboratory experiments the beam is focused along the out-of-plane direction, while it may be quite elongated along the experimental y-axis, while in the case of synchrotron based experiments a fully focused beam is used. The detector may either be a counter tube, or a two-dimensional area detector. While the first is employed for one-dimensional line scans in a lab environment, area detectors can be used to image the full three-dimensional shape of individual diffraction peaks.
A scan under the condition $\omega = \Theta$ corresponds to a line through the reciprocal along the $\vec{q}_z$ vector, e.g. the surface normal and is the main scanning method employed in the analysis of epitaxially grown thin films. In this condition, the scattering vector component q_z can be calculated as

$$q_z = \frac{4\pi}{\lambda} \sin(\theta) \tag{4.6}$$

where λ is the wavelength of the incident radiation. In the case of asymmetric diffraction maxima and when using an area detector, the data conversion becomes significantly more complex. The full data conversion procedure used in this work has been summarized to a small guide and can be found online [127].
Symmetric $\omega - 2\theta$-scans are used to identify the crystalline phase and purity of an epitaxial film often accompanied with an appropriate modelling or comparison to calculated peak positions. If an area detector is utilized, varying the sample angle ω for a fixed value of 2θ suffices to image the full three-dimensional shape of a diffraction maximum [128]. In a real system the shape of the diffraction maxima depends on parameters such as the crystal size, sample temperature and potential lattice defects. For a finite sized crystal, the shape of the diffraction peaks corresponds to a Fourier transform of the macroscopic crystalline shape s as

$$W(\Delta\vec{q}) = FT\{s(\vec{r})\} \text{ [121]} \tag{4.7}$$

with $\Delta\vec{q}$ as the distance from the peak centre. While for epitaxially grown films, diffraction peaks are elongated in the q_z-direction by the finite film thickness, the broadening in the xy-plane is strongly dependent on the grain size of the layer and therefore a hallmark for the film quality. Furthermore, the information about the shape of diffraction peaks may be related to the preferred shape of the individual grains [128].
If required for the analysis of XRD patterns, especially for the identification of feature connected to crystalline impurities and surface terminations, XRD patterns can

be modelled explicitly for a given structure. In this regard for van der Waals materials, a structure model is set up, consisting of individual layers and the XRD pattern is calculated taking reflection and transmission through the layers into account. In order to simulate disorder as present in real materials, an inhomogeneity in the sample thickness or ordering of the individual layers is accounted for by simulating a set of statistically distributed possible structures and averaging over the resulting patterns[121,128,129]. All XRD simulations presented in this thesis were conducted with the help of Prof. Sergio L. Morelhão, University of São Paulo.

X-ray reflectivity (XRR)

In the case of very grazing light incidence and in case of a $\omega - 2\theta$-bound geometry, the scattering vector $\vec{q}$ will become small compared to the size of a reciprocal lattice vector, such that no scattering signal from the lattice itself will be detected in this geometry. Instead, the small $\vec{q}$ – corresponding to large distances between the individual scattering planes – will approach the magnitude typical for thin films, e.g. sizes of several up to a few hundred nm[130]. As the refraction index for most materials is smaller then the vacuum value $n < 1$ a critical angle exists under which total reflection from the surface occurs. Above the critical angle, reflected intensity from the surface of a film and potentially from every interface in the structure at which the dielectric constant of the epitaxially grown layer structure changes will interfere and modulate the intensity detected under the angle 2Θ[130,131]. In the most simple case, viewing a thin film on a semi infinite substrate and neglecting material specific parameters, the interference will lead to an oscillating pattern in the reflected intensity. The oscillation period $\Delta\omega$ is connected to the film thickness d by

$$d = \frac{\lambda}{2\Delta\omega} \tag{4.8}$$

A complete derivation and incorporation of material specific parameters can be found in[131]. Especially for multi-layer systems a precise calculation can be very complex and for the analysis of XRR-patterns in this work the software toolkit *GenX* was be employed[132]. The program simulates the individual layers by their density and refractive index with a thickness d and an average surface roughness σ and further incorporates a set of experimental parameters to properly describe the angle-dependent reflection intensity. Using a differential evolution algorithm, the open parameters in the model are adapted to the experimental results to work out the thickness of the individual layers as well as the roughness of the respective surfaces. XRR naturally has limits in the

analysis of structures with very similar refractive indices, e.g. interfaces between Bi_2Te_3 and $MnBi_2Te_4$ cannot be clearly resolved.

Reflective High-Energy Electron Diffraction

Reflective high-energy electron diffraction (RHEED) is an electron diffraction method commonly used in combination with MBE growth. An electron beam with energies between 10 keV to 30 keV is guided onto the surface of the sample in a grazing incidence geometry. The beam is elastically scattered off the sample surface and detected by a phosphorous coated screen placed in the beam path. The grazing incidence geometry allows for RHEED to be conveniently combined with MBE growth setups, as source and detector can be placed perpendicular to the evaporation direction and therefore allow for the acquisition of diffraction patterns during sample growth. The implementation of this method in the relevant setup can be found in chapter 4.4.
RHEED is a diffraction method following the same mathematical formalism as described in Eq. 4.3 in the context of X-ray diffraction. Despite the high electron energies, the grazing angle of incidence with a perfectly flat surface leads to a low penetration depth of the electrons and thus to a surface-sensitive experiment. Consequently, the Laue condition along the surface normal is relaxed and the diffraction condition is only sharp for the in-plane wave vectors. The expected patterns will now be explained in more detail, depending on the surface structure.
Given a perfectly flat epitaxial layer and assuming the sample to be azimuthally aligned, e.g. the incident beam impinging along a high-symmetry direction of the surface, the diffraction process only fulfils the Laue equation for the in-plane direction, while for the out-of-plane direction a continuous set of diffraction vectors is allowed. Consequently, the diffraction pattern is expected to consist of discretely placed streaks, which appear as lines at the detection screen. The spacing of the lines scales inversely with the respective in-plane lattice constant, while the width can be interpreted as a measure of the crystal quality and grain size, when assuming a constant sample temperature.
If the growth results in a rough surface consisting of small islands, the assumption of a purely surface-sensitive experiment looses its validity. The beam can enter the small crystallites from the side, allowing only for discrete scattering vectors along all three spatial directions. The formerly discrete streaks acquire a modulation along the out-of-plane direction up to the point, where the screen depicts a clear pointed diffraction pattern along both in- and out-of-plane direction.
While the upper two cases both denote an oriented growth mode, a fully polycrystalline growth will result in a variety of small crystallites with all possible orientations at

the substrate surface. A beam impinging under this condition will result in a diffraction pattern as also present in Debye-Scherer or powder diffraction. The characteristic pattern for these growth conditions are semicircles on the RHEED screen centred around the incident beam direction [125].
In many MBE setups, RHEED also allows to monitor the growth of individual layers by oscillations of the RHEED intensity due to an alternating surface roughness caused by layer by layer growth. Due to their growth mode, this is only rarely possible for the van der Waals materials under investigation in this work and this aspect is not applicable here. A more comprehensive explanation of this technique can be found in [107].

Low-Energy Electron Diffraction

A closely related experimental technique is low-energy electron diffraction (LEED). Here the experimental geometry is fundamentally different with the electron beam impinging the surface along the surface normal. The elastically scattered electrons are visualized and filtered by an assembly of biased grids and a phosphorous screen, mounted spherically around the incident beam direction. LEED uses electron energies up to a few 100 eV and its surface sensitivity is given by the small inelastic mean free path of the electrons. The scattering process is again closely related to the description in the previous chapter. The in-plane scattering vectors are fully discrete, while the scattering vector along the surface normal allows for a continuous set of vectors with an energy dependent modulation due to the finite depth sensitivity of the experiment. LEED allows to image the two-dimensional diffraction pattern of the sample surface and can provide insight on the reciprocal lattice of the surface.
In the frame of this work, LEED is employed to probe a few main properties of the thin films under question. In hetero-epitaxial growth with lattice missmatch, LEED patterns of the surface can help in identifying superstructures and strain. These kind of superstructures are well known for thin surface layer on metallic substrates [133] and less likely to occur in van der Waals growth of thick films. LEED also allows to probe symmetry properties of the surface and is especially sensitive to the azimuthal alignment of films. It is therefore a very useful tool to estimate the degree of rotational alignment between substrate and epilayer. In the special case of the threefold rotational symmetry of the compounds used in this work, it can be used to estimate the degree of domain twinning during growth, although the results have to be interpreted with care, as the LEED patterns of e.g. Bi_2Te_3 can vary strongly between trigonal and hexagonal appearance depending on the beam energy. For a more profound discussion of the method, the reader is referred to e.g. [122].

Atomic Force Microscopy

Atomic force microscopy (AFM) – in contrast to the aforementioned diffraction techniques – is a real-space microscopy technique for the analysis of surface topography. In the often used tapping mode, the method uses an up to atomically sharp tip mounted on a vibrating cantilever. The tip is brought to oscillate in close vicinity to the sample surface, such that the interaction between tip and sample can already be described in terms of the Lennard-Jones potential[134]. This highly non-linear potential results in a change in resonant frequency as the distance of the tip from the sample is changed. By monitoring the change in vibration amplitude and frequency and adjusting the cantilever height, the sample topography can be mapped by rasterizing the sample surface. AFM is a highly local technique, imaging the sample surface on length scales of a few µm laterally, with a resolution of ~ 1 nm to 5 nm. Along the vertical direction especially high-resolutions of up to 1 Å can be achieved[135]. These properties render AFM a well suited method for probing the surface morphology of epitaxially grown films, mapping out quantities as mean island size, island shape, surface roughness and average step height. The data treatment of AFM images in this work is limited to data levelling by subtracting a mean plane oriented along flat terraces at the sample surface. For a more detailed explanation of the technique, the reader is referred to[134].

Transmission Electron Microscopy

Especially for the growth of heterostructures, a determination of the vertical sample structure is challenging with the above mentioned methods. Transmission electron microscopy (TEM), more specifically scanning TEM (STEM) as applied in this work is a microscopy technique, allowing to image the lateral sample structure. For the STEM measurements, the sample has to be very thin, to allow electrons to pass through. This is achieved in a multi-step process. First a lamella is cut out of the sample by a focused ion beam microscope. Subsequently the lamella is further thinned down by Ion-beam milling[136]. The experiments shown in this work were conducted with the help of Dr. Martin Kamp (RCCM - Universität Würzburg).
STEM uses a highly focused electron beam with energies in the 100 keV to MeV range[123]. The beam is guided onto a thin lamella of the sample, while a detector measures the transmission of the beam through the lamella. If the lamella is cut along a high-symmetry direction of the sample and oriented accordingly, the electron beam will encounter areas of high and low transmission when rasterizing the sample, depending on which part of the lattice structure is hit. The results can be seen as displaying the vertical and one direction of the lateral sample structure. In a first approximation, the

acquired image is interpreted as a convolution of the probe intensity function and the specimen object function. Here the latter represents the sample structure and consists of maxima in contrast at the atomic sites scaling with the nuclear charge number as $c \propto Z^2$ [137]. TEM images contain information about both, the position of atomic sites in the structure as well as their relative atomic charge averaged over the lamella thickness.

4.2. Photoemission Spectroscopy

Photoemission spectroscopy (PES) probes the electronic structure of a solid using the photoelectric effect. Over the last decades PES has involved into a powerful method for the analysis of the chemical composition of samples (X-ray photoelectron spectroscopy, XPS), the k-resolved probe of occupied valence band states (angle-resolved PES, ARPES) and even up to the spin structure of electronic states. In the following the basic theory and experimental conditions of PES experiments will be summarized. The main focus will be placed on the methods used in this work – ARPES, resonant photoemission spectroscopy (ResPES) and spin-resolved ARPES.

4.2.1. Formal Description of the Photoemission Process

The basis of the photoemission process is the interaction of an incoming photon with the electron system of a solid surface, leading to the emission of an electron into vacuum. The transition relevant for the photoelectric effect is described by a perturbative approach that leads to Fermi's golden rule. The photocurrent w_{fi} can be expressed as the overlap between an initial state $|\Phi_i\rangle$ and a final state $\left|\Phi_f\right\rangle$ mediated by the perturbation caused by the interaction with the photon H_{int} as

$$w_{\mathrm{fi}} = \frac{2\pi}{\hbar} \left|\langle \Phi_{\mathrm{f}} | H_{\mathrm{int}} | \Phi_{\mathrm{i}} \rangle\right|^2 \delta\left(E_{\mathrm{f}} - E_{\mathrm{i}} - \hbar\omega\right) \text{ [138]} \tag{4.9}$$

where the delta function ensures energy conservation. The interaction Hamiltonian caused by the photon is typically expressed in terms of the vector potential of the incoming photon $\vec{A}$ and its momentum $\vec{p}$ as

$$H_{\mathrm{int}} = \frac{1}{2m}\left[-2q\vec{A}\cdot\vec{p} + q^2\left|\vec{A}\right|^2\right] \tag{4.10}$$

The first part of the Hamiltonian corresponds to the direct photoemission process mediated by a single photon, while the second part denotes two photon processes and

is typically neglected. Eq. 4.9 generically describes the transition between an initial and final state of the N electron system of the solid. Two models for the process are used in the description of photoemission. The one-step model interprets the process of photon absorption and electron emission as a single transition between an initial state in the solid and a final state with free electron like character in the vacuum and a strong damping in the solid away from the surface. To better understand the assumptions of this model, the process is often broken down into the three-step model. First an electron is excited by a photon in the solid. Subsequently the photon may travel towards the surface. As only non-scattered photons carry information about the initial state in the solid, the depth from which electrons may escape as primary electrons is strongly limited by the high scattering probability in the solid. The relevant quantity is the inelastic mean free path (IMFP), which is approximately described by an universal curve[139]. The minimum of the IMFP lies in the range between 20 and 40 eV given by the typical plasmon energies in a solid and increases towards lower and higher photon energies. The photon energy of 12 eV repeatedly used in this work as well as the He I-α line utilized in lab experiments can be considered to be very surface-sensitive experiments, while $h\nu = 6.4\,\text{eV}$ for the LASER based photoemission experiments is often assigned a larger probing depth.
As a last step after reaching the surface, the electron has to transmit through the sample surface into vacuum. During this transition, the in-plane crystalline momentum of the electron $\vec{k}_\parallel$ is conserved, while the $\vec{k}_\perp$ along the surface normal is discontinuous due to the potential gradient along this axis. The energy of the electron is lowered by the work function of the surface during the transition.
Assuming that the transition of the electron from the initial to the final state happens on timescales faster than the reaction of the electron system to the process – effectively decoupling the initial and final state – the photocurrent can be rewritten in the so-called sudden approximation as

$$w_{\text{fi}} = \frac{2\pi}{\hbar} \sum_k \left|\Delta_{\kappa,k}\right|^2 A_k\left(\epsilon_\kappa - h\nu\right) \text{[140]} \tag{4.11}$$

where $A_k\left(\epsilon_\kappa - h\nu\right)$ is the spectral function, while $\Delta_{\kappa,k}$ is denoted as the photoemission matrix element. This representation of the photocurrent allows for a more thorough interpretation of the photoemission spectrum with respect to a system under investigation. Photoemission does not directly probe the occupied density of states (DOS), but rather the spectral function of a system, which can be derived as the imaginary part of the single particle Greens function[138,140]. In the description of an electron system in a crystalline lattice, typically the many-particle problem of interacting elec-

trons on a lattice is simplified to a single particle picture using quasiparticles occupying non-interacting states in what is often denoted as the band structure of a crystal. The approximation holds very well for systems with delocalised orbitals and states derived from s- and p-orbitals, while d- or even f-orbital derived states add interactions between the quasiparticles which are treated using the Hubbard model or similar approaches. The denominator of the spectral function contains the single particle energy ϵ_k^0 and the self energy $\Sigma(\vec{k},\omega)$, which describes all interactions screening the energy of the quasiparticle. The self-energy carrying an real and imaginary part leads to a shift in spectral energies as well as a line broadening. The spectral function can further be divided into a coherent and an incoherent part, where for mainly uncorrelated systems such as the p-state derived states covered in this work, the second part will be neglected. The form of the spectral function relevant for the material systems in this work is expressed as

$$A_{k_0,i}(\omega) = A_i \frac{\Delta_\epsilon}{(\omega - \epsilon_{k_0,i})^2 + \Delta_\epsilon^2} \tag{4.12}$$

with Δ_ϵ as the natural line width in energy, i denominating the respective state and A_i as an amplitude. The motivation of this expression can be found in[138], chapter 3, while notes on its application are presented in the supplements of[120,141]. The line width in the above expression only concerns the intrinsic contributions leading to a Lorentzian line shape, while the experimental resolution has to be treated individually, resulting in the Voigt profile often used for photoemission fitting.
The photoemission matrix element $\Delta_{\kappa,k}$ used in Eq. 4.11 incorporates all symmetry and orbital dependent parts of the photoemission probability. Asymmetries arising in the angle-dependent photoemission spectrum due to the selection rules implied by this factor allow to extract fundamental properties of the underlying orbital symmetries of the probed wave function. In this context two main quantities are relevant for this work. Using linearly polarised light, the spectra acquired with s- and p-polarised light are susceptible to different parts of the wave function and can be used to disentangle orbital alignments and parities contributing to a specific state. The term linear dichroism used in this work is defined as the asymmetry in the spectrum acquired with p-polarised light and can be calculated as $ld(k_\mathrm{x},k_\mathrm{y}) = I(k_\mathrm{x},k_\mathrm{y}) - I(-k_\mathrm{x},k_\mathrm{y})$ with k_x in the plane of light incidence. The asymmetry arising using circularly polarised light is called circular dichroism and is defined as $cd(k_\mathrm{x},k_\mathrm{y}) = I_+(k_\mathrm{x},k_\mathrm{y}) - I_-(k_\mathrm{x},k_\mathrm{y})$. Its origin and interpretation are in general complex. In spin-orbit coupled systems it was found to be susceptible to the orbital angular momentum of a state. In recent literature, significant advances in the understanding of both concepts have been made and the reader is re-

ferred to e.g.[7,142–144] for further insights.
When the energy of the incident light coincides with the transition from a core level to a valence band state, an additional photoemission channel may arise. The interaction operator in Eq. 4.9 is expanded to the lowest order by an additional term as

$$H^*_{\mathrm{int}} = V_{\mathrm{rad}} + V_{\mathrm{AI}} \sum_m \frac{|\Psi_m\rangle \langle \Psi_m|}{\hbar\omega + E_i - E_m + i\Sigma_m/2} V_{\mathrm{rad}} \text{ [145]} \tag{4.13}$$

Here V_{rad} describes the single electron excitation $\vec{A} \cdot \vec{p}$ term of the non-resonant case in Eq. 4.10. The second part of the sum describes the resonant autoionisation process. An electron is transferred to an intermediate state $|\Psi_m\rangle$ with N+1 valence electrons by the interaction with the initial photon. The Coulomb interaction represented by the auto ionisation operator V_{AI} causes the simultaneous process of filling the remaining core hole with a valence electron and emission of an additional electron by the transferred energy. E_m is the energy of the intermediate state. The width of the intermediate state Σ_m results in a certain energy width in which the resonant process is efficiently possible. The resonant nature of the process makes it highly efficient when the photon energy matches the necessary transition energy and both channels will start to interfere. When the photon energy approaches the resonant threshold energy, typically the photoemission intensity of the states connected by the resonant transition increases with respect to the overall valence band intensity. In the course of the photon energy matching the transition energy, the situation becomes more complex as next to the increased VB intensity also a signal of the Auger line may appear which is not subject to a constant binding energy[145,146]. Additional conditions, necessary for the process and applications of the resonant process apart from photoemission spectroscopy will be discussed in chapter 4.3 in the context of X-ray absorption spectroscopy.

4.2.2. Angle-Resolved Photoemission Spectroscopy

As the photoemission process conserves the $k_{\parallel}$ component of the crystalline momentum up to a reciprocal lattice vector, a measurement of the angle and energy dependent photoemission spectrum can be directly related to the spectral function of a sample. The most commonly used instrument for the acquisition of ARPES spectra is the hemispherical analyser, as depicted in Fig. 4.3a). It consists of an lens system mounted in the analyser neck, as well as two hemispheres enclosing the electron trajectory. The analyser as well as the experimental chamber are magnetically shielded to suppress any external magnetic fields and ensure a field free environment around the sample. Electrons are emitted into the half-space above the sample surface. The analyser-lens system has acceptance angles between 14 and 30°. Electrons emitted in this angle area

enter the electrostatic lens system of the analyser where they are projected onto a thin slit at the entrance of the two hemispheres (the inner one is omitted in the sketch). The slit will select a single cut from the k-space. The electrons subsequently enter the two hemispheres, between which a voltage is applied. Depending on the kinetic energy of the electrons their trajectory through the hemispheres differs and the radius they occupy after transmitting through the analyser is a function of the entry energy. The combination of kinetic energy and entry angle leads to a two-dimensional projection of the electrons onto an electron multiplier which is visualized by a screen and CCD-camera assembly. In order to map the full two-dimensional surface Brillouin zone, a mapping of the dispersion in the second k-direction is required. In many setups this is achieved by gradually tilting the sample around the respective rotation axis, while for modern analysers a set of deflectors may be used. In this kind of setup two sets of deflection lenses are inserted into the lens system, which are used to shift the electron beam with respect to the entrance slit[147]. The great advantage of such an assembly is the possibility of mapping the full k-space without changing the experimental geometry, positional stability of the emission spot as well as a clear definition of the plane of light incidence.

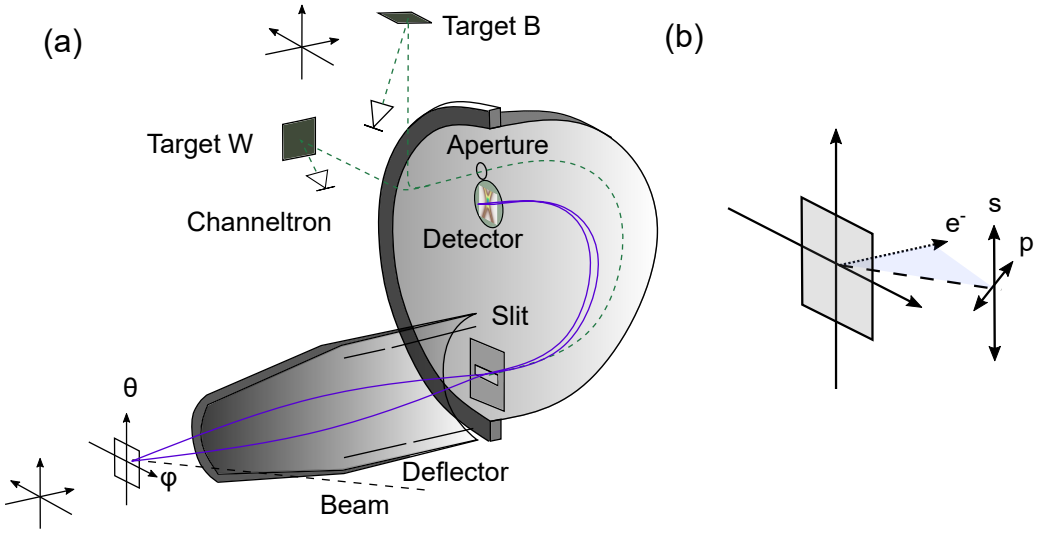

Figure 4.3.: Experimental geometry of the photoemission experiment. a) Sketch of a modern ARPES spectrometer. Electrons are excited from a sample and lead through an electrostatic lens system. An entry slit selects electrons from a thin line in k-space, which may transmit between the two hemispheres of the analyser. The electrostatic field between the hemispheres fans out the electrons depending on their kinetic energy. An additional Aperture with may be used to guide the electrons to a set of spin detectors[148]. b) Definition of the light polarisation directions s and p with respect to the plane of light incidence.

The natural measurement variables of this analyser are the kinetic energy of the electrons and the angles θ and ϕ under which the electrons leave the surface. During the experiment, the sample and analyser share a common ground, which allows to write the energy conservation as

$$E_{\text{kin}} = h\nu - \Phi_{\text{A}} - |E_{\text{B}}| \text{ [149]} \tag{4.14}$$

where $h\nu$ is the incident photon energy, E_{B} is the binding energy of the electron defined as its energy with respect to the Fermi energy $E - E_{\text{F}}$ and Φ_{A} is the work function of the analyser. Typically the analyser is coated with graphite on the relevant surfaces to ensure a homogeneous work function and Φ_{A} can be estimated as the work function of graphite. The relation between the electron emission angle and its in-plane wave vector can be denoted as

$$k_{\parallel} = \frac{1}{\hbar}\sqrt{2mE_{\text{kin}}}\sin(\theta) \text{ [149]} \tag{4.15}$$

where we define $k_{\parallel}$ as the wave vector within the sample surface plane. The transit through the hemisphere maps the straight shape of the entrance slit to a curved shape after passing to the detector. As a consequence, lines of constant kinetic energy appear curved on the image. Data treatment will thus include a correction of this curvature with dispersion less reference spectra or along calculated curvatures. Further data treatment may include the removal of periodic patterns caused by the detector assembly with the use of a dedicated Fourier filter.
As described above, the probability of the emission of an electron from one specific state is modified by the photoemission matrix element. In this light a precise definition of the experimental geometry including the light polarisation is of high importance. The polarisation directions are sketched in Fig. 4.3b). The plane of light incidence is defined by the vector of the incident photon beam and the surface normal of the sample. For linearly polarised light, two orthogonal directions are distinguished. S-polarised light has its polarisation vector normal to the plane of light incidence, while p-polarisation is defined in the plane and perpendicular to the light direction. Incident light may further carry circular polarisation, which is defined as $c+$ and $c-$ depending on the rotation of the light vector around the beam direction.

4.2.3. Spin-Resolved Photoemission Spectroscopy

For the study of magnetic or spin-orbit coupled materials it is often of interest to study the property of the electron spin as an additional degree of freedom in a photoemission

experiment. The description here will cover the currently most efficient one named VLEED-spin detector. In this type of detector electrons with rather low kinetic energies impinge on a thin oxygen passivated iron [001] target film, which is magnetized along one of the spin directions in question. The geometry of this experiment is depicted in Fig. 4.3a) as an addition to the conventional detector screen. VLEED setups are equipped with an additional aperture next to the detection screen of the setup. The size of the aperture can be changed and depending on its size it will integrate over a small range of angle and energy of the electron spectrum. The electrons travelling through the aperture are deflected by an electromagnetic lens system and guided onto one of two possible targets. For the experimental setups used in this work, the two targets are mounted such that both are parallel to the z-axis, while the second axis is either parallel to the x- or the y- direction of the coordinate frame.
The VLEED-detector exploits the fact that the scattering in a set of low-energy states of the magnetized iron film is highly dependent on the spin of the impinging electrons. The targets are magnetized in the respective measurement direction prior to the measurement and by sweeping the retarding voltage in the analyser, a distribution for varying electron kinetic energies (EDC) can be recorded. A measurement with two different polarities of the magnetisation will result in an intensity difference, which can be related to the electron spin [150].
The efficiency of the spin-selective detection is described by the effective Sherman-function S_{eff}, defined to connect the measured asymmetry A with the electron spin polarisation P.

$$A = \frac{I_{\text{L}} - I_{\text{R}}}{I_{\text{L}} + I_{\text{R}}} \tag{4.16}$$

$$P = \frac{A}{S_{\text{eff}}} \quad [150] \tag{4.17}$$

The spin asymmetry A is defined as the difference in intensity for the measurements in the two magnetisation directions. The spin polarisation is then given as the asymmetry divided by the Sherman function, which can ranges around 0.3 for common VLEED setups [151]. Using the spin polarisation, the actual spin spectra can be calculated by using the principal definition of P as

$$P = \frac{I_{\uparrow} - I_{\downarrow}}{I_{\uparrow} + I_{\downarrow}} \quad [150] \tag{4.18}$$

and furthermore assuming that $I_{\uparrow} + I_{\downarrow}$ equals to total amount of detected electrons as $I_L + I_R$. The electrons scattered from the targets are counted using channeltron detectors, allowing to count the absolute number of detection events. Hence, the error of the

spin polarisation can be calculated assuming a Poisson distribution and its respective uncertainty for the experimental intensities and applying error propagation. The error for the spin polarisation is then given as

$$\Delta P = \left(\frac{S_{\text{eff}}^{-2} - P^2}{N_{\text{l}} + N_{\text{r}}} \right)^{\frac{1}{2}} \quad [152] \tag{4.19}$$

and may be translated to the other quantities in question.
It should be noted that the spin polarisation measured in such an experiment is a result of the interplay between the initial and final state of the photoemission process and highly depends on the experimental geometry, orientation of the surface, light polarisation and photon energy. The amplitude of the experimentally observed spin polarisation is dependent on all of the aforementioned properties and may even revert upon a variation of some of them [153].

4.3. X-ray Absorption and Dichroism

The main tool used for the investigation of the local magnetic properties in this thesis is the method of X-ray absorption spectroscopy (XAS) and the X-ray magnetic circular dichroism (XMCD) effect. Contrary to typical magnetometry techniques and magnetotransport, XMCD allows the determination of the local spin and orbital magnetic moments specific for an element in question.

4.3.1. X-ray Absorption Spectroscopy (XAS)

In XAS the absorption of X-ray radiation by a sample is measured, while continuously varying the incident photon energy. As discussed in Eq. 4.13 in the context of ResPES, when the incident photon energy matches a transition between a core level and an empty valence band state, a highly efficient additional photoemission channel emerges. Over the transition, the absorption by the sample and also the current of emitted photons increases substantially, which allows to obtain the energy and shape of the individual transitions present in a material. As they denote the channel from a core level to the respective valence band state, the transitions are localized on a specific elemental species and are a hallmark for the presence of individual elements in the probed volume. Furthermore, the shape and precise position of the transition line depends on the chemical state and environment of the atom and can be used as a probe for its oxidation state, crystal field configuration and potential charge transfer processes [154].
The transition relevant for the XAS process is depicted schematically in Fig. 4.4a) for

the example of the $L_{3,2}$ transition typical for transition metals. The transition energies are in the range of the soft X-ray regime, ranging from several hundred to about 2.5 keV. In the resonant transition, an electron from the 2p core level is excited into the empty part of the valence or conduction band spectrum by the incident photon. As this is an optical transition the selection rule of $\Delta L = \pm 1$ applies for the transition. The resulting absorption spectrum is depicted in Fig. 4.4b) as the upper curve. The sample current strongly increases at the onset of the L_3 edge. The spectrum visibly contains two main contributions separated by about 10 eV, both of which have fine structures. While the fine-structure can be attributed to a variety of the aforementioned reasons, the splitting between the two main peaks is caused by the spin-orbit interaction of the core hole in the 2p level. Removing a single electron from the 2p shell leads to two possible states, with the core hole spin parallel or opposite to its orbital angular momentum. The strong SOC present in the core level then leads to a substantial splitting between the two states labelled by their resulting total angular moment $j = 1/2$ and $3/2$ [52].
The most straightforward measurement for the absorption of X-rays in a material is a measurement of the transmitted portion of X-rays through a very thin sample, which is experimentally only feasible in a very limited set of situations. In this thesis two main methods of XAS detection are applied. Total electron yield (TEY) is the most commonly used method in the soft X-ray regime, using the total number of emitted electrons and hence the sample drain current as a measure for the absorption strength. The signal is often normalised to a beam reference current acquired on the beam path before the sample. TEY is a highly surface-sensitive detection method, as the information depth is limited by the travel distance of electrons similar to the PES experiment. As the sample current also carries contributions from secondary electrons the probing depth is slightly higher than in typical PES experiments and estimated to 3-5 nm [155], exponentially decaying away from the surface. Fluorescence yield (FY) utilizes a radiative recombination process of the core hole and is acquired by an X-ray sensitive diode, which is placed facing the sample surface under a certain angle to avoid reflections of the incident beam. FY is substantially more depth sensitive and limited by the X-ray attenuation depth in the sample, which ranges up to several hundred nm [155,156]. FY is only rarely used in the soft X-ray regime, as electron yield is clearly the dominant recombination process and the re-absorption of photons (self absorption) may create a rather complex situation for the interpretation of line shapes and magnetic moments.

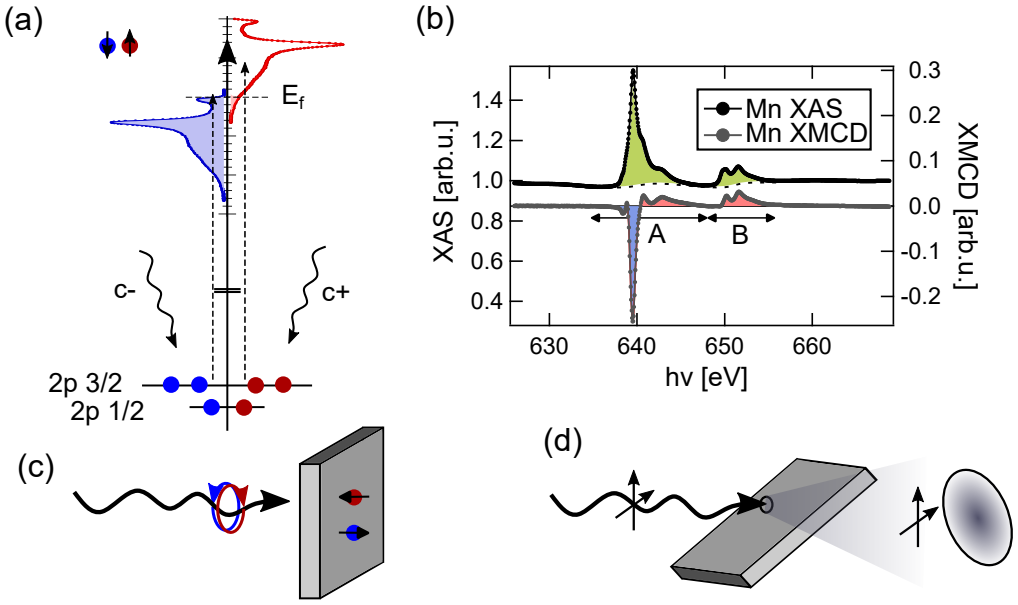

Figure 4.4.: XAS and dichroic effects. a) Resonant emission process depicting the transition from the 2p core level states to the unoccupied portion of the valence band on the example of the Mn DOS assuming a Stoner like picture [155]. b) XAS (upper) and XMCD (lower) spectrum of a $MnBi_2Te_4$ sample under a large external field, together with indicators relevant for a sum rule analysis. c) Probing geometry of the XMCD experiment. Incident circularly polarised light is sensitive to the spin polarisation along the light direction. d) Geometry of the XLD experiment. Linear polarised light is utilized as a probe for the deviation from a spherical distribution for the local wave function, which is often related to magnetic order.

4.3.2. Magnetic Circular and Linear Dichroism (XMCD, XMLD)

Next to the line shape of the XAS signal, the dichroism between two different light polarisations is a powerful tool for the analysis of local magnetic properties. X-ray magnetic circular dichroism (XMCD) allows to probe the spin and orbital magnetic moments in a surface and element specific way, while X-ray linear dichroism is sensitive to local asymmetries of the wave function and therefore often used to probe antiferromagnetic properties.

The initial stated includes a fully occupied core shell with spherical symmetry [52], which implies that the choice of basis states does not alter the transition probabilities. During the transition from the core level to the valence band, the light only interacts with the orbital part of the wave function, rendering the spin moment as a conserved quantity in the process [155]. The XMCD effect will be schematically explained on the example of the L-edge transition in the following. The initially fully occupied 2p core level yields six orthogonal eigenstates denoted as $|m_o\rangle|m_s\rangle$ with $m_o = \pm 1, 0$ and $s = \pm 1/2$. Taking

SOC into account, as previously mentioned a new set of eigenstates will be used, categorized as $2p-3/2$ and $2p-1/2$ with the relative occupancies 4:2. Upon absorption of an incident photon, transitions from these states to the 3d-orbital derived states occur. During such a transition the total angular momentum has to be conserved, imposing constraints on the possible transition matrix elements connected to the photon spin of $\pm$ 1. A calculation of the individual transition probabilities for all possible paths as presented in [52](p.393) yields a higher transition probability for spin up electrons under c+ polarised light and vice versa for c- polarisation. If now an asymmetry in the available final states – the number of available empty d-states – is introduced by an overall spin polarisation of the d-states as sketched within the concept of Stoner magnetism in Fig. 4.4, the transition probabilities for the two light polarisations integrated over all possible paths will differ. This difference is referred to as the XMCD effect and is related and directly proportional to a magnetic polarisation of the d-states.
A more quantitative approach is given by the XMCD sum rules and allows the determination of both the spin and orbital magnetic moment of an elemental species. The full integrated XAS signal for both light polarisations is proportional to the total number of available d-holes. The *charge sum rule* can be expressed as

$$I = c n_h, \tag{4.20}$$

where c is a proportionality constant given by the specific experimental conditions. The intensity in question corresponds to the green area in Fig. 4.4b). In practice, n_h is a known quantity, allowing for the determination of c. The corresponding XMCD signal displayed below can be separated in regions of the L_3 and L_2 transitions. If these can be well separated, the average spin moment m_s of the d-states can be calculated by the *spin sum rule* as

$$-A+2B = \frac{c}{\mu_\mathrm{B}} m_\mathrm{s} \tag{4.21}$$

where A and B are the respective integrated intensities of the two edges and c follows from Eq. 4.20. If the d-states furthermore exhibit an average orbital moment, the fully integrated XMCD signal does not cancel to zero, allowing to determine the m_o via the *orbital sum rule* as

$$-(A+B) = \frac{3c}{2\mu_\mathrm{B}} m_\mathrm{o}. \tag{4.22}$$

The application of sum rules requires an appropriate treatment of the step-like background, which can be observed for each absorption edge, as the increase in intensity

after the edge corresponds to non-resonant transitions, which are not part of the considerations made above. This is typically solved by the iterative adaption of a Shirley-background to the absorption signal. [1]

The geometry of an XMCD experiment is depicted in Fig. 4.4c) for a beam in normal incidence. The circularly polarised X-ray beam is impinging onto the sample surface. As the photon spin is oriented along its propagation direction, the XMCD effect is sensitive to the projection of the sample magnetisation along the incident light vector. The magnetic field is typically applied along the light incident direction and the sample is either oriented in normal or grazing incidence, depending on whether an out-of-plane or in-plane magnetisation is probed. Fig. 4.4d) depicts a second important probe often used in the frame of dichroism in X-ray absorption, namely X-ray linear dichroism (XLD). XLD uses linearly polarised incident light in the same energetically resonant condition as XMCD. In XLD, the dichroic effect is not caused by the photon spin directly. Instead, the direction of the light vector $\vec{E}$ with respect to the overall shape of the unoccupied part of the wave function – here the respective d-states – causes an asymmetry in the respective photocurrent. In simple terms: When the unoccupied part of the d-states is elongated along the direction of the electric field vector, an increase in photocurrent can be observed. A derivation of this effect is e.g. demonstrated in [52](p.403). The deviation from spherical symmetry of the unoccupied d-states can be caused by a variety of reasons, classified in two main categories. The *X-ray natural linear dichroism* is in general related to the crystalline or ligand structure of a material and therefore not a probe of its magnetic state. The *X-ray magnetic linear dichroism* (XMLD) on the contrary arises due to spin-orbit coupling (SOC) in the valence states of a compound. The orbital wave function of the d-states is influenced by a polarisation or preferred alignment direction of the spin part of the wave function. This typically causes a cylindrical deviation from the originally spherical shape, as schematically sketched in Fig. 4.4d). A measurement geometry chosen with the alignment axis along one of the polarisation directions may be used as a probe for these magnetic properties. Contrary to XMCD, XLD caused by a magnetic polarisation is sensitive to the square of the local magnetic moment m^2. It is therefore an useful tool for the study of antiferromagnetic materials, whose preferred magnetisation axis is given by a Néel vector $\vec{n}$.

[1] The sum rule analysis employed in this thesis was conducted by Dr. A. Tcakaev and a profound explanation of the approach and derivation of the error distribution can be found in [157].

4.4. Setup Implementation and Instrumentation

Next to the preparation of samples by MBE, which was conducted in the lab located in Würzburg, many of the methods employed in this thesis require the use of synchrotron radiation and took place at multiple synchrotron facilities. In the following, the most important setups and experimental endstations developed and used in the course of this thesis will be sketched along their relevant properties and conceptions. This includes the MBE chamber located in Würzburg, as well as several synchrotron based endstations specialised on various types of photoemission spectroscopy as well as X-ray absorption techniques.

Development of the MBE Setup in Würzburg

Within the course of this thesis, an MBE system for the growth of Te-based thin films in combination with a photoemission setup was developed. As this system was specifically designed and used for the growth of $MnBi_2Te_4$ systems and constitutes the main setup used in this work. Fig. 4.5 a) shows a full view of the experimental setup. The system is equipped with a main photoemission chamber exhibiting a Scienta SES 200-2 photoelectron analyser. The sample can either be kept on the main transfer manipulator for measurements or be transferred to a dedicated low temperature manipulator with a base temperature of ~ 7 K and six axes of freedom. The system has two main light sources, a Termo-VG Scientific dual anode X-ray gun (XR3E2) and a MBS-Scientific VUV Light Source System (MBS-L1T1). The two lamp-heads of the VUV-source are specialised to operate with He- and Xe-gas respectively. The energies accessible with this lamp therefore include the He I-α, He II-α, and Xe-I spectral lines (21.218 eV, 40.8135 eV and 8.437 eV[158]).

Samples are inserted into the system through a loadlock with an additional docking port for vacuum suitcases. The preparation chamber is equipped with a Ar-ion sputter gun and a long He-cryostat manipulator for sample transfer and allows for surface preparation and LEED investigations down to ~ 30 K. The LEED apparatus is a CF-150 OCI LEED with standard optics.
One the side of the preparation chamber an additional MBE system is mounted to the setup, which is used for the growth of Te based compounds. The MBE-chamber is a cylindrical chamber with double walls, where the inner wall can be cooled down to cryogenic temperatures using LN_2 as a cold trap for residual gases to lower the background pressure. The equipment of the MBE chamber is shown in Fig. 4.5 b) and includes multiple Knudsen evaporation cells arranged at the chamber bottom as well as

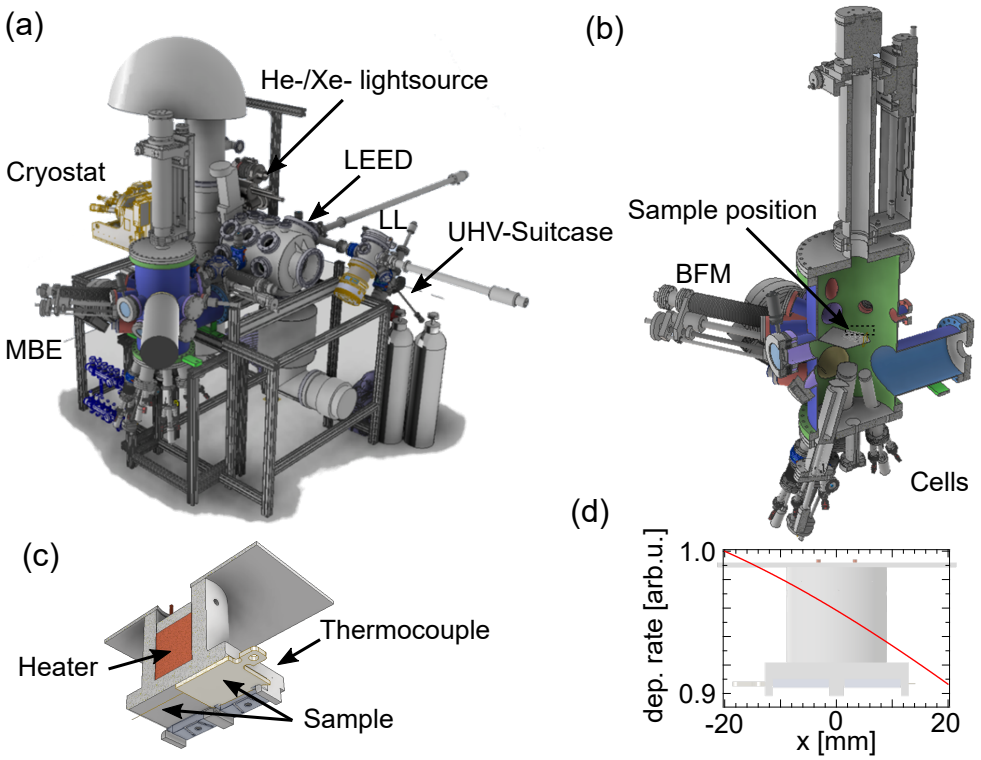

Figure 4.5.: Custom developed MBE and photoemission setup. a) Full view of the chamber system consisting of the MBE, a preparation and transfer chamber and the main photoemission chamber. b) Half open view of the MBE chamber with sample stage, beam flux monitor and Knudsen cell assembly. c) Manipulator head design with two sample slots and resistive heating cartridge. d) Simulations for film homogeneity considerations assuming fully ballistic transport and a filled cell. The distance between cell and sample is 16 cm, the cells are tilted of the main axis by 16 degrees.

several means of growth diagnosis. A beam flux monitor allows to acquire the beam equivalent pressure (BEP) and a RHEED system can be utilized to monitor the sample surface during and after deposition. The sample deposition stage (Fig. 4.5 c))is a custom design to allow for a maximal amount of temperature stability as well as for the simultaneous deposition on two substrates under identical conditions, which can be used as references in multi-step growth or for the deposition on different substrates.
Fig. 4.5 d) shows a simulation of the deposition rate coming from a single Knudsen cell mounted under an angle of 16° off the vertical axis, as shown for the cells in b). The simulation assumes a homogeneous evaporation behaviour from the full cell surface and ballistic transport through the chamber up to the sample surface. Assuming the typical dimensions of two samples mounted onto two sample holders to be 16 mm, the simulation shows the change in deposition rate over the full length to be maximally 3.8 %. Introducing continuous sample rotation to increase the sample homogeneity was not found to be necessary for the applications in this thesis.

To ensure full control over the experimental parameters, the setup of the system was accompanied by the development of a MBE control software nicknamed *Pillalab*. The software allows to control the individual cells, monitor the chamber conditions, an automated process to measure the beam equivalent pressure (BEP) and contains a functionality for logging all relevant parameters during a deposition process. It furthermore contains an interface to import custom growth recipes and automatize the individual steps. A more profound documentation can be found in the appendix of this thesis.

Asphere III at P04

In collaboration with the group of Kai Rossnagel (CAU Kiel), and within the frame of this thesis a twin MBE setup to the one developed in Würzburg was planned, acquired and set up at the synchrotron endstation Asphere III at beamline P04 (DESY, Hamburg). Fig. 4.6 shows a complete view of the endstation including a Scienta Omicron DA30 analyser and the MBE system. P04 is a beamline specialised on highly brilliant soft X-ray radiation. In combination with the endstation this allows for soft X-ray ARPES, spin-resolved and resonant photoemission experiments. During the time of this thesis, the chamber has been equipped with a set of focussing X-ray optics as well as with an highly precise sample manipulator, carried by a high-precision hexapod system to allow for spatially resolved measurements with a spot size of currently ~ 10µm. The control of the endstation is realized with a custom developed LabView program, unifying the communication with all necessary devices.

The MBE system is attached to the endstation via an UHV tunnel system with a magnetic sample train. The system includes three main chambers, a loadlock chamber, a small preparation chamber with high-temperature heater and a main MBE chamber (Scienta Omicron Lab 10), equipped with a set of Knudsen cells as well as one high-power electron beam evaporator. Similar to the aforementioned setup, the system is specialised on Te based MBE

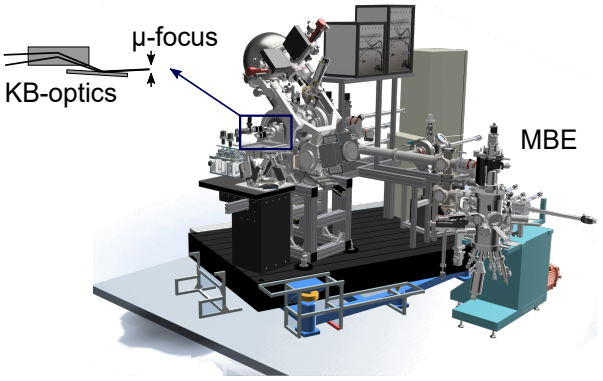

Figure 4.6.: Asphere 3 experimental endstation. The synchrotron endstation is equipped with a Scienta Omicron DA30 analyser and a μ-focus unit. A connection using a vacuum tunnel enables the transport of samples grown in the adjacent MBE system. CAD-files with courtesy of Tim Riedel.

processes and currently equipped for the growth of $MnBi_2Te_4$-based compound and Ta-based TMCD's.

ESPRESSO and the VLEED Laser Spin ARPES

The spin-resolved measurements in this thesis as mainly shown in chapter 7.1.2 were acquired at the ESPRESSO-endstation and the VLEED-Laser-Spin ARPES setup at the *HiSOR - Hiroshima Synchrotron Radiation Center* in Hiroshima, Japan. The ESPRESSO endstation is equipped with a Scienta R4000 Analyser with 2 VLEED-spin detectors, which are able to image all 3 spin directions. The setup is connected to the undulator beamline 9B of the HiSOR Synchrotron which allows for circular as well as linear polarised light in a photon energy range of 16 eV to 80 eV. A more profound documentation is e.g. given in [151,159].
Additionally, the Laser-based spin-polarised measurements were done in a similar setup based at the same facility. The VLEED-Laser-spin ARPES setup facilitates a pulsed Laser light source with an energy of 6.4 eV. Using suitable optics, the Laser beam is focused onto the sample resulting in a spot size of $\approx 10\,\mu m$ (an identical Laser setup described in [160]). The setup was further equipped with a Scienta Omicron DA30 Analyser and a VLEED-Spin detection setup. The sample stage was optimized for very low sample temperatures down to $\sim 7\,K$.

The 1^3 Endstation

The ARPES and specifically temperature dependent ARPES experiments shown in this work were mainly conducted at the 1^3-endstation of the Bessy II synchrotron in Berlin. The endstation uses a specialized He_3-cryostat to achieve a base temperature of approximately 1K. The energy resolution can be tuned up to a minimum of 1 meV for beamline and the Scienta-Omicron R8000 photoelectron analyser, separately. The Analyzer furthermore offers a DA-30 deflection mode and the beamline can provide linear as well as circular polarised light down to energies as low as $\sim 8\,eV$. A more detailed characterisation of the setup can be found in [161].

BOREAS Endstation at BL-29

The XAS and XMCD results presented in this thesis were acquired at the Hector endstation of the BOREAS-beamline (BL-29), ALBA Synchrotron, Spain [162]. The endstation is equipped with a vector magnet reaching up to 6T and yields a base temperature of $\sim 3.5\,K$ at the sample position of the He-cryostat. Signal detection is realized by cur-

rent measurements of the sample as well as a reference gold mesh. FY-detection can be realized by using a silicon-drift detector or an X-ray sensitive diode. A part of the measurements was also conducted at the high-field diffractometer at the BESSY II synchrotron in Berlin, which yields a similar design[163]. At both setups a docking connection for an UHV suitcase existed as well as an adapter system for flag style sample plates, enabling a full UHV sample transport from the growth setup to the respective experimental endstations.

5. Growth Dynamics of $MnBi_2Te_4$ Thin Films and Heterostructures

Overview

Apart from the investigation of the surface magnetic properties of $MnBi_2Te_4$ bulk crystals, all experiments in this work were performed on samples grown by molecular beam epitaxy in the setup described in chapter 4.4. In this chapter, each of the growth mechanisms is described in detail, starting with the growth of Bi_2Te_3 and $MnBi_2Te_4$ in the thick film limit, followed by the growth mechanisms used for heterostructures containing single $MnBi_2Te_4$ septuple layers. Each chapter covers the main growth mechanisms and outlines the phases that can be achieved along with a detailed sample characterisation.

Most of the discussion of diffraction experiments has already been published in [94,129] and a detailed discussion of the modelling approach can be found in the latter. Some of the results on the growth of $MnBi_2Te_4$ thin films and monolayers were discovered in the scope of the master thesis of Sebastian Buchberger, which was written in the course of this work. Further details may also be found there [164].

5.1. MBE Growth and Growth Dynamics of Bulk Bi_2Te_3 and $MnBi_2Te_4$ Films

At the present point, the growth of Bi_2Te_3 as bulk crystals and thin films is a well established technique, with crystals even available from commercial sources. Concerning the epitaxial growth of Bi_2Te_3 a variety of feasible approaches has been established, working with elemental or binary source materials, using stepped growth approaches and working with various substrates. Overall, high-quality films can be achieved in a large phase diagram [109,117,165–167]. In all mentioned approaches, Bi_2Te_3 is grown with an oversupply of Te to achieve a stoichiometric film composition and the Te flux can be utilized as a control parameter to tune the n-type doping in the films. The approach chosen in this thesis uses binary sources for the growth of Bi_2Te_3 and all further compounds, as pioneered in [118]. The reason for this choice is to simplify the growth

phase diagram, as the growth Bi_2Te_3 from a single source charged with Bi_2Te_3 is possible, while an additional Te offer can be introduced as a tuning parameter for the stoichiometry and defect control. In the case of elemental sources, a large flux ratio is required [166]. A significant obstacle in this approach is the availability of reproducible high-purity binary source materials and gradual changes in the source composition, which necessitates a partial recalibration of the growth parameters after longer periods of use. The beginning of this chapter will show, that indeed the chosen growth approach is viable in producing high quality films of Bi_2Te_3 on the BaF_2 substrate, suited for photoemission experiments. Subsequently, the growth of $MnBi_2Te_4$ will be worked out, by extending the growth mechanism.

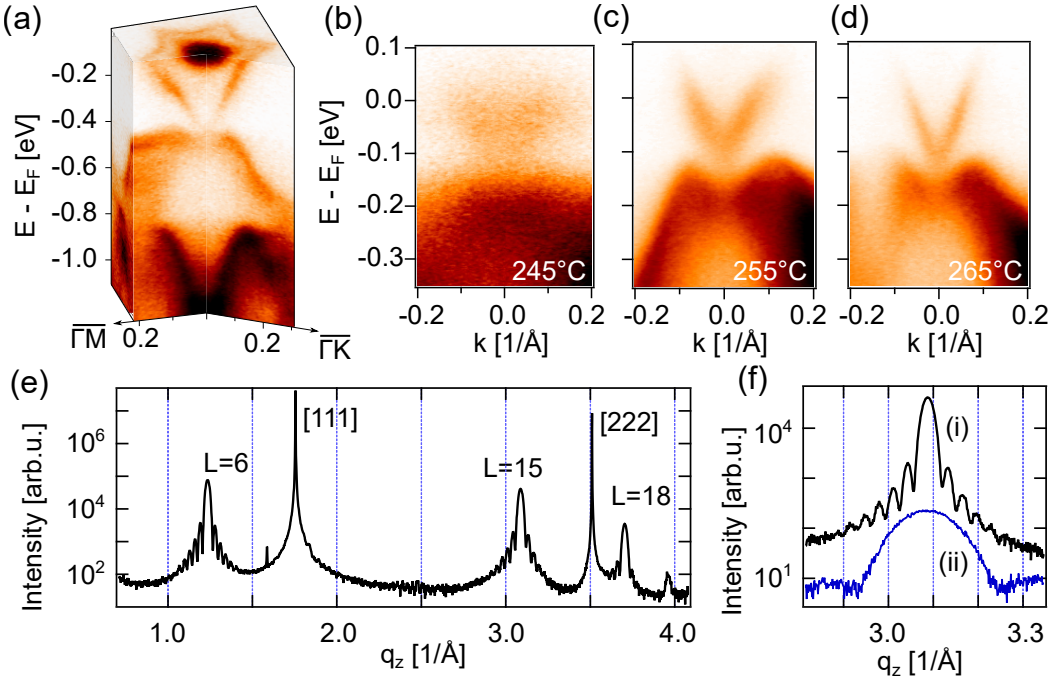

Figure 5.1.: Photoemission and XRD on Bi_2Te_3 thin films. a) ARPES map of a thick n-type Bi_2Te_3 film with faces along the $\overline{\Gamma K}$ and $\overline{\Gamma M}$ high-symmetry directions and a constant energy contour at the Fermi energy. b-d) Growth temperature dependence of the TSS and valence band structure showing a substantial increase in band sharpness while the n-doping is suppressed by a Te oversupply. e) XRD $\omega - 2\theta$ long range scan showing the BaF_2 [nnn] diffraction peaks and the typical diffraction pattern of a Bi_2Te_3 thin film. f) Enlarged Bi_2Te_3 [000 15] diffraction peak for a thick n-type film (i) and a thin carrier-compensated layer (ii). Both curves nicely depict the diffraction maximum with a set of interference fringes due to the finite sample thickness. *Figures a-d) adapted from [120] licensed under CC BY 4.0.*

Fig. 5.1 a) shows an ARPES data set, depicting a section of the 2D surface Brillouin zone centred around the $\overline{\Gamma}$-point of an epitaxially grown Bi_2Te_3 film. The sample was grown from a single Bi_2Te_3 source without additional Te offer at T_{sub}= 245 °C and the results

were acquired utilizing He I_α light in situ directly after the sample growth. The ARPES data displays a hexagonally warped surface state at the Fermi energy, linearly dispersing towards the Dirac point. As typical for Bi_2Te_3, while the upper branch of the TSS is clearly defined, the lower branch merges into the valence band structure. A comparison to previous publications allows to assign the observed electronic structure to Bi_2Te_3 with a high crystalline quality[74,116]. The clarity of the features and sharpness of the bands furthermore highlights the high surface quality of the epitaxial film. In the centre of the warped TSS at the Fermi energy, a clear maximum in intensity is visible, which can be assigned to a finite population of carriers in the bulk conduction band. The conduction band population indicates, that the sample resides in the metallic part of the phase diagram, as expected for the given growth conditions due to a Te deficit in the film[109]. Fig. 5.1 b-d) shows a series of ARPES spectra for samples grown with additional Te offer, which can be realized by the use of a source material with high Te content or the use of an additional Te cell. The samples were grown at substrate temperatures of 245, 255 and 265 °C. The evolution of the spectra clearly shows a substantial increase in the sharpness of the band structure with increasing temperature, reaching the same quality as a), while for all temperatures a population of the conduction band can be suppressed.

A characterisation of the structural properties of the films is further given by an XRD analysis. Fig. 5.1e) displays an $\omega - 2\theta$ scan of the sample along the q_z-axis of the reciprocal lattice with a logarithmic intensity scale. Two main sets of peaks are visible, corresponding to the [nnn] diffraction peaks of the BaF_2 substrate and the [000L] peaks corresponding to the Bi_2Te_3 film. The peak positions and relative intensities match previous reports[117]. The emergence of interference fringes at the flanks of the Bi_2Te_3 peaks indicates a thin epitaxial film with homogeneous thickness. The peaks for L = 9 and 12 do not appear in the diffraction curve, as they exhibit a very low structure factor for the Bi_2Te_3-lattice[117,128]. Next to a confirmation of the structural properties,the position of the L = 15 diffraction maximum at $\sim 3.1\,\text{Å}^{-1}$ as depicted in panel f) furthermore allows to conclude on the precise stoichiometry of the films. The enlarged section shows curves for two different samples, corresponding to the spectra depicted in a) (blue) and d) (black). Te deficiency in Bi_2Te_3 leads to an effective reduction of the mean inter-planar atomic distance, which directly reflects on the position of L=15 maximum. For small deviations to first order this is approximated as

$$\Delta q_z = \frac{2\pi}{\langle \Delta z \rangle} \tag{5.1}$$

$$\langle \Delta z \rangle = 2.035 - 0.025\,\delta(\text{Å}) \text{ [118,168]} \tag{5.2}$$

following from empirical findings, where δ is defined as $Bi_{2-\delta}Te_3$ and Δq_z is the deviation from the ideal peak position. Applying the equation to the films in question gives a δ of 0.053 ± 0.020 for a), while d) is taken as 0 within the margin of error.
Overall, the findings show, that using the mentioned growth mechanism in the MBE setup, the growth phase diagram for Bi_2Te_3 can be reproduced accurately. Furthermore the direct connection to a photoemission spectrometer allows to relate the structural properties directly to changes in the electronic structure and allows to visualize the correspondence between sample stoichiometry and the relative position of the Fermi energy. For the growth of heterostructures containing QLs of Bi_2Te_3, in the following growth parameters with a substrate temperature of $T_{sub} = 265\,^{\circ}C$ will be chosen. The additional Te flux is adjusted to

$$\Phi_{R,Te} = \frac{BEP_{Te}}{BEP_{Bi_2Te_3}} = 1. \tag{5.3}$$

The parameters are chosen such, that stoichiometric Bi_2Te_3 can be acquired, and the growth is robust against slight deviations of the cell fluxes due to the high substrate temperature. A more complete phase diagram of this growth mode can e.g. be found in [109].
After initial predictions, that $MnBi_2Te_4$ may exist as a thermodynamically stable compound [29], the crystal structure was first confirmed in crystals grown by flux methods [28,93,169,170]. In bulk crystals, the complex magnetic properties as well as the occurrence of antisite defects have lead to conflicting observations on the topological properties [39,40]. In order to further utilize $MnBi_2Te_4$ and its related compounds, establishing a method of growth by MBE is highly desirable, as it not only allows a higher control over the sample parameters away from thermodynamic equilibrium, but also enables the growth of heterostructures with alternating properties along the z-axis. During the course of this thesis, many paralleling approaches on the MBE growth of $MnBi_2Te_4$ have been realized, either utilizing co-evaporation or the alternating stacking of Bi_2Te_3 and MnTe layers [94,171–177]. In line with the growth mechanism for Bi_2Te_3, the approach chosen in this thesis aims to grow $MnBi_2Te_4$ by the co-evaporation of the binary precursors Bi_2Te_3 and MnTe as well as an additional offer of elemental Te.
While for the binary Bi_2Te_3, the growth is largely insensitive to small deviations in the flux offers, in the case of $MnBi_2Te_4$ both BiTe as well as Mn-based molecules exhibit a sticking coefficient close to 1. The stoichiometry of the resulting growth is thus strongly influenced by the respective flux ratio, which makes the ratio

$$\Phi_R = \frac{BEP_{Te}}{BEP_{Bi_2Te_3}} \tag{5.4}$$

the defining quantity for growth process[1]. Fig. 5.2a) shows an XRD pattern of a close to phase pure $MnBi_2Te_4$ film with a thickness of ~ 40 nm grown with $\Phi_R \approx 0.042$, which yields a growth rate of $\approx 0.35\,\mathrm{nm\,min^{-1}}$. Below the experimental data, a simulation of the diffraction curve of pure $MnBi_2Te_4$ with a thickness of 20 SL is displayed[2]. The diffraction pattern along the q_z-axis exhibits all even diffraction peaks expected for $MnBi_2Te_4$. The unit cell containing three SL blocks allows for the occurrence of the [000L] peaks with $L = 3n$ for integer values of n. The diffraction pattern is well in line with literature[174,175] and the diffraction maxima exhibit a broad and asymmetric shape and generally low structure factor even for pure phase $MnBi_2Te_4$.

To allow for a growth optimisation, Fig. 5.2c-e) depicts an assessment of the influence of flux imbalance on the growth and tries to identify the respective impurity phases and the connected fingerprints on the XRD pattern. In the family of $MnBi_2Te_4$ compounds, several Bi_2Te_3-rich ordered phases exist, consisting of an alternating stacking of Bi_2Te_3 and $MnBi_2Te_4$ building blocks, with the members belonging to the $MnBi_2Te_4(Bi_2Te_3)_n$ series[141,178]. Consequently, a surplus of Bi_2Te_3 during growth is expected to lead to the intercalation of Bi_2Te_3 layers in the structure, while in the MnTe-rich part of the phase diagram, hexagonal and cubic MnTe phases exist[179,180] as possible cluster phases.

Fig. 5.2c) shows X-ray reflectivity (XRR) curves for samples with increasing Φ_R for values of 0, 0.03 and 0.05, where the first corresponds to pristine Bi_2Te_3. While all given values correspond to Bi_2Te_3-rich sample phases, the occurrence of a clear interference fringe patterns in all datasets shows, that the films grow with a highly ordered and flat surface over the full range of flux parameters. Panel d) furthermore displays the L = 6 and 9 diffraction maxima for a set of $\Phi_R = 0.03$, 0.05 and 0.07. The patterns show a clear trend, where a splitting in the L = 6 peak and a shift in position of the L = 9 peak are indicators of the Bi_2Te_3-rich phase. The findings are supported by XRD simulations for structures with an increasing number of intercalated Bi_2Te_3 layers in the $MnBi_2Te_4$ structure. The ratio of both is defined as

$$\gamma_{SL} = \frac{n_{SL}}{n_{QL} + n_{SL}} \tag{5.5}$$

such that $\gamma_{SL} = 1$ corresponds to pure phase $MnBi_2Te_4$. The simulations nicely reproduce the experimental findings and furthermore allow to define an empirical law

[1] It should be noted, that while Φ_R is a reliable parameter during individual growth campaigns, the optimum strongly varies when using source materials of different suppliers. This is a result of small differences in the Te content to which the Bayert-Alpert gauge is highly sensitive and hence does not allow to give an overall optimal flux ratio. Systematics listed in this chapter will always stem from the same growth campaign and are therefore fully comparable. The values given for a pure phase of $MnBi_2Te_4$ will nevertheless vary between experiments resulting from different growth campaigns.

[2] All XRD simulations in this thesis were conducted by Prof. Dr. S. L. Morelhão. The general calculation scheme is found in [121], details on the application to $MnBi_2Te_4$ are published in [94,129]

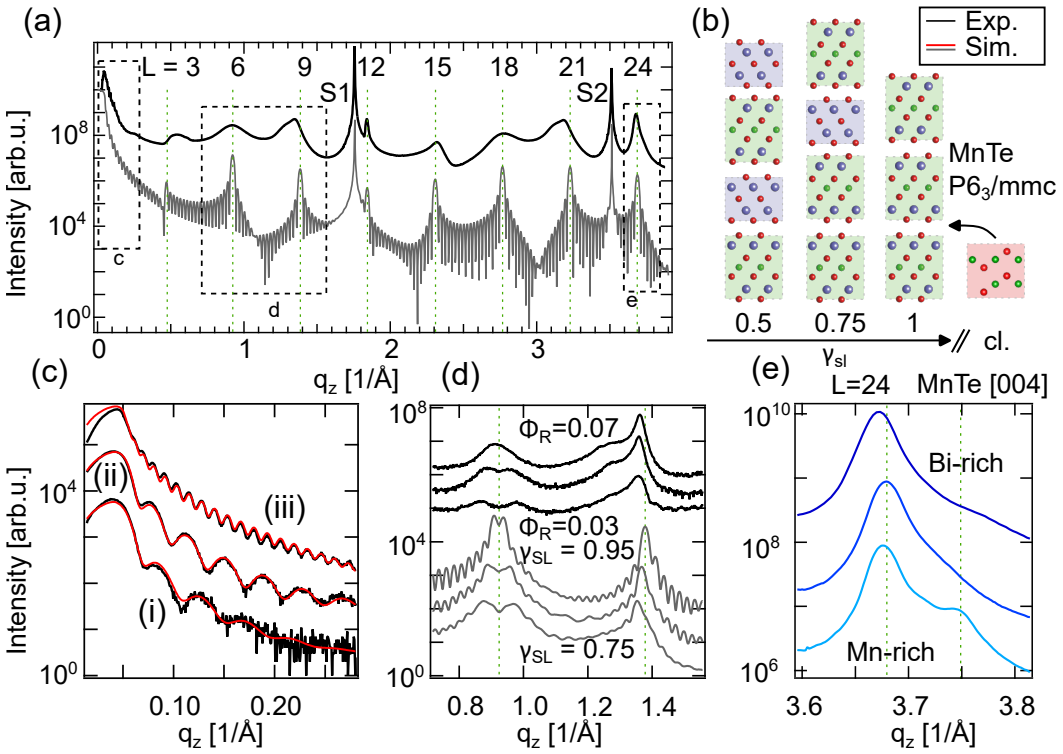

Figure 5.2.: Growth systematics by X-ray diffraction (XRD). a) XRD overview scan on close to pure phase $MnBi_2Te_4$ and simulated XRD pattern (grey). Peak positions are labelled with green dashed lines for $MnBi_2Te_4$, substrate peak positions are labelled with S. b) Structural models for different growth phases. Bi rich conditions with Bi_2Te_3 layer intercalation transition to a MnTe cluster rich phase. c) X-ray reflectivity curves for different thicknesses together with simulations from GenX (red). The estimated thicknesses d for i, ii and iii are 13.3, 15.6 and 46.0 nm, the samples were grown with $\Phi_R = 0$, 0.03 and 0.07. d) L=6 and 9 peak positions for increasing Φ_R and simulated patterns for increasing γ_{SL}. e) L=24 peak position with MnTe [222] impurity contributions for Mn-rich, pure and Bi rich phase. *Partially reproduced from [94], with the permission of AIP Publishing*

relating the sample stoichiometry to the splitting of the L=6 peak. The two satellite reflections are caused by the disordered superlattice of Bi_2Te_3 and $MnBi_2Te_4$ layers and the splitting was found to scale as

$$\Delta q_z \approx \frac{2\pi}{d_{SL}} \gamma_{SL} \tag{5.6}$$

with $d_{SL} = 1.36367$ nm.[3] From an extended modelling study on the XRD patterns it furthermore follows, that the satellite splitting occurs accentuated in the L=6 and 18 peaks, while a positional shift is found in the case of L=9 and 21, which may further be quantified [129]. Fig. 5.2e) depicts the L=24 diffraction peak area for samples grown

[3] The relationship practically used for the sample optimisation valid for the case of Cu K_α anode based XRD setups is published in [94].

with varying flux ratios on either side of the pure phase. The curves correspond to a MnTe rich, pure-phase and Bi_2Te_3-rich phase. In the MnTe-rich regime, the additional appearance of a feature at $3.75\,\text{Å}^{-1}$ is observed, which strongly increases for increasing MnTe offer. The position of the feature is identified with the [004] diffraction peak of the hexagonal MnTe phase[129,180]. As evident from the XRD pattern, the hexagonal $P6_3/mmc$ MnTe phase enters the structure in an epitaxially oriented way, but contrary to the Bi_2Te_3 intercalation results in an increased amount of structural disorder. In particular an increased amount of twinning in the film growth is found for MnTe rich phases[164]. From a flux series, by using linear interpolation of the apparent peaks, again an empirical law for the sample optimisation may be derived, which relates the ideal $\Phi_{\text{R,ideal}}$ to the experimentally used one by

$$\Phi_{\text{R,ideal}} = \frac{1.3649\,\Phi_R}{1.3649 + A_{\text{MnTe}}/A_{\text{MBT}}} \tag{5.7}$$

with $A_{\text{MnTe}}/A_{\text{MBT}}$ as the area ratio between the two peaks.

The layer structure of the films is furthermore corroborated by scanning TEM experiments as depicted in Fig. 5.3 for a film with $\gamma_{\text{SL}} = 0.8$. Panel a) displays an overview scan over the full sample structure. The scan shows three clearly distinguishable areas. The BaF_2 substrate at the lower parts with weak contrast, the film area in the centre and the darker protective Te capping layer at the top. The scan shows sharp interfaces between the individual parts and furthermore depicts the van der Waals structure of the film, where the individual building blocks are separated by vdW gaps. An enlarged section furthermore allows to identify the individual layers of the film, which consist of either seven- or five-atomic structures. Along with the line profile in panel b), the layers can be identified as $MnBi_2Te_4$ and Bi_2Te_3, matching well to the expected z-lattice constants for the two compounds. Fig. 5.3c) depicts the interface region between the BaF_2 substrate and the lowest $MnBi_2Te_4$ layers. While the atomic contrast for the substrate vanishes at the interface, a clear and sharp onset of the lowest layer can be identified. Consequently it may be concluded, that the BaF_2[111] surface is well suited for the epitaxial growth of $MnBi_2Te_4$ and no defect structures are induced by the interface. Panel d) furthermore displays a scanning TEM picture of two adjacent SL acquired with a specialized probe corrected setup[4]. The increased resolution allows to uniquely identify all seven atomic positions within the SLs by contrast. Contrast differences are especially found between the Mn and Bi sites.

Taken together these findings confirm a structure model, in which Bi_2Te_3 QLs and hexagonal MnTe clusters enter in between the $MnBi_2Te_4$ layers when deviating from

[4] These measurements were conducted at a probe corrected FEI Titan 80–300 at the IFW-Dresden with the support of Dr. Pavel L. Potapov

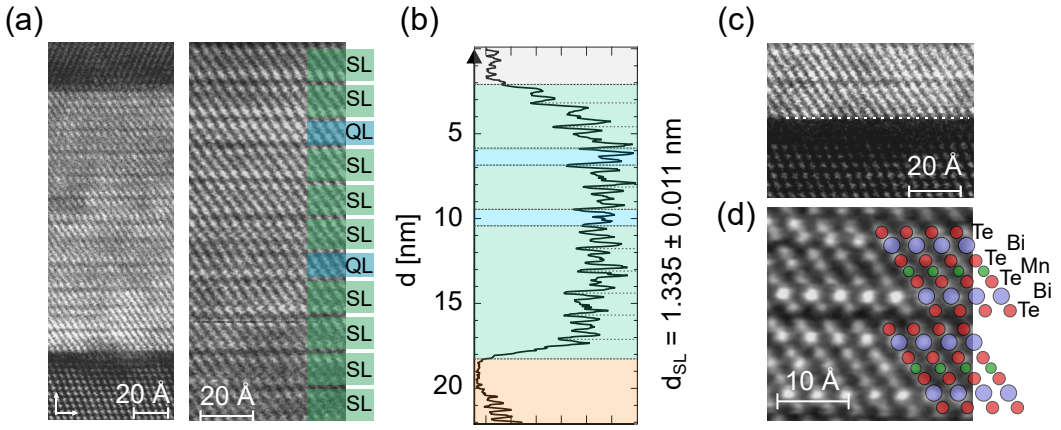

Figure 5.3.: Scanning transmission electron microscopy images of a $MnBi_2Te_4$ film. a) Large overview image of the full structure containing the BaF_2 substrate, the epilayer and a crystalline Te cap as surface protection. The right part of the figure displays a higher resolved image of the epilayer predominantly consisting of $MnBi_2Te_4$ SLs intercalated by two Bi_2Te_3 QLs due to stoichiometric inhomogeneities. b) Cross sectional representation of a full lamella. The individual vdW layers are separated by dashed lines and the average layer height nicely fits to the expected length scales for Bi_2Te_3 and $MnBi_2Te_4$ respectively. c) High-resolution images of the same structure acquired using a set of corrector lenses. The upper panel displays the high interface quality between substrate and film, while the lower panel shows an enlarged section depicting two SL of $MnBi_2Te_4$. All atomic positions are clearly visible and distinguished by contrast. *Partially reproduced from[94], with the permission of AIP Publishing*

an ideal stoichiometry. Both impurities grow epitaxially with the z-axis oriented along the [0001] direction of the $MnBi_2Te_4$ film. Bi_2Te_3 layers entering the layer structure in a defect free way is a direct consequence of the similar in-plane lattice constant and rotational symmetry of the two and paves the way towards the growth more complex heterostructures. Looking again at the high-resolution scanning transmission electron microscopy (STEM) images, the distinct contrast between the Mn and Bi sites is in strong contradiction to findings on bulk crystals grown by a flux method[93]. In these crystals, Mn and Bi sites appear with almost identical contrast, which is often attributed to a sizeable amount of antisite defects with implications both on the magnetic as well as electronic properties[34,40,44,93]. Consequently, the results on the thin films in this work show that the comparatively low temperatures systematically suppress the occurrence of antisite defects due to the insufficient thermal energy available. For a more thorough investigation of this indication, spatially resolved element sensitive methods such as TEM-EELS methods would be required.

An analysis of the full three-dimensional shape of the XRD maxima can further foster an understanding of the film structure on a nano- or micro-scale. Fig. 5.4a) depicts a 3D reciprocal space map (RSM) of the L = 21 diffraction peak of a 38 nm thick $MnBi_2Te_4$

film. The RSM shows an elongated droplet-shaped feature whose extent along the q_z-axis strongly exceeds its size in the $q_{x,y}$ plane. A projection of the intensity into the $q_{x,y}$ plane yields a pronounced spherical in-plane shape with traces of hexagonal symmetry. The hexagonal structure is further highlighted by a path integration over a full rotation through the data with six intensity maxima as displayed above the projection. The RSM reflects a film morphology, in which the typical domain sizes along the film plane strongly exceed the grain size in the growth direction, indicating a film with large and well ordered domains. The orientation of the RSM along the q_z-axis and the absence of any kind of canting furthermore supports the findings of a layer structure aligned with the surface plane of the substrate and confirms the very low degree of mosaicity in the film. The hexagonal shape of the x-y projection is reminiscent of the threefold rotational symmetry of the $MnBi_2Te_4$ film and reflects a preferred domain shape with the same symmetry. The feature is only weakly pronounced in contrast to RSMs of Bi_2Te_3, where it is a direct reflection of the trigonal pyramidal shape of the individual islands[181]. Together with AFM images of the film surface[5], the preferable growth mode of the films is found to be a layer by layer growth, in which the surface gradually evolves along the z-axis. This mode stands in contrast to the case of Bi_2Te_3, where islands nucleate and the QLs successively expand in the in-plane direction.
Fig. 5.4b-d) show the influence of the substrate temperature on both the crystalline quality as well as the surface dynamics during the growth. Panel c) depicts a rocking curve along the L = 21 diffraction peak of $MnBi_2Te_4$ for samples grown with increasing substrate temperature for values of 260, 280, 290 and 300 °C. Similar to the in-plane shape of the RSM, the curves reflect the film quality and grain size and show a decrease in peak width with increasing substrate temperature. A quantitative evaluation is given in Fig. 5.4b) and shows a gradual decrease in the peak width over the temperature range in question. Simultaneously a decrease in growth rate is observed with increasing sample temperature. The evolution of the shape of the L = 24 diffraction peak in 5.4d) shows, that the increased substrate temperature leads to the emergence of the MnTe cluster peak as a hallmark of the MnTe-rich side of the phase diagram. In conclusion, the findings show, that an increase in substrate temperature leads to a substantial increase in film quality and grain size up to the growth cutoff, which occurs around 320 °C. The decrease in growth rate is mainly driven by a reduced sticking coefficient for the BiTe molecules or an increased Bi desorption rate, overall shifting the equilibrium conditions at the sample surface. With increasing substrate temperature a larger Φ_R is required to keep the growth in phase pure conditions.

[5] Corresponding AFM images have been published in [94] and show a remarkable difference between the growth modes present in $MnBi_2Te_4$ as compared to pyramidal topography present in Bi_2Te_3.

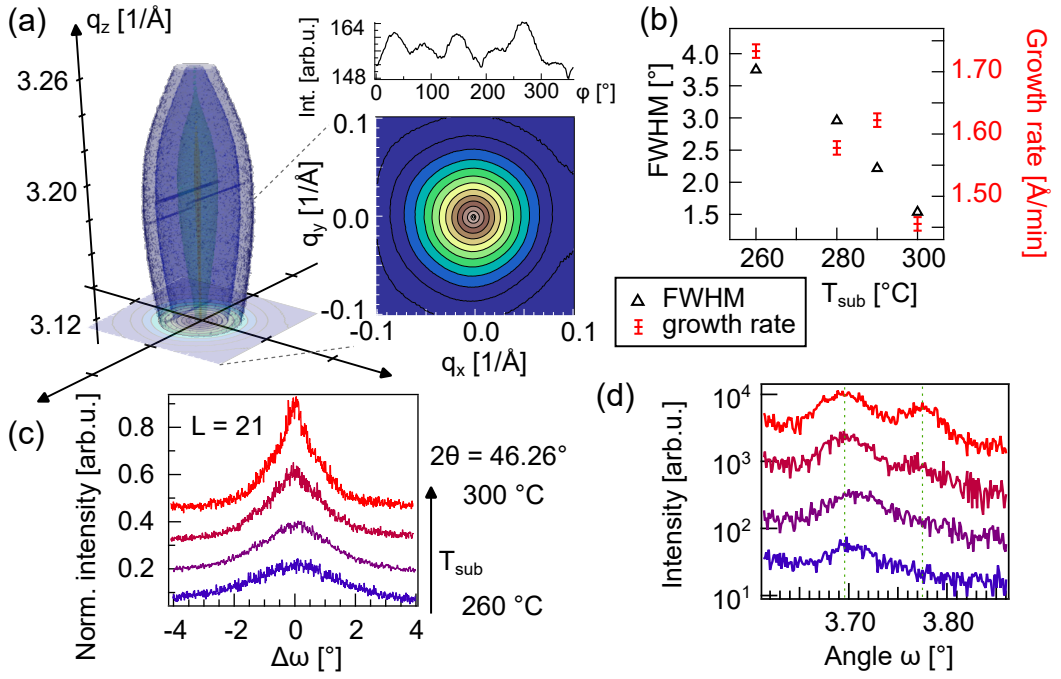

Figure 5.4.: XRD structure and crystalline grain size. a) Reciprocal space map (RSM) of the L = 21 diffraction maximum of a 38 nm thick $MnBi_2Te_4$ film. The panels on the right show a projection of the RSM into the xy-plane. To elucidate the slight hexagonal warping of the xy-structure, an intensity profile along a circular integration path is shown above. b) Substrate temperature systematics, showing an increased film quality and decrease in growth rate with increasing temperature up to a cutoff above 300 °C. c) Rocking curves through the L = 21 peak position for substrate temperatures of 260, 280, 290 and 300 °C. d) L = 24 peak window with an emerging MnTe signature for the same samples.

5.2. Growth Mechanisms for $MnBi_2Te_4$ in the Monolayer Limit

Following from the previous chapter a few general conclusions can be drawn about the compatibility of the growth schemes for Bi_2Te_3 and $MnBi_2Te_4$. Deduced from the spontaneous formation of $MnBi_2Te_4$ SLs and also apparent from the higher melting and growth temperatures (see chapter 3.1) it can be concluded that the $MnBi_2Te_4$ SL structure is energetically favoured over the coexistence of MnTe and Bi_2Te_3 phases. As the mobility along the out-of-plane axis is strongly limited by the nature of the MBE growth process, this fact can be exploited to grow controlled heterostructures of Bi_2Te_3 and $MnBi_2Te_4$ by controlling the individual beam fluxes and the substrate temperature during the growth. This chapter is concerned with the simplest type of heterostructure, namely the arrangement of a single SL of $MnBi_2Te_4$ on a Bi_2Te_3 3D TI. The growth mechanism is depicted in Fig. 5.5 and consists out of three main growth steps and the

initial substrate cleaning. Fig. 5.5a) shows a schematic of the growth process and the substrate temperature during the growth process is depicted in panel e).

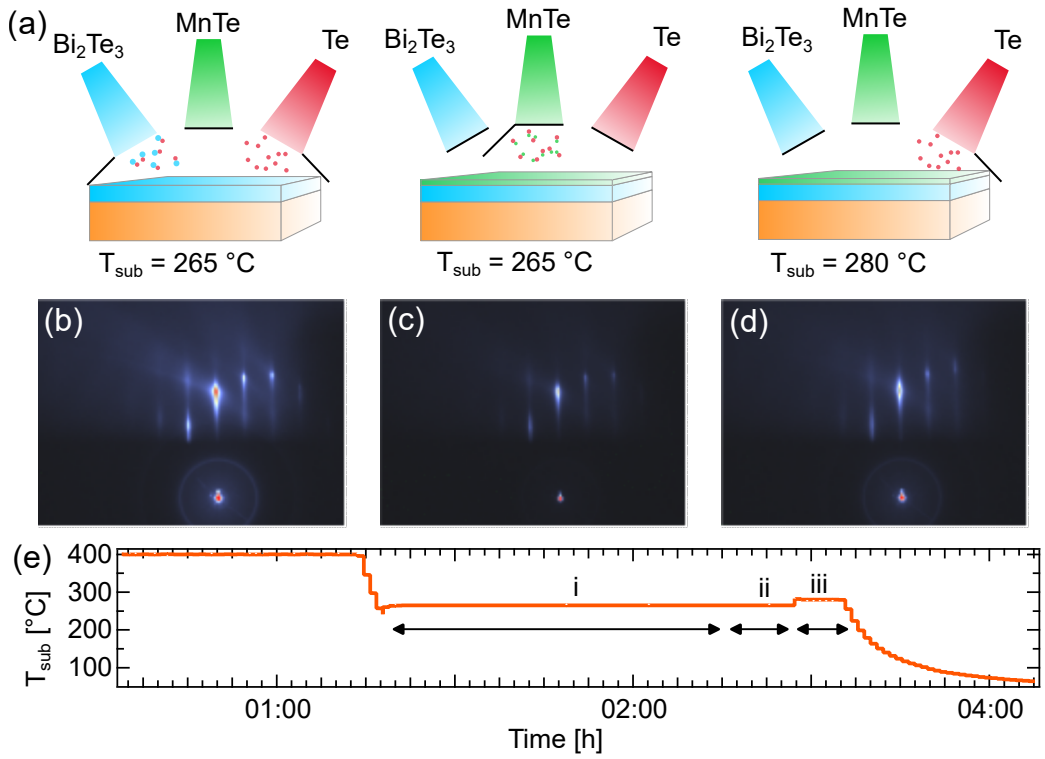

Figure 5.5.: Growth process of the ferromagnetic extension. a) Schematic growth procedure displaying the three stages of growth by the respective cells in use. Growth of the 3D TI layer, MnTe evaporation and annealing under Te atmosphere. b-d) RHEED patter during the growth displaying a high-quality Bi_2Te_3 surface, reduction by MnTe evaporation and restoration of high surface quality by annealing. e) Growth process diagram displaying the substrate temperature at different stages of the growth. The three phases depicted by small roman numbers correspond to the three phases shown above. *Figures adapted from*[120] *licensed under CC BY 4.0.*

After degassing and cleaning the substrate surface, a high-quality surface for epitaxial growth can be achieved. The 3D TI Bi_2Te_3 is then grown on the substrate using the co-evaporation of Bi_2Te_3 and additional Te, as described in the previous chapter. The growth at a substrate temperature of 265 °C using a flux ratio of $\Phi_{R,Te} \approx 1$ and a Bi_2Te_3 beam equivalent pressure of $3.4 \cdot 10^{-7}$ mbar yields a growth rate of $\sim 0.0022\,\mathrm{nm\,s^{-1}}$ (7.7 min/QL). The parameters are chosen to achieve Bi_2Te_3 in the stoichiometric phase without additional n-doping by Te vacancies. After the growth of the Bi_2Te_3-epilayer, a calibrated amount of MnTe is deposited onto the sample surface at constant substrate temperature. Typical parameters for this process are $\sim$ 9 min of growth at a beam equivalent pressure of $\sim 1 \cdot 10^{-8}$ mbar. The calibration of this parameter set is achieved by growing a calibration sample of stoichiometric $MnBi_2Te_4$ as described in the previous chapter

and deriving the equivalent flux and time needed for a single SL. As a subsequent optimization step for a very high surface quality, the parameters can be varied, slightly optimizing the band sharpness in in-situ photoemission experiments, which was found to be typically about 5 % lower in growth time. The difference may be related to the suppression of defects occurring with an MnTe oversupply as discussed below. Since the substrate temperature for high quality $MnBi_2Te_4$ films is higher than required for the growth of Bi_2Te_3, an additional annealing step is introduced. A high surface quality can be achieved by annealing the sample at 280 °C for 10 min. To avoid the desorption of Te at the elevated temperature, the annealing is conducted under a Te atmosphere ($\approx 1/3$ of the flux used during growth). The growth process can be monitored continuously by RHEED, as shown in Fig. 5.5 b-d). The initial high surface quality, apparent from a clear streak pattern and the additional appearance of Kikuchi-lines is significantly reduced by the MnTe deposition c). The annealing step suffices in restoring a high surface quality as confirmed by the re-emergence of a bright RHEED pattern in d). The specific parameters given for the growth, especially BEP values have to be interpreted with care and are mainly listed to allow for an estimation of the relative magnitude of the fluxes and timescales. Absolute values – especially when using binary cell materials – will always depend on the exact geometry of the growth chamber, placing of the flux monitor and filling of the cells.

The surface quality can subsequently be accessed by low-energy electron diffraction (LEED) as depicted in Fig. 5.6 for two different incident beam energies. Both images show a clear diffraction pattern with low background intensity and sharp individual spots. The LEED data indicates a highly ordered surface without any sign of strain induced superstructure. Furthermore, especially the image depicted in panel a) clearly resembles the trigonal rotational symmetry of the Bi_2Te_3 and $MnBi_2Te_4$ unit cell. While this is no direct probe, a low amount of twin domains can be deduced. Twin domain formation is typically an indicator of less optimal growth conditions and leads to a more rough surface morphology as the domains can not grow together[109].

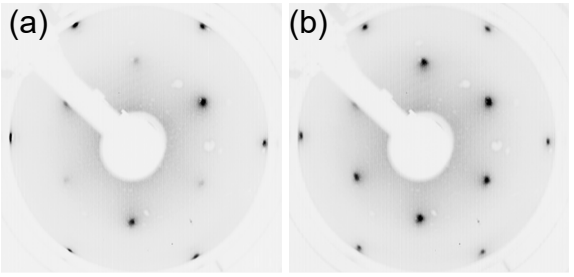

Figure 5.6.: LEED pattern of a single SL $MnBi_2Te_4$ on epitaxially grown Bi_2Te_3 on BaF_2 at 58 and 63 eV. The LEED pattern acquired at room temperature exhibits sharp spots and a trigonal symmetry as a hallmark for high crystalline quality and a low amount of twinning.

A very direct probe for the local lateral structure in heterostructure samples are cross-

sectional measurements using scanning transmission electron microscopy (STEM). Fig. 5.7 shows a STEM analysis of a representative heterostructure. The sample was capped with a protective Te capping layer to avoid oxidation of the surface before and during the measurement. The overview displayed in panel a) clearly shows the vdW layered structure of the sample. The Bi_2Te_3 QL structure is epitaxially growing on top of the substrate with its [0001] axis oriented along the [111] surface normal of BaF_2. The structure is terminated by a single layer with an extended lattice constant, which can be identified as the modified surface layer with the SL-structure of $MnBi_2Te_4$. All involved layers exhibit atomic resolution, which excludes any kind of rotational misalignment between the layers (e.g. rotation around the surface normal). A quantitative analysis of the lattice constants is shown in panel b) by extracting a line profile along the z-direction through the image shown in a). The contrast difference between epilayer, substrate and cap is clearly visible an can be assigned to the different atomic weights of the individual atomic species. The film furthermore shows a clear separation into individual vdW layers with minima in contrast corresponding to the vdW gaps. For the mean layer height of the Bi_2Te_3-epilayer a value of $d = (1.02 \pm 0.03)\,\mathrm{nm}$ can be extracted, while the extended layer on top exhibits a thickness of $\sim 1.35\,\mathrm{nm}$. Both values are well in line with the expected single vdW layer height for Bi_2Te_3 and $MnBi_2Te_4$. Magnifying a well resolved portion of the surface area further allows to distinguish between the individual atomic positions, as presented in Fig. 5.7c). The image shows the topmost two layers, where the change from quintuple- to septuple-structure is clearly visualized. All five and seven atomic position are clearly identifiable and distinguished by contrast, following from the increasing atomic mass in the order of $m_{\mathrm{Mn}} < m_{\mathrm{Te}} < m_{\mathrm{Bi}}$.

The STEM results furthermore allow to put the results of this growth process in context with findings made in previous publications on similar systems. The vdW gap between epilayer and the topmost SL is reminiscent of a well ordered and smooth interface and does not exhibit any pronounced difference to the underlying vdW gaps between the individual Bi_2Te_3 QLs. Similar to the findings in chapter 5.1, in the STEM results of the heterostructure, no systematic difference in contrast of the Bi sites away from the interface can be observed. This allows to conclude, that neither antisite mixing, nor the diffusion of Mn atoms to the lower lying Bi_2Te_3 layers does play a major role. This is well in line with the observations made in the previous chapter on the case of thick $MnBi_2Te_4$ films. In similar growth studies, it has been suggested, that the surface modification results in the occurrence of very extended surface layers (e.g. $Mn_4Bi_2Te_7$) which significantly define the magnetic properties of the structure [82]. While TEM is a local probe and therefore not suited to judge the properties of an entire film with statistical signi-

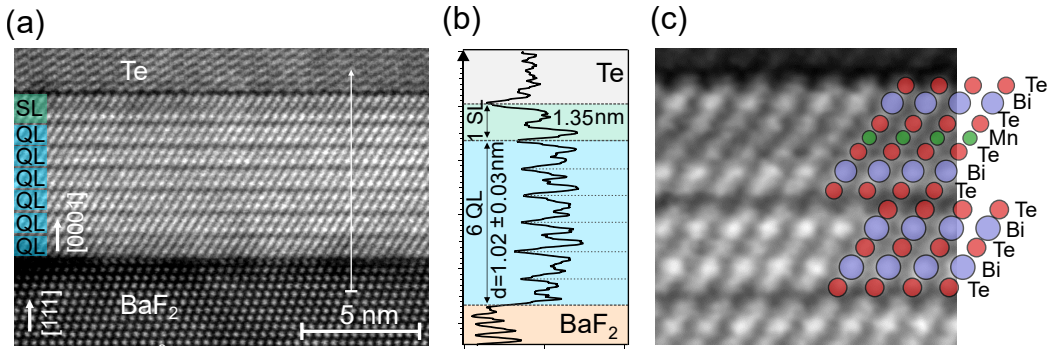

Figure 5.7.: Scanning transmission electron microscopy images of a $MnBi_2Te_4$-Bi_2Te_3 heterostructure. a) Large scale overview image of the full heterostructure. The image depicts the BaF_2 substrate with a sharp interface towards a Bi_2Te_3 epilayer with a thickness 6 QL. The structure is terminated by a single SL of $MnBi_2Te_4$ and a Te capping layer. A cross-sectional cut of the image showing the average layer distances is seen in panel b). c) Zoom in into the surface of the heterostructure. A clear quintuple-septuple layer structure is apparent, where all atomic positions can be differentiated by the respective atomic contrast. *Figures adapted from*[120] *licensed under CC BY 4.0.*

ficance, it can still be noted, that for the sample under investigation no such structure formation has been found, whereas they tend to play a role in less favourable growth conditions as presented in the next chapter. The only defect structures observed on this heterostructure were minor contributions of areas covered by 2 SL of $MnBi_2Te_4$ or partially unfinished layers.

As a more quantitative assessment of the sample structure, Fig. 5.8a) displays an X-ray diffraction (XRD) $\omega - 2\theta$-scan of the heterostructure. The general appearance of the diffraction curve is very reminiscent of the one shown in Fig. 5.1 for a pure Bi_2Te_3 epilayer. On closer inspection, an influence of the surface termination can be observed as a slight asymmetry in the main diffraction peaks. This asymmetry arises due to the extended septuple layer at the surface and can be interpreted as a leaning of the diffraction peaks towards the nearby diffraction maxima of bulk $MnBi_2Te_4$, namely the positions of the L = 9 and 21 diffraction peaks. Additional maxima are caused by the Te capping layer and will not be part of any further analysis. As a further probe for the sample thickness, panel b) shows a grazing incidence XRR scan. The scan clearly depicts XRR interference fringes with two different periodicities. The high frequency oscillation can be assigned to the thick Te capping layer, while the longer fringes stem from the epilayer and its surface termination. It should be noted here, that due to the very similar compositions and refractive indices of the Bi_2Te_3 epilayer and $MnBi_2Te_4$ surface, no substantial reflection from the interface is present and no additional interference pattern can be observed. The experimental results are adapted with an XRR

model of the complete sample structure – the BaF_2 substrate, the Bi_2Te_3 epilayer, 1 SL of $MnBi_2Te_4$ and the Te capping layer – and a very good agreement between model and experiment can be achieved. The fit yields an average Bi_2Te_3 thickness of 6.47 nm, which is in excellent agreement with the direct observations made by STEM.
The experimental XRD results in Fig. 5.8a) were adapted with XRD simulations by a superposition of several structural models in order to achieve the best fit to the experimental results. An optimal agreement could be achieved by assuming a Bi_2Te_3 epilayer fully covered by a single SL of $MnBi_2Te_4$. The thickness of the epilayer fluctuates between 5 and 7 QL, whereas the exact distribution is shown in the inset and nicely matches the XRR analysis. Due to the finite spatial resolution of the XRD experiment using a laboratory source, deviations from the model occur especially at small incident angles and the analysis is mainly focused on higher q_z.

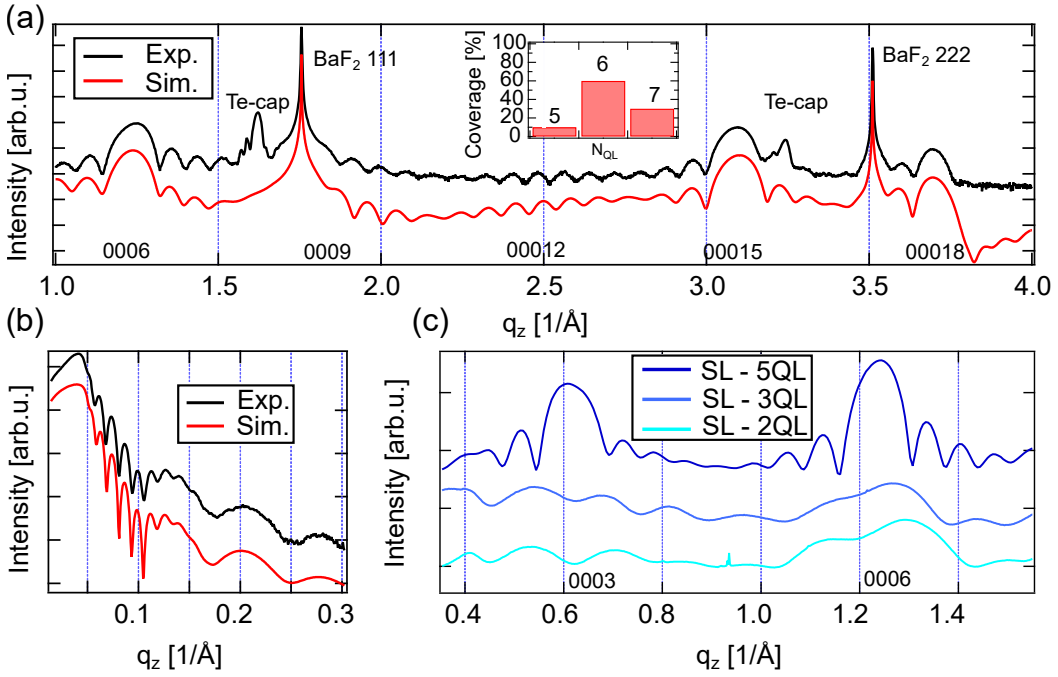

Figure 5.8.: XRD and XRR systematics on thin single SL $MnBi_2Te_4$-Bi_2Te_3 heterostructures. a) Large range XRD $\omega - 2\theta$ scan using a Cu K_α source. The scan depicts the [nnn] scans of the BaF_2 substrate as well as clear signatures from the thin film. The red curves show calculated XRD curves for the structure in excellent agreement with the experimental findings. The underlying thickness distribution of the simulation is shown in the inset. b) Grazing incidence XRR scan of a heterostructure capped with a protective Te layer. The experimental findings are displayed together with a simulation and show a clear oscillatory pattern indicative of a high surface quality. c) Synchrotron based high-resolution XRD $\omega - 2\theta$scan of a set of heterostructures with different thicknesses of the Bi_2Te_3-TI. The signature from the single SL of $MnBi_2Te_4$ emerges as a visible peak asymmetry of the [0003] and [0006] peaks, merging into a pronounced peak splitting when thinning down the buffer layer.

Fig. 5.8c) displays XRD $\omega - 2\theta$-scans over the L = 3 and 6 diffraction peaks of the structure acquired at the P08 endstation of the Petra III storage ring. The high flux and very focused light spot of the synchrotron source allows for the analysis of very thin sample structures, which are not reliably possible with conventional XRD setups. To assess the structure of the surface termination by XRD, X-ray diffraction experiments were conducted on very thin sample structures with a single SL of $MnBi_2Te_4$ on top of Bi_2Te_3 epilayers with a thickness between 2 and 5 QL. The results clearly show the asymmetric line shape of the L = 3 and 6 diffraction maxima, which develops into a pronounced peak splitting for smaller epilayer thickness. The findings furthermore indicate, that the surface modification approach is feasible even for very low layer thicknesses.

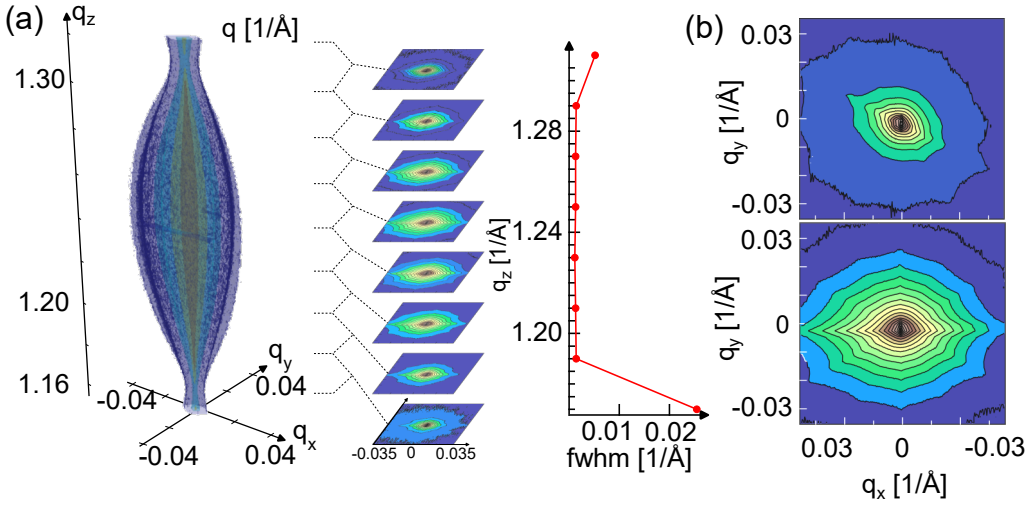

Figure 5.9.: Reciprocal space map of the heterostructure. a) Three-dimensional iso-surface representation of the RSM of a 1SL-5QL heterostructure. Next to the RSM, projections in the xy-plane for selected areas of q_z are displayed, together with an evolution plot of the respective FWHM along q_x. Along the length of the peak, no systematic changes in FWHM are observed. b) Projected RSM in the xy-plane for a SL-2QL and SL-5QL heterostructure. Both RSM exhibit a similar warped shap, differing mainly in a rotation within the projection plane.

A more detailed analysis of this matter can be found in the reciprocal space map (RSM) presented in Fig. 5.9a), which shows the three-dimensional shape of the L = 6 diffraction maximum in the SL-5QL heterostructure. The RSM exhibits a shape strongly elongated along the q_z axis, which confirms the growth of a thin film with large in-plane domains. As the peak asymmetry along the z-axis is mainly caused by the presence of the surface modification, the RSM was further divided in multiple slices along q_z, which are depicted on the right. All $q_{x,y}$-projections exhibit the same principal shape, which is slightly elongated along the q_x-axis and exhibits a twelvefold rotational

pattern. An estimation of the full width half maximum (FWHM) of the peak is furthermore depicted on the right. Interestingly neither the shape, nor the FWHM show any systematic changes along the main part of the RSM, which is in line with the fact, that the in-plane shape of the top layer domains do not significantly deviate from the one of the underlying Bi_2Te_3 epilayer followed from the AFM images depicted below. Fig. 5.9b) furthermore shows xy-projections of the SL-2QL and SL-5QL heterostructure. Both projections exhibit a similar round shape elongated along one axis and exhibiting twelve maxima during a full rotation. The reasons for the emergence of a twelvefold symmetry are not fully evident and further modelling would be required to relate them to a specific in-plane feature of the layer morphology.

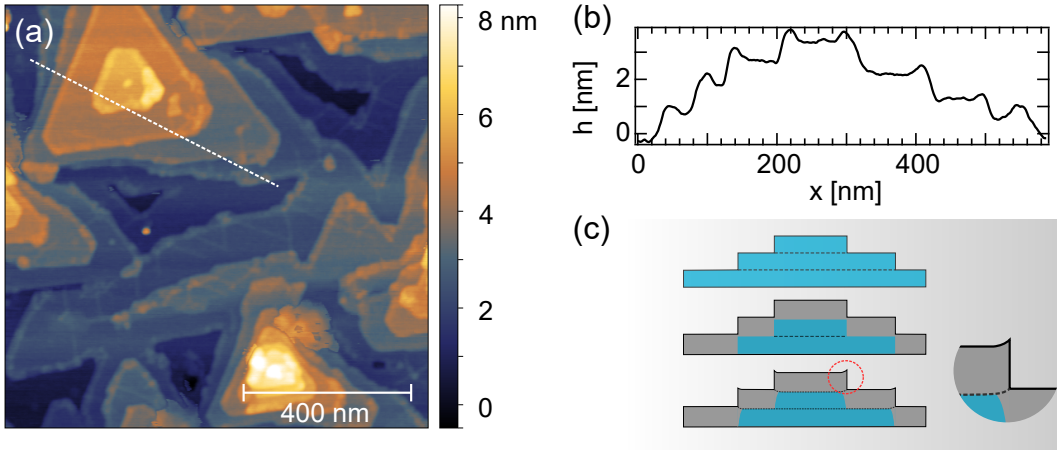

Figure 5.10.: Surface morphology of the ferromagnetic extension. a) AFM topography scan of the surface of a sample with an average thickness of 18.1 nm exhibiting a trigonal pyramidal surface structure. b) Topography cut along the white line in a), highlighting the elevated sample edges. c) Structure explanation model, assigning the lifted edge structure to interdiffusion at the surface steps.

Complementary to cross-sectional and diffraction techniques, the surface morphology was probed by AFM. Fig. 5.10a) depicts an AFM image of a 1x1 µm large area of a heterostructure surface. Using XRR, the sample was determined to have an average overall thickness of 18.1 nm, corresponding to a single SL on top of on average 16 to 17 QL of Bi_2Te_3. Overall, the surface morphology very much resembles the one of epitaxially grown Bi_2Te_3 films, showing large trigonally shaped islands with clear steps[94]. The image displays six clearly distinguishable film planes, whereas the lower lying layers seem to be completely closed in the selected area. A line cut over the most prominent island feature presented in panel b) shows steps with average plane to plane distance of $\Delta h = (0.916 \pm 0.094)$ nm, while a pronounced peak is located at the edge of each plane. The mean height between a plane and the peak maximum of the neighbouring plane

can be estimated to (1.294 ± 0.088) nm.
These peculiar effects in the sample morphology can most likely be related to the differing z-lattice constants of the Bi_2Te_3 epilayer and the septuple layer at the surface. As only the surface layer is converted to a SL, the morphology should closely follow the one of pristine Bi_2Te_3 with a surface raised up by the increased lattice constant globally. Taking into account imperfections as, e.g., a small amount of overlapping SLs caused by diffusion at the step edges, small bending effects can arise in this region. The effects is sketched in Fig. 5.10c). While other reasons such as surface oxidation can also be considered a cause of these effects, their absence in pristine Bi_2Te_3 indicates an origin connected to the surface modification.
Following from the discussion of the sample structure, the statement can be made, that the presented surface modification approach presents a reliable way to convert the topmost layer of Bi_2Te_3 into a full SL of the magnetic TI $MnBi_2Te_4$ with a high surface quality. The sharp van der Waals interface between epilayer and surface modification and overall flat surface structure of the samples make this an ideal system to study the interplay between the topology of the 3D TI and the surface magnetism. Furthermore, it can be concluded, that the overall morphology of the samples mainly depends on the morphology of the Bi_2Te_3 epilayer before modification. The optimisation of samples for different applications from photoemission to transport experiments can mainly be simplified to adjusting the growth parameters of Bi_2Te_3 to achieve the desirable properties, which has already been studied extensively in literature [109,181,182]. For experiments requiring very flat layer properties it may be possible to lower the nucleation density and therefore achieve larger domain sizes and a more flat surface by further raising the growth temperature [183].

5.3. Magnetic Heterostructures

The main hope connected with the emergent research interest in van der Waals bound structures has always been an easy stacking of the layers to achieve arbitrary heterostructures of materials and combine their respective physical properties [184]. The most common techniques used in this regard are sample stacking by exfoliation [14,86] and the growth by MBE [185], where both approaches are accompanied by their respective advantages and limitations. While exfoliated samples allow for almost arbitrary stacking of materials, MBE offers an extended amount of control over the individual layer properties but also requires the individual materials to be a suitable substrate for each other. This chapter aims to explore the transfer of the growth model for the ferromag-

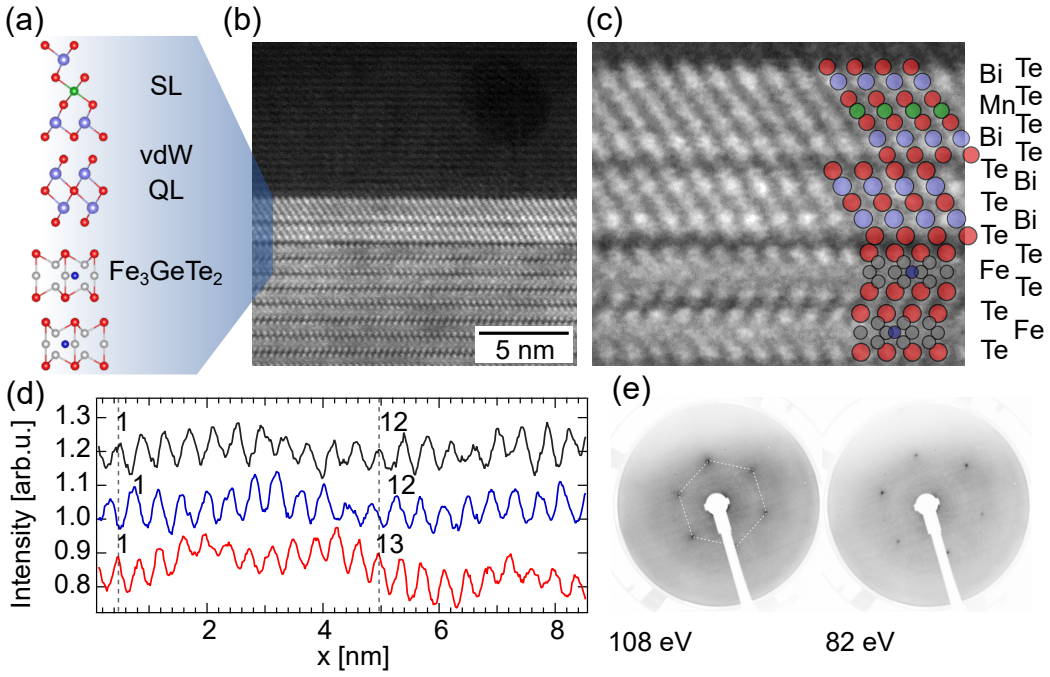

Figure 5.11.: Structural analysis of the magnetic heterostructures. a) Structural model for the $n = 1$ heterostructure consisting of the Fe_3GeTe_2 substrate, a single QL of Bi_2Te_3 and a surface layer of $MnBi_2Te_4$. b) STEM overview scan showing the bulk Fe_3GeTe_2 substrate, the two epitaxially grown layers and the protective Te cap. c) Enlarged section from b) with all atomic positions visible superimposed with the respective atomic species. d) Line integrations over individual atomic rows in b) for the uppermost Fe_3GeTe_2 layer (red), the Bi_2Te_3 (blue) and $MnBi_2Te_4$ (black) layers. The oscillations clearly visualize a 11:12 periodicity. e) LEED images on the heterostructure showing an ordered and rotationally aligned growth.

netically extension to different van der Waals type substrates, specifically the van der Waals magnet Fe_3GeTe_2 described in chapter 3.2.

The growth of the films was conducted following the description given in Fig. 5.5. Prior to the growth campaign, it has been confirmed, that Fe_3GeTe_2 is heat stable up to the required substrate temperatures and that the epitaxial growth of pristine Bi_2Te_3 on Fe_3GeTe_2 is feasible [186,187]. The main aim of the project is the investigation of the magnetic coupling between the Fe_3GeTe_2 substrate and the $MnBi_2Te_4$ monolayer, which makes the case of very thin Bi_2Te_3 epilayers the most interesting case in this study. Consequently, the samples under investigation consist out of Bi_2Te_3 layers with a nominal thickness of 1 up to 3 QL. The deposition rates were calibrated using XRR on reference samples on BaF_2 substrates. The Fe_3GeTe_2 crystals were prepared for the deposition by the *scotch-tape cleave* method, where the topmost vdW layers are removed by application of a sticky tape within UHV conditions. One of the desired structures is depicted in Fig. 5.11 a) consisting of a single SL $MnBi_2Te_4$ divided from a Fe_3GeTe_2 crystal by a

single QL of Bi_2Te_3. Especially the bulk sensitive characterisation techniques used in the context of MBE are of limited applicability, when investigating few nanometre thin epilayers on non-conventional substrates. The discussion of the sample properties will hence be limited to a discussion of the sample properties investigated by STEM and LEED. As visible from the overview scan in Fig. 5.11 b), the sample structure consists of vdW layers clearly separated by flat van der Waals gaps. Furthermore the surface of the last layer is covered by a protective Te capping. A magnified section of this image as depicted in c) shows the four vdW layers closest to the sample surface. Clearly, three different types of layer structure can be distinguished. The lowest two can be identified as one unit cell of the Fe_3GeTe_2 substrate, where the terminating Te sites are clearly pronounced, while the Fe-Ge structure within the layer can not be resolved. On top of the substrate an additional QL and SL structure is visible, which can be identified as the desired Bi_2Te_3-$MnBi_2Te_4$ surface termination similar to the observations in the previous chapter. As indicated in chapter 3 a nearly perfect lattice match between Bi_2Te_3 and $MnBi_2Te_4$ is expected, while for the Bi_2Te_3-Fe_3GeTe_2 interface a lattice mismatch of ~7.98 % is present. Indeed an analysis of the in-plane periodicity by integration over the most pronounced atomic row of each layer as depicted in 5.11 d) shows a periodicity of approximately 11:12 layers for the structure. Within the experimental error, this periodicity nicely matches the fraction of the two lattice constants, indicating that all layers grow free of strain with the respective equilibrium lattice constant.
The STEM results furthermore indicate, that all layers grow epitaxially and rotationally aligned. The latter can be concluded, as for a rotational misalignment, would fail to image the in-plane atomic arrangement for all layers simultaneously[188]. Further insight into the rotational alignment can be gained from LEED measurements as depicted in Fig. 5.11 e). The results were acquired on a Fe_3GeTe_2-QL-QL-SL structure and clearly show a hexagonal alignment of spots resulting from the topmost layers. While confirming the epitaxial character of the films, a comparison with Fig. 5.6 shows, that contrary to the growth on BaF_2, the patterns presented on Fe_3GeTe_2-substrates yield a purely hexagonal symmetry. In contrast to Bi_2Te_3 and the [111] surface of BaF_2, Fe_3GeTe_2 exhibits a full sixfold rotational symmetry. The two possible domain orientations of Bi_2Te_3 are therefore fully degenerate and islands of both are expected to grow in equal amounts.
Going back to the STEM images presented in Fig. 5.11, the high interface quality between the Fe_3GeTe_2 substrate and the epitaxial layers becomes apparent. A simple estimation of the centre positions of the two Te atoms at the boundary between the Fe_3GeTe_2 substrate and the Bi_2Te_3 layer corrected for drift by the Fe_3GeTe_2 lattice constant yields a size of the van der Waals gap of (0.354 ± 0.010) nm. As it will be shown in the context of

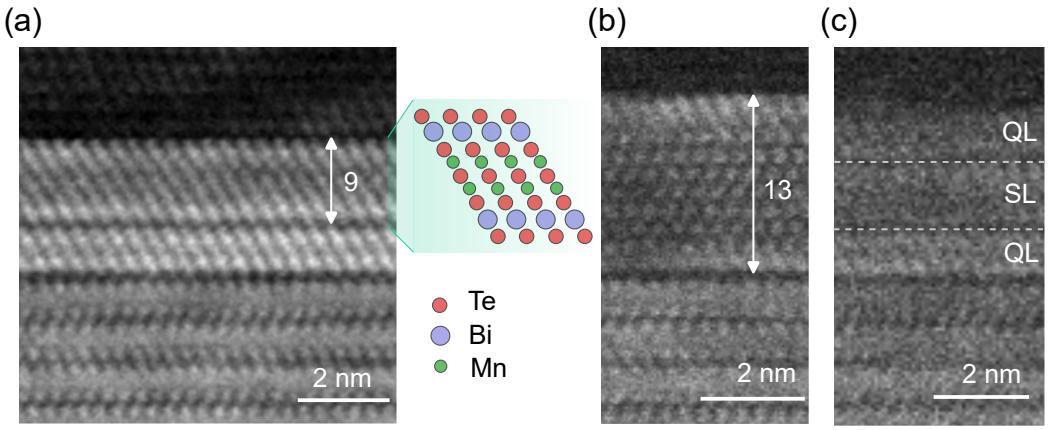

Figure 5.12.: Analysis for different defect types of a magnetic heterostructure consisting of the structure Fe_3GeTe_2– 1 QL Bi_2Te_3 – 1 SL $MnBi_2Te_4$. a) Nonuple layer of $Mn_2Bi_2Te_5$ as surface termination. b) 13-atomic layer block, potentially identified as $Mn_4Bi_2Te_7$. c) Bi_2Te_3-$MnBi_2Te_4$-Bi_2Te_3 termination.

the calculations presented in chapter 6.3, this distance is well in line with the relaxed mean distance resulting from DFT calculations on these types of structures. While the value resulting from STEM should only be taken as an estimate, it nevertheless shows, that the interfaces quality achieved by MBE is close to the lowest energy solution in the given case.

Next to a confirmation of the obtained structure, STEM measurements additionally allow for an analysis of possible defect structures, occurring when deviating from ideal flux conditions. Fig. 5.12a-c) shows a set of observed surface defects, which were found to occur on a sample grown with a ~ 7% oversupply of MnTe. The most likely feature depicted in Fig. 5.12a) can be identified as a layer of $Mn_2Bi_2Te_5$, corresponding to the intercalation of two MnTe layers in Bi_2Te_3. This material is known in literature and has found to be an intrinsic antiferromagnetic compound with the two Mn sublattices preferentially coupled antiferromagnetically[189,190]. Panel b) depicts a defect with a strongly enlarged building block. The structure most probably corresponds to a $Mn_4Bi_2Te_7$ layer as, e.g., observed in[82]. Fig.5.12c) indicates a defect structure, where the surface is terminated by an additional layer of Bi_2Te_3. In the case of the $MnBi_2Te_4$-Bi_2Te_3 heterostructures grown in the previous chapter it was furthermore found that MnTe deficient conditions will lead to a band structure very reminiscent of pristine Bi_2Te_3, which can most probably be interpreted as the formation of a Mn-doped surface layer. Overall these findings show, that the growth of single SL $MnBi_2Te_4$ is highly dependent on the evaporated amount of MnTe due to its high sticking coefficient. Deviations from the ideal stoichiometry may lead to a substantially different film structure, which has already lead to the observation of fully different magnetic properties[82]

or overall doubtful results on the magnetic and electronic properties [84].

6. Magnetism in $MnBi_2Te_4$ Based Compounds and Monolayers

Overview

The following chapter will address the magnetism in $MnBi_2Te_4$ and the related heterostructures investigated in this thesis. The first part mainly concerns the analysis of the magnetic coupling in multi-layer samples of $MnBi_2Te_4$ with a special focus on the surface magnetic properties. Following from there, the second part will describe the magnetic properties of a single septuple layer of $MnBi_2Te_4$ and investigate the properties necessary to achieve a two-dimensional magnetic order in the films. The third part of this chapter will contain an investigation of *synthetic* magnetism, e.g. heterostructures of multiple magnetic materials and show, how proximity induces magnetic coupling can be utilized to tune the magnetic properties of the 2D ferromagnetic SL of $MnBi_2Te_4$

Many of the findings in this chapter are published in [94,120], while the observations on the coupling in Fe_3GeTe_2-$MnBi_2Te_4$ heterostructures are currently prepared for publication.

6.1. Bulk and Surface Magnetism in $MnBi_2Te_4$

As previously detailed out, magnetism in $MnBi_2Te_4$ is defined by the ferromagnetic in-plane and the antiferromagnetic out-of-plane coupling. The in-plane coupling strongly exceeds the out-of-plane one with 0.09 meV/μ_B^2 in- and 0.022 meV/μ_B^2 out-of-plane [28]. On the question of the coupling between the intrinsic magnetism and the topological electronic structure in this family of compounds, the surface magnetic properties of the materials play a pronounced role. This chapter focusses on two main parts: the magnetic order at the surface of bulk $MnBi_2Te_4$ crystals and the magnetic properties observed in MBE grown thin films of $MnBi_2Te_4$.

Fig. 6.1a) shows XAS and XMCD spectra of the Mn $L_{3,2}$ absorption edge acquired at a sample temperature of T = 3.5 K and an external magnetic field of 2.6 T. The shape of the XAS signal is closely reminiscent to previous findings in literature on $MnBi_2Te_4$ and

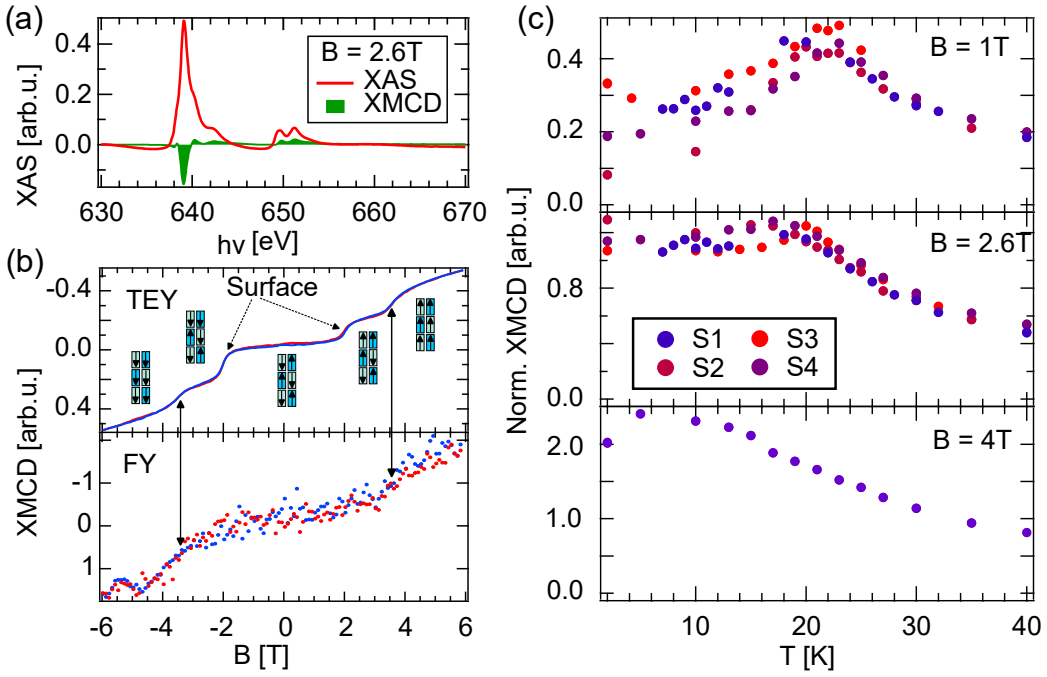

Figure 6.1.: Magnetic properties and surface magnetism in $MnBi_2Te_4$ bulk crystals. a) XAS and XMCD signal of the Mn $L_{3,2}$ absorption edge at B = 2.6 T and T = 3.5 K. b) Field dependent XMCD at the Mn L_3-edge in TEY and FY detection mode, clearly showing a bulk and surface spin-flop field for the crystal. c) Field- and temperature dependent XMCD amplitudes in TEY detection mode. The surface-sensitive detection allows to probe the phase transition present in the topmost SL of the $MnBi_2Te_4$ crystal.

the closely related $MnBi_6Te_{10}$ compound and is attributed to a predominant d^5 state of the Mn ion, with contributions from the d^6L and d^7L_2 charge transfer states [28,44,157]. The application of an external magnetic field leads to a clear XMCD signal, indicating that the field of 2.6 T introduces a sizeable spin polarisation in the antiferromagnetic compound. Following the XMCD signal over a large magnetic field range allows the acquisition of the sample magnetisation curve, as depicted in Fig. 6.1b).[1] The upper panel shows the field dependent XMCD using the surface-sensitive total electron yield detection. For fields between ±2 T, the XMCD remains close to zero, while at ±2 T and ±3.5 T the curve exhibits pronounced kinks, where the first corresponds to a sharp step, while the second exhibits a softer transition. Above the second kink, the XMCD exhibits a strong slope and does not saturate up to the highest available fields. The lower panel shows the XMCD amplitude recorded with fluorescence yield (FY) detection for the same field range. [2] The FY signal exhibits only two clear kinks at the higher field

[1] For all XMCD hysteresis scans, the XMCD signal is defined as the difference between c+ and c- polarisation, normalised to the respective pre-edge signal at each field point.

[2] In the photon energy range in question, TEY is the clearly dominant decay path, leading to the weak data statistics for the FY measurements [155].

points of ± 3.5 T, while the inner kinks are at most below the noise level.
To further elucidate these findings, Fig. 6.1c) shows the normalised XMCD amplitude over the sample temperature at three selected field points on the inner plateau (1 T), the intermediate plateaus (2.6 T) and after the second transition (4 T) for multiple samples S_i. All datasets are acquired in the surface-sensitive TEY mode. The temperature dependent XMCD at the lowest field is clearly reminiscent of an antiferromagnetic behaviour with a pronounced maximum in the signal around $T \approx 21$ K. The signal decays to both sides and reduces to ≈ 50 % of its maximum towards the lowest temperatures with large sample dependent deviations. In contrast, the behaviour found at 2.6 T does not exhibit a significant reduction of the XMCD towards lower temperatures albeit exhibiting a slight peak below 20 K. The curve at 4 T shows a clearly different course, with the maximum close to the lowest temperatures and a steady decay with rising sample temperatures.
Taken together, the findings show a remarkable difference between magnetic properties close to the surface and in the bulk of the $MnBi_2Te_4$ compound. The bulk-sensitive FY measurements yield results very similar to findings from different integral magnetic probes, giving a spin flop field of 3.7 T [93]. The additional features arising in a surface-sensitive probe are hence to be interpreted as the surface layer carrying different magnetic properties. The step feature occurring at a reduced field of ± (2.015 ± 0.010) T can be attributed to the spin-flop transition of the topmost layer, which aligns with the external field in a step-like process as indicated by the small insets [40]. Overall, for a layered antiferromagnet with a single domain, a surface sensitive probe would expect a non-zero remanent XMCD and ideally an open hysteresis loop at zero field. The absence of this feature indicates, that the average domain size of antiferromagnetic bulk $MnBi_2Te_4$ is smaller then the typical beam diameters in XAS experiments of around 200 µm, which is in line with other magnetic probes such as MFM [191] but contrasting to previous findings in XMCD [40]. The temperature and field dependent XMCD study furthermore supports the decreased spin flop field. While data at 1 T below the spin flop transition still shows a pronounced increase of the sample magnetisation towards a peak around T_N, the curves at 2.6 T still carry hallmarks of the phase transition at T_N from the sample bulk, but no substantial suppression of the magnetic polarisation below T_N is found. A last important aspect concerns the comparison between the field and temperature dependent behaviour of the surface magnetism. The T_N estimated from the XMCD at 1 T ranges around 21 K, which is lower then the bulk value of 24.6 K [93]. Both the reduction of the spin-flop field and of T_N can be attributed to the fact that the top layer lacks the upper partner for out-of-plane coupling. While the antiferromagnetic order is defined by this coupling term and therefore a strong decrease

in spin-flop field is observed, the effect on T_N is more subtle. Given the strong asymmetry between $J_\parallel$ and $J_\perp$, these findings may be interpreted such, that magnetism in $MnBi_2Te_4$ can be understood in a strongly layered fashion with strong ferromagnetic alignments within each SL, while the interlayer coupling mainly defines the A-type AFM order. They also clearly indicate, that contrary to earlier speculations, the surface of $MnBi_2Te_4$ indeed hosts magnetic polarisation comparable to its bulk properties.

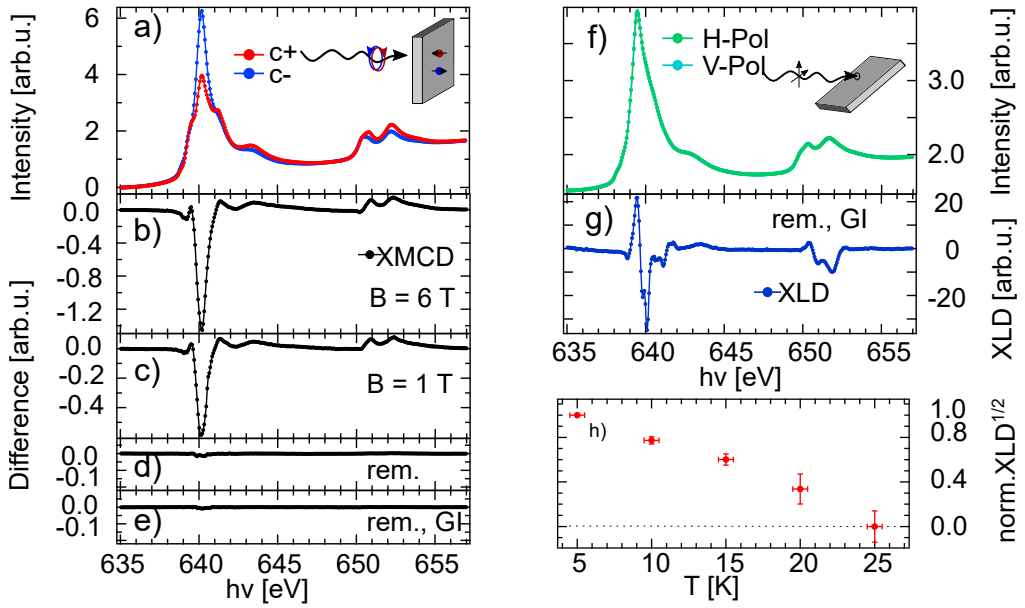

Figure 6.2.: XAS and XMCD spectroscopy on $MnBi_2Te_4$ thin films. a) XAS at a field of 6 T and a sample temperature of 5 K. b-d) XMCD signal for fields of 6 and 1 T and in remanence highlighting the decay in magnetisation. e) Absence of XMCD in grazing incidence without an external field. f) XAS with horizontal (H) and vertical (V) light polarisation. g) Respective XLD signal in grazing incidence and remanence. h) Temperature dependence of the square-root of the normalised XLD signal indicating a decaying magnetic order, which can be assigned to an antiferromagnetic ground state in the film. *Reproduced from [94], with the permission of AIP Publishing.*

Following the analysis of magnetism in bulk crystals, the rest of this chapter will address the magnetic properties of MBE grown thin films of $MnBi_2Te_4$, starting from the thick-film limit down to single SL samples. Fig. 6.2 shows an analysis of the magnetic properties of a thick MBE grown film of $MnBi_2Te_4$ probed by XAS, XMCD and XLD. Panel a) depicts the XAS signals for both light polarisations in a field of 6 T. The XAS line shape shows clear similarities to Fig. 6.1a) confirming a similar electronic environment for the Mn ions. The difference between the two polarisations, as shown in panel b) exhibits a pronounced XMCD signal and indicates a spin polarisation of the sample. Reducing the external field to zero, shows a decay of the XMCD to zero both for normal, as well as grazing incidence. Fig. 6.2f) furthermore shows XAS curves acquired

with both linear polarisations in remanence and grazing incidence. The difference as depicted in g) shows a clear linear dichroism pattern, strongly reminiscent of findings on bulk $MnBi_2Te_4$ crystals [192]. The temperature dependent behaviour of the linear dichroism pattern is shown in Fig. 6.2h) by plotting the square-root of the normalised amplitude over the sample temperature. The XLD decays with increasing temperature and fully vanishes at 25 K, which allows to assign it to a magnetic origin. Taken together the findings indicate an antiferromagnetic ground state of the film with a transition temperature close to the bulk value of 24.6 K [93].

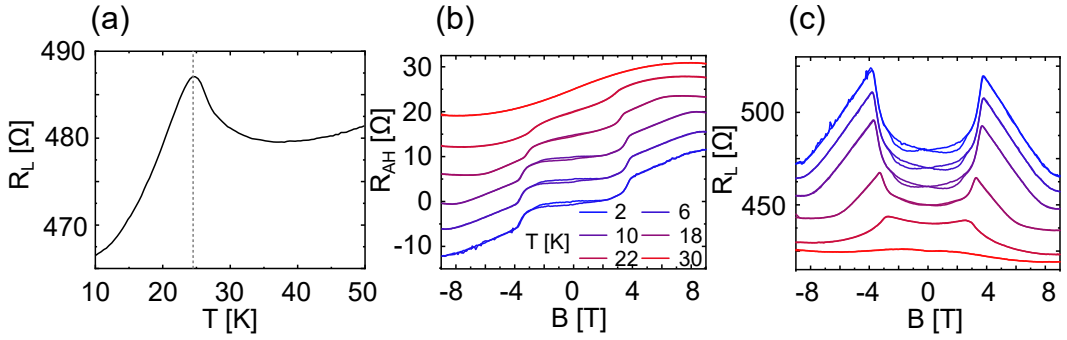

Figure 6.3.: Magnetotransport in thick $MnBi_2Te_4$ films in a pseudo Hall bar geometry. a) Temperature dependent longitudinal sample resistance, showing a clear peak around T_N of the sample. b) Anomalous Hall resistance for multiple temperatures, confirming the AFM nature of the sample magnetism and clearly showing the bulk spin flop transition. c) Longitudinal resistance over the magnetic field for multiple temperatures with pronounced maxima at the spin flop transition. [193]

The findings by XLD are furthermore supported by magnetotransport measurements as shown in Fig. 6.3. The dataset was acquired on a ~ 60 nm thick film in a pseudo Hall-bar geometry. The temperature dependent longitudinal resistance decays with decreasing temperature, which is disrupted by a kink-like increase due to the AFM transition around T_N. The behaviour reflects the critical fluctuations around the temperature of the phase transition, followed by a freezing of the magnon modes at temperatures below, which leads to the fast drop in resistance. Fig. 6.3b) and c) show the slope corrected anomalous Hall (AH) resistance and the longitudinal resistance respectively over the applied magnetic field for a set of sample temperatures. The AH resistance at $T = 2$ K shows a flat plateau between the two bulk spin flop fields, framed by two step-like transitions. At higher fields the curves maintain a sloped behaviour indicating incomplete saturation. When crossing T_N, the spin flop transition vanishes and the curve exhibits a pronounced S-like feature. The longitudinal resistance furthermore highlights the spin-flop transition as a strong increase in sample resistance, which decays with temperature. The combined XMCD/LD and magnetotransport study con-

firms the magnetic ground state in $MnBi_2Te_4$ films grown by molecular beam epitaxy, with a bulk spin flop field of $B_{SF} = (3.81 \pm 0.30)\,T$ and $T_N = (24.54 \pm 0.20)\,K$. Albeit the growth method can induce notable differences, especially in the defect structure of the ternary compound as discussed in chapter 5 in the context of antisite mixing, the magnetic properties observed on the MBE grown films are well in line with previous findings on $MnBi_2Te_4$ single crystals [28,93].

6.2. $MnBi_2Te_4$ in the Two-Dimensional Limit

The previous chapter has demonstrated that $MnBi_2Te_4$ thin-films grown by MBE exhibit antiferromagnetic order as known for bulk crystals, with the interlayer coupling defining the nature of the ground state. The question arising naturally is, whether magnetism in $MnBi_2Te_4$ can survive in the absence of this coupling or expressed differently, whether a single SL of $MnBi_2Te_4$ can host stable ferromagnetic order. In order to answer this question, this chapter will present a study on the magnetism in a single SL of $MnBi_2Te_4$ on the surface of a Bi_2Te_3 thin film as given in the aforementioned ferromagnetic extension. The magnetic properties are probed by element and surface-sensitive XMCD, which is later combined with magneto-transport experiments.

Fig. 6.4 a,b) present the XAS and XMCD signal of the Mn $L_{3,2}$ absorption edge on a single SL of $MnBi_2Te_4$ on a Bi_2Te_3 epilayer. The measurements were conducted at the base temperature of the system of $\sim 3.5\,K$ under an applied field of $0.5\,T$. The line shape of the XMCD signal is strongly reminiscent of the one also present in $MnBi_2Te_4$ thin films and $MnBi_2Te_4$ single crystals, resulting from the nearly identical chemical environment for the Mn atoms in these structures. The presence of a sizeable XMCD signal under applied field confirms the presence of a local spin-magnetic moment on the Mn sites. To estimate the local spin and orbital magnetic moments, a sum rule analysis was conducted[3], systematically varying all parameters within their respective uncertainties [44,194]. The resulting distributions for spin and orbital magnetic moment are shown in Fig. 6.4 and yield a spin-magnetic moment of $m_s = (1.93 \pm 0.16)\,\mu_B$, while the orbital magnetic moment is found to be negligibly small. The full suppression of the orbital moment is well in line with the expectation for the 5d configuration of the Mn sites. The spin-moment is significantly lower than typical values found for both $MnBi_2Te_4$ and its derivatives [44], which range up to $5.9\,\mu_B$ per Mn atom. This discrepancy is e.g. discussed in a study on the $MnBi_6Te_{10}$ compound where by XMCD a moment of $(2.30 \pm 0.25)\,\mu_B$ was found and is attributed to the surface-sensitive character of the XMCD method and a potential reduction of the magnetisation at the sample sur-

[3] See chapter 4.3 and [44] for details on the evaluation methods.

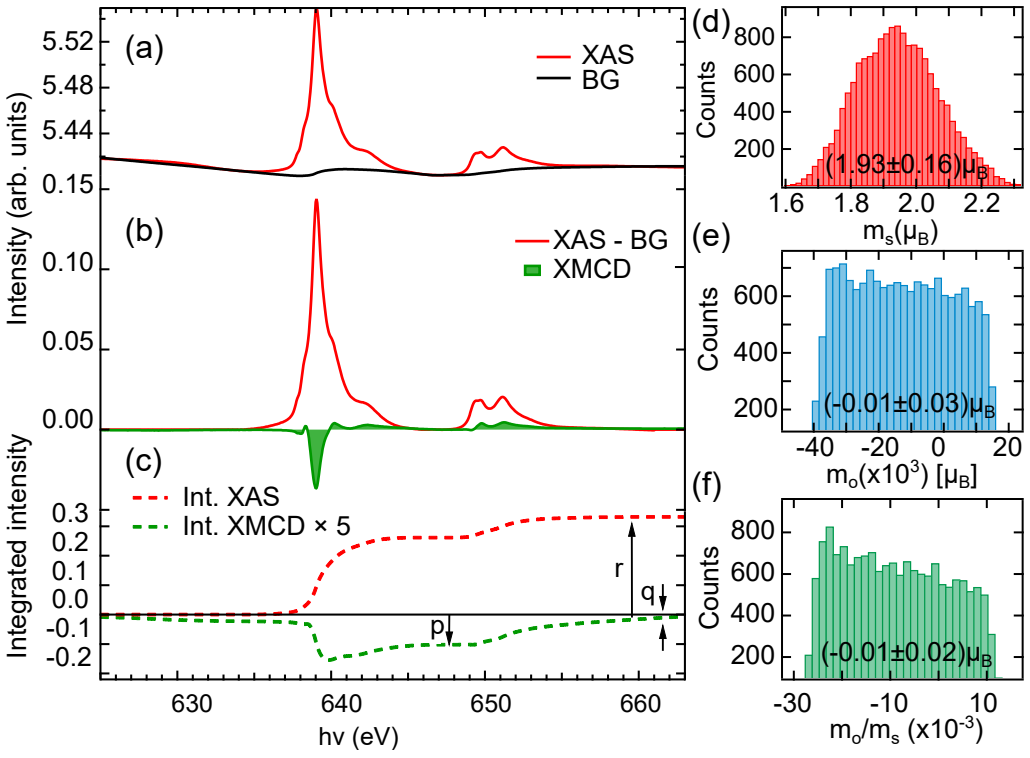

Figure 6.4.: XAS, XMCD and sum rule analysis. a) XAS signal of the Mn $L_{3,2}$ absorption edge acquired on a single SL of $MnBi_2Te_4$ grown on Bi_2Te_3. The data shows the pure XAS signal as well as the adapted background intensity. b) Background removed XAS signal and corresponding XMCD. c) Cumulative XAS and XMCD intensities used for the sum rule analysis. d-f) Probability distributions for spin and orbital moment as well as the ratio $\frac{m_o}{m_s}$ showing a large spin- and negligibly small orbital moment.[194]

face[44]. In this regard the monolayer of $MnBi_2Te_4$ may pose an ideal model system to gain further insight into this apparent discrepancy upon the application of bulk magnetometry methods.

To probe the magnetic nature of the single SL, Fig. 6.5 a) shows a hysteresis loop of the XMCD asymmetry of the Mn L_3-edge in normal incidence and 70° off-normal, where normal incidence corresponds to probing the spin polarisation along the surface normal. Applying a field normal to the sample surface results in a rectangular shaped hysteresis loop, confirming a stable ferromagnetic ground state in the single $MnBi_2Te_4$ SL. The sample exhibits a remanent spin polarisation of ~ 90 %, as estimated from additional XMCD spectra at zero field. These results are further corroborated by the magnetotransport measurements in panel b). The data shows the anomalous Hall resistance after removing the contribution from the ordinary Hall effect as a linear slope. The measurements clearly display an anomalous Hall effect with a coercive field up to 90 mT. The temperature series presented in Fig. 6.5 c) indicates a decay of the ferromagnetic contribution towards higher temperatures.

The magnetisation loop in grazing incidence shown in the lower panel of Fig. 6.5a)

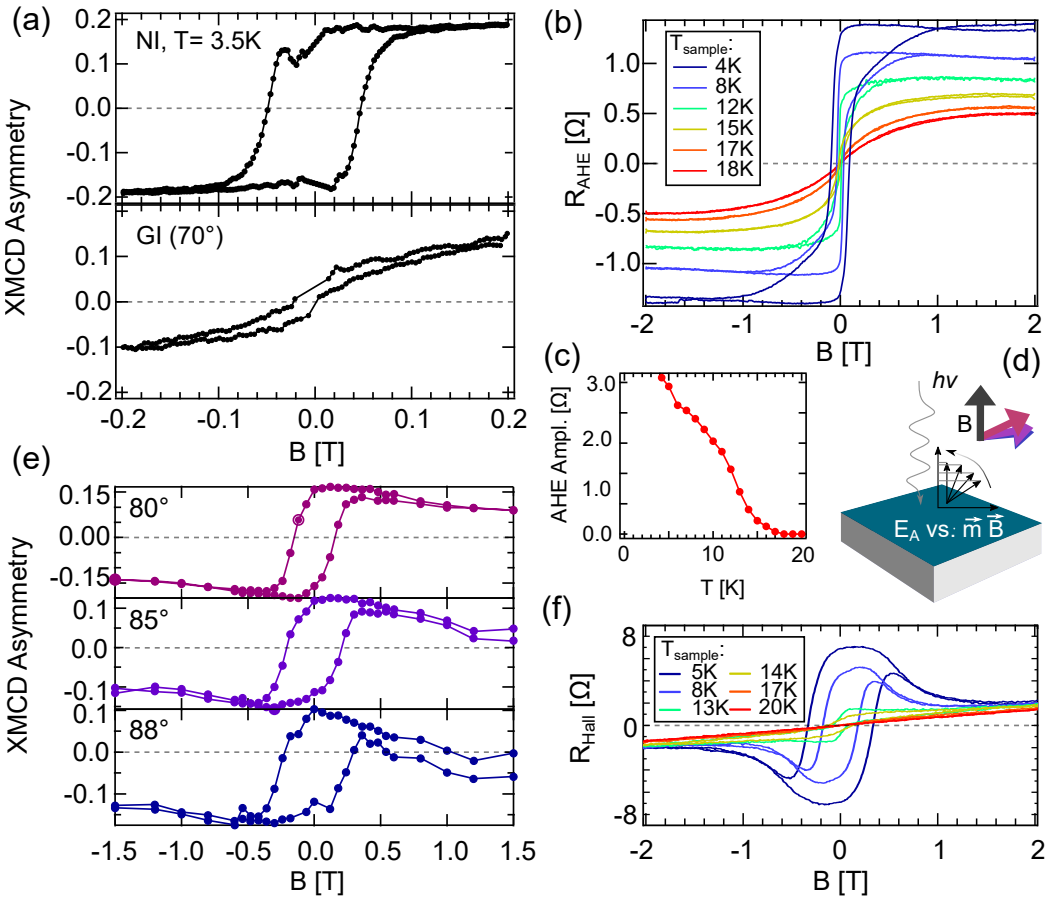

Figure 6.5.: Hysteresis in a single SL $MnBi_2Te_4$. a) Hysteresis loops on the Mn L_3-edge in normal and grazing incidence. b) Field-resolved magnetotransport experiments for several sample temperatures. c) Temperature dependence of the AHE amplitude decaying with temperature. d) Experimental geometry of the XMCD experiments in e) with light incidence along the surface normal and magnetic fields applied gradually in-plane. e) XMCD asymmetry of the single SL probed along the surface normal for magnetic fields applied close to the in-plane direction, indicating a strong uniaxial anisotropy of the magnetic polarisation. f) Magnetotransport experiments with the magnetic field applied in the sample plane.

presents a rather soft magnetic behaviour with a pronounced s-shape and indicates a strong uniaxial anisotropy in the Mn spin moment. A deeper insight in this matter is then given by XMCD measurements under canted fields. The geometry is displayed in Fig. 6.5 d) and the resulting magnetisation curves are seen in panel e). The three field loops were recorded with the sample facing the beam in normal incidence geometry, while exploiting the vector magnet of the endstation in order to apply a field gradually tilted towards the in-plane direction. The field loops can be understood as the out-of plane magnetic polarisation of the SL under a close to in-plane field. All three curves show a gradual alignment of the sample magnetisation with the direction of the

external field upon increasing field strength, while relaxing the external field causes the sample magnetisation to regain its out-of-plane orientation to a large extent. For field angles nearly approaching the in-plane directions, the hysteresis loop does not fully close and instead ends in a nearly demagnetized stated. This re-magnetisation behaviour can be understood as a direct competition between the energy scales assigned with Zeeman- and anisotropy energy as sketched in d), where only an almost completely in-plane field will allow for a demagnetisation of the sample by breaking the magnetisation into domains after a full field cycle. A similar effect can also be observed in magneto-transport experiments as shown in f) for an external field applied fully in-plane. The figure shows the full Hall-resistance of the ferromagnetic extension for a series of sample temperatures. Deep in the ferromagnetic phase the Hall resistance increases strongly towards smaller fields with a round shape and reverses sign, when the overall magnetisation slowly reverses. As magnetotransport in a Hall geometry inherently probes the out-of-plane components of magnetisation and magnetic field, the results can be interpreted in the same light as Fig. 6.5 e) as a competition between Zeeman- and anisotropy terms. The magnetic field points of the spin flip along the field direction are well in line with observations on the meta-magnetic compound $MnBi_4Te_7$ [195]. With the local magnetic moment resulting from the sum-rule analysis, the corresponding anisotropy energy can be estimated from Figs. 6.5e,f). The magnetisation gradually turns to an in-plane alignment at $B \approx 1\,\mathrm{T}$. The Zeeman-energy at this field corresponds to an energy of $\sim 0.11\,\mathrm{meV}$, which can be taken as a first approximate for the anisotropy energy per Mn atom. The estimated value is in good agreement with calculations for the related bulk material $MnBi_4Te_7$ of 0.12 eV [196] and is more then an order of magnitude smaller then in other 2D magnets such as Fe_3GeTe_2 [197,198].

Fig. 6.6 shows the relative amplitudes of the temperature-dependent remanent XMCD signal of a single SL $MnBi_2Te_4$ with the linear representation given in c). The decaying signal is shown in a) in a double logarithmic representation of the renormalised temperature axis with

$$\tau = 1 - \frac{T}{T_c} \tag{6.1}$$

with T_c as the ferromagnetic transition temperature of the sample. Assuming the magnetic order to follow a power-law behaviour (see chapter 2.1.1) allows to determine T_c as the temperature at which all data points lie on a straight line in the double-logarithmic representation. After determining T_c as 14.89 K, the critical coefficient β

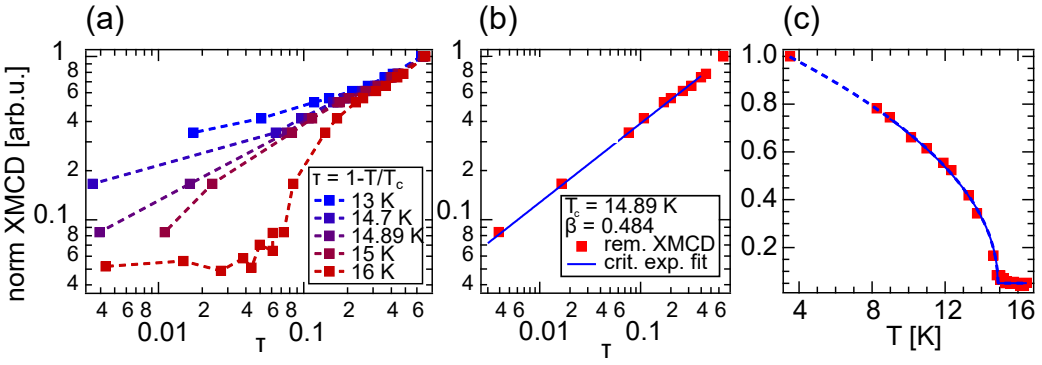

Figure 6.6.: Temperature dependence and critical behaviour of the single SL magnetism. a) XMCD amplitude plotted over rescaled temperature τ for different values of T_c, determining the critical temperature as $T_c = 14.89\,\mathrm{K}$. b) Linear fit in the double logarithmic representation resulting in $\beta = 0.484$. c) Linear representation of the temperature dependent XMCD amplitude together with the critical behaviour. The range of the fit is indicated by the solid blue line. *Figures adapted from [120] licensed under CC BY 4.0.*

can be fitted to the data as the slope of a linear fit on a bi-logarithmic axes. Concluding from the analysis, the ferromagnetic extension follows a power-law with a critical exponent of $\beta = 0.484$, which is capable of describing the temperature evolution of the magnetic order parameter over the entire temperature range.

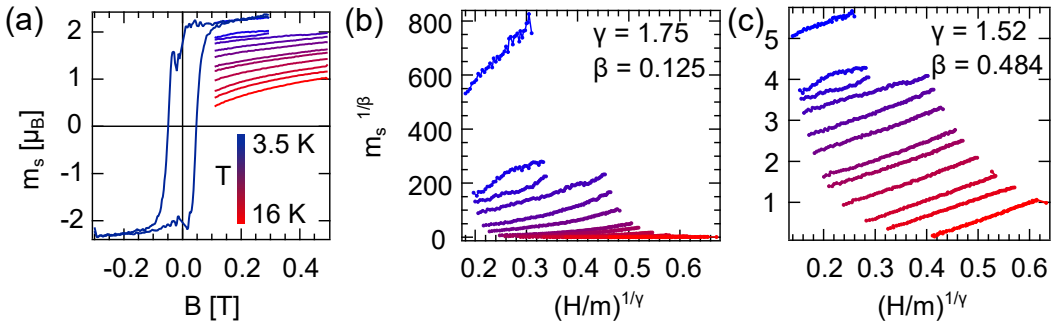

Figure 6.7.: Magnetic field dependent magnetisation and modified Arrott-Noakes plot. a) Hysteresis loop as shown in Fig. 6.5a) together with field dependent curves for multiple sample temperatures up to well above T_c. b) Modified Arrott-Noakes plot for critical exponents resulting from the 2D Ising model. c) Same representation with the independently determined β coefficient and best fit for γ.

In addition, the field and temperature dependent behaviour of the 2D magnet can be used to determine the critical coefficient γ, describing the scaling law of the susceptibility χ of the sample. Fig. 6.7 a) depicts the full magnetic field loop of the ferromagnetic extension with the y-axis rescaled to the saturation spin-moment together with a set of temperature and field dependent datasets on the area outside of the open hysteresis loop. The colour gradient describes the transition from the base temperature (blue) up

to well above the critical temperature (red). Resulting from the general scaling behaviour of the order parameter m and the susceptibility χ an expression can be derived connecting the externally applied magnetic field to the resulting sample magnetisation as

$$\left(\frac{B}{M}\right)^{1/\gamma} = \frac{T - T_c}{T_1} + \left(\frac{M}{M_1}\right)^{1/\beta} \tag{6.2}$$

where T_1 and M_1 are additional material specific, B is the external magnetic field and M the sample magnetisation. A full derivation of this equation and the concept of the modified Arrott-Noakes plot can be found in [199]. Following from this equation it is evident, that for the correct set of critical coefficients the rescaled field dependent magnetisation curves should all show a fully linear behaviour with identical slope and a temperature dependent offset. Reversing this argument, the parallelity and linearity of the isothermal lines can be used as a criterion to determine a set of suitable critical coefficients for a magnetic system.

The interpretation of these results is somewhat peculiar and has to take all the findings in this chapter into account. The results found in Fig. 6.5 indicate that a single SL of $MnBi_2Te_4$ hosts a strong uniaxial anisotropy in the out-of-plane direction, effectively narrowing the full three-dimensional phase space for the spin orientation down to one dimension. Next to a sufficiently strong spin-spin coupling, the anisotropy term is an important stability criterion for the two-dimensional magnetism. Out of the two known two-dimensional magnetic models (see Tab. 2.1) we can therefore clearly assign a 2D Ising-like nature to the system based on its spin dimensionality. Interestingly, the critical coefficients known for the 2D Ising model do not suffice to describe the magnetic behaviour in the system. Fig. 6.7b) shows a modified Arrott-Noakes plot for the critical coefficient set known for the 2D Ising model, which exhibits strong deviations from the required linearity criteria. Attempting to achieve a good fit to the data, panel c) shows a plot for the β coefficient as determined in Fig. 6.6. The optimum for the coefficient γ was determined by a variation of its value over a large parameter range, setting parallelism and linearity of the curves as the main criterion. The resulting coefficient $\gamma = 1.52 \pm 0.30$ yields a set of parallel and linear isotherms, indicating a good fit. The resulting set of coefficients can not be assigned to a single magnetic model, but rather seems to fit into the frame of the 2D Ising model concerning the sample susceptibility, while the scaling of the order parameter behaves in a mean-field like fashion. While for other magnetic systems a close fit between model and experiment can be achieved [57], the magnetism in single SL $MnBi_2Te_4$ probably deviates from a simple 2D Ising model, either by non-negligible next-nearest neighbour coupling terms or additional interac-

tion channels as e.g. proposed by the coupling of the sample magnetism to the TSS [200]. As a side note, the value found for β is indeed in close agreement with results found for bulk $MnBi_2Te_4$ and its derivatives [201], which will be discussed further in chapter 8.

6.3. Magnetic Coupling in $MnBi_2Te_4/Fe_3GeTe_2$ Heterostructures

Following the discussion of the interlayer coupling by super-super exchange in chapter 2.1.2 and establishing the isolated SL of $MnBi_2Te_4$ as a stable ferromagnet, the question arises how the proximity to other magnetic materials can be utilized to alter its magnetic properties. This question is driven by two main points of motivation: searching for ways to increase the very low magnetic transition temperature of the ferromagnetic extension as e.g. attempted in [202] and selectively controlling the magnetisation of individual layers in a potential heterostructure, as motivated in chapter 2.2.4 in the context of axion-insulator physics. The latter falls in the category of exchange bias and heterostructure magnetism, which has already been studied on a variety of systems. This chapter will look at the interface between Fe_3GeTe_2 and Bi_2Te_3-$MnBi_2Te_4$ structures, whose growth is described in chapter 5.3. The experimental approach mainly relies on XAS and XMCD as a probe, as the element and surface-sensitive character of the method allows to straightforward disentangle magnetism on the different atomic species and look at substrate and film individually. The material combination has been chosen, because Fe_3GeTe_2 is a vdW compound with a comparably high curie temperature and out-of-plane anisotropy, making it a straightforward choice for the combination with $MnBi_2Te_4$.

Fig. 6.8a) shows an XAS scan and the corresponding XMCD of the Fe $L_{3,2}$ absorption edge of a Fe_3GeTe_2– 2QL Bi_2Te_3 – 1 SL $MnBi_2Te_4$ heterostructure (n=2).[4] The line shape of the XAS shows the two main edges of the Fe 2p - 3d transition, where each of the peaks contains a fine structure consisting of two main contributions. As Fe_3GeTe_2 exhibits two inequivalent positions of the Fe ions in its structure the two contributions can be attributed to a Fe 2+ and 3+ valence state in the material [101,203]. At the applied field of 0.8 T, the sample exhibits a sizeable XMCD signal with a maximum at $h\nu \approx 706.5$ eV. A sum rule analysis yields a spin-moment of $m_s = (1.24 \pm 0.21)\,\mu_B$/Fe

[4] All samples discussed in the following will consist of a bulk crystal of Fe_3GeTe_2, whose surface is covered with n QLs of Bi_2Te_3 and a single SL of $MnBi_2Te_4$. To simplify the naming convention, the structure Fe_3GeTe_2– n QL Bi_2Te_3 – 1 SL $MnBi_2Te_4$ will in the following be referred to by the number of QLs only as n = 0, 1 or 2.

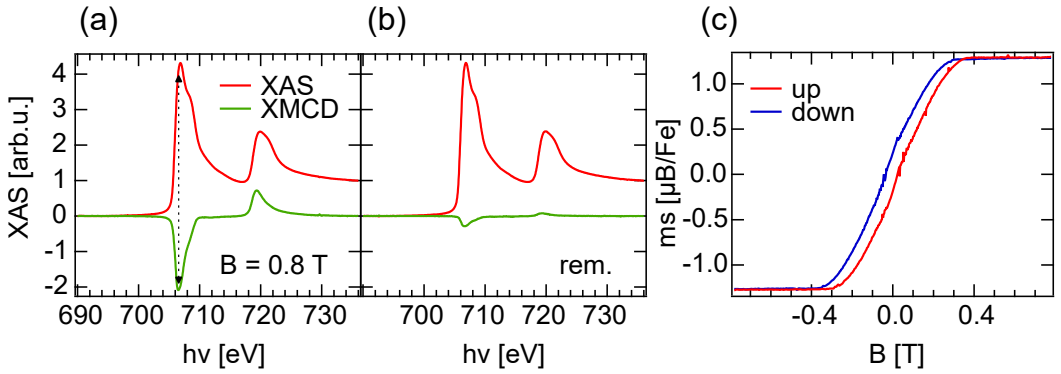

Figure 6.8.: Magnetic properties of the Fe_3GeTe_2-substrate. a) XAS and XMCD on the Fe $L_{3,2}$ absorption edge at $B = 0.8\,T$ in saturation at a sample temperature of $\sim 3.5\,K$. b) XAS and remanent XMCD of the ferromagnet. c) XMCD-hysteresis scan on the Fe L_3-edge as marked in a), depicting the soft ferromagnetic behaviour of the Fe_3GeTe_2 bulk crystal.

and an orbital moment of $m_l = (0.088 \pm 0.015)\,\mu_B/Fe$ [194]. After reducing the external field to zero, the XMCD as shown in Fig. 6.8b) confirms a remanent magnetisation and the ferromagnetic ground state, but is strongly reduced to $\approx 12\,\%$ of the saturation magnetisation. A field dependent XMCD-hysteresis on the aforementioned photon energy is depicted in Fig. 6.8c). The sample magnetisation saturates at fields above 0.4 T and shows an open hysteresis loop in the range between the saturation points. Contrary to the case of $MnBi_2Te_4$ in Fig. 6.5, the magnetisation curve carries a strong slope and the actual hysteresis area is very narrow. The soft ferromagnetic behaviour is known to appear in Fe_3GeTe_2 due to the easy formation of ferromagnetic domains along the out-of-plane ferromagnetic easy axis [102,104,204], as described in chapter 3.2. Overall it was found that the magnetic behaviour of Fe_3GeTe_2 does not change significantly with the surface terminations n = 0 to 2 and therefore the findings in Fig. 6.8 can be taken as the magnetic properties of Fe_3GeTe_2 in all structures in question.

In a next step, XAS and XMCD on the Mn $L_{3,2}$ absorption edge allow to investigate the magnetic properties of the single SL of $MnBi_2Te_4$. In this regard three structures were chosen, where the distance between the substrate surface and the $MnBi_2Te_4$-SL is gradually increased by intercalating QLs of Bi_2Te_3, starting with a direct interface for n = 0 up to n = 2 with a 2QL spacing. The respective XAS spectra at sample temperatures of 3.5 K are shown in Fig. 6.9a-c). For all three samples, the line shape of the XAS exhibits the same multiplet structure, closely similar to the one of the single SL in Fig. 6.4, while differences can be found in the slope of the background due to the different layer thickness on the substrate. These findings are well in line with the expectation from the structural characterisation, as the nearest neighbour environment is identical in all samples. To assess the coupling to the substrate and the resulting change in magnetic

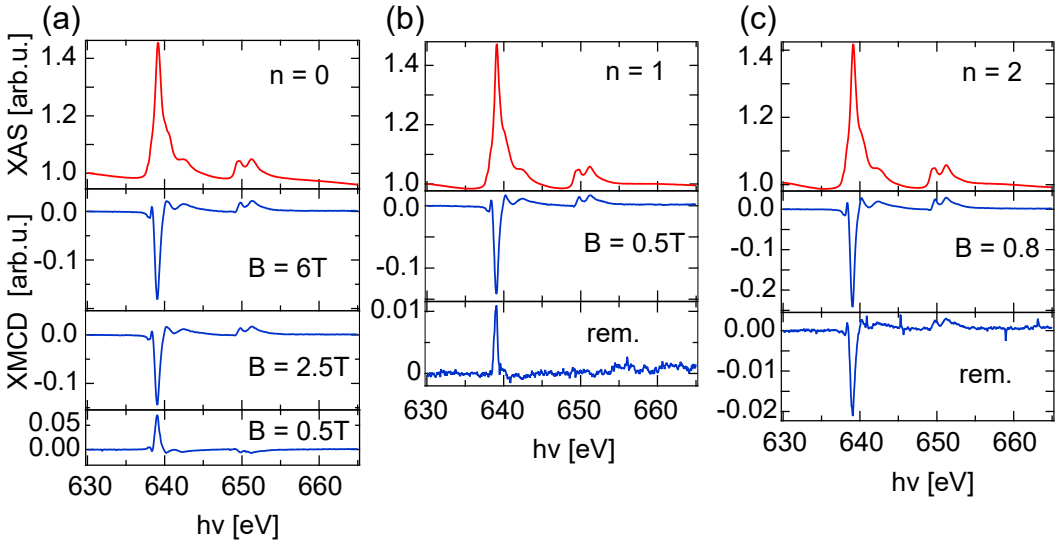

Figure 6.9.: XAS and XMCD of Fe_3GeTe_2 – n QL Bi_2Te_3 – 1 SL $MnBi_2Te_4$ heterostructures with n = 0, 1 and 2. a) n = 0 heterostructure with a direct Fe_3GeTe_2-$MnBi_2Te_4$ interface, showing the XAS (red) signal and the corresponding XMCD signals for multiple fields. b,c) XAS and XMCD at multiple fields for the n = 1 b) and n = 2 c) and heterostructure. For the cases of n = 0 and 1, a spin alignment against the external magnetic field is found below a certain field strength, while the n = 2 case does not show this behaviour.

properties, the XMCD signals for all three structures at several relevant field points are plotted in the lower panels of Fig. 6.9. For the direct interface (n = 0), applying a field of $B = 6\,\mathrm{T}$ results in a large XMCD signal, which reduces slightly when reducing the external field to 2.5 T, indicating an overall alignment of the sample magnetisation with the external field. Further reducing the external field to $B = 0.5\,\mathrm{T}$ leads to a reversal of the XMCD signal. As the external magnetic field still carries the same sign and taking into account the magnetic behaviour of the Fe_3GeTe_2 substrate, the sign reversal indicates an alignment of the Mn magnetisation against both external field and substrate magnetisation. Similar results are also found for the case of n = 1 in Fig. 6.9b), although the sign reversal is only observed close to zero external field. The structure with (n = 2) on the contrary does not show a sign reversal even in remanence, but the size of the XMCD signal decreases to ~ 10 % of the saturation value. Overall, the XAS and XMCD results indicate a strong interaction between the ferromagnetic substrate and the single magnetic SL of $MnBi_2Te_4$, whose nature and strength changes with the number of intercalated Bi_2Te_3 QLs.

To investigate this coupling in detail, Fig. 6.10a-c) shows the magnetic field dependence of the XMCD amplitude at the Mn L_3-edge for all three samples. The three graphs are displayed over the relevant field range and shall be discussed in the following. The y-axis is scaled to the respective moment determined from the individual XAS and

XMCD curves by the sum-rule analysis and therefore allows a direct comparison of the local magnetic moments for all structures. The n = 0 structure depicted in Fig. 6.10a) exhibits a complicated magnetisation curve with multiple sign changes, as the magnetic field is swept between ±2.5 T. For large external magnetic fields, the spin-moment is aligned with the respective external field and the substrate magnetisation, as sketched in the lower panel (Fig. 6.10d). Reducing the magnitude of the external field shows a local spin-flop on the Mn sites occurring at $B_{SF} \approx 1.2$ T. The spin-flop leads to a sign reversal of the Mn spin moment against substrate and external field, increasing in magnitude up to ~ 0.2 T and subsequently fully reverting in sign when crossing zero external field. Notably, the sign reversal happens along the soft ferromagnetic behaviour of the Fe_3GeTe_2 substrate and exhibits an open hysteresis loop around zero field, which is inverted to the one of the substrate. The field dependent magnetisation strongly suggests an antiferromagnetic coupling between the $MnBi_2Te_4$ SL and the Fe_3GeTe_2 substrate, with a coupling constant smaller but comparable in size to the one between the individual layers in thick films of $MnBi_2Te_4$. Interestingly XMCD measurements in a grazing incidence geometry (see appendix) do not show any traces of an alignment against the external magnetic field, indicating that the observed coupling carries a pronounced anisotropy along the magnetic easy axis of both materials.

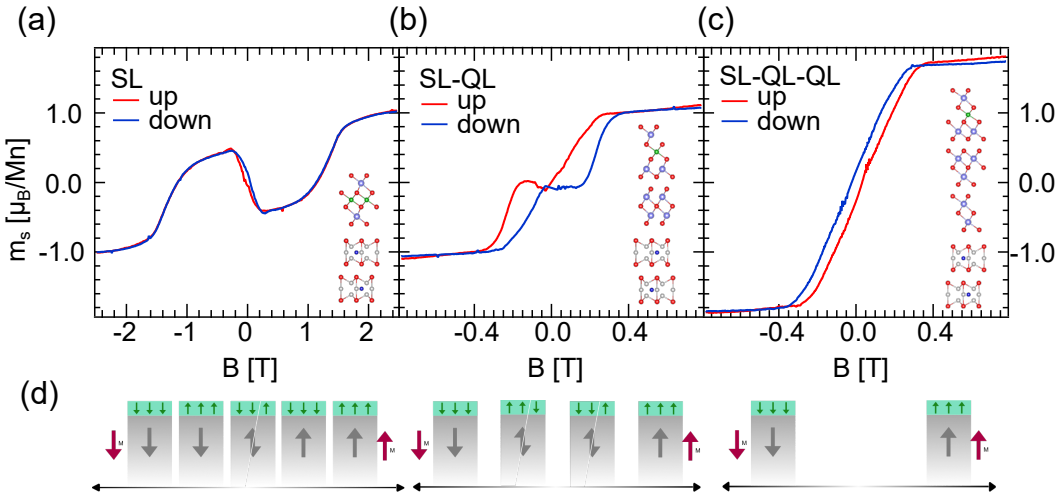

Figure 6.10.: XMCD-hysteresis behaviour for the Fe_3GeTe_2 – n QL Bi_2Te_3 – 1 SL $MnBi_2Te_4$ heterostructures with n = 0, 1 and 2 on the Mn L_3 edge maximum. a) Strong antiferromagnetic coupling between the Fe_3GeTe_2 substrate and the $MnBi_2Te_4$ SL. The respective spin orientations are depicted in d) and show a pronounces spin flop transition at fields of ~ ±1.2 T. b) Weakened antiferromagnetic alignment for n = 1 case, where the reduced coupling leads to a complex shape of the magnetisation curve. c) Ferromagnetic hysteresis in the case of n = 2. The respective sample surface structure is depicted as an inset in each graph.

The structure with n = 2 and hence the largest spacing is depicted in Fig. 6.10c). The Mn magnetisation shows a clear saturation above $B = \pm 0.4\,\mathrm{T}$ and a soft ferromagnetic hysteresis loop, remarkably similar to findings on the substrate magnetism. The interaction can be described as weakly ferromagnetic at most, as detailed out later. The intermediate case with n = 1 shows a mixture of the two fringe cases previously discussed. Above $B = \pm 0.4\,\mathrm{T}$ the magnetisation is aligned with the external field and the substrate and shows a flat course with a small linear slope. Below the saturation field, the magnetisation shows a sharp decrease ending in a flat plateau, which eventually leads to a gradual increase in magnitude after the external field switches sign. The sign of the plateau can not be read reliably from the hysteresis loop, but the XMCD spectra in Fig. 6.9 show, that the magnetisation indeed reverses with the sharp decline [5]. Taken together, the curve can be interpreted such, that the antiferromagnetic coupling as observed in the case of n = 0 is still present but weakened up to a point at which the spin flop field coincides with the saturation field of the substrate. While the magnetisation of the $MnBi_2Te_4$ SL reverts against the external field and the substrate, the substrate magnetisation simultaneously decreases, leading to the flat plateau, where both movements cancel each other out.

Modelling

In order understand the rather complex magnetic behaviour of the Fe_3GeTe_2 – n QL Bi_2Te_3 – 1 SL $MnBi_2Te_4$ heterostructures, a simple model can be developed to describe the substrate and field dependent magnetisation of the $MnBi_2Te_4$ monolayer. In accordance with the previous findings for the monolayer and the understanding of Fe_3GeTe_2 from literature [99], both substrate and the SL are magnets with a pronounced uniaxial anisotropy and can be described by a simple two spin state model with up and down orientation as depicted in Fig. 6.11a). Due to the large volume of the crystal compared to the single layer, the high T_c and in accordance with the previous findings, the hysteresis of the Fe_3GeTe_2 will be modelled by a simple model with saturation areas, a linear decay and a hysteresis loop opening. The respective numerical values are adapted from the experimental findings in Fig. 6.8 and the resulting curves can be seen in black in Fig. 6.11b-d). The model furthermore assumes that the demagnetisa-

[5] As XAS and XMCD in TEY always include free electrons moving in an large magnetic field, field dependent XMCD is strongly prone to fluctuations especially for small fields. Typically close to zero field, the effective electron yield changes sharply which together with the switching of the magnetic power supply renders the zero field region of the hysteresis scans difficult to obtain reliably. In the full XMCD spectra on the contrary, this effect is removed by proper normalisation, as the magnetic field is constant during the measurement.

tion in Fe_3GeTe_2 follows from the formation of domains and therefore the normalised substrate magnetisation can be written as

$$\frac{m_{\text{subst}}}{|m_{\text{subst,sat}}|} = p_\uparrow - p_\downarrow \tag{6.3}$$

with $p_\uparrow + p_\downarrow = 1$. Above a single domain of the substrate, the energetics of the $MnBi_2Te_4$ SL are defined by three main contributions, which will all be given in dimensionless quantities. The model is designed such a way that the magnetic field axis corresponds to the experimental findings in absolute values. The two independent parameters are thus the relative size of coupling J and the temperature scale k_bT with respect to B. The energy of the monolayer above a substrate domain may thus be written as

$$E_{\text{ml}} = J\,\vec{s}_{\text{ml}} \cdot \vec{s}_{\text{subst}} + \vec{B} \cdot \vec{s}_{\text{ml}} \tag{6.4}$$

where the projection of $\vec{s}$ along the z-axis may take values of ± 1. In a simple thermodynamic picture, the probability of the film orientations is given by Maxwell-Boltzmann statistics and the average magnetisation can be expressed in the same way as described in Eq. 2.1. Taking into account the two possible domains of the substrate, the full model for the magnetisation of the top-layer is written as

$$\frac{m_{\text{ml}}}{|m_{\text{ml,sat}}|} = p_\uparrow \frac{e^{(B+J/k_BT)} - e^{-(B+J/k_BT)}}{e^{(B+J/k_BT)} + e^{-(B+J/k_BT)}} + p_\downarrow \frac{e^{(B-J/k_BT)} - e^{-(B-J/k_BT)}}{e^{(B-J/k_BT)} + e^{-(B-J/k_BT)}}. \tag{6.5}$$

The two parts of the equation correspond to the contributions of the two substrate domains, such that in the exponent the relative sign in front of the coupling constant J changes. The two exponential functions within the each part describe the relative probability of spin up and down orientation of the top-layer for a given external field and substrate polarisation. This model allows to calculate the response and therefore the average magnetisation of the top-layer for a magnetic field sweep, where the $p_{\uparrow/\downarrow}$ are calculated from Eq. 6.3.

Employing this model to the situations given in Fig. 6.10 allows to simulate the hysteresis for all three cases by only varying the coupling constant J to match the experimental observations as depicted in Fig. 6.11b-d). For the largest negative coupling constant, the fundamental observations of Fig. 6.10a) can be reproduced. The competing energy scales of Zeeman-energy and antiferromagnetic coupling $J < 0$ lead to a spin flop field at the position where both become equal. In the range of the substrate coercive field, the top-layer magnetisation reverses inversely to the substrate. Reducing the coupling constant such, that the spin flop field coincides with the coercive

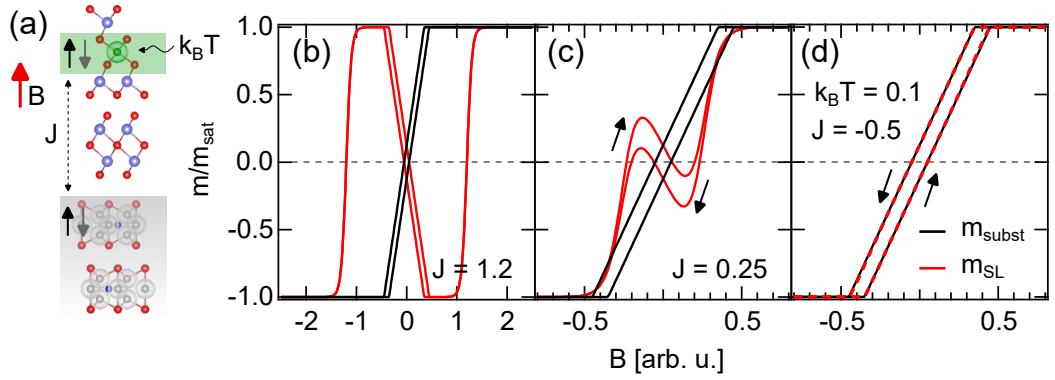

Figure 6.11.: Simple statistical model for the coupling between the single SL of $MnBi_2Te_4$ and the ferromagnetic Fe_3GeTe_2 substrate. a) The $MnBi_2Te_4$-SL is modelled as a single macro-spin with two possible orientations. The relevant energies are the Zeeman energy, the substrate-layer coupling J and the thermal energy k_BT. b-d) Three simulated hysteresis curves with varying J. The values of J are chosen such, that the relevant points on the B-axis correspond to the experimental observations in Fig. 6.10 a-c). The model nicely reflects the experimental observations and the transition from antiferromagnetic to ferromagnetic coupling.

field of the substrate, leads to the complex situation in panel c), which nicely models the behaviour found for the structure with n = 1. When reverting the sign of J assuming a ferromagnetic coupling, the top-layer starts to mimic the hysteresis of the substrate already for moderate sizes of J, which again allows to model the behaviour found for the n = 2 case in Fig. 6.10c). Overall, the employed model allows to explain the observed magnetic behaviour of the single SL of $MnBi_2Te_4$ for all structures. The fundamental assumptions are mainly concerning the domain nature of the magnetism and will be discussed and justified in more detail later. The implementation of the model as well as further systematics can be found in the appendix of this thesis.

Temperature dependence of the magnetisation

Going back to chapter 6.1, parallels can be drawn between the investigation of the surface layer in bulk $MnBi_2Te_4$ and the situation given for the n = 0 case. In both situations, a single SL of $MnBi_2Te_4$ at the surface is coupled to a bulk system over one van der Waals gap. In $MnBi_2Te_4$, this coupling suffices in raising the critical temperature from ~ 15 K close to the Néel temperature for the bulk compound. Similarly, here the question arises whether the coupling to the magnetic substrate can enhance the magnetic properties and especially lead to an extension of the region in which a remanent magnetic polarisation can be found in the Mn layer. Figs. 6.12a,b) show two hysteresis loops for the n = 0 case at sample temperatures of 10 and 15 K. In both cases, the gen-

eral shape of the curve including the sign changes and the open hysteresis loop persists even at the elevated temperatures. Remarkably even at 15 K a remanent magnetisation can be found on the Mn species. With the rising temperature two trends can be found. The overall magnetic moment decreases due to the increase in thermal energy and the spin-flop transition softens and gradually approaches a linear behaviour. For all temperatures, two fix points exist in the hysteresis at which all curves cross (see appendix, Fig. A.2). Going back to the model these fix points correspond to the Zeeman-energy and the coupling energy to be of equal magnitude such that an influence of the sample temperature at these points is minimized. These points allow to precisely determine the spin-flop field for the structure to be $\mu H_{\mathrm{sf}} = (1.261 \pm 0.010)\,\mathrm{T}$. As contrary to normal ferromagnets no natural choice for the reading exists in this case, to quantitatively evaluate the decay of magnetisation with temperature, the XMCD signal has been evaluated at three different positions in the hysteresis loop. The three means of evaluation include the maximal XMCD amplitude at a field of $\pm 2.5\,\mathrm{T}$, the maximum negative amplitude at $\pm 0.45\,\mathrm{T}$ and the area of the small hysteresis loop. Interestingly, after normalisation to the lowest temperature all three means reflect a closely similar behaviour, such that in Fig. 6.12c) the average of all three methods is shown with errors reflecting the statistical error between the different methods. The data reflects a decay in magnetisation with temperature, which does not show any characteristics of a sharp phase transition. Especially no signs of a feature at the critical temperature of the isolated monolayer can be found. Employing the aforementioned toy-model to this decay allows to fit the curve over the full temperature range. Here the main fitting parameters are a global scaling factor and the conversion factor from the experimental temperature to the dimensionless energy scale required in the model $k_{\mathrm{B}}T = \alpha \cdot T_{\mathrm{exp}}$, while the coupling constant is adapted from the spin flop field observed at the lowest temperatures.

While further datasets and an extended analysis of the temperature dependent magnetisation can be found in the appendix of this work, a few remarks can be made here. In the case of the n = 1 structure, the complex behaviour around zero external field gradually softens. Around $\sim 12\,\mathrm{K}$ the shape resembles the one of an inverted ferromagnetic hysteresis loop (not shown). In the case of n = 2, the shape of the hysteresis does not change significantly between the lowest temperature and $\sim 13\,\mathrm{K}$, indicating, that the interplay with the substrate indeed also stabilizes the magnetisation in the ferromagnetic case. Overall it can be concluded, that for all structures, a significant stabilization of the magnetic order above the critical temperature of the isolated monolayer can be observed. The absence of a clear phase transition together with the descriptive

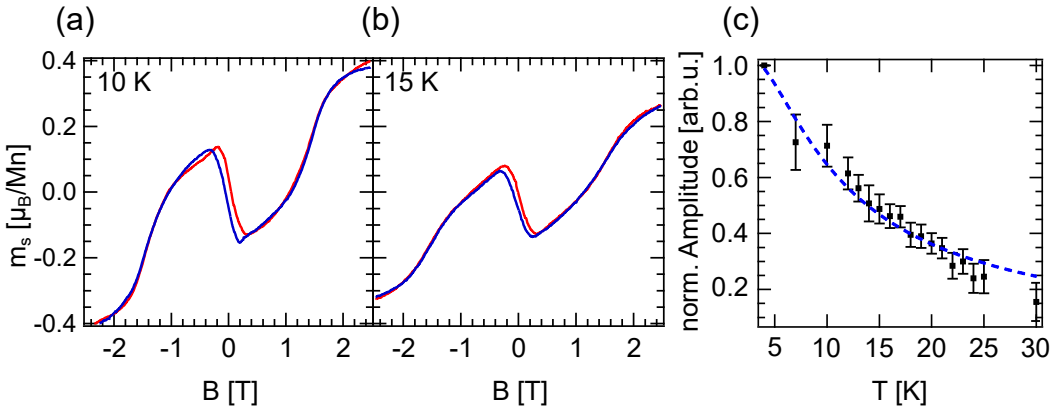

Figure 6.12.: Temperature dependent behaviour of the n = 0 heterostructure. a) Magnetisation curve for a sample temperature of 10 K and b) 15 K, showing a softened by still pronounced AFM behaviour. c) Temperature dependence of the magnetic polarisation in the $MnBi_2Te_4$ SL, extracted off different characteristic features of the hysteresis loops. The dashed line corresponds to a fit with the aforementioned model.

power of the simple modelling approach indicates, that the originally 2D ferromagnetic nature of the isolated SL is significantly altered by the coupling.

Magnetic Microstructure, Moments and Coupling

Fig. 6.13a) shows the hysteresis behaviour of the n = 2 structure in comparison to the hysteresis of the isolated monolayer, as also depicted in Fig. 6.5. It clearly reflects, that the magnetic behaviour is significantly altered with respect to the isolated case. The originally hard ferromagnetic behaviour with small coercive field changes towards a more soft ferromagnetic hysteresis extending over a significantly larger field range. Overlaying the same behaviour onto the magnetisation of the substrate over two individual y-axes in Fig. 6.13b) furthermore confirms, that the soft behaviour stems from an alignment with the substrate magnetisation.

While strongly indicating a ferromagnetic interaction between substrate and top-layer, the change in hysteresis shape can not be fully deduced without considering the microscopic structure of the magnetism of the substrate, namely the domain nature as already indicated in the basic assumptions of the modelling approach. The magnetic microstructure of thick Fe_3GeTe_2 is known to consist of bubble-like magnetic domains with lateral dimensions up to a few µm [102,105,205] and the soft behaviour with a gradual decrease of magnetisation is a direct consequence of the formation of these domains. The ratio of domain size to the typical distance between substrate and top-layer in the case of n = 2 is in the order of 10^3 and allows to assume, that the bias field felt locally

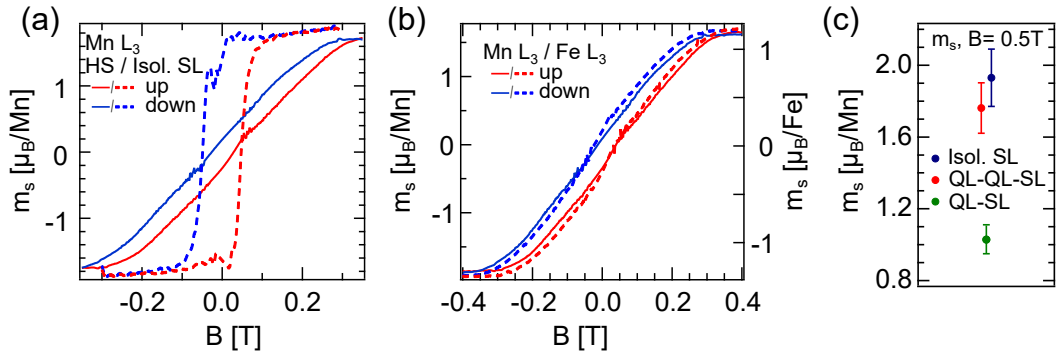

Figure 6.13.: Magnetic behaviour of the n = 2 heterostructure. a) XMCD hysteresis plot on the Mn L_3 edge for the n = 2 case in comparison to the case of an magnetically isolated single SL of $MnBi_2Te_4$ (dashed line) showing a significant change in shape. b) Same hysteresis on the n = 2 sample in comparison to the XMCD observed on the Fe L_3 edge (dashed lines). Both curves are plotted on the respective local spin moment on individual axis and the striking adaption of the Mn hysteresis shape becomes apparent. c) Comparison on the magnetic spin moment derived from XMCD sum rules for the n = 1 and 2 structures and the isolated SL.

in the top-layer is strongly dominated by the underlying domain of the substrate. Together with the change in the hysteresis shape, this argumentation indicates, that the hysteresis of the coupled $MnBi_2Te_4$ layer is mainly defined by the layer replicating the domain structure present on the surface of the Fe_3GeTe_2 structure. Given that the domain structure of Fe_3GeTe_2 can be manipulated by the sample thickness up to a single domain magnet for films with a thickness below 100 nm [104], these findings pose the hope, that a well structured substrate may allow to further engineer the magnetisation in the single SL of $MnBi_2Te_4$.

Figure 6.13c) shows the resulting local magnetic moments of the $MnBi_2Te_4$ SL at a magnetic field of $B = 0.5\,T$ as resulting from a sum rule analysis [194]. The analysis shows that while the local spin magnetic moment is still substantially reduced for the case of n = 1, in the case of n = 2, it recovers back to the saturation value found for the isolated monolayer. It further corroborates the presence of an antiferromagnetic coupling in the cases of n = 0 and 1, which reduces the energy-difference between the two spin-orientations with respect to the thermal energy scale and therefore leads to a decrease in magnetic moment even above the spin flop transition.

Fig. 6.14 shows the results of a DFT calculation on the case of the n = 0 heterostructure [206]. The corresponding calculated structure is depicted in a), consisting of one full Fe_3GeTe_2 unit cell and a single SL of $MnBi_2Te_4$ on its surface. The $MnBi_2Te_4$ layer carries four Mn atoms. The aim of the calculation was to first find the equilibrium position of the interface distance d (see Fig. 6.14a)) and in a second step determine the

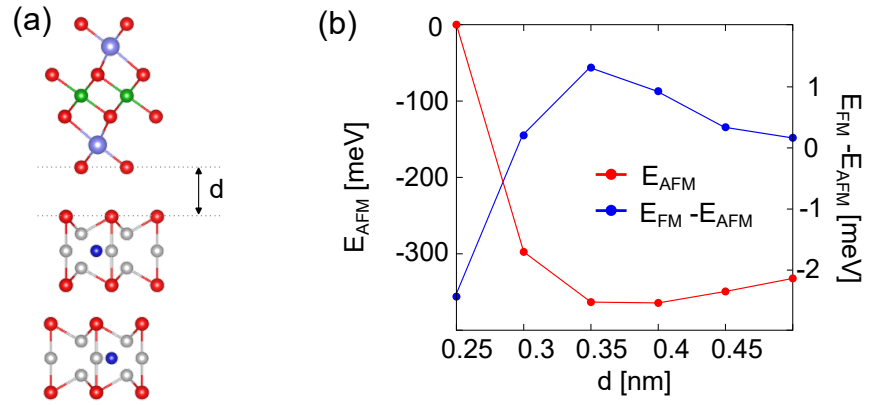

Figure 6.14.: Structure and DFT calculations for the n = 0 heterostructure. a) Side view of the crystal structure used for the DFT calculations. The van der Waals gap size d is defined as the distance between the two limiting Te planes. b) Total energy of the AFM configuration and energetic difference $E_{\mathrm{FM}} - E_{\mathrm{AFM}}$ for varying sizes of the vdW gap.

magnetic coupling as the difference between the ferro- (FM) and antiferromagnetic (AFM) alignment. Within each vdW-layer and for the substrate as a whole, a ferromagnetic configuration is assumed and only the relative orientation between the $MnBi_2Te_4$ layer and the Fe_3GeTe_2 substrate is varied[6]. The resulting energies are depicted in Fig. 6.14b). The red curve corresponds to the total energy of the antiferromagnetically aligned configuration displayed over the size of the vdW gap at the interface. The curve shows an energetic minimum at ~ 0.35 nm, which is well in line with the estimation from STEM results in chapter 5.3 of $d = (0.354 \pm 0.010)$ nm and shows, that the MBE growth results in an interface distance close to the energetic optimum. The energy is highly unfavourable for closer distances, and increases monotonically but weaker towards larger distance.

The nature of the coupling is defined by the energy difference between the two possible alignments along the out-of-plane direction. The relevant quantity $E_{\mathrm{FM}} - E_{\mathrm{AFM}}$ is depicted by the blue curve and can be understood such, that for positive values an AFM-alignment of the magnetisation is preferred. At the experimentally determined size of the vdW gap, the difference reaches a maximum of ~ 1.3 meV, which confirms the presence of an antiferromagnetic coupling in the structure as indicated by the experimental findings.

In a simple picture, the spin flop field corresponds to the value of the magnetic field B,

[6] Following from the TEM analysis, for the DFT calculation the lattice parameters from bulk samples were used for the DFT calculation. The van der Waals gap size d was left as the only unknown parameter. The calculations were conducted by J.I. Facio, more details on the method and similar calculations can be found e.g. in [44].

for which the two configurations of the Mn layer are degenerate in energy, which may be expressed as

$$\Delta m_{\mathrm{SL}} \cdot B_{\mathrm{SF}} = E_{\mathrm{FM}} - E_{\mathrm{AFM}}. \tag{6.6}$$

The volume in the calculation contains four Mn atoms and in the case of an isolated monolayer, the moment per Mn atom can be estimated to be $m_s = (1.93 \pm 0.16)\,\mu_{\mathrm{B}}/\mathrm{Mn}$ and Δm_{SL} is hence given by $2\mu_{\mathrm{B}} m_{\mathrm{s}}$. On the basis of the experimental spin flop field, $E_{\mathrm{FM}} - E_{\mathrm{AFM}}$ can be estimated as (1.127 ± 0.023) meV. The estimation gets reasonably close to the theoretical expectation from Fig. 6.14b). As observed in chapter 5.3, the difference in lattice constant leads to a 11:12 periodicity of the lattices, which can effectively be interpreted as the presence of multiple different stackings, where the $MnBi_2Te_4$ unit cell carries an increasing lateral offset towards the substrate. As in the given calculation the structure was approximated as an relaxed $MnBi_2Te_4$ structure centred on top of the Fe_3GeTe_2 unit-cell, a more in depth handling of the lateral structure may very well explain the small discrepancies. While the employed calculations do not allow to relate the coupling to a specific mechanism, the strong dependence on the vdW gap size nevertheless indicates, that the coupling is mediated by an orbital overlap over the van der Waals gap, which was also found or proposed as the main mechanism in other synthetic van der Waals magnets [85,185].

When extending the concepts from this chapter to other materials systems, the question arises, which material combinations have the potential to host a coupling of similar strength. Naturally this question is highly complex and impossible to be answered based on the experimental evidence presented above. Nevertheless, beyond considerations concerning the feasibility of sample growth, in a last step a closer look can be taken at the respective densities of state of the individual elements in substrate and overlayer. By using soft X-ray radiation and resonant photoemission spectroscopy (ResPES), the density of states of the Fe and Mn species in the heterostructures may be assessed individually, as schematically sketched in Fig. 6.15a). The resulting energy distribution curves (EDCs) integrated over the full accessible angle range are depicted in Fig. 6.15b) and d). Both panels show multiple curves corresponding to sweeping the photon energy across the nominal energy of the respective Fe- and Mn L_3-absorption edge. On the example of Fig. 6.15b) it is clearly visible, that when approaching the energy of the Fe absorption edge, two peak-like features clearly increase in intensity, which can be interpreted as the two main contributions of the Fe 3d DOS to the valence band intensity. The main feature is located around $E - E_{\mathrm{F}} = 3.6\,\mathrm{eV}$ and a smaller feature arises at $E - E_{\mathrm{F}} = 0.7\,\mathrm{eV}$. The peak positions are estimated from the $h\nu$ dependent

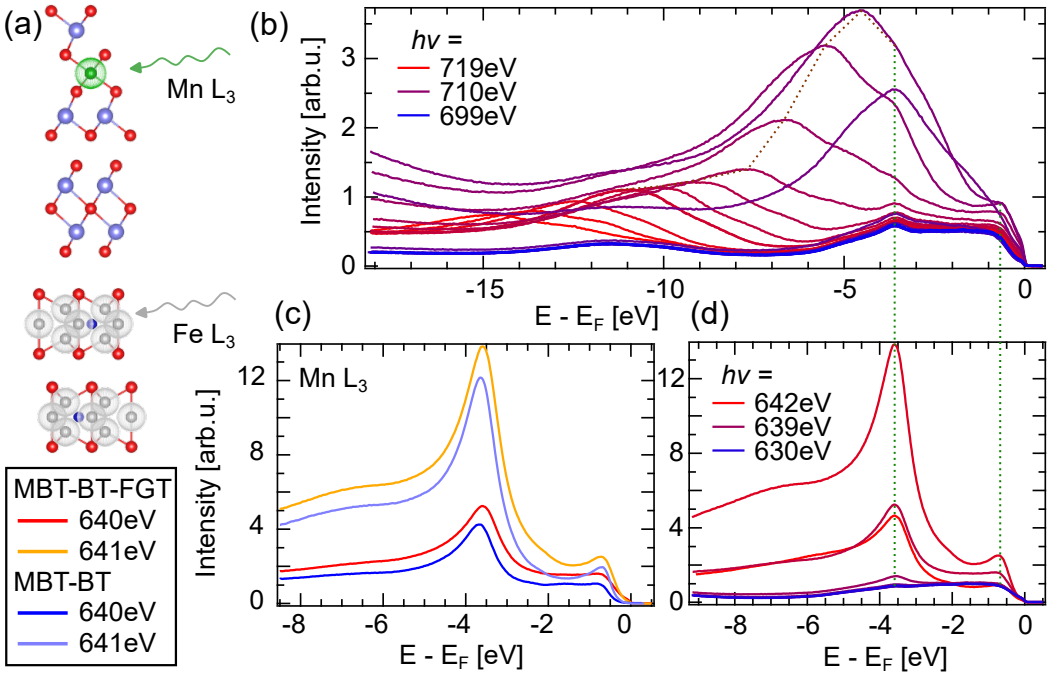

Figure 6.15.: Density of states of the Mn and Fe 3d-states in the Fe_3GeTe_2– 1 QL Bi_2Te_3 – 1 SL $MnBi_2Te_4$ heterostructure. a) Sketch of the experimental principle. In the resonant condition, X-rays with photon energies on the Mn and Fe L_3 absorption edges selectively excite electrons from the Mn and Fe 3d states respectively, which consequently originate either from the $MnBi_2Te_4$ surface layer or the Fe_3GeTe_2 substrate. b) EDCs of a $h\nu$-series over the Fe L_3 absorption edge energy depicting the rise of two distinct spectral features marked by green dashed lines and the transition of the resonant into an Auger process. c) EDCs for selected energies on the Mn L_3 edge selected from the $h\nu$-series depicted in the right panel of c). The curves are compared to results obtained on a single $MnBi_2Te_4$ grown on Bi_2Te_3. The main positions of spectral features are marked in the right panel and the energy axis is to scale with b) to highlight the positional match.

spectra in the region in which the peak appears at a fixed binding energy. At higher photon energies, the feature significantly moves in binding energy as expected due to the increasingly Auger-like character of the transition [146]. A similar analysis on the Mn L_3 edge (Fig. 6.15d)) shows the occurrence of two main peaks. Interestingly, the energetic positions fully coincide with the features observed in the Fe-DOS. As evident from Fig. 6.15c), the shape of the resonant EDC is closely similar to the one of an isolated SL of $MnBi_2Te_4$ and well in line with previous findings on $MnBi_2Te_4$ single crystals [207]. The main feature at $E-E_F = 3.6\,eV$ corresponds to the spin-majority states in $MnBi_2Te_4$ with contributions of both e_g and t_{2g} states. The feature at $E-E_F = 0.7\,eV$ results from p-d hybridisation with the neighbouring Te 5p-states, which hybridize with the Mn t_{2g} states [208]. This hybridisation allows for the partial occupation of the spin-minority states close to the Fermi energy, as found in multiple MnTe based materials [207–209]. Furthermore Fig. 6.15c) shows a small shift of the Mn DOS towards smaller binding

energies in the case of the heterostructure, which leads to the close to perfect match of the energy positions with the ones of Fe_3GeTe_2. Taken together, this analysis indicates, that the material combination $MnBi_2Te_4$ - Fe_3GeTe_2 is accompanied by a remarkably close match of the energetic positions of the respective 3d densities of states. While this should be noted as a mere observation at the present point, it nevertheless opens an intriguing question. By comparing the coupling found in materials based on different 3d transition metals, it might be possible to elucidate, whether an energetic overlap of the magnetic DOS is beneficial in the case of van der Waals magnetic coupling.

7. Interplay Between Magnetism and Topology in $MnBi_2Te_4$ Based Heterostructures

Overview

The following chapter will describe the electronic structure arising at the surface of the ferromagnetic extension – namely the epitaxially grown heterostructure of a single SL of $MnBi_2Te_4$ on the surface of a Bi_2Te_3 film – and present a close investigation of the interplay between the topological surface state (TSS) arising at the ferromagnetically extended surface and the magnetism present in the single $MnBi_2Te_4$ SL. The first part of the chapter will describe the TSS in detail, concerning its dispersion and energetic position compared to the parent compounds Bi_2Te_3 and $MnBi_2Te_4$, its photoemission cross section and its spin and orbital texture. The second part contains an analysis of the magnetic exchange gap opening in the TSS when crossing the critical temperature. The chapter will work out its extent in k-space and bring its temperature dependent behaviour in context with the magnetic properties of the surface.

Most of the findings in this chapter have been published in [120] and the corresponding supplementary material.

7.1. Band Structure of the Ferromagnetic Extension

Given a sufficiently *perfect* interface, the ferromagnetic extension can be viewed as a surface modification of the 3D TI Bi_2Te_3 by the single SL of $MnBi_2Te_4$. In both cases, the topological surface state is derived from Te and Bi p_z orbitals intermixed with in-plane contributions [29,50,210]. As described in chapter 2.2.4, as a consequence the TSS is expected to partially relocate into the modified surface layer and be subjected to a different electromagnetic environment. Even in the absence of magnetic polarisation in the $MnBi_2Te_4$ layer, the electronic structure of the TSS is likely to be influenced by this modification, which is then followed by the coupling to the emergent magnetic polarisation.

7.1.1. Electronic Structure and Symmetries

Fig. 7.1a) displays an ARPES map of the $MnBi_2Te_4$-Bi_2Te_3 heterostructure. The spectrum shows the TSS of the heterostructure located at the $\overline{\Gamma}$-point of the surface Brillouin zone (BZ). The two open faces of the spectrum are cut along the $\overline{\Gamma K}$ and $\overline{\Gamma M}$ high-symmetry directions of the BZ and the top surface displays a constant energy contour at the Fermi energy. The map clearly displays a linearly dispersing state with a crossing point of the linear bands at $E_D \approx 140\,\text{meV}$. Moving away from the Dirac point (DP) the bands start to bend outwards, especially in the $\overline{\Gamma M}$-direction and the Fermi surface clearly shows a strong warping of the TSS. This warping structure is typically assigned to 3rd order terms in the crystalline momentum dependence influencing the otherwise linear dispersion and is known to occur in Bi_2Te_3 and $MnBi_2Te_4$ derivatives [196,211]. The TSS clearly resides in the centre of the bulk band gap and no other electronic states are visible in this energy range. Panel b) shows DFT calculations for three different structures, namely pure Bi_2Te_3, a single $MnBi_2Te_4$ layer on top of Bi_2Te_3 in the ferromagnetic state and a single layer of $GeBi_2Te_4$ on top of Bi_2Te_3 as the closest non-magnetic structural analogue. While for Bi_2Te_3 the DP is located within a valley in the valence band, for both of the heterostructures it is strongly shifted upwards towards the middle of the band gap. This shift of the DP position by the surface modification has already been proposed for other non-magnetic TI heterostructures and can be understood when considering the work function and band-gap differences of the two materials under question [48,212]. The calculations for the $MnBi_2Te_4$-Bi_2Te_3 heterostructure host a large gap at the DP of the TSS, caused by the magnetic polarisation and can therefore not be used as a reference for the experimental observation in the paramagnetic phase. A comparison to the $GeBi_2Te_4$-Bi_2Te_3 heterostructure on the other hand helps to identify a set of characteristic features. The DP resides within the band gap, and the linear dispersion of the TSS evolves into a strong warping especially along the $\overline{\Gamma M}$-direction, as also evident in our experimental findings. The lower branches of the TSS smoothly connect to the bulk valence band, as also illustrated by additional data in the appendix. By an analysis of single EDCs for a set of momenta close to the DP, the group velocity of the TSS can be determined as $v_g = (5.110 \pm 0.056)\, 10^5 \text{m/s}$, which reflects a TSS-dispersion, steeper than e.g. in Bi_2Te_3 [74]. Further systematics on the photoemission results are also presented in the appendix of this thesis.

Fig. 7.2a) shows photoemission spectra over a larger energy range for several photon energies. Within the displayed $h\nu$ range, a strong decay of the photoemission cross-section for the TSS, as well as the connected M-shaped states is apparent, while the intensity of features at higher binding energies gradually increases. Over the full displayed energy range, no $h\nu$-shift of the visible features is observed, indicating a negli-

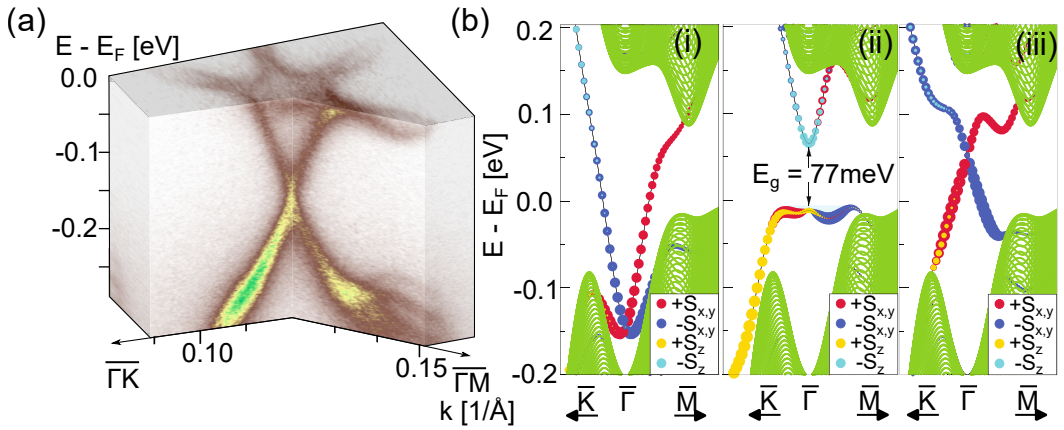

Figure 7.1.: Band structure of the ferromagnetic extension and DFT calculations. a) 3D representation of the surface Brillouin zone centre, acquired with $h\nu = 12\,\text{eV}$ as a sum of both circular light polarisations at $T = 20\,\text{K}$. The data shows the Fermi surface as well as the two high-symmetry directions $\overline{\Gamma K}$ and $\overline{\Gamma M}$. b) Spin-resolved DFT calculations for (i) Bi_2Te_3, (ii) a ferromagnetic SL of $MnBi_2Te_4$ on Bi_2Te_3 and (iii) a single SL of $GeBi_2Te_4$ on Bi_2Te_3. *Figure a) adapted from [120] licensed under CC BY 4.0. b) used and adapted with permission of IOP Publishing, Ltd, from [48]; permission conveyed through Copyright Clearance Center, Inc.*

gible k_z dependence and pronounced two-dimensional character of the band structure observed in this parameter range. Panel b) more systematically displays the relative intensity of the TSS normalised to the integrated valence band intensity[1]. The cross-section has a sharp peak centred around $h\nu = 12\,\text{eV}$ and rapidly decays towards both, higher and lower energies. Interestingly even for significantly higher photon-energies up to the soft X-ray range, no reoccurrence of the spectral weight for the TSS could be observed.

A peculiar $h\nu$ dependence of the photoemission cross section for the TSS was already debated for the parent compound $MnBi_2Te_4$, as the TSS only exhibited a non-negligible photoemission cross-section at very low photon energies with most experiments conducted at Laser-ARPES facilities using $h\nu \approx 6.4\,\text{eV}$ [41,170]. On the contrary the TSS of Bi_2Te_3 shows a sizeable photoemission cross-section over a large range of photon energies even in the soft X-ray range. One possible explanation on this matter results from a comparison of the real-space localisation of the TSS wave function predicted by DFT for the ferromagnetic extension of Bi_2Te_3 and $MnBi_2Te_4$ (Fig. 2.3 and [48]) and the case of bulk $MnBi_2Te_4$ [34]. It can be seen that in both cases, the TSS is localized over at least two vdW-layers away from the surface, while in the case of the Bi_2Te_3 family the spectral weight is localised closer to the surface [213]. Consequently, the $h\nu$-dependent

[1] This normalisation approach was chosen as no reliable probe of the total beamline flux at the given photon energy was available due to necessary manual adjustments of the beamline pointing. The increase of the fraction towards higher energies is most likely caused by a general decay in cross-section of the valence band states and not related to an increased cross-section of the TSS.

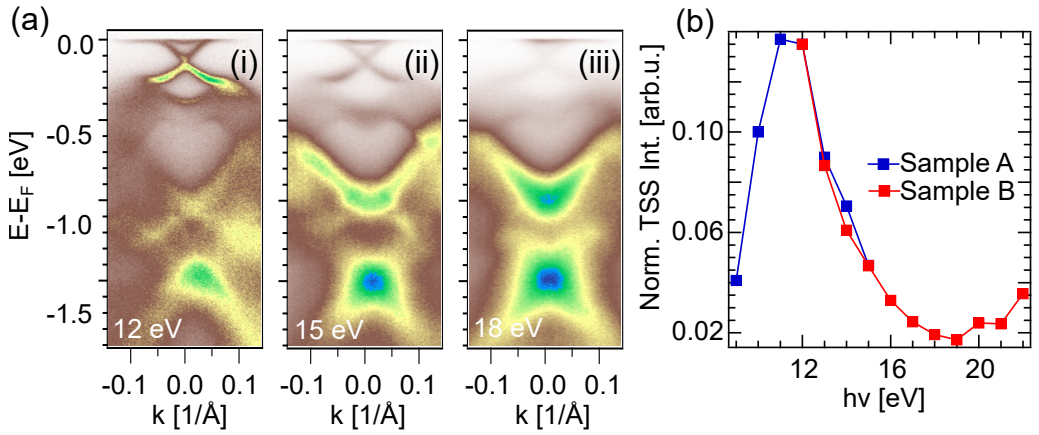

Figure 7.2.: *hv* dependence of the TSS intensity. a) Valence band spectra acquired with incident photon energies of 12, 15 and 18 eV, depicting the TSS and a large portion of the valence band structure. b) Intensity of the TSS normalised by the full integrated valence band intensity for two structurally identical samples. The photoemission cross section of the TSS depicts a pronounced maximum around ~ 12 eV and strongly decays away from there.

cross sections in the $MnBi_2Te_4$-Bi_2Te_3 heterostructure follow the systematics observed in $MnBi_2Te_4$, and a connection may be established with the real-space localisation of the TSS in these structures.

7.1.2. Spin Structure of the Topological Surface State

Using the light polarisation as an additional degree of freedom allows to study the character and orbital nature of electronic states in more detail and has found various applications on Rashba-type and topological systems in the past [133,141]. Fig. 7.3a) shows the circular dichroism of the TSS perpendicular to the plane of light incidence. Panel b) depicts a cut through the surface BZ. The linear dichroism pattern was acquired by an anti-symmetrisation of the spectrum as described in chapter 4.2. While the circular dichroism amounts to less than 10 % of the overall intensity, the linear dichroism is larger than 50 % and is strongly pronounced within the experimental plane. The circular dichroism is displayed within the k_y plane and switches sign in the k_x-plane. Although the experimental plane did not coincide with a crystalline high-symmetry direction due to technical limitations, the dichroism is nevertheless found to be strictly symmetric towards the $\overline{\Gamma}$ point and no artefacts arising from the slight misalignment could be observed.

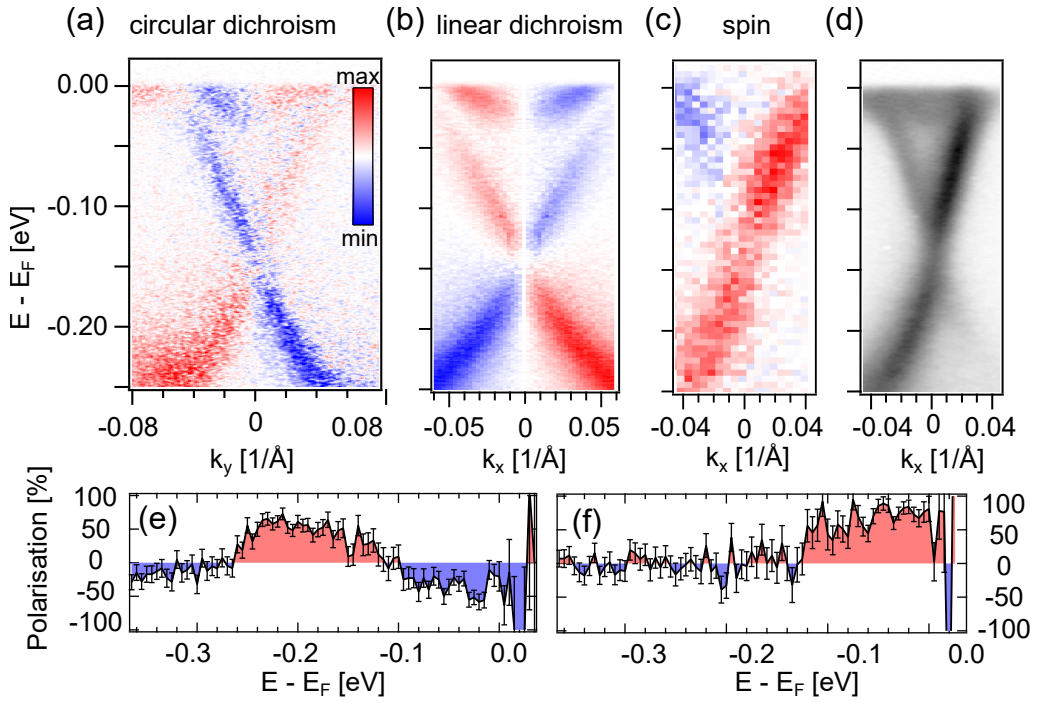

Figure 7.3.: Dichroism and spin polarisation of the TSS. a) Circular dichroism of the TSS. b) Linear dichroism in the same geometry by anti-symmetrisation of a spectrum acquired with p-polarised light. c) Spin-resolved Laser-ARPES measurement showing the y-spin polarisation along k_x direction. d) ARPES image of the TSS under the same conditions as in c). e,f) Single spin polarisation spectra for two EDCs, depicting the y-spin component at $k_x \mp 0.03\,\text{Å}^{-1}$. The polarisation is clearly significant within the error margin. a,b) Acquired at $h\nu = 12\,\text{eV}$, c-f) at $h\nu = 6.4\,\text{eV}$.

Fig. 7.3 e,f) show the spin polarisation along two EDCs within the experimental k_x plane. The spectra were acquired at a photon energy of $h\nu = 6.4\,\text{eV}$ for k-vectors with $k_x = \pm 0.03\,\text{Å}^{-1}$, using an experimental setting sensitive to the y-component of the electron spin. The corresponding spin-integrated intensity at these photon energies is shown in panel d). The spin polarisation in e) shows two main spin-polarised bands with a clear sign change slightly below $E - E_F = -0.1\,\text{eV}$. The experimental spin polarisation is strongly pronounced and ranges above 50 %. A comparison with the spin-integrated ARPES spectrum d) allows to assign the two maxima to the upper and lower branch of the TSS, respectively. Fig. 7.3 f) corresponds to a cut through the right side of the TSS depicted in d), where the linear dichroism strongly suppresses the intensity of the lower branch of the TSS. Consequently, the experimental results show a strongly pronounced spin polarisation for the upper branch, while the polarisation approaches zero below the DP. Having confirmed a spin polarisation clearly above the level of statistical fluctuations as indicated by the experimental errors, gradually varying the k-position along the k_x plane allows to map the evolution of the spin y-component for

the full dispersion displayed in d). The resulting spectrum is displayed in panel c) and shows the pure spin spectra $I_\uparrow - I_\downarrow$ as defined by Eq. 4.18. The spectrum displays a sign change of the spin polarisation between the two branches of the upper cone, while the intensity of the negative branch is again suppressed in the lower part. The weak relative weight of the negative branch and overall positive sign in the spectrum is also resulting from the strong linear dichroism in the sample. The presence of spin polarisation as well as its chiral structure has further been verified and detailed in experiments using different light polarisations, photon energies and directions of the measured spin (not shown in this thesis).
Taken together, the observation of the dichroism patterns and strong spin polarisation strengthen the interpretation of the linearly dispersing pair of states as the topological surface state of the ferromagnetic extension. The results are overall well in line with findings on similar and especially also non-magnetic TSS-systems and allow to draw conclusions on the orbital and spin nature of the TSS [214]. Both, in-plane p_{xy} as well as out-of-plane p_z orbitals contribute to the surface state with the linear dichroism arising from the mixed $p_{x,z}$ contributions in the experimental plane [75,215]. The presence of circular dichroism as well as spin polarisation in the strongly spin-orbit coupled system indicate, that both orbital angular momentum as well as spin polarisation switch sign between the two branches under observation [75,142]. Each respective branch carries a single sign over the full band gap of the TI, which allows to identify it as a single state spanning over the bulk band gap of the material. This is in contrast to the closely related material system $MnBi_4Te_7$, where in close vicinity to the DP additional parabolic states emerge with strong spectral weight [141].

7.2. Temperature Evolution of the TSS

As outlined in chapter 2.2.2, magnetic polarisation along the surface normal breaks time-reversal symmetry and introduces an additional mass term to the effective Hamiltonian of the TSS. As a consequence, an exchange gap is expected to open at the Dirac point of the TSS. Up to date, in most systems under consideration, no such effect has been resolved directly by ARPES. The following chapters will show, that the ferromagnetic extension approach indeed shows a sizeable influence of the magnetic order on the TSS and subsequently, that this effect can be uniquely assigned to a direct coupling to the sample magnetism.

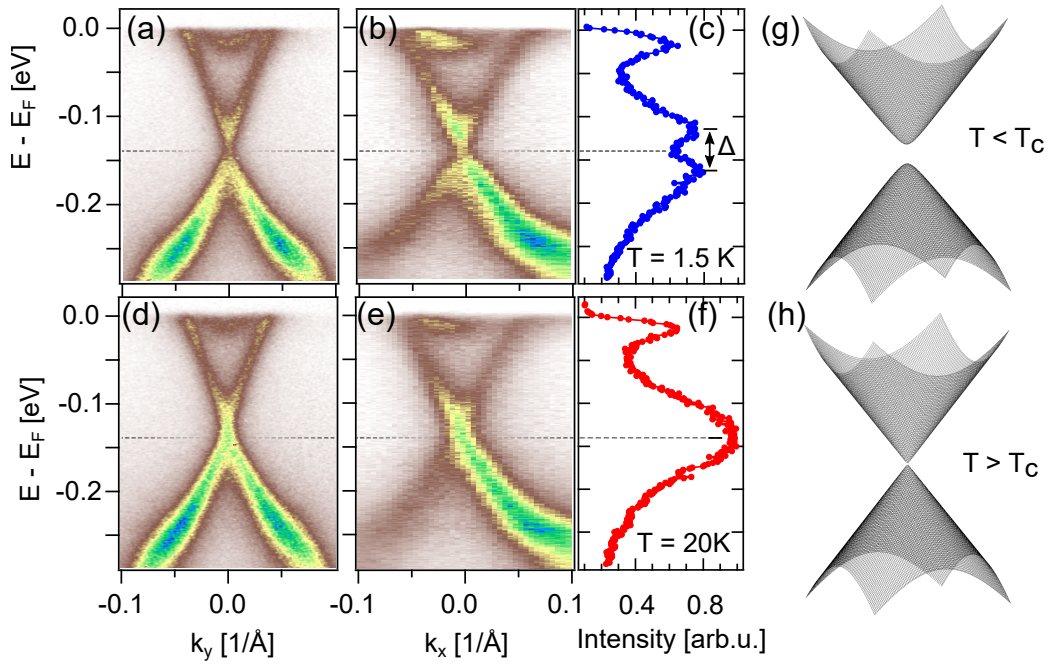

Figure 7.4.: Magnetic gap opening in the TSS induced by the ferromagnetic surface. a,b) Dispersion of the TSS along k_x and k_y measured by ARPES below the critical temperature at $h\nu = 12\,\text{eV}$. c) EDC extracted along $\vec{k} = \vec{0}$ clearly depicting a gap at the Dirac point. d,e) ARPES measurements under the same conditions above Tc. The corresponding EDC f) shows a single maximum of intensity, indicating a closed gap state. g,h) Toy model spectrum to visualize the expected influence of a magnetic gap onto the TSS for an open and closed gap state. *Figures adapted from [120] licensed under CC BY 4.0.*

7.2.1. Large Magnetic Exchange Gap Opening

Fig. 7.4 displays the angle- and energy-resolved photoemission intensity of the TSS in the two directions perpendicular to (a,d) and within (b,e) the experimental plane. The lower row shows datasets acquired above the critical temperature of the ferromagnetic transition, while the upper row was taken at the base temperature of the system at ~ 1.5 K. The lower panel depicts the linear dispersion of the topological surface state with a clearly closed gap in both directions. Panel f) displays an EDC integrated through the photoemission map along $\vec{k} = 0$, which clearly depicts a single maximum of intensity at the DP. Next to the apparent changes at the DP, a small n-type shift can be observed for the band structure at 1.5 K, as compared to the high-temperature case. While the possible reasons are manifold[2] and do not influence the fundamental observation, a careful treatment will be necessary when comparing absolute energy positions.

[2] The possible reasons here are either a movement of the chemical potential with temperature due to a highly asymmetric density of states at the Fermi energy or a doping of the sample surface by adsorption of residual gas molecules at the very low sample temperatures.

The visible changes in the dispersion are well in line, with the expectation from the simple toy model as described in chapter 2.2.2. Fig. 7.4 again displays the resulting 2d models for an open and a closed gap state in a linearly dispersion TSS, which nicely reflect the experimental results. A careful analysis by adapting the toy model to the photoemission results considering the finite resolution of the photoemission experiment results in a size of the magnetically induced gap of ~ 35 meV. The complete analysis will be detailed out in the next chapter.

As apparent from the experimental results, the changes in the electronic structure are limited to the k-space close to the DP. Concluding from the spectrum of the perturbed toy Hamiltonian (Eq. 2.19), the changes should be localized in k-space in a range defined by the ratio of the perturbing mass term and the group velocity of the TSS as

$$\Delta k \approx \frac{m_z}{v_g \hbar} \tag{7.1}$$

where m_z is the size of the magnetic exchange gap. Using the relevant parameters from our experimental data, the relevant k-scale for the extent of the gap opening can be estimated to be ~ 0.01 Å^{-1}. In order to compare this assessment to the experimental findings, Fig. 7.5 shows a set of EDCs through the experimental datasets along different k_x-values above and below the critical temperature. Given the apparent shift in the Fermi energy for both temperatures, the energy scale is aligned to the DP of the respective TSS. While the EDC at $k_x = 0$ shows a clear difference between the two temperatures, this influence quickly decays towards higher momenta. For the EDCs at ±0.01 Å^{-1}, the signature of the magnetic gap is already negligible except for a small dichroic contribution at negative momenta. Consequently an excellent agreement between the experimental results and the naive expectation from the toy model can be found even at a quantitative level.

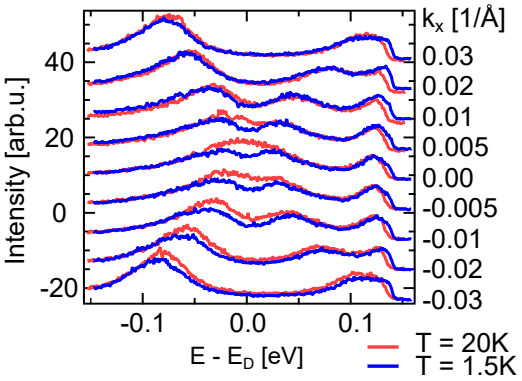

Figure 7.5.: Selected EDCs from the low- and high-temperature data as shown in Fig. 7.4 for different values of k_x. The energy scale is shifted to align the Dirac points of both samples and highlight the influence of the gap opening on the dispersion.

7.2.2. Scaling Analysis and Magnetic Origin

Following from the observation of a reversible and large magnetic gap opening, the question arises, how far the temperature evolution of the magnetic gap can be related

to the strength of the magnetic polarisation in the $MnBi_2Te_4$ layer. Put in different words, the question to ask is, in how far the simple assumption

$$\Delta_g \propto \langle m \rangle \tag{7.2}$$

will hold. As apparent from Fig. 7.2b), the TSS of the ferromagnetic extension has its highest cross-section at $h\nu \approx 12\,\text{eV}$ and all spectra have been taken at this photon energy. The use of these rather low excitation energies makes the experiment very prone to experimental line-broadening, especially caused by insulating patches on the surface of the mechanically de-capped samples[3]. As a consequence, the experimental conditions result in a non-negligible k-resolution of the experiment, which has to be taken into account when extracting the size of a magnetic gap in the photoemission spectra. To incorporate the experimental details, the size of the magnetic exchange gap will be extracted, employing a simple photoemission toy model, which is fitted to the experimental data for each temperature step. The group velocity v_g estimated from Fig. 7.4d) together with Eq. 2.20 allows to write down the TSS dispersion as

$$E_{\pm}(k) = E_D \pm \sqrt{(\hbar v_g k)^2 + \frac{\Delta_g}{2}^2} \tag{7.3}$$

for a cut through the 2D k-space. In order to obtain the photoemission intensity the model spectrum is now calculated as a spectral function along the TSS dispersion (see Eq. 4.12) convolved with a two-dimensional Gaussian

$$I(E,k) = \sum_{\pm} \int_{\omega} A_{\pm}(E,k) \frac{\Delta_\epsilon}{(\omega - E_{\pm}(k))^2 + \Delta_\epsilon^2} d\omega * G_{\Delta_k,\Delta_E} \tag{7.4}$$

where $A_{\pm}(E,k)$ is the respective band DOS taken as an amplitude multiplied with a delta function along the dispersion of the TSS. Δ_ϵ denotes the intrinsic line width and G_{Δ_k,Δ_E} a Gaussian distribution with the experimental resolution parameters Δ_k, Δ_E along k- and energy direction. The intrinsic parameter Δ_ϵ is adapted from previous work on the very similar $MnBi_6Te_{10}$ system (see. SI of[141]).

Fig. 7.6 shows the simulated photoemission intensity for the toy model in the case of a fully open and a closed magnetic gap. The data is simulated with a non-zero k- and energy-resolution and it is apparent, that the model is sufficient in simulating the main features of the experimental spectra including the slightly elongated appearance of the crossing at the DP. To further elaborate the effect of the experimental resolution, Fig.

[3] Typically photoemission experiments with a lower excitation energy will result in a higher k-resolution due to the conversion between detection angle and wave vector. The case here is special in that regard, as the increased influence of local fields at the sample surface outweighs the former effect.

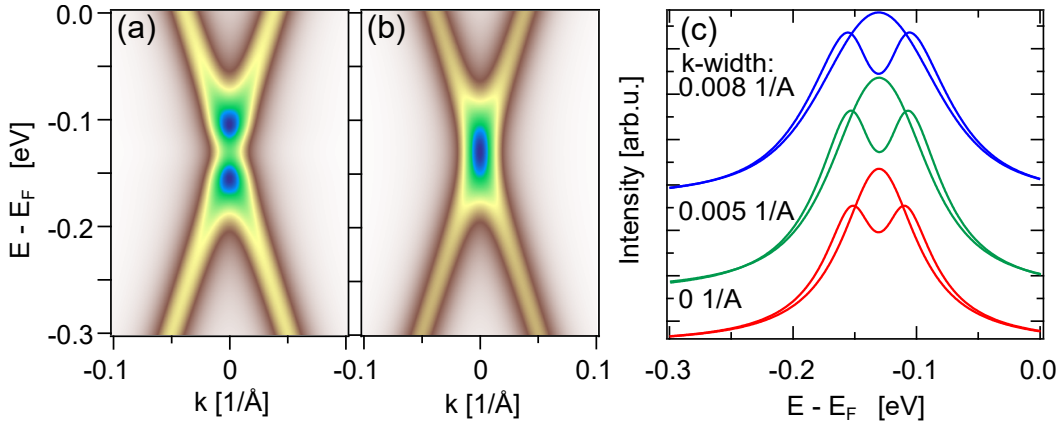

Figure 7.6.: Photoemission toy-model simulations. a,b) k vs. energy simulation of the TSS dispersion for a gap of 35 meV a) and a fully closed gap b). Both simulations assume an experimental k-resolution of 0.005 $Å^{-1}$. c) EDCs of the simulated spectra for different experimental k-resolution parameters depicting the cross-influence between perceived gap-size and experimental resolution.

7.6c) shows EDCs along the $\overline{\Gamma}$-point of the model for open and closed gap-states and different experimental k-resolution parameters. It is apparent, that the perceived size of the magnetic gap changes substantially with the experimental resolution as an interplay between the very steep shape of the TSS and the broadening in momentum direction. To adapt this model to the experimentally observed temperature dependence, a two-step approach is employed. Fig. 7.7a) shows experimental EDCs for the highest and lowest observed experimental temperature, where the gap can be assumed to be open for T = 1.5 K and zero for 20 K. Using these assumptions, the experimental resolution parameters and relative intensities of the two states can now be adapted to the two datasets, achieving a reasonable description of both spectra. In the second step, all temperature dependent EDCs are fitted, using the toy-model EDCs as a fitting function. All experimental parameters are kept fixed over the entire range and only the gap-size Δ_g and an overall intensity are allowed as fitting parameters. The experimental datasets and the modelled curves are displayed in Fig. 7.7b) and show a good agreement between experimental observation and fit over the entire temperature range.

To assess the scaling behaviour of the gap, Fig. 7.8 shows the fit results for Δ_g together with the remanent magnetic polarisation and the adjusted power law as shown in Fig. 6.6. The critical power law is normalised to one and all other curves are normalised such, that the respective lowest temperature point coincides with the power law fit. Within the boundary of experimental fluctuations Fig. 7.8 shows a striking resemblance between the magnetic scaling behaviour and the opening of the magnetic exchange gap, indicating a direct proportionality of $\Delta_g \propto \langle m \rangle$ with a full magnetic gap

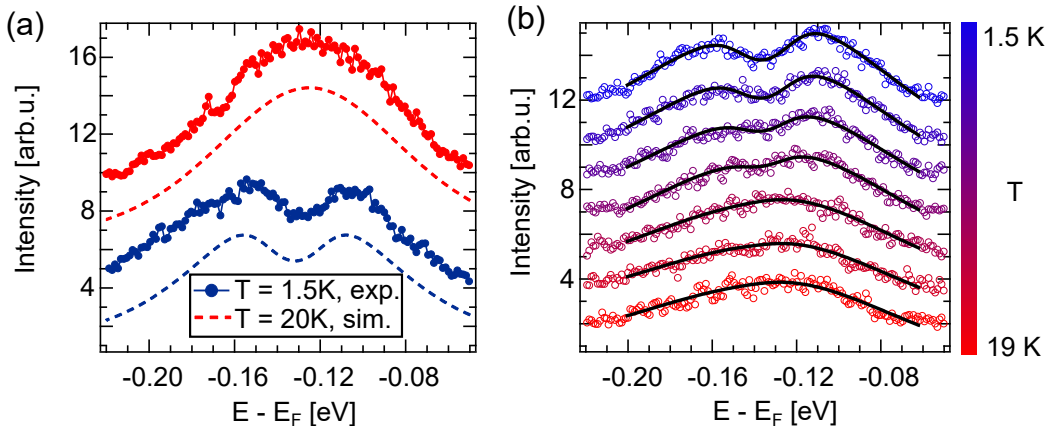

Figure 7.7.: Analysis of the T-dependent magnetic gap using the toy-model simulations. a) Experimental EDCs for two sample temperatures (see Fig. 7.4) together with the adapted model EDCs incorporating all relevant spectral features including slight differences in the band intensities. b) Full temperature series of another sample for temperatures between 1.5 and 19 K together with the fitted model curves (black lines). The fit results in a good description of the experimental data over the entire temperature range.

size of ~ 35 meV.

The congruence between the size of the magnetic gap and the remanent magnetic polarisation nicely visualized the direct coupling between the magnetic polarisation and the topological properties of the material. In this regards, a few remarks concerning the differences between the two experiments can be made. The ARPES experiments presented above are conducted in a strongly magnetically screened environment (see chapter 4.2.2) suppressing any natural magnetic fields present. It is therefore to be expected that, while the sample does enter a ferromagnetic groundstate below Tc, no global magnetisation is present and both possible domain directions develop equally. In contrast in XMCD experiments the sample is cooled in an external magnetic field and the remanent magnetisation is probed in an almost fully polarised state. In the standard derivation of mean field theory, the equilibrium state is derived as the self-sustaining magnetisation caused by the neighbouring ensemble of spins, when taking the limit of the ex-

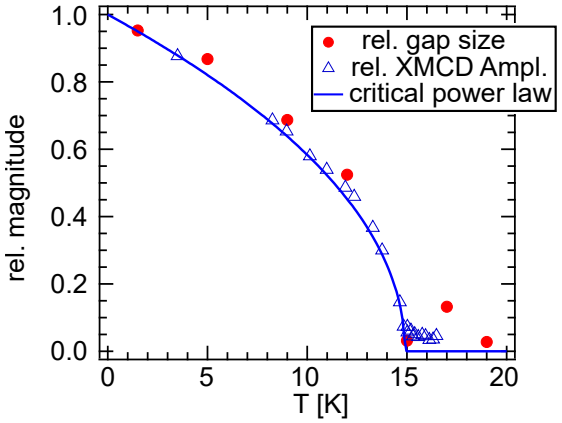

Figure 7.8.: Temperature dependent behaviour of Δ_g, remanent magnetisation and the adjusted power law. All experimental data is scaled to the power law at the lowest available temperature point and shows an overall agreement between magnetic properties and the magnetic gap opening.

ternal field going to zero [52]. As the in-plane superexchange-coupling in $MnBi_2Te_4$ is dominant for the nearest neighbour case [28], it can be assumed that the local order parameter in a magnetic domain of the 2d magnetic surface does not significantly differ from the one in the pre-magnetised case. After establishing this link, the results of this chapter furthermore imply that the size of the magnetic domains are large enough to fully break TRS locally for the TSS, and the typical length scale of a magnetic domain is larger than the coherence length of the TSS. Comparing this system to the closely related cases of Bi_2Te_3 with a coherence length of the TSS in the order of 260 nm [216] and $MnBi_2Te_4$ with a typical lateral domain size of several µm implies, that these conclusions can be reasonably met by the chosen material combination.

8. Discussion

This thesis brings together two research fields, which have both posed intriguing fundamental questions in the recent years: The field of magnetic topological insulators around the primary question how magnetism can be introduced in topological materials[16] and the field of 2D magnetism aiming to find ultra thin stable magnetic materials[56]. In three main parts, the thesis describes the growth of magnetic topological heterostructures by molecular beam epitaxy (MBE), the magnetic properties of the surface, and the interplay between the topological surface state (TSS) and the emerging magnetism. The samples under question are heterosystems of Bi_2Te_3 terminated by a single layer of the intrinsic magnetic TI $MnBi_2Te_4$ as well as more complex systems involving the layered ferromagnet Fe_3GeTe_2. In the $MnBi_2Te_4$ surface layer, stable two-dimensional ferromagnetism is found, which induces a large magnetic gap in the otherwise gapless TSS.

The MBE growth mechanisms employed in the fabrication process consist of a mixture of co-evaporation and surface modification techniques. For the growth of thick films of $MnBi_2Te_4$ a mechanism of coevaporation has been established using binary precursors and the highest film quality occurs close to the growth cutoff at 300 °C. Furthermore, fabricating a single SL of $MnBi_2Te_4$ on top of the 3D TI Bi_2Te_3 has been found to be feasible by evaporation of MnTe on the Bi_2Te_3 surface and subsequent annealing. Typically, the growth of van der Waals materials and in particular materials of the Bi_2Te_3 family by MBE results in the formation of large stepped pyramidal islands[181]. While in this way a film with a high crystalline and surface quality can be achieved, the growth of a precise number of layers is difficult to control. Findings in the course of this work show, that in the very thin film limit the fluctuation in layer height decreases. Nevertheless, creating a single layer thickness for a well defined topological state as e.g. proposed for thin $MnBi_2Te_4$ films[31] remains elusive. A certain contribution of ± 1 QL has even been found in the case of samples with a thickness of 5 QL and a precise layer number could only be achieved for the growth of one or two SL. In this regard, the surface modification by MnTe evaporation and annealing has proven to be highly successful. It allows for the creation of an uniform surface termination with a single SL of $MnBi_2Te_4$ and negligible defect contributions and therefore makes the magnetic state of the sample largely insensitive to small fluctuations in the thickness of the Bi_2Te_3 epilayer. This allows for the growth of atomically precise heterostructures and has the potential to

open a playing-field to study the topology-magnetism interplay in depth in more complex structures.

The fundamental novelty in this work is the reliable observation of a magnetic exchange gap in the topological surface state of a 3D TI by the use of the ferromagnetic extension approach [47,48], together with the observation, that a single SL of $MnBi_2Te_4$ indeed hosts a ferromagnetic ground state. The use of a 2D magnet at the surface shows, that a local magnetic polarisation interacting with the topological surface state indeed suffices in introducing a sizeable magnetic gap in the TSS and no global magnetisation of the sample is required, well in line with initial predictions [9].

By following the magnetism of $MnBi_2Te_4$ from the surface of a bulk crystal over thin films down to the monolayer limit as shown in chapter 6, it is possible to observe, that the inherently layered nature of the magnetism with a pronounced in-plane coupling is a key ingredient in order to allow for stable 2D magnetism in a single SL of $MnBi_2Te_4$. The uniaxial anisotropy along the surface normal furthermore stabilizes this ferromagnetic order and enables its existence even in the monolayer limit. The anisotropy energy is estimated to $\sim 0.11\,\mathrm{meV}$ and is significantly smaller then in other 2D magnets such as Fe_3GeTe_2 [197,198], which might contribute to the comparably low critical temperature of the monolayer. Using the temperature and field dependent magnetisation and the evaluation with a modified Arrott-Noakes plot allows to determine the critical coefficients of a single SL of the heterosystem to be $\beta = 0.484$ and $\gamma = 1.52$. Interestingly, the coefficients do not indicate a change in dimensionality when approaching the two-dimensional limit but compare well to results on bulk $MnBi_2Te_4$ [201]. The coefficients observed for the phase transition in the two-dimensional case do not reflect the 2D Ising model as potentially imposed by the uniaxial anisotropy. The cause of this discrepancy is unclear, but indicates, that the magnetic interaction within the single SL plane might deviate from the simple picture of a next-nearest neighbour coupled Ising model. One proposal made in this regard stems from the implications of the interaction between TSS and magnetic moments on the latter. Theoretically, this interplay introduces a Dzyaloshinskii-Moriya interaction (DMI), which can mediate an additional magnetic interaction in the surface region [200]. Consequently, the structures investigated in this work exhibit a well suited model system to study this interplay. Burying the layer of $MnBi_2Te_4$ in the centre of a structure can pose a way to study the evolution of the magnetic properties, when gradually decreasing the interaction between TSS and the Mn layer by an increase in spatial separation. First findings in this regard indeed indicate a weakening of the magnetic properties and especially a lower critical temperature for the buried SL, but a more profound structural analysis will be required to clearly assign a reason to this effect.

In the ferromagnetic extension approach, the coupling between TSS and magnetism is enlarged by the use of a magnetic surface layer, which is structurally very similar to the underlying 3D TI, resulting in the reversible opening of a large gap in the TSS. The size of the magnetically induced gap of ~ 35 meV corresponds to a temperature scale of ~ 406 K and effectively eliminates thermal excitations as a limiting factor for the observation of a quantized conductance. The size of the gap furthermore confirms the strong coupling between TSS and magnetic order, as the size of the gap would correspond to an external magnetic field with a lower limit of $B > 3.56\,\mathrm{T}$.[1] The results thus show, that the approach has the strong potential to overcome the fundamental limitations which are still present in other surface modification systems such as δ-doped TI [19]. If the Fermi level is tuned into the magnetic gap over the full scale of a device, the ferromagnetic extension approach might enable the occurrence of a quantum anomalous Hall effect (QAHE) up to the critical temperature of the surface layer. Within the frame of ongoing collaborations, efforts are taken to observe a quantized Hall conductance and test the potential of this approach. Next to the established growth mechanisms, these experiments strongly benefit from the insulating surface capping and contacting techniques developed in this work. The starting point for such a transport experiment could be a Bi_2Te_3 film, with both surfaces terminated by a ferromagnetically extended surface, e.g. a single SL of $MnBi_2Te_4$. Due to the n-type character of the films, an appropriate gating and structuring process has to be employed. If a sample under these conditions enables the observation of a stable QAH effect, the system at hand can be utilized to study its evolution as a function of sample thickness and more general device geometry and layer structure. In this regard, the MBE process grants a large amount of flexibility in the design of heterostructures especially along the out-of-plane direction and interfaces to other functional materials can be grown in situ.

One main advantage of the surface magnetic approach over bulk magnetic TI is the fact that for a sufficient layer thickness in a device with two magnetic surfaces, the two magnetic layers may be decoupled and the magnetisation can be controlled individually for the top and bottom surface. In the past, plenty of approaches have been taken, trying to enable an individual switching of top and bottom surface in the presence of an external field. These approaches range from the use of different doping species, aiming to achieve differing coercive fields at the surfaces [81] up to building heterostructures between different magnetic materials, introducing an exchange bias to the mag-

[1] This estimate is derived from the spacing of Landau levels in Dirac like states of $\Delta = v_F\,(2eB\hbar)^{1/2}$ with the Fermi velocity of the TSS v_F. Quantum-transport experiments in an external magnetic field have shown, that the relation tends to strongly overestimate the gap size due to inhomogeneities [217,218], indicating that the actual equivalent external field might be substantially higher. The equation furthermore poses the question, whether the slim shape of the TSS with a high group velocity in the $MnBi_2Te_4$-Bi_2Te_3 heterostructure might be beneficial for the appearance of a large magnetic gap.

netic layers [86,219]. The interface coupling found in this thesis at the interface between $MnBi_2Te_4$ and Fe_3GeTe_2 describes one of the possibilities of building such a structure, where the bottom magnetic layer is pinned by the substrate magnetisation, while the surface layer may be switched freely. In previous works on van der Waals heterostructures both positive and negative exchange bias effects have been observed [219–221]. The main novelty of the findings in this thesis however is the size of the effect. Contrary to the attempts using exfoliated flakes, the growth by MBE allows for a more direct and well oriented interface. Given the crucial dependence of the coupling on the wave function overlap and therefore the size of the van der Waals gap, the heterostructures presented in this thesis exhibit a coupling between film and substrate, whose spin-flop field of (1.261 ± 0.010) T strongly exceeds the previous observations of an exchange bias of ~ 50 mT to 100 mT [86,219]. The strength of the coupling goes beyond the idea of exchange bias towards the concept of synthetic antiferromagnetism [185] and furthermore allows to stabilize a remanent sample magnetisation far beyond the critical temperature of the isolated SL.

The findings of the coupling to ferromagnetic substrates allow to think of further, more complex heterostructures, where the magnetisation at top and bottom surface is manipulated individually and prospects such as a layer Hall effect and switchable zero plateau Hall phases me be realized [14,31]. While Fe_3GeTe_2 is a problematic choice in this regard due to its metallic character, the closely related semiconducting ferromagnet $Cr_2Ge_2Te_6$ is a suitable candidate for further transport experiments. Studies on this material combination are part of ongoing projects and have already shown the feasibility of using $Cr_2Ge_2Te_6$ as a substrate for the growth.

In the initial proposal of the ferromagnetic extension approach, the heterostructures Bi_2Te_3-$MnBi_2Te_4$ and $GeBi_2Te_4$-$MnBi_2Te_4$ were named as specific material combinations [47,48]. The limitation of these proposals however is the relatively low critical temperature observed in $MnBi_2Te_4$, especially in the monolayer limit. Trying to overcome this limitation hosts several obstacles, mainly related to the choice of materials. The combination Bi_2Te_3-$MnBi_2Te_4$ is special as such, as it combines two materials, with an identical surface symmetry and lattice constant. Even the termination of the individual van der Waals layers is identical for both. Furthermore $MnBi_2Te_4$ is known to be an intrinsic magnetic TI in its bulk form, such that when combined, the topological boundary is shifted from the Bi_2Te_3–$MnBi_2Te_4$ interface to the surface of the respective heterosystem. The number of known 2D magnets in literature has significantly increased in the recent years and materials such as CrI_3 and Fe_3GeTe_2 have been found to achieve comparably high critical temperatures even in the monolayer limit [97,204,222]. In order to allow the TSS to extend into the surface modification and

especially to potentially observe a quantized Hall conductance, an insulating or semiconducting band gap in the chosen TI as well as in the surface magnetic layer and a sufficiently good band matching is another necessary condition, further narrowing down the range of available materials. At the present point $MnBi_2Te_4$ and the sister-compound $MnSb_2Te_4$ have been at the centre of the research on intrinsic magnetic TI [28,223], such that the choice of materials at the present point is strongly limited and the search for novel higher T_c intrinsic magnetic TI poses a highly intriguing research field.

Lastly, similar to the use of Sb to pin the Fermi level to the Dirac point in V-doped $(Bi,Sb)_2Te_3$ [224], the existence of both $MnBi_2Te_4$ and its sister compound $MnSb_2Te_4$ raises the idea, that in a similar way, the n-type character of the heterostructures in this thesis might be compensated. While the direct partial substitution of Bi with Sb has proven to be ill suited due to a strongly increased amount of disorder at the then quaternary surface, the growth of heterostructures with a Sb_2Te_3 -Bi_2Te_3 p-n junction are part of ongoing investigations. Applying the surface modification approach to the BT terminated surface – e.g. creating heterostructures of the type Sb_2Te_3 – Bi_2Te_3 – 1 SL $MnBi_2Te_4$ with a decreasing thickness of Bi_2Te_3 – of this junction allows to influence the position of the Fermi level up to the surface. The surface still exhibits stable ferromagnetic order and the critical temperature was even found to increase by ~ 14 % upon p-doping, as summarised in [225].

During the course of this thesis the field of intrinsic magnetic topological insulators has strongly evolved. Starting off with the discovery of $MnBi_2Te_4$, the family of these compounds has grown, containing e.g. $MnBi_4Te_7$, $MnBi_6Te_{10}$, $MnBi_8Te_{13}$, as well as the Sb based $MnSb_2Te_4$ compounds [141,178,223]. Especially the materials with larger spacing between the individual magnetic layers and later the presented ferromagnetic extension approach have finally led to the observation of a clear magnetic fingerprint, manifesting as a gap in the topological surface state which can be observed by the direct probe of photoemission spectroscopy [46,120]. Showing, that these materials indeed allow to overcome previous limitations in sample quality and order gives strong impulses to utilize these materials both in the context of fundamental research as well as in the field of spintronics. As outlined in the previous discussion, the flexibility given by the fabrication via MBE leaves plenty of open questions, which can be addressed by the growth of more complex functional heterostructures and may give substantial insights into the peculiarities of magnetic TI.

A. Appendix

This chapter aims to be a collection of supplementary information and additional data, that did not find their place in the main text. It contains notes on the evaluation of data as presented in this work and code used for simulations in order to allow to comprehend the results presented in the main text, as well as a more detailed documentation of the main experimental setup. The chapter will start with a collection of conventions and notations used in this work, followed by a profound explanation of models employed in this work as well as additional experimental data.

A.1. Notations and Conventions

In the course of this thesis a lot of methods and topics occur, for which naturally a set of different units, evaluation methods and definitions have to be applied. The following list is aiming to help in interpreting the notations used in this work.

MBE Growth

In the description of MBE processes, all temperatures are given in °C as the respective thermocouple reading and are prone to an experiment specific offset. Beam-flux values are determined as beam equivalent pressure (BEP) and are measured using a Bayert-Alpert pressure gauge as averaged $P_{open} - P_{res}$ in mbar. The precise process of acquisition is shown in Fig. A.1e)

For the growth of Bi_2Te_3 and $MnBi_2Te_4$ this thesis uses the notations of QL (quintuple layer) and SL (septuple layer) to denote a single building block with 5/7 atoms thickness, separated by van der Waals gaps in contrast to the notation of an unit cell, which in both cases consists out of three of these blocks.

The difference in lattice constants is an important quantity in MBE growth, especially concerning the in-plane lattice constants. The relevant quantity here is defined as lattice mismatch and defined as

$$f = 100\,\% \cdot \frac{a_s - a}{a} \text{ [115]} \tag{A.1}$$

with a_s and a as lattice constants of substrate and overlayer and by convention defined in percent.

X-ray Diffraction

All atomic length scales in this thesis are given in nm. By convention, all scattering vectors calculated from XRD experiments will be denoted in $Å^{-1}$.Here the k_z direction is defined along the surface normal of the sample, k_x corresponds to the in-plane direction in the experimental plane opened by the impinging beam and the surface normal and k_y denotes the scattering vector perpendicular to the experimental plane.

XAS and XMCD

The base units in XAS-measurements are negative currents. The XAS signal is defined as sample-current divided by a reference current, typically from a gold mesh, the corresponding quantity is positive and unit less. Typically XAS signals are normalised on a flat region before the absorption edge, a linear slope and offset are removed and afterwards the step over the entire edge is again normalised to one. In this thesis this is applied wherever applicable. As for $MnBi_2Te_4$a strong contribution from the Te absoption edge is still influencing the general shape of the background at the Mn $L_{3,2}$ position, for Mn edges only a simple normalisation is applied.
XMCD signals in this work are defined by convention as I_{c-} - I_{c+}, such that an alignment of the spins-polarisation with a positive external field will result in a negative XMCD signal. This quantity is given in arbitrary units. The magnitude of the XMCD effect is straightforward defined as the XMCD asymmetry, as $\frac{I_{c-}-I_{c+}}{I_{c-}+I_{c+}}$. When using sum-rules to determine the local spin-moment, XMCD amplitudes are given in units of μ_B/atom.

Photoemission

Photoemission intensities are given in arbitrary units, as the detection mode does not facilitate a true proportionality counter. Spin-resolved measurements are acquired using a proportionality counter and can therefore be given in abolute counts, errors follow from a Poisson-distribution in this case. Energy scales are given as E-E_F in eV, the wave vectors $\vec{k}$ are denoted in $Å^{-1}$. By convention k_x is always defined in the plane of light incidence, k_y in the respective perpendicular in-plane direction.

A.2. Design and Concept of the MBE chamber

The MBE chamber as depicted in Fig. 4.5 was custom designed and set up in the course of this thesis and is specialised on the growth of Te based compounds. Next to the

layout shown in Fig. 4.5, the following will contain a more detailed documentation of the equipment and design of the system. The system is to date equiped with:

- Multiple ports for Knudsen evaporation cells. This includes two large CF-63 mid temperature cells for the evaporation of Bi_2Te_3 and Te, three CF-40 Knudsen cells filled with Tm, MnTe and Sb_2Te_3 as well as one high-temperature cell for the evaporation of BaF_2. All cells are water-cooled and controlled by individual PID-controllers. Each PID is then again integrated into the custom-developed control software. The cells are equipped with individual shutters, which can also be controlled remotely.

- Growth diagnosis mainly includes a retractable beam flux monitor mounted slightly below the sample position as well as a RHEED system (Dr. Gassler 30 kV RHEED system with beam rocking and deflection). The beam flux monitor uses a Bayert-Alpert ion gauge with back-shielding to protect the sample surface during measurements and can be used to measure partial beam pressures at the sample position. The RHEED system is used to probe the sample surface and the resulting diffraction pattern is subsequently imaged by a phosphorescent screen.

- The sample deposition stage (Fig. 4.5 c), main text) is a custom design to allow for a maximal amount of temperature stability as well as for the simultaneous deposition on two substrates under identical conditions. The head is made from molybdenum and uses a high-temperature heater cartridge (heat-wave-labs, model 101136) heating the head from the inside. The temperature is read by a K-type thermocouple mounted on the back of the sample drawer. The design of the fully enclosed heating capsule is chosen such that the offset and time delay of the temperature reading to the sample temperature are minimized as compared to radiative or electron-beam heated systems.

In order to monitor and partially automatise deposition processes at the chamber, the lab control software *Pillalab* was developed in parallel to setting up the system. Fig. A.1 shows the main functionalities and design approach for the software. The program was designed in Python and is written in a fully modular fashion to allow for the adaption to various systems. The core of the system is the main control file subsequently importing a set of hardware drivers as well as user interfaces. Each user interface has access to a set of methods provided by the core allowing it to operate all connected hardware. The user interfaces are created using Page [226] in the Tkinter framework. The software furthermore allows for the import and execution of scripts used to automatise growth processes.

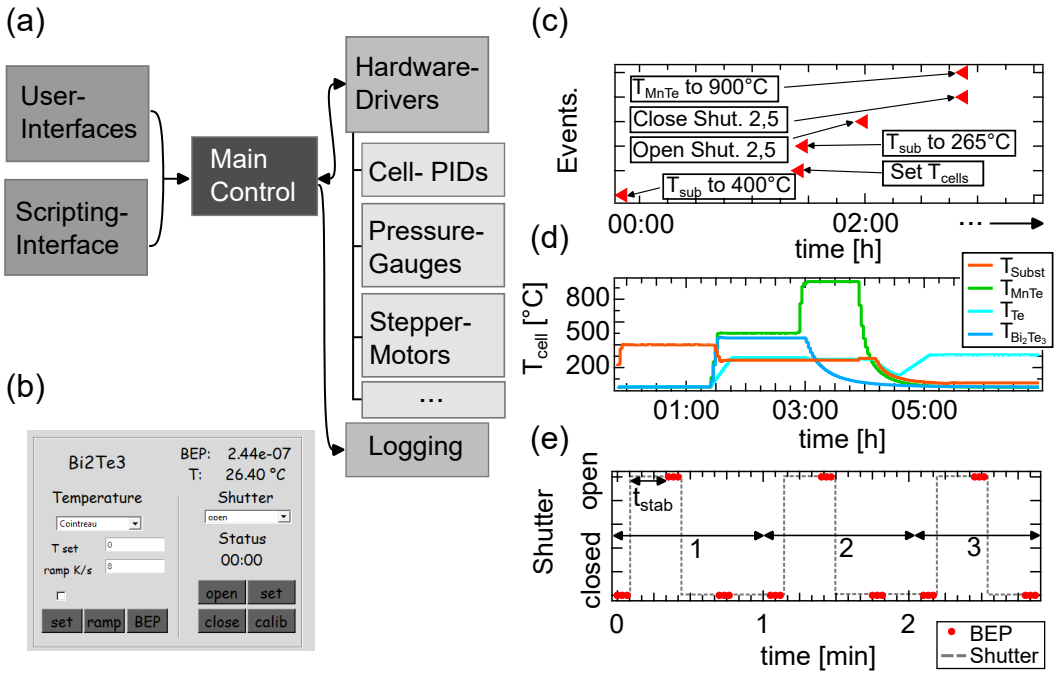

Figure A.1.: Concept and functions of the custom-developed MBE control software. a) Modular software concept. Interfaces and hardware-drivers are imported into to core module to enable adaption of the software to different use-cases. b) Single cell control panel, allowing to control temperature and shutters. c) System-log during a growth project tracking all commands issued with timestamps. d) Cell temperature log during a thin-film growth. e) Cycle of a BEP-measurement. The grey-dashed lines indicate the shutter state, the red markers are points of measurement. The BEP is calculated by averaging over three open and close cycles.

The communication with the hardware is realized via serial ports and includes communication with the PID-controllers for the individual cells, all pressure gauges as well as a set of stepper-motors used for operating the cell shutters. An exemplary element of the user interface is shown in Fig. A.1b). The software is further equipped with a logging function, logging all system parameters during a deposition process into a *hdf5* file format. An example log is shown in c,d) showing the logging of events during the growth process, as well as the continuous observation of sample and cell temperatures. Fig. A.1e) depicts the scheme in which beam equivalent pressures are acquired. To reach a high accuracy of the measurement, each measurement includes three measurement cycles of open and closed shutter states. The individual measurement points are shown in red after the respective equilibration times. The BEP is calculated as the statistical average of open and closed states for each cycle, averaged over all cycles, where the statistical error of the outer average can be seen as a measure for flux stability.

A.3. Magnetic Heterostructures

The description in terms of equations used to model the heterostructures consisting of a single SL of $MnBi_2Te_4$ on the ferromagnetic substrate Fe_3GeTe_2 can be found in chapter 6.3. The model was implemented using *python* with the widely used numerical handling package *numpy*. The code below was optimized for *python v.3.7.2*.

```
import numpy as np
def toplayer_magnetisation(Baxis,msubst,J,T):
        '''
                Baxis: magnetic field axis used for the model
                msubst: pre-determined magnetisation of the substrate
                J: coupling constant
                T: thermal energy scale
        '''
    results = np.zeros(len(msubst))
    for i in range(len(results)):
        # fraction of substrate domains with up-spin
        pup = 1 - ((1 - msubst[i])/2)
        # fraction of substrate domains with down-spin
        pdown = ((1 - msubst[i])/2)

        # average film m on up domain
        exp1 = (np.exp(((Baxis[i]-J)/T)) - np.exp(-((Baxis[i]-J)/T)))
                /(np.exp(((Baxis[i]-J)/T)) + np.exp(-((Baxis[i]-J)/T)))
        # average film m on down domain
        exp2 = (np.exp(((Baxis[i]+J)/T)) - np.exp(-((Baxis[i]+J)/T)))
                /(np.exp(((Baxis[i]+J)/T)) + np.exp(-((Baxis[i]+J)/T)))
        results[i] = pup * exp1 + pdown * exp2
    return results
```

All energyscales in the model are given relative to the temperature scale $k_B T$, giving a free choice on how to adapt the model to fit to the experimental findings. In this regard, the magnetic field axis is fixed to the experimental findings by defining the substrate hysteresis to match the experiment with a linear slope and hysteresis opening at $B = 0.4$. In a second step the coupling constant J can be adapted to match the spin flop fields observed in the heterostructures.

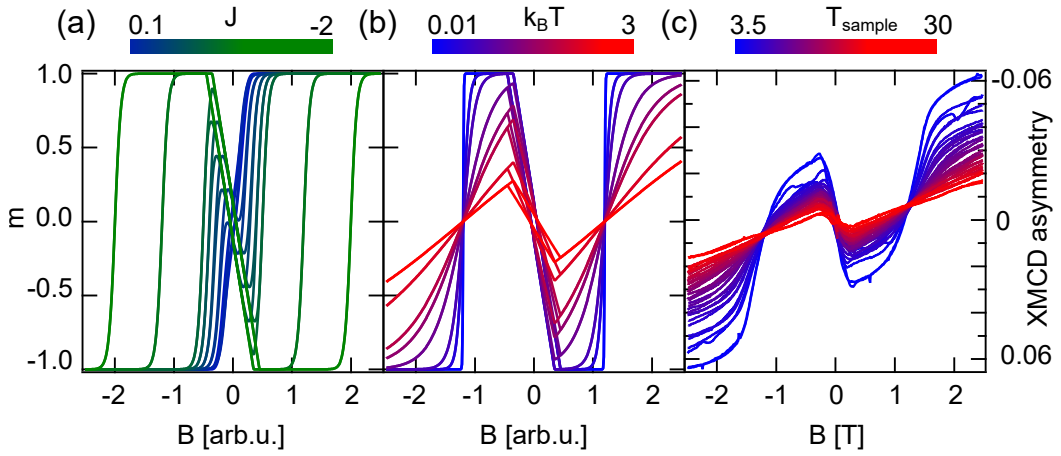

Figure A.2.: Systematics of the coupling model. a) J-dependent magnetisation of the top layer for J ranging from the ferromagnetic case of 0.1 up to the antiferromagnetic case of -2 for T = 0.1. b) Temperature dependent behaviour of the simulation for the case of J = -1.2. The curves reflect a transition from a clear spin flop field to a linear behaviour with a step in the centre. c) Experimental temperature dependence of the Mn magnetisation in the n = 0 heterostructure. The occurrence of a spin flop transition is clearly visible in both graphs.

As apparent from Fig. A.2a), a variation of J results in a change of the spin flop field, where the condition $m = 0$ is met in the case of $J = B$. For the structures with n = 0 and 1, J is estimated to -1.2 and -0.4, while the shape of the ferromagnetic n = 2 case is matched for $J = 0.5$. The model further allows to study the temperature dependence of the magnetisation in more detail. Fig. A.2b) depicts magnetisation simulations for the case of $J = 1.2$ next to the experimentally observed field dependent XMCD asymmetry in Fig. A.2c). The simulation can nicely follow the experimental observations. It especially allows to identify the crossing points of all curves as the position of the spin-flop field. Furthermore both show the transition from a shape with multiple plateaus and sharp transitions to a linear behaviour with a step in the region of the substrate hysteresis.

Fig. A.3 depicts an analysis of the magnetic state in the n = 0 heterostructure, when the external magnetic field is applied 60° away from the surface normal. The geometry is chosen such, that the light incidence is parallel to the external field, probing the polarisation along the same axis. Both, the Mn as well as Fe XMCD b,c) show a sizeable XMCD signal, under an applied field of 6 T. The sign of the XMCD corresponds to an alignment of the magnetisation with the external magnetic field. Contrary to the findings in chapter 6.3, when lowering the external magnetic field to B = 0.3 T, the magnetisation in both species significantly decreases but no reversal can be observed. The strong decay of the Fe magnetisation mainly reflects the strong uniaxial anisotropy of

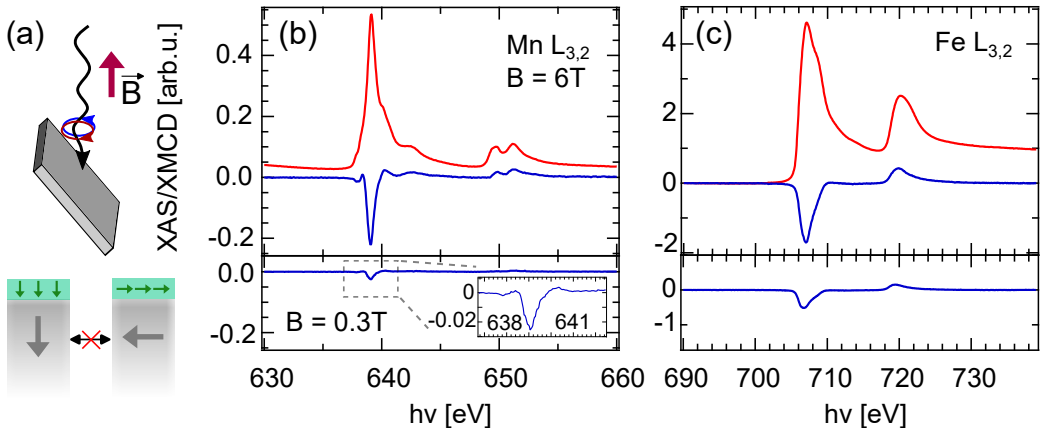

Figure A.3.: Grazing incidence XAS and XMCD of the n = 1 heterostructure. a) Sketch of the sample geometry with the field applied along the incident light axis and the sample surface normal tilted away by 60°. The lower panel depicts the two possible coupling arrangements. b) Mn XAS (red) and XMCD (blue) for a field of 6 T depicting a large XMCD and an alignment of the Mn spin polarisation with the external field. The lower panel depicts the XMCD for B = 0.3 T. c) Fe XAS and XMCD under identical conditions to b).

Fe_3GeTe_2. The absence of a sign reversal in the Mn species furthermore highlights, that the antiferromagnetic coupling path found along the surface normal exhibits a strongly anisotropic behaviour as well and strongly decays for an in-plane spin orientation.

Bibliography

[1] K. v. Klitzing, G. Dorda and M. Pepper. New method for high-accuracy determination of the fine-structure constant based on quantized Hall resistance. *Phys. Rev. Lett.*, **45**, 6, 494 (1980). doi: 10.1103/physrevlett.45.494.

[2] D. J. Thouless, M. Kohmoto, M. P. Nightingale and M. den Nijs. Quantized Hall conductance in a two-dimensional periodic potential. *Phys. Rev. Lett.*, **49**, 6, 405 (1982). doi: 10.1103/physrevlett.49.405.

[3] M. König, S. Wiedmann, C. Brüne, A. Roth, H. Buhmann, L. W. Molenkamp, X.-L. Qi and S.-C. Zhang. Quantum spin hall insulator state in HgTe quantum wells. *Science*, **318**, 5851, 766 (2007). doi: 10.1126/science.1148047.

[4] C. L. Kane and E. J. Mele. Quantum spin Hall effect in graphene. *Phys. Rev. Lett.*, **95**, 22, 226801 (2005). doi: 10.1103/physrevlett.95.226801.

[5] B. A. Bernevig, T. L. Hughes and S.-C. Zhang. Quantum spin Hall effect and topological phase transition in HgTe quantum wells. *Science*, **314**, 5806, 1757 (2006). doi: 10.1126/science.1133734.

[6] L. Fu. Topological crystalline insulators. *Phys. Rev. Lett.*, **106**, 10, 106802 (2011). doi: 10.1103/physrevlett.106.106802.

[7] M. Ünzelmann, H. Bentmann, T. Figgemeier, P. Eck, J. N. Neu, B. Geldiyev, F. Diekmann, S. Rohlf, J. Buck, M. Hoesch, M. Kalläne, K. Rossnagel, R. Thomale, T. Siegrist, G. Sangiovanni, D. D. Sante and F. Reinert. Momentum-space signatures of Berry flux monopoles in the Weyl semimetal TaAs. *Nat. Commun.*, **12**, 1 (2021). doi: 10.1038/s41467-021-23727-3.

[8] X. L. Qi, T. L. Hughes and S. C. Zhang. Topological field theory of time-reversal invariant insulators. *Phys. Rev. B*, **78**, 19 (2008). doi: 10.1103/PhysRevB.78.195424.

[9] X. L. Qi and S. C. Zhang. Topological insulators and superconductors. *Rev. Mod. Phys.*, **83**, 4 (2011). doi: 10.1103/RevModPhys.83.1057.

[10] R. Yu, W. Zhang, H.-J. Zhang, S.-C. Zhang, X. Dai and Z. Fang. Quantized anomalous Hall effect in magnetic topological insulators. *Science*, **329**, 5987, 61 (2010). doi: 10.1126/science.1187485.

[11] B. A. Bernevig, C. Felser and H. Beidenkopf. Progress and prospects in magnetic topological materials. *Nature*, **603**, 7899, 41 (2022). doi: 10.1038/s41586-021-04105-x.

[12] C. Z. Chang, J. Zhang, X. Feng, J. Shen, Z. Zhang, M. Guo, K. Li, Y. Ou, P. Wei, L. L. Wang, Z. Q. Ji, Y. Feng, S. Ji, X. Chen, J. Jia, X. Dai, Z. Fang, S. C. Zhang, K. He, Y. Wang, L. Lu, X. C. Ma and Q. K. Xue. Experimental observation of the quantum anomalous Hall effect in a magnetic topological insulator. *Science*, **340**, 6129, 167 (2013). doi: 10.1126/science.1234414.

[13] N. P. Armitage and L. Wu. On the matter of topological insulators as magnetoelectric. *Scipost Phys*, **6**, 4 (2019). doi: 10.21468/SciPostPhys.6.4.046.

[14] A. Gao, Y.-F. Liu, C. Hu, J.-X. Qiu, C. Tzschaschel, B. Ghosh, S.-C. Ho, D. Bérubé, R. Chen, H. Sun, Z. Zhang, X.-Y. Zhang, Y.-X. Wang, N. Wang, Z. Huang, C. Felser, A. Agarwal, T. Ding, H.-J. Tien, A. Akey, J. Gardener, B. Singh, K. Watanabe, T. Taniguchi, K. S. Burch, D. C. Bell, B. B. Zhou, W. Gao, H.-Z. Lu, A. Bansil, H. Lin, T.-R. Chang, L. Fu, Q. Ma, N. Ni and S.-Y. Xu. Layer Hall effect in a 2D topological axion antiferromagnet. *Nature*, **595**, 7868, 521 (2021). doi: 10.1038/s41586-021-03679-w.

[15] L. Šmejkal, Y. Mokrousov, B. Yan and A. H. MacDonald. Topological antiferromagnetic spintronics. *Nat. Phys.*, **14**, 3, 242 (2018). doi: 10.1038/s41567-018-0064-5.

[16] J. Y. Liu and T. Hesjedal. Magnetic topological insulator heterostructures: A review. *Adv. Mater.* (2021). doi: 10.1002/adma.202102427.

[17] C. Z. Chang, W. Zhao, D. Y. Kim, H. Zhang, B. A. Assaf, D. Heiman, S. C. Zhang, C. Liu, M. H. Chan and J. S. Moodera. High-precision realization of robust quantum anomalous Hall state in a hard ferromagnetic topological insulator. *Nat. Mater.*, **14**, 5, 473 (2015). doi: 10.1038/nmat4204.

[18] M. Mogi, M. Kawamura, R. Yoshimi, A. Tsukazaki, Y. Kozuka, N. Shirakawa, K. S. Takahashi, M. Kawasaki and Y. Tokura. A magnetic heterostructure of topological insulators as a candidate for an axion insulator. *Nat. Mater.*, **16**, 5, 516 (2017). doi: 10.1038/nmat4855.

[19] M. Mogi, R. Yoshimi, A. Tsukazaki, K. Yasuda, Y. Kozuka, K. S. Takahashi, M. Kawasaki and Y. Tokura. Magnetic modulation doping in topological insulators toward higher-temperature quantum anomalous Hall effect. *Appl. Phys. Lett.*, **107**, 18 (2015). doi: 10.1063/1.4935075.

[20] D. Xiao, J. Jiang, J.-H. Shin, W. Wang, F. Wang, Y.-F. Zhao, C. Liu, W. Wu, M. H. Chan, N. Samarth and C.-Z. Chang. Realization of the axion insulator state in quantum anomalous Hall sandwich heterostructures. *Phys. Rev. Lett.*, **120**, 5, 056801 (2018). doi: 10.1103/physrevlett.120.056801.

[21] S. Grauer, S. Schreyeck, M. Winnerlein, K. Brunner, C. Gould and L. W. Molenkamp. Coincidence of superparamagnetism and perfect quantization in the quantum anomalous Hall state. *Phys. Rev. B*, **92**, 20 (2015). doi: 10.1103/PhysRevB.92.201304.

[22] C. I. Fornari, H. Bentmann, S. L. Morelhão, T. R. F. Peixoto, P. H. O. Rappl, A.-V. Tcakaev, V. Zabolotnyy, M. Kamp, T.-L. Lee, C.-H. Min, P. Kagerer, R. C. Vidal, A. Isaeva, M. Ruck, V. Hinkov, F. Reinert and E. Abramof. Incorporation of europium in Bi_2Te_3 topological insulator epitaxial films. *J. Phys. Chem. C*, **124**, 29, 16048 (2020). doi: 10.1021/acs.jpcc.0c05077.

[23] A. Tcakaev, V. B. Zabolotnyy, C. I. Fornari, P. Rüßmann, T. R. F. Peixoto, F. Stier, M. Dettbarn, P. Kagerer, E. Weschke, E. Schierle, P. Bencok, P. H. O. Rappl, E. Abramof, H. Bentmann, E. Goering, F. Reinert and V. Hinkov. Incipient antiferromagnetism in the Eu-doped topological insulator Bi_2Te_3. *Phys. Rev. B*, **102**, 18, 184401 (2020). doi: 10.1103/physrevb.102.184401.

[24] T. R. F. Peixoto, H. Bentmann, P. Russmann, A. V. Tcakaev, M. Winnerlein, S. Schreyeck, S. Schatz, R. C. Vidal, F. Stier, V. Zabolotnyy, R. J. Green, C. H. Min, C. I. Fornari, H. Maass, H. B. Vasili, P. Gargiani, M. Valvidares, A. Barla, J. Buck, M. Hoesch, F. Diekmann, S. Rohlf, M. Kallane, K. Rossnagel, C. Gould, K. Brunner, S. Blugel, V. Hinkov, L. W. Molenkamp and F. Reinert. Non-local effect of impurity states on the exchange coupling mechanism in magnetic topological insulators. *npj Quantum Mater.*, **5**, 1, 1 (2020). doi: 10.1038/s41535-020-00288-0.

[25] K. M. Fijalkowski, N. Liu, P. Mandal, S. Schreyeck, K. Brunner, C. Gould and L. W. Molenkamp. Quantum anomalous Hall edge channels survive up to the Curie temperature. *Nat. Commun.*, **12**, 1, 5599 (2021). doi: 10.1038/s41467-021-25912-w.

[26] K. N. Gordon, H. Sun, C. Hu, A. G. Linn, H. Li, Y. Liu, P. Liu, S. Mackey, Q. Liu, N. Ni and D. Dessau. Strongly gapped topological surface states on protected surfaces of antiferromagnetic $MnBi_4Te_7$ and $MnBi_6Te_{10}$ (2019). doi: 10.48550/arXiv.1910.13943.

[27] E. Golias, E. Weschke, T. Flanagan, E. Schierle, A. Richardella, E. D. L. Rienks, P. S. Mandal, A. Varykhalov, J. Sánchez-Barriga, F. Radu, N. Samarth and O. Rader. Magnetization relaxation and search for the magnetic gap in bulk-insulating V-doped (Bi, Sb)$_2$Te$_3$. *Appl. Phys. Lett.*, **119**, 13 (2021). doi: 10.1063/5.0070557.

[28] M. M. Otrokov, I. I. Klimovskikh, H. Bentmann, D. Estyunin, A. Zeugner, Z. S. Aliev, S. Gass, A. U. B. Wolter, A. V. Koroleva, A. M. Shikin, M. Blanco-Rey, M. Hoffmann, I. P. Rusinov, A. Y. Vyazovskaya, S. V. Eremeev, Y. M. Koroteev, V. M. Kuznetsov, F. Freyse, J. Sanchez-Barriga, I. R. Amiraslanov, M. B. Babanly, N. T. Mamedov, N. A. Abdullayev, V. N. Zverev, A. Alfonsov, V. Kataev, B. Buchner, E. F. Schwier, S. Kumar, A. Kimura, L. Petaccia, G. Di Santo, R. C. Vidal, S. Schatz, K. Kissner, M. Unzelmann, C. H. Min, S. Moser, T. R. F. Peixoto, F. Reinert, A. Ernst, P. M. Echenique, A. Isaeva and E. V. Chulkov. Prediction and observation of an antiferromagnetic topological insulator. *Nature*, **576**, 7787, 416 (2019). doi: 10.1038/s41586-019-1840-9.

[29] J. Li, Y. Li, S. Du, Z. Wang, B.-L. Gu, S.-C. Zhang, K. He, W. Duan and Y. Xu. Intrinsic magnetic topological insulators in van der Waals layered MnBi$_2$Te$_4$-family materials. *Sci. Adv.*, **5**, 6 (2019). doi: 10.1126/sciadv.aaw5685.

[30] R. S. K. Mong, A. M. Essin and J. E. Moore. Antiferromagnetic topological insulators. *Phys. Rev. B*, **81**, 24 (2010). doi: 10.1103/PhysRevB.81.245209.

[31] M. M. Otrokov, I. P. Rusinov, M. Blanco-Rey, M. Hoffmann, A. Y. Vyazovskaya, S. V. Eremeev, A. Ernst, P. M. Echenique, A. Arnau and E. V. Chulkov. Unique thickness-dependent properties of the van der Waals interlayer antiferromagnet MnBi$_2$Te$_4$ films. *Phys. Rev. Lett.*, **122**, 10 (2019). doi: 10.1103/PhysRevLett.122.107202.

[32] S. H. Lee, Y. Zhu, Y. Wang, L. Miao, T. Pillsbury, H. Yi, S. Kempinger, J. Hu, C. A. Heikes, P. Quarterman, W. Ratcliff, J. A. Borchers, H. Zhang, X. Ke, D. Graf, N. Alem, C.-Z. Chang, N. Samarth and Z. Mao. Spin scattering and noncollinear spin structure-induced intrinsic anomalous Hall effect in antiferromagnetic topological insulator MnBi$_2$Te$_4$. *Phys. Rev. Res.*, **1**, 1, 012011 (2019). doi: 10.1103/PhysRevResearch.1.012011.

[33] D. A. Estyunin, I. I. Klimovskikh, A. M. Shikin, E. F. Schwier, M. M. Otrokov, A. Kimura, S. Kumar, S. O. Filnov, Z. S. Aliev, M. B. Babanly and E. V. Chulkov. Signatures of temperature driven antiferromagnetic transition in the electronic structure of topological insulator MnBi$_2$Te$_4$. *APL Mater.*, **8**, 2 (2020). doi: 10.1063/1.5142846.

[34] M. Garnica, M. M. Otrokov, P. C. Aguilar, I. I. Klimovskikh, D. Estyunin, Z. S. Aliev, I. R. Amiraslanov, N. A. Abdullayev, V. N. Zverev, M. B. Babanly, N. T. Mamedov, A. M. Shikin, A. Arnau, A. L. V. de Parga, E. V. Chulkov and R. Miranda. Native point defects and their implications for the Dirac point gap at $MnBi_2Te_4$ (0001). *npj Quantum Mater.*, **7**, 1 (2022). doi: 10.1038/s41535-021-00414-6.

[35] H. Li, S. Y. Gao, S. F. Duan, Y. F. Xu, K. J. Zhu, S. J. Tian, J. C. Gao, W. H. Fan, Z. C. Rao, J. R. Huang, J. J. Li, Y. Yan, Z. T. Liu, W. L. Liu, Y. B. Huang, Y. L. Li, Y. Liu, G. B. Zhang, P. Zhang, T. Kondo, S. Shin, H. C. Lei, Y. G. Shi, W. T. Zhang, H. M. Weng, T. Qian and H. Ding. Dirac surface states in intrinsic magnetic topological insulators $EuSn_2As_2$ and $MnBi_{2n}Te_{3n+1}$. *Phys. Rev. X*, **9**, 4 (2019). doi: 10.1103/PhysRevX.9.041039.

[36] D. Nevola, H. X. Li, J. Q. Yan, R. G. Moore, H. N. Lee, H. Miao and P. D. Johnson. Coexistence of surface ferromagnetism and a gapless topological state in $MnBi_2Te_4$. *Phys. Rev. Lett.*, **125**, 11 (2020). doi: 10.1103/PhysRevLett.125.117205.

[37] P. Swatek, Y. Wu, L. L. Wang, K. Lee, B. Schrunk, J. Q. Yan and A. Kaminski. Gapless Dirac surface states in the antiferromagnetic topological insulator $MnBi_2Te_4$. *Phys. Rev. B*, **101**, 16 (2020). doi: 10.1103/PhysRevB.101.161109.

[38] C. H. Yan, S. Fernandez-Mulligan, R. B. Mei, S. H. Lee, N. Protic, R. Fukumori, B. H. Yan, C. X. Liu, Z. Q. Mao and S. L. Yang. Origins of electronic bands in the antiferromagnetic topological insulator $MnBi_2Te_4$. *Phys. Rev. B*, **104**, 4 (2021). doi: 10.1103/PhysRevB.104.L041102.

[39] A. M. Shikin, D. A. Estyunin, N. L. Zaitsev, D. Glazkova, I. I. Klimovskikh, S. O. Filnov, A. G. Rybkin, E. F. Schwier, S. Kumar, A. Kimura, N. Mamedov, Z. Aliev, M. B. Babanly, K. Kokh, O. E. Tereshchenko, M. M. Otrokov, E. V. Chulkov, K. A. Zvezdin and A. K. Zvezdin. Sample-dependent Dirac-point gap in $MnBi_2Te_4$ and its response to applied surface charge: A combined photoemission and ab initio study. *Phys. Rev. B*, **104**, 11 (2021). doi: 10.1103/PhysRevB.104.115168.

[40] A. M. Shikin, D. A. Estyunin, I. I. Klimovskikh, S. O. Filnov, E. F. Schwier, S. Kumar, K. Miyamoto, T. Okuda, A. Kimura, K. Kuroda, K. Yaji, S. Shin, Y. Takeda, Y. Saitoh, Z. S. Aliev, N. T. Mamedov, I. R. Amiraslanov, M. B. Babanly, M. M. Otrokov, S. V. Eremeev and E. V. Chulkov. Nature of the Dirac gap modulation and surface magnetic interaction in axion antiferromagnetic topological insulator $MnBi_2Te_4$. *Sci Rep-Uk*, **10**, 1 (2020). doi: 10.1038/s41598-020-70089-9.

[41] Y. J. Chen, L. X. Xu, J. H. Li, Y. W. Li, C. F. Zhang, H. Li, Y. Wu, A. J. Liang, C. Chen, S. W. Jung, C. Cacho, H. Y. Wang, Y. H. Mao, S. Liu, M. X. Wang, Y. F. Guo, Y. Xu, Z. K. Liu, L. X. Yang and Y. L. Chen. Topological electronic structure and its temperature evolution in antiferromagnetic topological insulator $MnBi_2Te_4$. *Phys. Rev. X*, **9**, 4, 041040 (2019). doi: 10.1103/PhysRevX.9.041040.

[42] C.-Z. Chang, C.-X. Liu and A. H. MacDonald. *Colloquium* : Quantum anomalous Hall effect. *Rev. Mod. Phys.*, **95**, 1, 011002 (2023). doi: 10.1103/revmodphys.95.011002.

[43] X. Xu, S. Yang, H. Wang, R. Guzman, Y. Gao, Y. Zhu, Y. Peng, Z. Zang, M. Xi, S. Tian, Y. Li, H. Lei, Z. Luo, J. Yang, Y. Wang, T. Xia, W. Zhou, Y. Huang and Y. Ye. Ferromagnetic-antiferromagnetic coexisting ground state and exchange bias effects in $MnBi_4Te_7$ and $MnBi_6Te_{10}$. *Nat. Commun.*, **13**, 1 (2022). doi: 10.1038/s41467-022-35184-7.

[44] A.-V. Tcakaev, B. Rubrecht, J. I. Facio, V. B. Zabolotnyy, L. T. Corredor, L. C. Folkers, E. Kochetkova, T. R. F. Peixoto, P. Kagerer, S. Heinze, H. Bentmann, R. J. Green, P. Gargiani, M. Valvidares, E. Weschke, M. W. Haverkort, F. Reinert, J. van den Brink, B. Büchner, A. U. B. Wolter, A. Isaeva and V. Hinkov. Intermixing-driven surface and bulk ferromagnetism in the quantum anomalous Hall candidate $MnBi_6Te_{10}$. *Adv. Sci.*, 2203239 (2023). doi: 10.1002/advs.202203239.

[45] C. Yan, Y. Zhu, L. Miao, S. Fernandez-Mulligan, E. Green, R. Mei, H. Tan, B. Yan, C.-X. Liu, N. Alem, Z. Mao and S. Yang. Delicate ferromagnetism in $MnBi_6Te_{10}$. *Nano Lett.*, **22**, 24, 9815 (2022). doi: 10.1021/acs.nanolett.2c02500.

[46] R. Lu, H. Sun, S. Kumar, Y. Wang, M. Gu, M. Zeng, Y.-J. Hao, J. Li, J. Shao, X.-M. Ma, Z. Hao, K. Zhang, W. Mansuer, J. Mei, Y. Zhao, C. Liu, K. Deng, W. Huang, B. Shen, K. Shimada, E. Schwier, C. Liu, Q. Liu and C. Chen. Half-magnetic topological insulator with magnetization-induced Dirac gap at a selected surface. *Phys. Rev. X*, **11**, 1, 011039 (2021). doi: 10.1103/physrevx.11.011039.

[47] M. M. Otrokov, T. V. Menshchikova, I. P. Rusinov, M. G. Vergniory, V. M. Kuznetsov and E. V. Chulkov. Magnetic extension as an efficient method for realizing the quantum anomalous Hall state in topological insulators. *Jetp Lett.*, **105**, 5, 297 (2017). doi: 10.1134/S0021364017050113.

[48] M. M. Otrokov, T. V. Menshchikova, M. G. Vergniory, I. P. Rusinov, A. Y. Vyazovskaya, Y. M. Koroteev, G. Bihlmayer, A. Ernst, P. M. Echenique, A. Arnau

and E. V. Chulkov. Highly-ordered wide bandgap materials for quantized anomalous Hall and magnetoelectric effects. *2d Mater*, **4**, 2 (2017). doi: 10.1088/2053-1583/aa6bec.

[49] Y. Xia, D. Qian, D. Hsieh, L. Wray, A. Pal, H. Lin, A. Bansil, D. Grauer, Y. S. Hor, R. J. Cava and M. Z. Hasan. Observation of a large-gap topological-insulator class with a single Dirac cone on the surface. *Nat. Phys.*, **5**, 6, 398 (2009). doi: 10.1038/nphys1274.

[50] H. Zhang, C.-X. Liu, X.-L. Qi, X. Dai, Z. Fang and S.-C. Zhang. Topological insulators in Bi_2Se_3, Bi_2Te_3 and Sb_2Te_3 with a single Dirac cone on the surface. *Nat. Phys*, **5**, 6, 438 (2009). doi: 10.1038/Nphys1270.

[51] M. Z. Hasan and C. L. Kane. Colloquium: Topological insulators. *Rev. Mod. Phys.*, **82**, 4, 3045 (2010). doi: 10.1103/RevModPhys.82.3045.

[52] J. Stöhr and H. C. Siegmann. *Magnetism From Fundamentals to Nanoscale Dynamics*. Springer, Heidelberg, 1st edition (2006). ISBN 9783540302834.

[53] W. Nolting. *Quantum theory of magnetism*. Springer, Heidelberg, 1st edition (2009). ISBN 9783540854166.

[54] F. Schwabl. *Statistische Mechanik (Springer-Lehrbuch)*. Springer, Heidelberg, 3rd edition (2006). ISBN 9783540310952.

[55] T. Fliessbach. *Statistische Physik*. Spektrum Akademischer Verlag, Heidelberg, 5th edition (2010). ISBN 9783827425270.

[56] M. Gibertini, M. Koperski, A. F. Morpurgo and K. S. Novoselov. Magnetic 2D materials and heterostructures. *Nat. Nanotechnol.*, **14**, 5, 408 (2019). doi: 10.1038/s41565-019-0438-6.

[57] A. Bedoya-Pinto, J. R. Ji, A. K. Pandeya, P. Gargiani, M. Valvidares, P. Sessi, J. M. Taylor, F. Radu, K. Chang and S. S. P. Parkin. Intrinsic 2D-XY ferromagnetism in a van der Waals monolayer. *Science*, **374**, 6567, 616 (2021). doi: 10.1126/science.abd5146.

[58] K. He. $MnBi_2Te_4$-family intrinsic magnetic topological materials. *npj Quantum Mater.*, **5**, 1 (2020). doi: 10.1038/s41535-020-00291-5.

[59] H. Li, S. Ruan and Y.-J. Zeng. Intrinsic van der waals magnetic materials from bulk to the 2d limit: New frontiers of spintronics. *Adv. Mater.*, **31**, 27, 1900065 (2019). doi: 10.1002/adma.201900065.

[60] Y. Guo, B. Wang, X. Zhang, S. Yuan, L. Ma and J. Wang. Magnetic two-dimensional layered crystals meet with ferromagnetic semiconductors. *InfoMat*, **2**, 4, 639 (2020). doi: 10.1002/inf2.12096.

[61] X. Jiang, Q. Liu, J. Xing, N. Liu, Y. Guo, Z. Liu and J. Zhao. Recent progress on 2D magnets: Fundamental mechanism, structural design and modification. *Appl. Phys. Rev.*, **8**, 3, 031305 (2021). doi: 10.1063/5.0039979.

[62] N. Wang, H. Tang, M. Shi, H. Zhang, W. Zhuo, D. Liu, F. Meng, L. Ma, J. Ying, L. Zou, Z. Sun and X. Chen. Transition from ferromagnetic semiconductor to ferromagnetic metal with enhanced Curie temperature in $Cr_2Ge_2Te_6$ via organic ion intercalation. *J. Am. Chem. Soc.*, **141**, 43, 17166 (2019). doi: 10.1021/jacs.9b06929.

[63] P. W. Anderson. New approach to the theory of superexchange interactions. *Phys. Rev.*, **115**, 1, 2 (1959). doi: 10.1103/physrev.115.2.

[64] E. Pavarini, E. Koch, F. Anders and M. Jarrell. *Correlated Electrons: From Models to Materials*, volume 2 of *Autumn School on Correlated Electrons*. Forschungszentrum Jülich (2012). ISBN 978-3-89336-796-2.

[65] H. Padmanabhan, M. Poore, P. K. Kim, N. Z. Koocher, V. A. Stoica, D. Puggioni, H. H. Wang, X. Shen, A. H. Reid, M. Gu, M. Wetherington, S. H. Lee, R. D. Schaller, Z. Mao, A. M. Lindenberg, X. Wang, J. M. Rondinelli, R. D. Averitt and V. Gopalan. Interlayer magnetophononic coupling in $MnBi_2Te_4$. *Nat. Commun.*, **13**, 1 (2022). doi: 10.1038/s41467-022-29545-5.

[66] M.-C. Wang, C.-C. Huang, C.-H. Cheung, C.-Y. Chen, S. G. Tan, T.-W. Huang, Y. Zhao, Y. Zhao, G. Wu, Y.-P. Feng, H.-C. Wu and C.-R. Chang. Prospects and opportunities of 2D van der Waals magnetic systems. *Ann. Phys.*, **532**, 5, 1900452 (2020). doi: 10.1002/andp.201900452.

[67] H. Kurebayashi, J. H. Garcia, S. Khan, J. Sinova and S. Roche. Magnetism, symmetry and spin transport in van der Waals layered systems. *Nat. Rev. Phys*, **4**, 3, 150 (2022). doi: 10.1038/s42254-021-00403-5.

[68] Z. Fei, B. Huang, P. Malinowski, W. Wang, T. Song, J. Sanchez, W. Yao, D. Xiao, X. Zhu, A. F. May, W. Wu, D. H. Cobden, J.-H. Chu and X. Xu. Two-dimensional itinerant ferromagnetism in atomically thin Fe_3GeTe_2. *Nat. Mater.*, **17**, 9, 778 (2018). doi: 10.1038/s41563-018-0149-7.

[69] Strange phonomena in matter's flatlands - popular science background - the nobel prize in physics 2016. *The Royal Swedish Academy of Sciences* (2016).

[70] L. Landau. On the theory of phase transitions. *Zh. Eksp. Teor. Fiz*, **7**, 19 (1937).

[71] M. König, H. Buhmann, L. W. Molenkamp, T. Hughes, C.-X. Liu, X.-L. Qi and S.-C. Zhang. The quantum spin Hall effect: Theory and experiment. *J. Phys. Soc. Jpn.*, **77**, 3, 031007 (2008).

[72] B. Bradlyn, L. Elcoro, J. Cano, M. G. Vergniory, Z. Wang, C. Felser, M. I. Aroyo and B. A. Bernevig. Topological quantum chemistry. *Nature*, **547**, 7663, 298 (2017). doi: 10.1038/nature23268.

[73] C. L. Kane and E. J. Mele. Z_2 topological order and the quantum spin Hall effect. *Phys. Rev. Lett.*, **95**, 14, 146802 (2005). doi: 10.1103/physrevlett.95.146802.

[74] Y. L. Chen, J. G. Analytis, J.-H. Chu, Z. K. Liu, S.-K. Mo, X. L. Qi, H. J. Zhang, D. H. Lu, X. Dai, Z. Fang, S. C. Zhang, I. R. Fisher, Z. Hussain and Z.-X. Shen. Experimental realization of a three-dimensional topological insulator, Bi_2Te_3. *Science*, **325**, 5937, 178 (2009). doi: 10.1126/science.1173034.

[75] H. Bentmann, H. Maass, J. Braun, C. Seibel, K. A. Kokh, O. E. Tereshchenko, S. Schreyeck, K. Brunner, L. W. Molenkamp, K. Miyamoto, M. Arita, K. Shimada, T. Okuda, J. Kirschner, C. Tusche, H. Ebert, J. Minar and F. Reinert. Profiling spin and orbital texture of a topological insulator in full momentum space. *Phys. Rev. B*, **103**, 16 (2021). doi: 10.1103/PhysRevB.103.L161107.

[76] F. Schwabl. *Quantenmechanik für Fortgeschrittene (QM II)*. Springer, Heidelberg (2005). ISBN 9783540259046.

[77] S. Grauer, K. M. Fijalkowski, S. Schreyeck, M. Winnerlein, K. Brunner, R. Thomale, C. Gould and L. W. Molenkamp. Scaling of the quantum anomalous Hall effect as an indicator of axion electrodynamics. *Phys. Rev. Lett.*, **118**, 24, 246801 (2017). doi: 10.1103/PhysRevLett.118.246801.

[78] C. Liu, Y. Wang, H. Li, Y. Wu, Y. Li, J. Li, K. He, Y. Xu, J. Zhang and Y. Wang. Robust axion insulator and Chern insulator phases in a two-dimensional antiferromagnetic topological insulator. *Nat. Mater.*, **19**, 5, 522 (2020). doi: 10.1038/s41563-019-0573-3.

[79] K. M. Fijalkowski, N. Liu, M. Hartl, M. Winnerlein, P. Mandal, A. Coschizza, A. Fothergill, S. Grauer, S. Schreyeck, K. Brunner, M. Greiter, R. Thomale,

C. Gould and L. W. Molenkamp. Any axion insulator must be a bulk three-dimensional topological insulator. *Phys. Rev. B*, **103**, 23 (2021). doi: 10.1103/PhysRevB.103.235111.

[80] D. M. Nenno, C. A. C. Garcia, J. Gooth, C. Felser and P. Narang. Axion physics in condensed-matter systems. *Nat. Rev. Phys*, **2**, 12, 682 (2020). doi: 10.1038/s42254-020-0240-2.

[81] M. Mogi, M. Kawamura, A. Tsukazaki, R. Yoshimi, K. S. Takahashi, M. Kawasaki and Y. Tokura. Tailoring tricolor structure of magnetic topological insulator for robust axion insulator. *Sci. Adv.*, **3**, 10 (2017). doi: 10.1126/sciadv.aao1669.

[82] T. Hirahara, M. M. Otrokov, T. T. Sasaki, K. Sumida, Y. Tomohiro, S. Kusaka, Y. Okuyama, S. Ichinokura, M. Kobayashi, Y. Takeda, K. Amemiya, T. Shirasawa, S. Ideta, K. Miyamoto, K. Tanaka, S. Kuroda, T. Okuda, K. Hono, S. V. Eremeev and E. V. Chulkov. Fabrication of a novel magnetic topological heterostructure and temperature evolution of its massive Dirac cone. *Nat. Commun.*, **11**, 1, 4821 (2020). doi: 10.1038/s41467-020-18645-9.

[83] T. Fukasawa, S. Kusaka, K. Sumida, M. Hashizume, S. Ichinokura, Y. Takeda, S. Ideta, K. Tanaka, R. Shimizu, T. Hitosugi and T. Hirahara. Absence of ferromagnetism in $MnBi_2Te_4/Bi_2Te_3$ down to 6 k. *Phys. Rev. B*, **103**, 20 (2021). doi: 10.1103/PhysRevB.103.205405.

[84] Q. Li, C. X. Trang, W. Wu, J. Hwang, D. Cortie, N. Medhekar, S. K. Mo, S. A. Yang and M. T. Edmonds. Large magnetic gap in a designer ferromagnet-topological insulator-ferromagnet heterostructure. *Adv. Mater.*, e2107520 (2022). doi: 10.1002/adma.202107520.

[85] H. Fu, C.-X. Liu and B. Yan. Exchange bias and quantum anomalous Hall effect in the $MnBi_2Te_4/CrI_3$ heterostructure. *Sci. Adv.*, **6**, 10 (2020). doi: 10.1126/sciadv.aaz0948.

[86] Z. Ying, B. Chen, C. Li, B. Wei, Z. Dai, F. Guo, D. Pan, H. Zhang, D. Wu, X. Wang, S. Zhang, F. Fei and F. Song. Large exchange bias effect and coverage-dependent interfacial coupling in $CrI_3/MnBi_2Te_4$ van der Waals heterostructures. *Nano Lett.*, **23**, 3, 765 (2022). doi: 10.1021/acs.nanolett.2c02882.

[87] P. W. Lange. Ein vergleich zwischen Bi_2Te_3 und Bi_2Te_2S. *Sci. Nat.*, **27**, 8, 133 (1939). doi: 10.1007/bf01490284.

[88] D. Wright. Thermoelectric properties of bismuth telluride and its alloys. *Nature*, **181**, 834 (1958).

[89] Materials data on Bi_2Te_3 by materials project (2020). doi: 10.17188/1206742.

[90] T. Harman, B. Paris, S. Miller and H. Goering. Preparation and some physical properties of Bi_2Te_3, Sb_2Te_3, and As_2Te_3. *J. Phys. Chem. Solids*, **2**, 3, 181 (1957). doi: 10.1016/0022-3697(57)90081-1.

[91] B. Jariwala, D. Shah and N. Ravindra. Influence of doping on structural and optical properties of Bi_2Te_3 thin films. *Thin Solid Films*, **589**, 396 (2015). doi: 10.1016/j.tsf.2015.05.020.

[92] E. D. L. Rienks, S. Wimmer, J. Sánchez-Barriga, O. Caha, P. S. Mandal, J. Růžička, A. Ney, H. Steiner, V. V. Volobuev, H. Groiss, M. Albu, G. Kothleitner, J. Michalička, S. A. Khan, J. Minár, H. Ebert, G. Bauer, F. Freyse, A. Varykhalov, O. Rader and G. Springholz. Large magnetic gap at the dirac point in $Bi_2Te_3/MnBi_2Te_4$ heterostructures. *Nature*, **576**, 7787, 423 (2019). doi: 10.1038/s41586-019-1826-7.

[93] A. Zeugner, F. Nietschke, A. U. B. Wolter, S. Gass, R. C. Vidal, T. R. F. Peixoto, D. Pohl, C. Damm, A. Lubk, R. Hentrich, S. K. Moser, C. Fornari, C. H. Min, S. Schatz, K. Kissner, M. Unzelmann, M. Kaiser, F. Scaravaggi, B. Rellinghaus, K. Nielsch, C. Hess, B. Buchner, F. Reinert, H. Bentmann, O. Oeckler, T. Doert, M. Ruck and A. Isaeva. Chemical aspects of the candidate antiferromagnetic topological insulator $MnBi_2Te_4$. *Chem. Mater.*, **31**, 8, 2795 (2019). doi: 10.1021/acs.chemmater.8b05017.

[94] P. Kagerer, C. I. Fornari, S. Buchberger, S. L. Morelhão, R. C. Vidal, A. Tcakaev, V. Zabolotnyy, E. Weschke, V. Hinkov, M. Kamp, B. Büchner, A. Isaeva, H. Bentmann and F. Reinert. Molecular beam epitaxy of antiferromagnetic $(MnBi_2Te_4)(Bi_2Te_3)$ thin films on BaF_2 (111). *J Appl Phys*, **128**, 13, 135303 (2020). doi: 10.1063/5.0025933.

[95] D. S. Lee, T. H. Kim, C. H. Park, C. Y. Chung, Y. S. Lim, W. S. Seo and H. H. Park. Crystal structure, properties and nanostructuring of a new layered chalcogenide semiconductor, Bi_2MnTe_4. *CrystEngComm*, **15**, 27, 5532 (2013). doi: 10.1039/c3ce40643a.

[96] C. Gong, L. Li, Z. Li, H. Ji, A. Stern, Y. Xia, T. Cao, W. Bao, C. Wang, Y. Wang, Z. Q. Qiu, R. J. Cava, S. G. Louie, J. Xia and X. Zhang. Discovery of intrinsic ferromagnetism in two-dimensional van der Waals crystals. *Nature*, **546**, 7657, 265 (2017). doi: 10.1038/nature22060.

[97] B. Huang, G. Clark, E. Navarro-Moratalla, D. R. Klein, R. Cheng, K. L. Seyler, D. Zhong, E. Schmidgall, M. A. McGuire, D. H. Cobden, W. Yao, D. Xiao, P. Jarillo-Herrero and X. Xu. Layer-dependent ferromagnetism in a van der Waals crystal down to the monolayer limit. *Nature*, **546**, 7657, 270 (2017). doi: 10.1038/nature22391.

[98] T. J. Kim, S. Ryee and M. J. Han. Fe_3GeTe_2: a site-differentiated Hund metal. *npj Comput. Mater.*, **8**, 1 (2022). doi: 10.1038/s41524-022-00937-x.

[99] V. Y. Verchenko, A. A. Tsirlin, A. V. Sobolev, I. A. Presniakov and A. V. Shevelkov. Ferromagnetic order, strong magnetocrystalline anisotropy, and magnetocaloric effect in the layered telluride $Fe_{3-\delta}GeTe_2$. *Inorg Chem*, **54**, 17, 8598 (2015). doi: 10.1021/acs.inorgchem.5b01260.

[100] H. L. Zhuang, P. R. C. Kent and R. G. Hennig. Strong anisotropy and magnetostriction in the two-dimensional Stoner ferromagnet Fe_3GeTe_2. *Phys. Rev. B*, **93**, 13, 134407 (2016). doi: 10.1103/physrevb.93.134407.

[101] H. J. Deiseroth, K. Aleksandrov, C. Reiner, L. Kienle and R. K. Kremer. Fe_3GeTe_2 and Ni_3GeTe_2 - two new layered transition-metal compounds: Crystal structures, HRTEM investigations, and magnetic and electrical properties. *Eur. J. Inorg. Chem.*, **2006**, 8, 1561 (2006). doi: 10.1002/ejic.200501020.

[102] N. Leon-Brito, E. D. Bauer, F. Ronning, J. D. Thompson and R. Movshovich. Magnetic microstructure and magnetic properties of uniaxial itinerant ferromagnet Fe_3GeTe_2. *J Appl Phys*, **120**, 8 (2016). doi: 10.1063/1.4961592.

[103] W.-Z. Xu, C.-G. Chu, Z.-C. Pan, J.-J. Chen, A.-Q. Wang, Z.-B. Tan, P.-F. Zhu, X.-G. Ye, D.-P. Yu and Z.-M. Liao. Proximity-induced superconducting gap in the intrinsic magnetic topological insulator $MnBi_2Te_4$. *Phys. Rev. B*, **105**, 18, 184515 (2022). doi: 10.1103/PhysRevB.105.184515.

[104] C. Tan, J. Lee, S. G. Jung, T. Park, S. Albarakati, J. Partridge, M. R. Field, D. G. McCulloch, L. Wang and C. Lee. Hard magnetic properties in nanoflake van der Waals Fe_3GeTe_2. *Nat. Commun.*, **9** (2018). doi: 10.1038/s41467-018-04018-w.

[105] G. D. Nguyen, J. Lee, T. Berlijn, Q. Zou, S. M. Hus, J. Park, Z. Gai, C. Lee and A.-P. Li. Visualization and manipulation of magnetic domains in the quasi-two-dimensional material Fe_3GeTe_2. *Phys. Rev. B*, **97**, 1, 014425 (2018). doi: 10.1103/physrevb.97.014425.

[106] X. Wang, J. Tang, X. X. Xia, C. L. He, J. W. Zhang, Y. Z. Liu, C. H. Wan, C. Fang, C. Y. Guo, W. L. Yang, Y. Guang, X. M. Zhang, H. J. Xu, J. W. Wei, M. Z. Liao, X. B. Lu, J. F. Feng, X. X. Li, Y. Peng, H. X. Wei, R. Yang, D. X. Shi, X. Zhang, Z. Han, Z. D. Zhang, G. Y. Zhang, G. Yu and X. F. Han. Current-driven magnetization switching in a van der Waals ferromagnet Fe_3GeTe_2. *Sci. Adv.*, **5**, 8 (2019). doi: 10.1126/sciadv.aaw8904.

[107] M. A. Herman and H. Sitter. *Molecular Beam Epitaxy Fundamentals and Current Status*. Springer Berlin / Heidelberg (2013). ISBN 9783642800627.

[108] U. W. Pohl. *Epitaxy of Semiconductors Physics and Fabrication of Heterostructures*. Springer, Heidelberg (2020). ISBN 9783030438685.

[109] C. I. Fornari, P. H. O. Rappl, S. L. Morelhão, G. Fornari, J. S. Travelho, S. de Castro, M. J. P. Pirralho, F. S. Pena, M. L. Peres and E. Abramof. Structural defects and electronic phase diagram of topological insulator bismuth telluride epitaxial films. *Mater. Res. Express*, **5**, 11, 116410 (2018). doi: 10.1088/2053-1591/aadeb7.

[110] D. S. H. Liu, M. Hilse and R. Engel-Herbert. Sticking coefficients of selenium and tellurium. *J. Vac. Sci. Technol. A*, **39**, 2, 023413 (2021). doi: 10.1116/6.0000736.

[111] M.-H. Du, J. Yan, V. R. Cooper and M. Eisenbach. Tuning fermi levels in intrinsic antiferromagnetic topological insulators $MnBi_2Te_4$ and $MnBi_4Te_7$ by defect engineering and chemical doping. *Adv. Funct. Mater.*, **31**, 3, 2006516 (2020). doi: 10.1002/adfm.202006516.

[112] R. F. Brebrick and F. T. J. Smith. Partial and total vapor pressures over molten Bi_2Te_3. *J. Electrochem. Soc.*, **118**, 6, 991 (1971). doi: 10.1149/1.2408239.

[113] T. S. L. Narasimhan, R. Viswanathan and R. Balasubramanian. Congruent vaporization of solid manganese monotelluride and the effects of phase transitions: A high-temperature mass spectrometric study. *J. Phys. Chem. B*, **102**, 51, 10586 (1998). doi: 10.1021/jp982174x.

[114] C. Summers, B. Wagner and R. Benz. Chemical beam epitaxy of $Hg_{1-x}Cd_xTe$ and related binaries. *Prog. Cryst. Growth Charact. Mater.*, **29**, 1-4, 161 (1994). doi: 10.1016/0960-8974(94)90006-x.

[115] M. I. B. Utama, Q. Zhang, J. Zhang, Y. Yuan, F. J. Belarre, J. Arbiol and Q. Xiong. Recent developments and future directions in the growth of nanostructures by van der Waals epitaxy. *Nanoscale*, **5**, 9, 3570 (2013). doi: 10.1039/c3nr34011b.

[116] C. I. Fornari, P. H. O. Rappl, S. L. Morelhão, T. R. F. Peixoto, H. Bentmann, F. Reinert and E. Abramof. Preservation of pristine Bi_2Te_3 thin film topological insulator surface after ex situ mechanical removal of Te capping layer. *APL Mater.*, **4**, 10, 106107 (2016). doi: 10.1063/1.4964610.

[117] O. Caha, A. Dubroka, J. Humlíček, V. Holý, H. Steiner, M. Ul-Hassan, J. Sánchez-Barriga, O. Rader, T. N. Stanislavchuk, A. A. Sirenko, G. Bauer and G. Springholz. Growth, structure, and electronic properties of epitaxial bismuth telluride topological insulator films on BaF_2 (111) substrates. *Cryst. Growth Des.*, **13**, 8, 3365 (2013). doi: 10.1021/cg400048g.

[118] C. I. Fornari, P. H. O. Rappl, S. L. Morelhão and E. Abramof. Structural properties of Bi_2Te_3 topological insulator thin films grown by molecular beam epitaxy on (111) BaF_2 substrates. *J. Appl. Phys.*, **119**, 16, 165303 (2016). doi: 10.1063/1.4947266.

[119] A. R. Mazza, J. Lapano, H. M. Meyer, C. T. Nelson, T. Smith, Y.-Y. Pai, K. Noordhoek, B. J. Lawrie, T. R. Charlton, R. G. Moore, T. Z. Ward, M.-H. Du, G. Eres and M. Brahlek. Surface-driven evolution of the anomalous Hall effect in magnetic topological insulator $MnBi_2Te_4$ thin films. *Adv. Funct. Mater.*, **32**, 28, 2202234 (2022). doi: 10.1002/adfm.202202234.

[120] P. Kagerer, C. I. Fornari, S. Buchberger, T. Tschirner, L. Veyrat, M. Kamp, A. V. Tcakaev, V. Zabolotnyy, S. L. Morelhão, B. Geldiyev, S. Müller, A. Fedorov, E. Rienks, P. Gargiani, M. Valvidares, L. C. Folkers, A. Isaeva, B. Büchner, V. Hinkov, R. Claessen, H. Bentmann and F. Reinert. Two-dimensional ferromagnetic extension of a topological insulator. *Phys. Rev. Res.*, **5**, 2, l022019 (2023). doi: 10.1103/physrevresearch.5.l022019.

[121] S. L. Morelhão. *Computer Simulation Tools for X-ray Analysis*. Springer International Publishing, Switzerland, 1st edition (2016). ISBN 978-3-319-19553-7. Springer.

[122] M. A. V. Hove, W. H. Weinberg and C.-M. Chan. *Low-Energy Electron Diffraction*. Springer-Verlag (1986). ISBN 0387162623. doi: 10.1007/978-3-642-82721-1.

[123] H. Lüth. *Solid surfaces, interfaces and thin films*. Springer, Heidelberg (2010). ISBN 9783642135910.

[124] P. West. *Introduction to Atomic Force Microscopy: Theory, Practice, Applications*. Pacific Nanotechnology (2006).

[125] B. D. Cullity and S. R. Stock. *Elements of X-ray Diffraction Pearson New International Edition*. Pearson Education, Limited, Essex, 3rd edition (2013). ISBN 9781292040547.

[126] K. Kopitzki and P. Herzog. *Einführung in die Festkörperphysik*. Vieweg+Teubner Verlag, Wiesbaden, 6th edition (2007). ISBN 9783835101449.

[127] R. F. S. Penacchio, M. B. Estradiote, S. L. Morelhão, C. I. Fornari, P. Kagerer, M. Dittmar, S. Müller and F. Reinert. A simple recipe to create three-dimensional reciprocal space maps. *arXiv* (2022). doi: 10.48550/arXiv.2210.05427.

[128] S. L. Morelhão, C. I. Fornari, P. H. O. Rappl and E. Abramof. Nanoscale characterization of bismuth telluride epitaxial layers by advanced X-ray analysis. *J. Appl. Crystallogr.*, **50**, 2, 399 (2017). doi: 10.1107/s1600576717000760.

[129] R. F. Penacchio, C. I. Fornari, Y. G. Camillo, P. Kagerer, S. Buchberger, M. Kamp, H. Bentmann, F. Reinert and S. L. Morelhão. Statistical modeling of epitaxial thin films of an intrinsic antiferromagnetic topological insulator. *Thin Solid Films*, **750**, 139183 (2022). doi: 10.1016/j.tsf.2022.139183.

[130] A. Gibaud, M. S. Chebil and T. Beuvier. X-ray reflectivity. In *Surface Science Techniques*, 191–216. Springer Berlin Heidelberg (2013).

[131] E. Chason and T. M. Mayer. Thin film and surface characterization by specular X-ray reflectivity. *Crit. Rev. Solid State Mater. Sci.*, **22**, 1, 1 (1997). doi: 10.1080/10408439708241258.

[132] M. Bjrck and G. Andersson. GenX: an extensible X-ray reflectivity refinement program utilizing differential evolution. *J. Appl. Crystallogr.*, **40**, 6, 1174 (2007). doi: 10.1107/S0021889807045086.

[133] M. Ünzelmann, H. Bentmann, P. Eck, T. Kißlinger, B. Geldiyev, J. Rieger, S. Moser, R. C. Vidal, K. Kißner, L. Hammer, M. A. Schneider, T. Fauster, G. Sangiovanni, D. D. Sante and F. Reinert. Orbital-driven Rashba effect in a binary honeycomb monolayer AgTe. *Phys. Rev. Lett.*, **124**, 17, 176401 (2020). doi: 10.1103/physrevlett.124.176401.

[134] R. García. Dynamic atomic force microscopy methods. *Surf. Sci. Rep.*, **47**, 6-8, 197 (2002). doi: 10.1016/s0167-5729(02)00077-8.

[135] Veeco Instuments Inc. *SPM Training Notebook*. Veeco Instuments Inc. (2003).

[136] R. M. Langford and A. K. Petford-Long. Preparation of transmission electron microscopy cross-section specimens using focused ion beam milling. *J. Vac. Sci. Technol. A*, **19**, 5, 2186 (2001). doi: 10.1116/1.1378072.

[137] E. James and N. Browning. Practical aspects of atomic resolution imaging and analysis in STEM. *Ultramicroscopy*, **78**, 1-4, 125 (1999). doi: 10.1016/s0304-3991(99)00018-2.

[138] A. Tejeda and D. Malterre. *A Primer in Photoemission: Concepts and Applications*. EDP Sciences, France (2019). ISBN 9782759820658.

[139] M. P. Seah and W. A. Dench. Quantitative electron spectroscopy of surfaces: A standard data base for electron inelastic mean free paths in solids. *Surf. Interface Anal.*, **1**, 1, 2 (1979). doi: 10.1002/sia.740010103.

[140] F. Reinert and S. Hüfner. Photoemission spectroscopy—from early days to recent applications. *New J. Phys.*, **7**, 97 (2005). doi: 10.1088/1367-2630/7/1/097.

[141] R. C. Vidal, H. Bentmann, J. I. Facio, T. Heider, P. Kagerer, C. I. Fornari, T. R. F. Peixoto, T. Figgemeier, S. Jung, C. Cacho, B. Buchner, J. van den Brink, C. M. Schneider, L. Plucinski, E. F. Schwier, K. Shimada, M. Richter, A. Isaeva and F. Reinert. Orbital complexity in intrinsic magnetic topological insulators $MnBi_4Te_7$ and $MnBi_6Te_{10}$. *Phys. Rev. Lett.*, **126**, 17, 176403 (2021). doi: 10.1103/PhysRevLett.126.176403.

[142] M. Ünzelmann. Interplax of inversion symmetry breaking and spin-orbit coupling - from the Rashba effect to Weyl semimetals. Ph.D. thesis, Julius-Maximilians-Universität Würzburg (2021).

[143] S. Moser. An experimentalist's guide to the matrix element in angle resolved photoemission. *J. Electron Spectrosc. Relat. Phenom.*, **214**, 29 (2017). doi: 10.1016/j.elspec.2016.11.007.

[144] S. Moser. A toy model for dichroism in angle resolved photoemission. *J Electron Spectros Relat Phenomena*, **262**, 147278 (2023). doi: 10.1016/j.elspec.2022.147278.

[145] A. Verdini, P. Krueger and L. Floreano. Resonant photoelectron diffraction. In *Surface Science Techniques*, 217–247. Springer Berlin Heidelberg (2013).

[146] S. Hüfner, S.-H. Yang, B. S. Mun, C. S. Fadley, J. Schäfer, E. Rotenberg and S. D. Kevan. Observation of the two-hole satellite in Cr and Fe metal by resonant photoemission at the $2p$ absorption energy. *Phys. Rev. B*, **61**, 19, 12582 (2000). doi: 10.1103/physrevb.61.12582.

[147] Scienta Omicron GmbH. *DA30-L Angle Resolved Electron Spectrometer* (2023).

[148] B. Lv, T. Qian and H. Ding. Angle-resolved photoemission spectroscopy and its application to topological materials. *Nat. Rev. Phys*, **1**, 10, 609 (2019). doi: 10.1038/s42254-019-0088-5.

[149] A. Damascelli. Probing the electronic structure of complex systems by ARPES. *Phys. Scr.*, **T109**, 61 (2004). doi: 10.1238/physica.topical.109a00061.

[150] T. Okuda. Recent trends in spin-resolved photoelectron spectroscopy. *J. Phys.: Condens. Matter*, **29**, 48, 483001 (2017). doi: 10.1088/1361-648x/aa8f28.

[151] T. Okuda, K. Miyamoto, A. Kimura, H. Namatame and M. Taniguchi. A double VLEED spin detector for high-resolution three dimensional spin vectorial analysis of anisotropic Rashba spin splitting. *J Electron Spectrosc*, **201**, 23 (2015). doi: 10.1016/j.elspec.2014.10.010.

[152] J. Kessler. Electron spin polarization by low-energy scattering from unpolarized targets. *Rev. Mod. Phys.*, **41**, 1, 3 (1969). doi: 10.1103/RevModPhys.41.3.

[153] H. Bentmann, H. Maass, E. E. Krasovskii, T. R. F. Peixoto, C. Seibel, M. Leandersson, T. Balasubramanian and F. Reinert. Strong linear dichroism in spin-polarized photoemission from spin-orbit-coupled surface states. *Phys. Rev. Lett.*, **119**, 10 (2017). doi: 10.1103/PhysRevLett.119.106401.

[154] G. van der Laan and B. T. Thole. Strong magnetic X-ray dichroism in $2p$ absorption spectra of $3d$ transition-metal ions. *Phys. Rev. B*, **43**, 16, 13401 (1991). doi: 10.1103/physrevb.43.13401.

[155] G. van der Laan and A. I. Figueroa. X-ray magnetic circular dichroism—a versatile tool to study magnetism. *Coord. Chem. Rev.*, **277-278**, 95 (2014). doi: 10.1016/j.ccr.2014.03.018.

[156] B. Henke, P. Lee, T. Tanaka, R. Shimabukuro and B. Fujikawa. Low-energy X-ray interaction coefficients: Photoabsorption, scattering, and reflection. *At. Data Nucl. Data Tables*, **27**, 1, 1 (1982). doi: 10.1016/0092-640x(82)90002-x.

[157] A.-V. Tcakaev. Soft X-ray spectroscopic study of electronic and magnetic properties of magnetic topological insulators. Ph.D. thesis, Universität Würzburg (2023). doi: 10.25972/OPUS-30378.

[158] S. Souma, T. Sato, T. Takahashi and P. Baltzer. High-intensity xenon plasma discharge lamp for bulk-sensitive high-resolution photoemission spectroscopy. *Rev. Sci. Instrum.*, **78**, 12, 123104 (2007). doi: 10.1063/1.2818806.

[159] T. Okuda, K. Miyamaoto, H. Miyahara, K. Kuroda, A. Kimura, H. Namatame and M. Taniguchi. Efficient spin resolved spectroscopy observation machine at Hiroshima Synchrotron Radiation Center. *Rev. Sci. Instrum.*, **82**, 10, 103302 (2011). doi: 10.1063/1.3648102.

[160] H. Iwasawa, E. F. Schwier, M. Arita, A. Ino, H. Namatame, M. Taniguchi, Y. Aiura and K. Shimada. Development of laser-based scanning μ-ARPES system with ultimate energy and momentum resolutions. *Ultramicroscopy*, **182**, 85 (2017). doi: 10.1016/j.ultramic.2017.06.016.

[161] S. V. Borisenko. "one-cubed" ARPES user facility at BESSY II. *Synchrotron Radiat. News*, **25**, 5, 6 (2012). doi: 10.1080/08940886.2012.720159.

[162] A. Barla, J. Nicolás, D. Cocco, S. M. Valvidares, J. Herrero-Martín, P. Gargiani, J. Moldes, C. Ruget, E. Pellegrin and S. Ferrer. Design and performance of BOREAS, the beamline for resonant X-ray absorption and scattering experiments at the ALBA synchrotron light source. *J. Synchrotron Radiat.*, **23**, 6, 1507 (2016). doi: 10.1107/s1600577516013461.

[163] E. Weschke and E. Schierle. The UE46 PGM-1 beamline at BESSY II. *J. Large-Scale Res. Facil.*, **4** (2018). doi: 10.17815/jlsrf-4-77.

[164] S. Buchberger. Molecular beam epitaxy and spectroscopic characterisation of the antiferromagnetic topological insulator $MnBi_2Te_4$ on BaF_2 (111). Master's thesis, Julius-Maximilians-Universität Würzburg (2021).

[165] J. Krumrain, G. Mussler, S. Borisova, T. Stoica, L. Plucinski, C. Schneider and D. Grützmacher. MBE growth optimization of topological insulator Bi_2Te_3 films. *J. Cryst. Growth*, **324**, 1, 115 (2011). doi: 10.1016/j.jcrysgro.2011.03.008.

[166] G. Wang, X.-G. Zhu, Y.-Y. Sun, Y.-Y. Li, T. Zhang, J. Wen, X. Chen, K. He, L.-L. Wang, X.-C. Ma, J.-F. Jia, S. B. Zhang and Q.-K. Xue. Topological insulator thin films of Bi_2Te_3 with controlled electronic structure. *Adv. Mater.*, **23**, 26, 2929 (2011). doi: 10.1002/adma.201100678.

[167] X. Liu, D. J. Smith, J. Fan, Y.-H. Zhang, H. Cao, Y. P. Chen, J. Leiner, B. J. Kirby, M. Dobrowolska and J. K. Furdyna. Structural properties of Bi_2Te_3 topological insulators grown by molecular beam epitaxy on GaAs(001) substrates. *Appl. Phys. Lett.*, **99**, 17, 171903 (2011). doi: 10.1063/1.3655995.

[168] H. Steiner, V. Volobuev, O. Caha, G. Bauer, G. Springholz and V. Holý. Structure and composition of bismuth telluride topological insulators grown by molecular beam epitaxy. *J. Appl. Crystallogr.*, **47**, 6, 1889 (2014). doi: 10.1107/s1600576714020445.

[169] J.-Q. Yan, Q. Zhang, T. Heitmann, Z. Huang, K. Y. Chen, J.-G. Cheng, W. Wu, D. Vaknin, B. C. Sales and R. J. McQueeney. Crystal growth and magnetic structure of $MnBi_2Te_4$. *Phys. Rev. Mater.*, **3**, 6, 064202 (2019). doi: 10.1103/physrevmaterials.3.064202.

[170] Y.-J. Hao, P. Liu, Y. Feng, X.-M. Ma, E. F. Schwier, M. Arita, S. Kumar, C. Hu, R. Lu, M. Zeng, Y. Wang, Z. Hao, H.-Y. Sun, K. Zhang, J. Mei, N. Ni, L. Wu, K. Shimada, C. Chen, Q. Liu and C. Liu. Gapless surface dirac cone in antiferromagnetic topological insulator $MnBi_2Te_4$. *Phys. Rev. X*, **9**, 4, 041038 (2019). doi: 10.1103/PhysRevX.9.041038.

[171] S.-K. Bac, K. Koller, F. Lux, J. Wang, L. Riney, K. Borisiak, W. Powers, M. Zhukovskyi, T. Orlova, M. Dobrowolska, J. K. Furdyna, N. R. Dilley, L. P. Rokhinson, Y. Mokrousov, R. J. McQueeney, O. Heinonen, X. Liu and B. A. Assaf. Topological response of the anomalous Hall effect in $MnBi_2Te_4$ due to magnetic canting. *npj Quantum Mater.*, **7**, 1 (2022). doi: 10.1038/s41535-022-00455-5.

[172] Y. Bai, Y. Li, J. Luan, R. Liu, W. Song, Y. Chen, P.-F. Ji, Q. Zhang, F. Meng, B. Tong, L. Li, Y. Jiang, Z. Gao, L. Gu, J. Zhang, Y. Wang, Q.-K. Xue, K. He, Y. Feng and X. Feng. Quantized anomalous Hall resistivity achieved in molecular beam epitaxy-grown $MnBi_2Te_4$ thin films. *ArXiv* (2022). doi: 10.48550/ARXIV.2206.03773.

[173] Y. Gong, J. Guo, J. Li, K. Zhu, M. Liao, X. Liu, Q. Zhang, L. Gu, L. Tang, X. Feng, D. Zhang, W. Li, C. Song, L. Wang, P. Yu, X. Chen, Y. Wang, H. Yao, W. Duan, Y. Xu, S.-C. Zhang, X. Ma, Q.-K. Xue and K. He. Experimental realization of an intrinsic magnetic topological insulator ($mnbi_2te_4$). *Chin. Phys. Lett.*, **36**, 7, 076801 (2019). doi: 10.1088/0256-307x/36/7/076801.

[174] N. Liu, S. Schreyeck, K. Fijalkowski, M. Kamp, K. Brunner, C. Gould and L. Molenkamp. Antiferromagnetic order in $MnBi_2Te_4$ films grown on Si(1 1 1)

by molecular beam epitaxy. *J. Cryst. Growth*, **591**, 126677 (2022). doi: 10.1016/j.jcrysgro.2022.126677.

[175] S.-H. Su, J.-T. Chang, P.-Y. Chuang, M.-C. Tsai, Y.-W. Peng, M. K. Lee, C.-M. Cheng and J.-C. A. Huang. Epitaxial growth and structural characterizations of $MnBi_2Te_4$ thin films in nanoscale. *Nanomaterials*, **11**, 12, 3322 (2021). doi: 10.3390/nano11123322.

[176] Y.-F. Zhao, L.-J. Zhou, F. Wang, G. Wang, T. Song, D. Ovchinnikov, H. Yi, R. Mei, K. Wang, M. H. W. Chan, C.-X. Liu, X. Xu and C.-Z. Chang. Even-odd layer-dependent anomalous Hall effect in topological magnet $MnBi_2Te_4$ thin films. *Nano Lett.*, **21**, 18, 7691 (2021). doi: 10.1021/acs.nanolett.1c02493.

[177] K. Zhu, Y. Bai, X. Hong, Z. Geng, Y. Jiang, R. Liu, Y. Li, M. Shi, L. Wang, W. Li, Q.-K. Xue, X. Feng and K. He. Investigating and manipulating the molecular beam epitaxy growth kinetics of intrinsic magnetic topological insulator ($mnbi_2te_4$) with in situ angle-resolved photoemission spectroscopy. *J. Phys.: Condens. Matter*, **32**, 47, 475002 (2020). doi: 10.1088/1361-648x/aba06d.

[178] R. C. Vidal, A. Zeugner, J. I. Facio, R. Ray, M. H. Haghighi, A. U. B. Wolter, L. T. C. Bohorquez, F. Caglieris, S. Moser, T. Figgemeier, T. R. F. Peixoto, H. B. Vasili, M. Valvidares, S. Jung, C. Cacho, A. Alfonsov, K. Mehlawat, V. Kataev, C. Hess, M. Richter, B. Buchner, J. van den Brink, M. Ruck, F. Reinert, H. Bentmann and A. Isaeva. Topological electronic structure and intrinsic magnetization in $MnBi_4Te_7$: A Bi_2Te_3 derivative with a periodic Mn sublattice. *Phys. Rev. X*, **9**, 4 (2019). doi: 10.1103/PhysRevX.9.041065.

[179] E. Janik, E. Dynowska, J. Back-Misiuk, M. Leszczynski, W. Szuszkiewicz, T. Wojtowicz, G. Karczewski, A. Zakrzewski and J. Kossut. Structural properties of cubic MnTe layers grown by MBE. *Thin Solid Films*, **267**, 1-2, 74 (1995). doi: 10.1016/0040-6090(95)06632-2.

[180] D. Kriegner, H. Reichlova, J. Grenzer, W. Schmidt, E. Ressouche, J. Godinho, T. Wagner, S. Y. Martin, A. B. Shick, V. V. Volobuev, G. Springholz, V. Holý, J. Wunderlich, T. Jungwirth and K. Výborný. Magnetic anisotropy in antiferromagnetic hexagonal MnTe. *Phys. Rev. B*, **96**, 21, 214418 (2017). doi: 10.1103/physrevb.96.214418.

[181] C. I. Fornari, E. Abramof, P. H. O. Rappl, S. W. Kycia and S. L. Morelhão. Morphology control in van der Waals epitaxy of bismuth telluride topological insulators. *MRS Advances*, **5**, 35-36, 1891 (2020). doi: 10.1557/adv.2020.202.

[182] Y.-Y. Li, G. Wang, X.-G. Zhu, M.-H. Liu, C. Ye, X. Chen, Y.-Y. Wang, K. He, L.-L. Wang, X.-C. Ma, H.-J. Zhang, X. Dai, Z. Fang, X.-C. Xie, Y. Liu, X.-L. Qi, J.-F. Jia, S.-C. Zhang and Q.-K. Xue. Intrinsic topological insulator Bi_2Te_3 thin films on Si and their thickness limit. *Adv. Mater.*, **22**, 36, 4002 (2010). doi: 10.1002/adma.201000368.

[183] W. Mortelmans, S. D. Gendt, M. Heyns and C. Merckling. Epitaxy of 2D chalcogenides: Aspects and consequences of weak van der Waals coupling. *Appl. Mater. Today*, **22**, 100975 (2021). doi: 10.1016/j.apmt.2021.100975.

[184] A. K. Geim and I. V. Grigorieva. Van der Waals heterostructures. *Nature*, **499**, 7459, 419 (2013). doi: 10.1038/nature12385.

[185] P. Gargiani, R. Cuadrado, H. B. Vasili, M. Pruneda and M. Valvidares. Graphene-based synthetic antiferromagnets and ferrimagnets. *Nat. Commun.*, **8** (2017). doi: 10.1038/s41467-017-00825-9.

[186] E. Mantel. Quantifizierung in XPS - stöchiometriebestimmung ausgewählter modellsysteme. Bachelor thesis, Julius-Maximilians-Universität Würzburg (2021).

[187] T. Benra. Wachstum und charakterisierung von topologischen isolatoren auf den substraten BaF_2 und dem ferromagneten Fe_3GeTe_2. Bachelor thesis, Julius-Maximilians-Universität Würzburg (2022).

[188] H. Yi, L.-H. Hu, Y. Wang, R. Xiao, J. Cai, D. R. Hickey, C. Dong, Y.-F. Zhao, L.-J. Zhou, R. Zhang, A. R. Richardella, N. Alem, J. A. Robinson, M. H. W. Chan, X. Xu, N. Samarth, C.-X. Liu and C.-Z. Chang. Crossover from Ising- to Rashba-type superconductivity in epitaxial Bi_2Se_3/monolayer $NbSe_2$ heterostructures. *Nat. Mater.*, **21**, 12, 1366 (2022). doi: 10.1038/s41563-022-01386-z.

[189] L. Cao, S. Han, Y.-Y. Lv, D. Wang, Y.-C. Luo, Y.-Y. Zhang, S.-H. Yao, J. Zhou, Y. B. Chen, H. Zhang and Y.-F. Chen. Growth and characterization of the dynamical axion insulator candidate $Mn_2Bi_2Te_5$ with intrinsic antiferromagnetism. *Phys. Rev. B*, **104**, 5, 054421 (2021). doi: 10.1103/physrevb.104.054421.

[190] Y. Li, Y. Jiang, J. Zhang, Z. Liu, Z. Yang and J. Wang. Intrinsic topological phases in $Mn_2Bi_2Te_5$ tuned by the layer magnetization. *Phys. Rev. B*, **102**, 12, 121107 (2020). doi: 10.1103/physrevb.102.121107.

[191] P. M. Sass, J. Kim, D. Vanderbilt, J. Q. Yan and W. D. Wu. Robust a-type order and spin-flop transition on the surface of the antiferromagnetic topological insulator $MnBi_2Te_4$. *Phys. Rev. Lett.*, **125**, 3 (2020). doi: 10.1103/PhysRevLett.125.037201.

[192] R. C. Vidal. Spectroscopic investigation of the three dimensional topological insulators $(MnBi_2Te_4)(Bi_2Te_3)_n$ and HgTe: band structure, orbital symmetries and influence of the cation *d*-states. Ph.D. thesis, Julius-Maximilians-Universität Würzburg (2023).

[193] L. Veyrat. personal communication (2023).

[194] A. Tcakaev. personal communication (2020).

[195] A. Tan, V. Labracherie, N. Kunchur, A. U. Wolter, J. Cornejo, J. Dufouleur, B. Büchner, A. Isaeva and R. Giraud. Metamagnetism of weakly coupled antiferromagnetic topological insulators. *Phys. Rev. Lett.*, **124**, 19, 197201 (2020). doi: 10.1103/physrevlett.124.197201.

[196] I. I. Klimovskikh, M. M. Otrokov, D. Estyunin, S. V. Eremeev, S. O. Filnov, A. Koroleva, E. Shevchenko, V. Voroshnin, A. G. Rybkin, I. P. Rusinov, M. Blanco-Rey, M. Hoffmann, Z. S. Aliev, M. B. Babanly, I. R. Amiraslanov, N. A. Abdullayev, V. N. Zverev, A. Kimura, O. E. Tereshchenko, K. A. Kokh, L. Petaccia, G. D. Santo, A. Ernst, P. M. Echenique, N. T. Mamedov, A. M. Shikin and E. V. Chulkov. Tunable 3D/2D magnetism in the $(MnBi_2Te_4)(Bi_2Te_3)_{(m)}$ topological insulators family. *npj Quantum Mater.*, **5**, 1 (2020). doi: 10.1038/s41535-020-00255-9.

[197] Y.-P. Wang, X.-Y. Chen and M.-Q. Long. Modifications of magnetic anisotropy of Fe_3GeTe_2 by the electric field effect. *Appl. Phys. Lett.*, **116**, 9, 092404 (2020). doi: 10.1063/1.5144032.

[198] S. Y. Park, D. S. Kim, Y. Liu, J. Hwang, Y. Kim, W. Kim, J.-Y. Kim, C. Petrovic, C. Hwang, S.-K. Mo, H. jun Kim, B.-C. Min, H. C. Koo, J. Chang, C. Jang, J. W. Choi and H. Ryu. Controlling the magnetic anisotropy of the van der Waals ferromagnet Fe_3GeTe_2 through hole doping. *Nano Lett.*, **20**, 1, 95 (2019). doi: 10.1021/acs.nanolett.9b03316.

[199] A. Arrott and J. E. Noakes. Approximate equation of state for nickel near its critical temperature. *Phys. Rev. Lett.*, **19**, 14, 786 (1967). doi: 10.1103/PhysRevLett.19.786.

[200] M. Scholten, J. I. Facio, R. Ray, I. M. Eremin, J. van den Brink and F. S. Nogueira. Finite temperature fluctuation-induced order and responses in magnetic topological insulators. *Phys. Rev. Res.*, **3**, 3, l032014 (2021). doi: 10.1103/physrevresearch.3.l032014.

[201] L. Ding, C. Hu, F. Ye, E. Feng, N. Ni and H. Cao. Crystal and magnetic structures of magnetic topological insulators $MnBi_2Te_4$ and $MnBi_4Te_7$. *Phys. Rev. B*, **101**, 2, 020412 (2020). doi: 10.1103/PhysRevB.101.020412.

[202] A. A. Baker, A. I. Figueroa, K. Kummer, L. J. Collins-McIntyre, T. Hesjedal and G. van der Laan. Magnetic proximity-enhanced Curie temperature of Cr-doped Sb_2Te_3 thin films. *Phys. Rev. B*, **92**, 9, 094420 (2015). doi: 10.1103/physrevb.92.094420.

[203] J. X. Zhu, M. Janoschek, D. S. Chaves, J. C. Cezar, T. Durakiewicz, F. Ronning, Y. Sassa, M. Mansson, B. L. Scott, N. Wakeham, E. D. Bauer and J. D. Thompson. Electronic correlation and magnetism in the ferromagnetic metal Fe_3GeTe_2. *Phys. Rev. B*, **93**, 14 (2016). doi: 10.1103/PhysRevB.93.144404.

[204] R. Roemer, C. Liu and K. Zou. Robust ferromagnetism in wafer-scale monolayer and multilayer Fe_3GeTe_2. *npj 2d Mater. Appl.*, **4**, 1 (2020). doi: 10.1038/s41699-020-00167-z.

[205] J. Yi, H. Zhuang, Q. Zou, Z. Wu, G. Cao, S. Tang, S. A. Calder, P. R. C. Kent, D. Mandrus and Z. Gai. Competing antiferromagnetism in a quasi-2D itinerant ferromagnet: Fe_3GeTe_2. *2D Mater.*, **4**, 1, 011005 (2016). doi: 10.1088/2053-1583/4/1/011005.

[206] J. I. Facio. personal communication (2022).

[207] R. C. Vidal, H. Bentmann, T. R. F. Peixoto, A. Zeugner, S. Moser, C. H. Min, S. Schatz, K. Kissner, M. Unzelmann, C. I. Fornari, H. B. Vasili, M. Valvidares, K. Sakamoto, D. Mondal, J. Fujii, I. Vobornik, S. Jung, C. Cacho, T. K. Kim, R. J. Koch, C. Jozwiak, A. Bostwick, J. D. Denlinger, E. Rotenberg, J. Buck, M. Hoesch, F. Diekmann, S. Rohlf, M. Kallane, K. Rossnagel, M. M. Otrokov, E. V. Chulkov, M. Ruck, A. Isaeva and F. Reinert. Surface states and Rashba-type spin polarization in antiferromagnetic $MnBi_2Te_4$(0001). *Phys. Rev. B*, **100**, 12, 121104 (2019). doi: 10.1103/PhysRevB.100.121104.

[208] S.-H. Wei and A. Zunger. Alloy-stabilized semiconducting and magnetic zinc-blende phase of MnTe. *Phys. Rev. Lett.*, **56**, 22, 2391 (1986). doi: 10.1103/physrevlett.56.2391.

[209] M. F. Islam, C. M. Canali, A. Pertsova, A. Balatsky, S. K. Mahatha, C. Carbone, A. Barla, K. A. Kokh, O. E. Tereshchenko, E. Jiménez, N. B. Brookes, P. Gargiani, M. Valvidares, S. Schatz, T. R. F. Peixoto, H. Bentmann, F. Reinert, J. Jung, T. Bathon, K. Fauth, M. Bode and P. Sessi. Systematics of electronic and magnetic properties in the transition metal doped Sb_2Te_3 quantum anomalous Hall platform. *Phys. Rev. B*, **97**, 15, 155429 (2018). doi: 10.1103/physrevb.97.155429.

[210] Y. Cao, J. A. Waugh, X.-W. Zhang, J.-W. Luo, Q. Wang, T. J. Reber, S. K. Mo, Z. Xu, A. Yang, J. Schneeloch, G. D. Gu, M. Brahlek, N. Bansal, S. Oh, A. Zunger and D. S. Dessau. Mapping the orbital wavefunction of the surface states in three-dimensional topological insulators. *Nat. Phys*, **9**, 8, 499 (2013). doi: 10.1038/Nphys2685.

[211] L. Fu. Hexagonal warping effects in the surface states of the topological insulator Bi_2Te_3. *Phys. Rev. Lett.*, **103**, 26, 266801 (2009). doi: 10.1103/physrevlett.103.266801.

[212] T. V. Menshchikova, M. M. Otrokov, S. S. Tsirkin, D. A. Samorokov, V. V. Bebneva, A. Ernst, V. M. Kuznetsov and E. V. Chulkov. Band structure engineering in topological insulator based heterostructures. *Nano Lett.*, **13**, 12, 6064 (2013). doi: 10.1021/nl403312y.

[213] W. Zhang, R. Yu, H.-J. Zhang, X. Dai and Z. Fang. First-principles studies of the three-dimensional strong topological insulators Bi_2Te_3, Bi_2Se_3 and Sb_2Te_3. *New J. Phys.*, **12**, 6, 065013 (2010). doi: 10.1088/1367-2630/12/6/065013.

[214] S. R. Park, J. Han, C. Kim, Y. Y. Koh, C. Kim, H. Lee, H. J. Choi, J. H. Han, K. D. Lee, N. J. Hur, M. Arita, K. Shimada, H. Namatame and M. Taniguchi. Chiral orbital-angular momentum in the surface states of Bi_2Te_3. *Phys. Rev. Lett.*, **108**, 4, 046805 (2012). doi: 10.1103/physrevlett.108.046805.

[215] Z.-H. Zhu, C. Veenstra, S. Zhdanovich, M. Schneider, T. Okuda, K. Miyamoto, S.-Y. Zhu, H. Namatame, M. Taniguchi, M. Haverkort, I. Elfimov and A. Damascelli. Photoelectron spin-polarization control in the topological insulator Bi_2Se_3. *Phys. Rev. Lett.*, **112**, 7, 076802 (2014). doi: 10.1103/physrevlett.112.076802.

[216] D. Rosenbach, N. Oellers, A. R. Jalil, M. Mikulics, J. Kölzer, E. Zimmermann, G. Mussler, S. Bunte, D. Grützmacher, H. Lüth and T. Schäpers. Quantum transport in topological surface states of selectively grown Bi_2Te_3 nanoribbons. *Adv. Electron. Mater.*, **6**, 8, 2000205 (2020). doi: 10.1002/aelm.202000205.

[217] Y. Xu, I. Miotkowski and Y. P. Chen. Quantum transport of two-species Dirac fermions in dual-gated three-dimensional topological insulators. *Nat. Commun.*, **7**, 1 (2016). doi: 10.1038/ncomms11434.

[218] Y. Xu, I. Miotkowski, C. Liu, J. Tian, H. Nam, N. Alidoust, J. Hu, C.-K. Shih, M. Z. Hasan and Y. P. Chen. Observation of topological surface state quantum Hall effect in an intrinsic three-dimensional topological insulator. *Nat. Phys.*, **10**, 12, 956 (2014). doi: 10.1038/nphys3140.

[219] J.-Z. Fang, H.-N. Cui, S. Wang, J.-D. Lu, G.-Y. Zhu, X.-J. Liu, M.-S. Qin, J.-K. Wang, Z.-N. Wu, Y.-F. Wu, S.-G. Wang, Z.-S. Zhang, Z. Wei, J. Zhang, B.-C. Lin, Z.-M. Liao and D. Yu. Exchange bias in the van der Waals heterostructure $MnBi_2Te_4/Cr_2Ge_2Te_6$. *Phys. Rev. B*, **107**, 4, l041107 (2023). doi: 10.1103/physrevb.107.l041107.

[220] R. Zhu, W. Zhang, W. Shen, P. K. J. Wong, Q. Wang, Q. Liang, Z. Tian, Y. Zhai, C. wei Qiu and A. T. S. Wee. Exchange bias in van der Waals $CrCl_2/Fe_3GeTe_2$ heterostructures. *Nano Lett.*, **20**, 7, 5030 (2020). doi: 10.1021/acs.nanolett.0c01149.

[221] T. Zhang, Y. Zhang, M. Huang, B. Li, Y. Sun, Z. Qu, X. Duan, C. Jiang and S. Yang. Tuning the exchange bias effect in 2D van der Waals ferro-/antiferromagnetic Fe_3GeTe_2 /CrOCl heterostructures. *Adv. Sci.*, **9**, 11, 2105483 (2022). doi: 10.1002/advs.202105483.

[222] S. Jiang, L. Li, Z. Wang, K. F. Mak and J. Shan. Controlling magnetism in 2D CrI_3 by electrostatic doping. *Nat. Nanotechnol.*, **13**, 7, 549 (2018). doi: 10.1038/s41565-018-0135-x.

[223] S. Wimmer, J. Sanchez-Barriga, P. Kuppers, A. Ney, E. Schierle, F. Freyse, O. Caha, J. Michalicka, M. Liebmann, D. Primetzhofer, M. Hoffman, A. Ernst, M. M. Otrokov, G. Bihlmayer, E. Weschke, B. Lake, E. V. Chulkov, M. Morgenstern, G. Bauer, S. Gunther and O. Rader. Mn-rich $MnSb_2Te_4$: A topological insulator with magnetic gap closing at high Curie temperatures of 45-50 k. *Adv. Mater.*, **33**, 42 (2021). doi: 10.1002/adma.202102935.

[224] M. Winnerlein, S. Schreyeck, S. Grauer, S. Rosenberger, K. M. Fijalkowski, C. Gould, K. Brunner and L. W. Molenkamp. Epitaxy and structural properties of $(V,Bi,Sb)_2Te_3$ layers exhibiting the quantum anomalous Hall effect. *Phys. Rev. Mater.*, **1**, 1, 011201 (2017). doi: 10.1103/physrevmaterials.1.011201.

[225] M. Dittmar. Fermi level tuning of a $MnBi_2Te_4$ septuple layer by epitaxial growth of a p-n-junction. Master's thesis, Julius-Maximilians-Universität Würzburg (2023).

[226] D. Rozenberg. Page - python automatic gui generator - v7.0. https://page.sourceforge.net/ (2021).

Publications

- **P. Kagerer**, C. I. Fornari, S. Buchberger, S. L. Morelhão, R. C. Vidal, A. Tcakaev, V. Zabolotnyy, E. Weschke, V. Hinkov, M. Kamp, B. Büchner, A. Isaeva, H. Bentmann and F. Reinert. Molecular beam epitaxy of antiferromagnetic $(MnBi_2Te_4)(Bi_2Te_3)$ thin films on BaF_2 (111). *J. Appl. Phys.*, **128**, 13, 135303 (2020). doi: 10.1063/5.0025933.

- C. I. Fornari, H. Bentmann, S. L. Morelhão, T. R. F. Peixoto, P. H. O. Rappl, A.-V. Tcakaev, V. Zabolotnyy, M. Kamp, T.-L. Lee, C.-H. Min, **P. Kagerer**, R. C. Vidal, A. Isaeva, M. Ruck, V. Hinkov, F. Reinert and E. Abramof. Incorporation of europium in Bi_2Te_3 topological insulator epitaxial films. *J. Phys. Chem. C*, **124**, 29, 16048 (2020). doi: 10.1021/acs.jpcc.0c05077.

- A. Tcakaev, V. B. Zabolotnyy, C. I. Fornari, P. Rüßmann, T. R. F. Peixoto, F. Stier, M. Dettbarn, **P. Kagerer**, E. Weschke, E. Schierle, P. Bencok, P. H. O. Rappl, E. Abramof, H. Bentmann, E. Goering, F. Reinert and V. Hinkov. Incipient antiferromagnetism in the Eu-doped topological insulator Bi_2Te_3. *Phys. Rev. B*, **102**, 18, 184401 (2020). doi: 10.1103/physrevb.102.184401.

- R. C. Vidal, H. Bentmann, J. I. Facio, T. Heider, **P. Kagerer**, C. I. Fornari, T. R. F. Peixoto, T. Figgemeier, S. Jung, C. Cacho, B. Buchner, J. van den Brink, C. M. Schneider, L. Plucinski, E. F. Schwier, K. Shimada, M. Richter, A. Isaeva and F. Reinert. Orbital complexity in intrinsic magnetic topological insulators $MnBi_4Te_7$ and $MnBi_6Te_{10}$. *Phys. Rev. Lett.*, **126**, 17, 176403 (2021). doi: 10.1103/PhysRevLett.126.176403.

- B. A. Kawata, C. I. Fornari, **P. Kagerer**, J. Heßdörfer, H. Bentmann, F. Reinert, A. K. Okazaki, P. H. O. Rappl and E. Abramof. Properties of topological crystalline insulator $Pb_{0.5}Sn_{0.5}Te$ epitaxial films doped with bismuth. *J. Appl. Phys.*, **131**, 8, 085302 (2022). doi: 10.1063/5.0080329.

- R. F. Penacchio, C. I. Fornari, Y. G. Camillo, **P. Kagerer**, S. Buchberger, M. Kamp, H. Bentmann, F. Reinert and S. L. Morelhão. Statistical modeling of epitaxial thin films of an intrinsic antiferromagnetic topological insulator. *Thin Solid Films*, **750**, 139183 (2022). doi: 10.1016/j.tsf.2022.139183.

- U. Müller, P. Spenst, **P. Kagerer**, M. Stolte, F. Würthner and J. Pflaum. Photon-correlation studies on multichromophore macrocycles of perylene dyes. *Adv. Opt. Mater.*, **10**, 14, 2200234 (2022). doi: 10.1002/adom.202200234.

- R. F. Penacchio, M. B. Estradiote, S. L. Morelhão, C. I. Fornari, **P. Kagerer**, M. Dittmar, S. Müller and F. Reinert. A simple recipe to create three-dimensional reciprocal space maps. *arXiv* (2022). doi: 10.48550/arXiv.2210.05427.

- A.-V. Tcakaev, B. Rubrecht, J. I. Facio, V. B. Zabolotnyy, L. T. Corredor, L. C. Folkers, E. Kochetkova, T. R. F. Peixoto, **P. Kagerer**, S. Heinze, H. Bentmann, R. J. Green, P. Gargiani, M. Valvidares, E. Weschke, M. W. Haverkort, F. Reinert, J. van den Brink, B. Büchner, A. U. B. Wolter, A. Isaeva and V. Hinkov. Intermixing-driven surface and bulk ferromagnetism in the quantum anomalous Hall candidate $MnBi_6Te_{10}$. *Adv. Sci.*, 2203239 (2023). doi: 10.1002/advs.202203239.

- **P. Kagerer**, C. I. Fornari, S. Buchberger, T. Tschirner, L. Veyrat, M. Kamp, A. V. Tcakaev, V. Zabolotnyy, S. L. Morelhão, B. Geldiyev, S. Müller, A. Fedorov, E. Rienks, P. Gargiani, M. Valvidares, L. C. Folkers, A. Isaeva, B. Büchner, V. Hinkov, R. Claessen, H. Bentmann and F. Reinert. Two-dimensional ferromagnetic extension of a topological insulator. *Phys. Rev. Res.*, **5**, L022019 (2023). doi: 10.1103/PhysRevResearch.5.L022019.

- B. Geldiyev, M. Ünzelmann, P. Eck, T. Kißlinger, J. Schusser, T. Figgemeier, **P. Kagerer**, N. Tezak, M. Krivenkov, A. Varykhalov, A. Fedorov, L. Nicolaï, J. Minár, K. Miyamoto, T. Okuda, K. Shimada, D. Di Sante, G. Sangiovanni, L. Hammer, M. A. Schneider, H. Bentmann and F. Reinert. Strongly Anisotropic Spin and Orbital Rashba Effect at a Tellurium – Noble Metal Interface. *arXiv* (2022). doi: 10.48550/arXiv:2308.02372.

Danksagung

Entgegen des typischen Klischees, wird Wissenschaft (zumindest meistens) nicht alleine von einem Menschen im Elfenbeinturm gemacht, sondern ist im Gegenteil eine große Teamleistung. Da ein Großteil der Experimente in dieser Arbeit während einer Pandemie stattgefunden hat, musste ich den ersten Ansatz (man tausche Elfenbeinturm gegen 2-Zimmer Wohnung im vierten Stock) trotzdem ausprobieren und kann einwandfrei feststellen: im Team funktionierts besser. Daher möchte ich an dieser Stellen ganz vielen Menschen danken, die direkt oder indirekt zum Entstehen dieser Arbeit beigetragen haben. Vorweg genommen: es waren ein paar wirklich ereignisreiche, tolle Jahre, die ich sehr genossen habe.

- Mein Dank geht zuallererst an Prof. Dr. Hendrik Bentmann, der mich damals während meiner Masterarbeit recht unkompliziert zum Bleiben überredet hatte und sich auch bereit erklärt hat, meine Arbeit als Doktorvater zu betreuen. Vielen Dank für die großartige Betreuung! Und vor allem konnte ich jetzt in der Rückschau feststellen, dass er mit einem Großteil seiner Ideen zur Frage wo es spannende Physik zu finden gibt sehr richtig lag. Im selben Zug möchte ich auch Prof. Dr. Friedrich Reinert dafür danken, dass ich meine Arbeit an seinem Lehrstuhl anfertigen durfte. Wie vielleicht aus dem Methodenteil ersichtlich, beinhaltete meine Arbeit eine große Menge an Neuanschaffungen, Setup-Bau und Dienstreisen. Dabei wurde mir durchwegs genug Freiraum gegeben und Vertrauen entgegengebracht, um meine Ideen und Projekte umsetzten zu können. Ich hätte mir für diese Arbeit kaum eine bessere Umgebung vorstellen können!

- Ein großes Dankeschön geht an alle aktuellen und ehemaligen Mitglieder der EP7, die ich über die letzten Jahre kennenlernen durfte und mit denen ich sehr viel Zeit auf Messzeiten, anschließenden Kurzurlauben oder einfach in der Uni verbringen durfte. Ich habe mich im Lehrstuhl von Anfang an gut aufgehoben gefühlt und die Arbeit hier stets als tolle Arbeitsatmosphäre empfunden. Insbesondere erwähnen möchte ich hier einige langjährige Bürokollegen, in zeitlich wechselnder Besetzung. Allen voran Hendrik Bostelmann-Arp, den ich seit dem Beginn meiner Masterarbeit für ca. vier Jahre durch Bildschirme hinweg anstarren durfte! Anschließend Tim Figgemeier und Max Ünzelmann, die mich großzügig in ihr Büro mit aufgenommen haben. Max, Tim und Katharina Kißner ver-

danke ich es auch, aufgrund von vielen abendlichen rein-universitätsbezogenen Zoom-sessions während des ein oder anderen Lockdowns nicht völlig verrückt geworden zu sein.

- Ein riesiges Dankeschön geht an Dr. Celso Fornari, den ich bereits zu Beginn meiner Masterarbeit hier kennenlernen durfte und der meinen Werdegang am Lehrstuhl quasi über die gesamte Zeit begleitet hat. Ohne seine Epitaxie-Expertise und Begeisterung für das gemeinsame Optimieren von Setups und Proben wäre wohl ein großer Teil der Arbeit so nicht möglich gewesen. Ob spät Abends noch mit Pizza am Lehrstuhl, völlig übernächtigt auf Messzeiten oder mit leichtem Sonnenbrand und einer Kokosnuss am Strand, es war durchwegs eine großartige Zeit!

- Ein Großteil der Daten in dieser Arbeit stammt von vielen vielen Messzeiten rund um den Globus und wurde größtenteils nachts und völlig übernächtigt zusammen mit vielen Kollegen gemessen. Daher geht ein großer Dank an alle Beteiligten, allen voran dafür dass die Messzeiten trotz meist sehr schräger Umstände durchwegs recht glatt gelaufen sind. An Dr. Thiago Peixoto, der mich auf meine erste Messzeit nach Hamburg geschleppt hat, der immer gute Antworten auf relativ absurde Fragestellungen über Zustandsdichten parat hatte und – mein persönliches Highlight – mit dem ich in Osaka einen alten Mann suchen durfte, der einen Straßenimbiss betreibt. An Raphael Crespo Vidal, der mich Stück für Stück in die Wissenschaft der magnetischen TI's eingeführt hat und mit dem ich unzählige Nachtschichten überall zwischen Japan, dem EP7 Seminarraum und Hamburg durchmachen durfte. An Tim, der mir gezeigt hat, dass man mit soft X-ray Strahlung auch Bänder messen kann, und Max ...hier gilt festzustellen, dass ich nach vielen Erklärungen jetzt langsam das Gefühl habe das mit den Matrixelementen im Ansatz verstanden zu haben. An Begmuhammet Geldiyev, der in den letzten Jahren immer dabei war, wenn Messzeiten mal richtig gut funktioniert haben und mit dem ich mir bereits zweimal einen Sonnenbrand am Strand holen durfte (also ich zumindest). Mit unzähligen Klimmzugwettbewerben, Laufrunden und Tischtennis-matches hat er das Prinzip Work-Sport Balance auf alle Fälle auf ein neues Level gehoben. An Simon Widmann, der sich aus mir nicht ganz klaren Gründen zu einem wirklich sehr langen Roadtrip nach Spanien bereiterklärt hat. Und an Abdul-Vakhab Tcakaev, von dem ich wirklich viel über XMCD gelernt habe und mit dem ich mir bereits einige Nächte zusammen um die Ohren schlagen durfte. Seine Expertise in Sachen Sum-rule Analyse von XMCD Daten hat an einigen Stellen ihren Platz in dieser Arbeit gefunden.

- Da das MBE Labor sich weder selbst aufgebaut, noch in Stand gehalten hat, vielen vielen Dank and das gesamte MBE Team in wechselnder Besetzung. Celso, der dem ganzen Unterfangen von Anfang an seine Expertise zur Verfügung gestellt hat. Sebastian Buchberger, der während seiner Masterarbeit und danach als *HiWi* einen großen Anteil daran hatte, die ganzen Wachstumsprozesse auszuarbeiten und der mir – nach einigen etwas frustrierenden Versuchen an hübsche Bänder zu kommen – abends während ich auf Messzeit war das erste Spektrum der Monolage geschickt hat, die jetzt einen Großteil dieser Arbeit ausmacht. An Chul-Hee Min, Simon Müller und Felix Spriestersbach, die das Labor mit aufgebaut haben und seit dem mit vielen 4f Elementen kontinuierlich für einen guten Kammerdruck gesorgt haben. Und natürlich an zwei weitere Masteranden, die ich betreuen und mit denen ich zusammenarbeiten durfte, Marco Dittmar und Eduard Mantel, die im letzten Jahr noch einige Herzensprojekte von mir vorangetrieben haben.

- Mein großer Dank geht auch an die vielen Menschen an sehr vielen Synchrotron-Endstadtions und Kollaborationspartner, mit denen ich in den letzten Jahren zusammenarbeiten durfte und von denen ich von Anfang an sehr viel lernen konnte. An Matthias Kalläne, Jens Buck, Florian Dieckmann, Sebastian Rohlf und Tim Riedel mit denen ich über Jahre hinweg an Asphere III in Hamburg arbeiten, planen, schrauben und komissionieren durfte und ohne die der Aufbau einer MBE dort um einiges komplizierter gewesen wäre. An Louis Veyrat und Teresa Tschirner, die einen großen Anteil an allem hatten, das mit Transportmessungen an unseren Proben zu tun hatte und die sich gemeinsam mit uns durch die ersten Misserfolge gequält haben. Anna Isaeva und Laura Folkers, die viel ihrer Experise aus dem Einkristall-Wachstum in unsere MBE Projekte eingebracht haben. Felix Friedrich und Artem Odobesko, die uns noch zu ein wenig Supraleitung inspiriert haben...und Felix insbesondere auch für die Einführung in die Kunst der Verwendung von Sauerteig. And switching language a bit... to Manuel Valvidares and Pierluigi Gargiani from the ALBA Synchrotron, who had a non-neglegible part in many of the results in this work, have brought plenty of new ideas and shown me how to properly enjoy spanish and italian cuisine. To Prof. Dr. Kenya Shimada, who has agreed to host me in the course of the JSPS summer program in Hiroshima and introduced me to his group. I had a few wonderful and inspiring months there, to a large part also thanks to the technical expertise of Taichi Okuda, Kenta Kuroda and Shiv Kumar. A big thanks also to Shiv and Yogendra Kumar for a great time on a personal level. A lot of thanks also go to Alexander Fedorov, Emil Rienks and Eugen Weschke (Bessy II), Stefan Schuppler and Pe-

ter Nagel (KIT Karlsruhe), Meng-Jie Huang and Moritz Hoesch (DESY) and Eike Schwier (HiSOR and later Würzburg) for a lot of help during a lot of beamtimes.

- Neben vielen wissenschaftlichen Projekte, hatte ich während meiner Dissertation auch die Gelegenheit in einigen Organisationskomitees am Lehrstuhl und im Exzellenzcluster zu sitzen und dabei mit vielen tollen Leuten viele Retreats und Konferenzen zu organisieren. Danke an Tim, mit dem ich unseren EP7-Retreat mit vielen kulinarischen Highlights organisieren durfte, an das EP7 Weihnachtsfeier-team (Tim und Max) und an das Cluster-Admin Team, insbesondere Katharina Leiter und Kerstin Brankatschk mit denen die Orga immer ein besonderes Highlight war. Des weiteren geht ein großer Dank an unsere Sekretärinnen Rosmarie Riegel und Hiltrud Eaton für all die viele Hilfe bei viel Organisation. Und ein sehr großer Dank an Monika Seifer, auf deren Hilfe man sich immer verlassen konnte.

- Tausend Dank an alle, die sich bereit erklärt haben, diese Arbeit gegen zu lesen und viele hilfreiche Kommentare einzubringen, hier insbesondere Sebastian Buchberger, Maximilian Ünzelmann und Celso Fornari.

- Rückschauend, geht ein großer Dank an alle, die mich seit meiner Masterarbeit Stück für Stück in die Arbeit mit Vakuum-Anlagen und Photoemission eingeführt haben, insbesondere Katharina Kißner, Max Ünzelmann, Sonja Schatz und Raphael Crespo Vidal.

- Ein riesiges Dankeschön geht an meine Familie, meinen Bruder, und ganz viele Freunde, die die letzten Jahre besonders gemacht haben. An die Kommilitonen, die sich zusammen mit mir durchs Physikstudium gekämpft haben und sich teilweise immer noch oder inzwischen mit mir durch das Promotionsstudium quälen und mich selbst jetzt noch dazu bringen hin und wieder neue Seiten von Würzburg zu entdecken. Insbesondere möchte ich hier noch einmal meinen Eltern danken, die mit ihrer immerwährenden Unterstützung dieses Studium und meinen ganzen Werdegang erst möglich gemacht haben!